Experimental Study and Finite Element Analysis of Machining Behaviour of Tungsten Heavy Alloys

THESIS

Submitted in partial fulfilment
of the requirements for the degree of

DOCTOR OF PHILOSOPHY

by

CHITHAJALU KIRAN SAGAR

ID.NO. 2015PHXF0010H

Under the Supervision of

Dr. AMRITA PRIYADARSHINI

and co-supervision of

Prof. AMIT KUMAR GUPTA

BITS Pilani
Pilani | Dubai | Goa | Hyderabad

BIRLA INSTITUTE OF TECHNOLOGY AND SCIENCE, PILANI

2021

BIRLA INSTITUTE OF TECHNOLOGY AND SCIENCE, PILANI

CERTIFICATE

This is to certify that the thesis entitled "**Experimental Study and Finite Element Analysis of Machining Behaviour of Tungsten Heavy Alloys**" submitted by **Chithajalu Kiran Sagar,** ID No **2015PHXF0010H** for award of Ph.D. of the Institute, embodies original work done by him under our supervision.

Signature of the Supervisor: Amrita..

Name in capital letters: **AMRITA PRIYADARSHINI**

Designation: **Assistant Professor**

Department of Mechanical Engineering
BITS-Pilani Hyderabad Campus.
Shamirpet-Keesara road, Jawahar Nagar,
shameerpet, Hyderabad, Telangana 500078

Date: 26-3-2021

Signature of the Co-Supervisor: Agupta.

Name in capital letters: **AMIT KUMAR GUPTA**

Designation: **Professor**

Department of Mechanical Engineering
BITS-Pilani Hyderabad Campus.
Shamirpet-Keesara road, Jawahar Nagar,
shameerpet, Hyderabad, Telangana 500078

Date: 26/03/21.

ACKNOWLEDGEMENTS

"In the quest for knowledge, the beliefs of man hold the key to success." Success does not come without acknowledging the help of others. So, we have the right to work and dream of achieving it.

First of all, I wholeheartedly praise and thank God, the Paramatma, for blessing me with the immense strength, confidence, and opportunity to undertake this research work and complete it successfully.

I express my deepest gratitude to my supervisor Dr. Amrita Priyadarshini (Assistant Professor) and co-supervisor Prof. Amit Kumar Gupta (Professor) of Mechanical engineering department BITS Pilani, Hyderabad campus for their unreserved guidance, constructive suggestions, thought-provoking discussion, and unabashed inspiration in nurturing this research work.

I would like to express my most profound appreciation to Doctoral Research Committee (DRC) members for providing valuable support during this research work. I also want to thank the Doctoral Advisory Committee (DAC) members, Dr. Kurra Suresh and Dr.Sujith R, for their constructive advice and insightful comments at various research work stages.

I am grateful to express my gratitude to Prof. G Sundar, current Director and Prof. V Sambasiva Rao, former Director, BITS-Pilani, Hyderabad Campus, to provide me with all research facilities resources at the campus to carry out my research.

I extend my special thanks to Prof. Souvik Bhattacharyya, Vice-Chancellor of BITS-Pilani, Hyderabad Campus, for providing me an excellent platform for carrying my doctoral research work at the institute.

I would like to extend my sincere thanks to Prof. Vamsi Krishna Venuganti, current Associate dean AGSRD, and Prof. Vidya Rajesh, former Associate dean AGSRD their support throughout the research work.

I warmly thank Prof. S S Deshmukh, Associate dean SWD, BITS Pilani, Hyderabad campus, for their constant support during the period of Ph.D.

I sincerely extend my thanks to all faculty members of the Department of Mechanical Engineering, BITS Pilani, Hyderabad campus, for their support and encouragement to carry out my research work.

It would have been impossible to present results in this thesis without utilizing the facilities provided by a few of the laboratories. I sincerely thank Prof. and head Narala Suresh Kumar Reddy, faculty in-charge of the central workshop, Dr. Nitin R. Kotkunde, faculty in-charge of the Material testing lab, Dr. Pavan Kumar P faculty in-charge of Tribology lab, Dr. Satish

Kumar Dubey, and Prof. Jeevan Jaidi, faculty in-charge of Heat transfer lab, Prof. S P Regella, faculty in-charge of CPDR lab and Prof. Ramakrishnan Ganesan faculty in-charge of Central Analytical Laboratory for their constant support in utilizing the facilities.

I extend my thanks to all the technicians of various laboratories at BITS Pilani, Hyderabad campus, for there helpful advice while performing experiments. Especially Mr. Jinu Paul, Mr. P Sreedhar, Mr. B Chandrashekar, Mr. M Narsing Rao, and Mr. B. Laxman laboratory staff and technicians of the Department of Mechanical Engineering, for providing assistance and support while performing various experiments in the laboratory.

I would like to express my heartful gratitude to Dr. T K Nandy, Scientist G, Head, Powder Metallurgy division, DMRL, Hyderabad, for reviewing the material behaviour studies and moral support for my research work.

I am thankful to student colleagues Mr. Abhiram Chilukuri, Mr. Sidharth Kumar Shukla, Mr. Tarun Kumar, Mr. Sana Ganesh, Ms. Shreya Sexana, Ms. Devanshi Mathur, Mr. Manmohan Dash and Mr. Abhideep Tripathy for helping me while performing experiments and research discussion in various directions.

I thank all my Ph.D. colleagues at BITS Pilani, Hyderabad campus, who shared many unforgettable moments and helped me during my research work. I extend my special thanks to Mr. A Uday Kumar, Mr. Hemanth Mithun Praveen, Mr. V R Shanmukha Sundaram, Dr. M Sai Sudhakar, Dr. Swagatika Mohanty, Dr. Sonia Antil, Mr. Pavan Chauhan, Mr. Pavan Datta Jadhav, Mr. Akhil Bhardwaj, and Mr. Mohd Abdul Wahed for their friendship, research ideas and a constant source of motivation during most challenging moments of my life.

Last but not least, I am deeply indebted to my family Late Mr. C Anand Sagar (father), Mrs. C Shyamala (Mother), and Dr. C Bhaskar Rao (Brother) for their unconditional support, understanding, and sacrifices throughout all these years and standing by my side with never-ending trust and encouragement.

Besides this, I thank every individual who directly or indirectly helped me complete my thesis work successfully.

Chithajalu Kiran Sagar

ABSTRACT

Tungsten Heavy Alloy (WHA) is a two phase composite alloy having a unique combination of high density, high thermal conductivity, high strength, moderate ductility and good corrosion resistance. Due to these excellent properties, WHAs are ideally suitable for a wide range of density application, especially in kinetic energy penetrator (KEP). WHAs and depleted uranium (DU) alloys are currently the basic materials for KEPs. However, DU alloys have raised serious concerns about long-term environmental pollution and health issues. Hence, a considerable effort has been focused on improving the manufacturability of WHAs. Manufacturing of KEP involves liquid phase sintering or extrusion followed by swaging to form bars with non-uniform cross section area. Therefore, to get the desired finish/shape as well as a precise dimension, machining is indispensable as a secondary operation. However, the properties that make WHA as one of the prospective materials for KEPs, pose a challenge while machining them into long rods of desired dimensions and finish.

Present study focuses on the machinability of WHAs in terms of different machining characteristics such as chip morphology, material removal rate, cutting forces, surface roughness and tool wear under varied cutting conditions. From the machinability tests, there exists a strong relationship between various machining outputs, such as chip morphology, material removal rate, cutting force and surface roughness and input parameters namely, cutting velocity, feed rate, tool geometry and tungsten content. Furthermore, experimental tool wear results show that flank wear growth significantly affects other machining outputs. The predominant wear mechanism is identified as adhesion based on SEM analysis and three commonly used analytical tool wear rate models and one newly proposed model (modified Zhao model) are utilized for the prediction of flank wear growth and tool life. It is observed that the modified Zhao model could predict tool flank wear fairly well within error percentage of 4-7%.

The fundamental understanding of the chip formation mechanism leads to proper choice of cutting tools, workpiece fixture, cutting parameters and its optimization. However, the trial and error experimental tests are very time consuming and

expensive. Hence, a 2D FE model has been developed to overcome the limitations of experimental tests. Various parametric studies are performed to fine-tune the input parameters (especially related to material models) with the aim of producing results closer to experimental ones. It is well known that the chip formation in machining operation involves high strain-rates and temperatures, large plastic deformations, localization of failure of target material, etc. This predominantly adds complications in modelling the material behavior accurately undergoing deformation during FE simulations. Thus, four different sets of JC constants, namely, M1, M2, M3 and M4 are considered. The first three models are based on experimental approach wherein the high strain rate test data are taken from literature and material constants are determined using conventional optimization technique, GA and ABC algorithm, respectively. Whereas, M4 is determined from machining tests using the analytical approach in conjunction with PSO algorithm. Besides, damage model constants are also determined for the given grades of WHAs using a combined experimental–numerical approach. To validate the identified material and damage constants, machining outputs (cutting forces, temperature and shear strain) are predicted considering M1, M2, M3 and M4 along with the damage constants as input under different cutting conditions and compared with the corresponding experimental values. The predicted outputs obtained using M4 closely matched with that of the experimental ones with error percentage well within 10%. FE based analysis provided detailed qualitative and quantitative insight to the chip formation process that is very much required for profound understanding of the influence of machining parameters and their optimization.

Finally, multi-objective optimization is performed using two different approaches, namely, L27 orthogonal array design and full factorial design. The first approach used experimental test data, whereas the second approach used the developed FE model to generate full factorial data. The former used Grey Relational Analysis (GRA) while the latter used evolutionary algorithms, namely NSGA II, Hybrid ABC (HABC) and Hybrid Cuckoo Search (HCS) to perform multi-objective optimization. The data for GRA is derived from experimental tests based on L27 orthogonal array. While, FE simulations are performed for generating the full factorial data for the evolutionary algorithms. The optimum combinations predicted by each method is compared and

validated by performing confirmation tests. HCS outperformed others while NSGA II showed higher deviation in the predicted values. The optimum cutting conditions predicted using HCS algorithm can be employed in precise machining of WHAs for manufacture of KEPs that require stringent design tolerances.

TABLE OF CONTENTS

LIST OF TABLES

LIST OF FIGURES

LIST OF ACRONYMS

ANOVA	Analysis of Variance
ABC	Artificial Bee Colony Algorithm
ASTM	American Society for Testing And Materials
ALE	Arbitrary Lagrangian-Eulerian
AP	Armour-Piercing
BUE	Built-Up Edge
CNC	Computer Numerical Control
CS	Cuckoo Search Algorithm
CPE4RT	Four-Node Plane Strain Thermally Coupled Quadrilateral, Bilinear Displacement and Temperature
C3D8RT	Eight-Noded Thermally Coupled Brick, Trilinear Displacement, and Temperature
CPU	Central Processing Unit
DU	Depleted Uranium
DE	Differential Evolution
DOE	Design of Experiments
EDS	Energy-Dispersive X-Ray Spectroscopy
FEM	Finite Element Method
GRA	Grey Relational Analysis
GA	Genetic Algorithm
GRG	Grey Relational Grades
HABC	Hybrid Artificial Bee Colony Algorithm
HCS	Hybrid Cuckoo Search Algorithm
IFS	Initiation of Fracture Strain
JC	Johnson-Cook Model
KEP	Kinetic Energy Penetrator
LPS	Liquid Phase Sintering
MRR	Material Removal Rate
MTS	Mechanical Threshold Stress
NSGA-II	Non-Dominating Sorting Genetic Algorithm

PCBN	Polycrystalline Cubic Boron Nitride
PCD	Polycrystalline Diamond
RSM	Response Surface Method
SPS	Spark Plasma Sintering
SEM	Scanning Electron Microscope
SHPB	Split Hopkinson Pressure Bar
SA	Simulated Annealing
S/N	Signal to Noise
STD	Standard Deviation
UTS	Ultimate Tensile Strength
WHA	Tungsten Heavy Alloy
XRF	X-Ray Fluorescence Spectrometry

LIST OF SYMBOLS

A	yield strength (MPa)
a	Tolerance limit
B	hardening modulus (MPa)
B_e	Experiment wear rate constant
C	coefficient of strain rate dependency
C_C	Contiguity
C_P	specific heat of work piece (J/kg K)
C_d	Constant of element diffused layer at contact surface
C_0	ratio of shear plane length by thickness of primary shear zone
D_t	Constant co-efficient
$D_1 to D_5$	JC damage model constants
d	depth of cut (mm)
E_r	error of predicted force (%)
F_C	cutting force (N)
F_t	thrust force (N)
F_{ti}	Initial thrust force for one pass (N)
F_{min}	Minimum cutting force predicted
F_i	Non dominated front
f_1 to f_3	function equation of polynomial regression equations
f	Feed (mm/rev)
$\overline{G}$	Average grain size
G_f	Fracture energy per unit area
H	Dimension index
i	Nectar amount of food source in the position
k	Number of repeated trials for each i^{th} factor
k_w	thermal conductivity of work piece (W/mK)
K	Boolean value
K_{IC}	Fracture toughness (MPa $m^{1/2}$)
l_c	Tool flank-workpiece contact length (mm)
Lb	Lower bound input parameters

L	Levy's flight length scale
L_m	Machining length (mm)
L_{int}	interface length between tool–chip
m	coefficient of thermal softening
M	correlation coefficient
n	strain hardening exponent
n_{eq}	equivalent strain hardening exponent
N_W	Number of tungsten grains
N_M	Number of matrix grains
N_{WW}	Number of tungsten-tungsten intercepts per unit length
N_{WM}	Number of tungsten-matrix intercepts per unit length
P_1, P_2	acceleration constants
P_{ei}	Peclet number
P_k	Pressure at specific loading condition
P_i	probability associated with that food source
P_a	Probability of discovering the alien eggs
Q	Rate of heat supply (W)
q_{AB}	shear flow stress across shear plane (MPa)
R_1 - R_4	Fitted slope coefficient
R_a	Surface roughness
r_t	ratio of chip thickness
S_{ei}	Endurance limit (MPa)
S_1 - S_4	Fitted intercept coefficient
s	Actual random flight
T_m	work piece melting temperature (℃)
T	present temperature (℃)
T_k	present temperature at specific loading condition (℃)
T_r	Room temperature (℃)
t_1	chip thickness before cutting (mm)
t_2	cut chip thickness (mm)
t_m	Machining time (min.)
T_k	Temperature at specific loading condition

T_{AB}	shear plane temperature (℃)
T_{int}	average temperature across tool–chip interface (℃)
T_{min}	Minimum cutting temperature predicted
Ub	Upper bound input parameters
u, v	Solution vector
v_c	cutting velocity (m/min)
v_B	Flank wear (μm)
V_W	Tungsten volume fraction
V_M	Matrix volume fraction
v_i	new temporary food source
$V_{B\,min}$	Minimum tool flank wear (μm)
W_i	Initial weight of work piece before machining
W_f	Final weight of work piece after machining
x_g	Global optimum input variables
y_i	Experimental observed values for i^{th}experiment
Y_{opt}	Optimum value of each output factor
$y_i^*(k)$	Analogous sequence
$y_i(k)$	Mean of repeated trials
$y_0^*(k)$	Reference sequence
Z	Cutting force for combination of temperature and flank wear
Z_t	Hardness of cutting tool
Z_g	Global optimum cutting forces for combination of temperature and flank wear

Greek letters	
α	rake angle (°)
β	Relief angle (°)
β_w	Random walk factor
χ	Discriminate coefficient
Δ	absolute error
δs_1	secondary deformation zone thickness (mm)
δs_2	primary deformation zone thickness (mm)
$\delta_{io}(k)$	Deviation sequence

δ_{max}	Maximum deviation sequence
δ_{min}	Minimum deviation sequence
ε	equivalent plastic strain
$\dot{\varepsilon}_0$	reference strain-rate (s^{-1})
$\dot{\varepsilon}$	present strain-rate (s^{-1})
$\dot{\varepsilon}_k$	present strain-rate at specific loading condition (s^{-1})
ε_{AB}	equivalent strain along shear plane
$\dot{\varepsilon}_{AB}$	equivalent strain-rate along shear plane (s^{-1})
ε_k	Strain at specific loading condition
ε_f	Fracture strain
ε_{fk}	IFS at specific loading condition
ϕ	shear angle (°)
φ_i^e	randomly selected real number in the interval [-1,1]
γ_{pre}	Predicted grey relational grade
Γ	standard gamma function
λ	average friction angle between tool-chip interface (°)
λ_i	Total mean grey relational grade
λ_o	Mean grey relational grade at optimum level
ν	Poisson's ratio
θ_f	Temperature (°C)
$\Delta\theta_{Exp}$	Average experimental Temperature rise (°C)
$\Delta\theta_{At}$	Analytical Temperature rise (°C)
θ_{fi}	Initial temperature for one pass (°C)
ρ	Density of workpiece (kg/m^3)
σ	flow stress (MPa)
σ_n	Normal stress (MPa)
σ_k	Equivalent plastic strain at specific loading condition
σ_L	Levy flight function
ψ	angle between the resultant cutting force and shear plane (°)
ψ_i	Grey relational grade for i^{th} experiment
$\zeta_i(k)$	Grey relation coefficient

ζ	ratio of plastic zone tool–chip interface thickness to chip thickness

Chapter1 INTRODUCTION

The current chapter briefly describes the broad research area, provides the background of the study and gives an overview of the proposed research work. Finally, the objectives of the current research work and outline of the thesis are presented.

1.1 Tungsten heavy alloys and its applications

Tungsten Heavy Alloy (WHA) is a two phase composite alloy consisting of a primary phase (nearly spherical) tungsten particles and a secondary phase of a matrix of iron-nickel elements. These alloys provide a unique combination of high density, high thermal conductivity, high strength, moderate ductility and good corrosion resistance. The most outstanding property of WHA is the high density of 17-19 g/cm^3. Such comparable densities are only reached by gold or platinum metals, which are considerably more expensive. Other exotic materials like rhenium, uranium or tantalum achieve these densities, but are either too difficult or expensive to obtain, or have unsatisfactory mechanical characteristics. Due to these excellent properties, WHAs are ideally suitable for a wide range of density applications such as counterweights, inertial masses, radiation shielding, sporting goods, and ammunitions (Hong, Ryu and Baek 2002, Kiran, et al. 2016), as shown in Figure 1.1

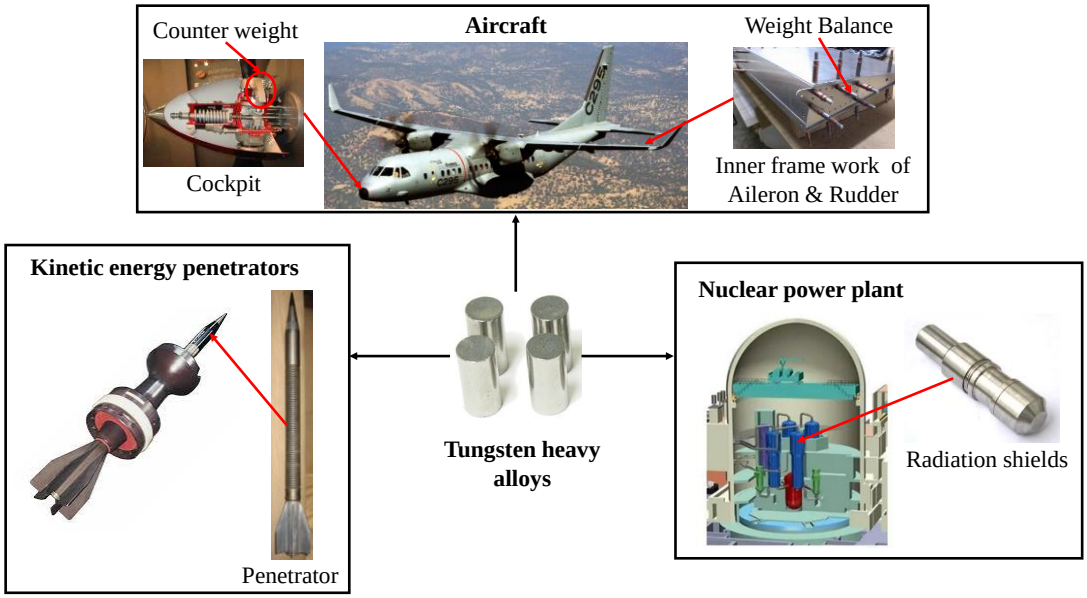

Figure 1.1 Applications of WHAs

1.2 Kinetic energy penetrators

A kinetic energy penetrator (KEP) is a type of weapon that does not contain explosives, like that of a bullet, instead uses kinetic energy to penetrate the target. High density materials enable the long rod penetrators to bring a large amount of kinetic energy to bear upon a small presented area of a target, while high strength and good ductility ensure penetrators surviving the severity of their launch and touchdown. WHAs and depleted uranium (DU) alloys are currently the basic materials for KEPs. However, DU alloys have raised serious concerns about long-term environmental pollution and health issues, so a considerable effort has been focused on improving the susceptibility of WHAs. WHAs with tungsten content 90-97% possess an excellent combination of mechanical properties comparable to DU, thus, replacing DU in various high density applications. Table 1.1 shows the mechanical properties of both DU and WHA.

Table 1.1 Mechanical properties of DU and WHA

Mechanical Properties	**DU** (Crowe, Hasson and Joyce 1980)	**WHA** (Das,et al. 2010)
Tensile Strength	1130-1580 MPa	580- 1400 MPa
Elongation	2-25%	5-30%
Density	18-18.6 g/cm^3	16-18.8 g/cm^3
Hardness	Up to 42 HRC	>29.5 HRC
High temperature stability	Up to 960 °C	Up to 1000 °C
Thermal conductivity	27.5-35 W/m-K	50-70 W/m-K
Liquid phase temperature	1100-1200 °C	1200-1350 °C

The density of WHAs increases with the tungsten content, which makes it indeed a material of choice for high density applications. But with the increase in density, ductility of the material decreases and hardness increases, making these alloys as one of the difficult to cut materials (Islam, et al. 2007, Magness Jr. 1994). As it is known that parts of critical weight and tight tolerance essentially require some secondary machining operations, understanding the machining behaviour of WHAs is very much necessary.

1.3 Research motivation and scope

The defense industry is a strategically important sector in our country that continuously demands technological advancements in ammunitions. The KEP is a

type of ammunition that typically refers to a modern armor-piercing weapon, known as armor-piercing fin-stabilized discarding sabot (APFSDS), a type of long-rod penetrator. These penetrators are different from small arms bullets. APFSDS is used to attack modern vehicle armors such as tanks, aircrafts and ships. The basic principle of the KEP is that it uses its kinetic energy, which is a function of mass and velocity, to compel its way through armor. The modern KEP maximizes kinetic energy and minimizes the area over which it is delivered. This is achieved by firing with a very high muzzle velocity concentrating the force in a small impact area. While doing this, it still retains a relatively large mass maximizing the mass of whatever (though small) volume is occupied by the projectile. This demands the use of densest metals as the most feasible solution. The core of a KEP is made up of WHA which is commonly 10–30 mm in diameter and 500–800 mm in length. As more modern penetrators are developed, their length tends to increase and the diameter tends to decrease.

1.4 Need of study on machining of Tungsten heavy alloys

The efficiency of KEPs depends on self-sharpening ability, high density, and high strength to withstand the impact (Das , et al. 2014, Venkatesan 1985). WHAs with higher tungsten content possess such characteristic features. These alloys are processed by liquid phase sintering followed by swaging (Prabhu, Kumar and Nandy 2018, Liang and Wang 1996). Generally, the swaged tungsten alloy bars that form the cores of KEPs may develop a non-uniform cross-section and poor surface finish (Dikshit 1998). Therefore, to get the desired finish/shape as well as a precise dimension, machining is indispensable as a secondary operation. However, the properties that make WHA as one of the prospective materials for KEPs, pose a challenge while machining them into long rods of desired dimensions and finish. WHAs are generally considered to have machinability similar to gray cast iron because of its abrasiveness and formation of small fragmented chips. Not only this, with high elastic stiffness, WHAs require greater cutting forces which essentially demands rigid tooling and adequate spindle torque for effective machining. Tool wear occurs at a much faster rate while machining WHAs because of tungsten's abrasiveness as well as high temperatures attained due to the heat generated in high speed and heavy feed machining. Hence, to avoid frequent tool replacements

(because of tool failures) and chatter (because of higher forces), Metal Removal Rate (MRR) has to be relatively low. This causes longer machining time, which leads to a lower productivity, certainly, an issue that needs utmost attention.

The age old techniques of trial and error experimental tests have, no doubt, laid the foundation stone in the area of metal cutting studies; but they are very time consuming and expensive. The focus, nowadays, is mainly to simulate the real machining operation by Finite Element (FE) models, which may substitute the expensive cutting experiments to a great extent (Becker, et al. 2018). These simulations predict some of the difficult to measure variables (stress, strain and machining temperature) that provide a detailed insight into the chip formation process. Furthermore, FE simulations take into consideration the material properties and non-linearity better than analytical models, thereby predicting results with higher accuracy. This motivates us to develop an FE model and understand the machining behavior of WHAs under varied cutting conditions using commercial FE package ABAQUS. Much of the focus would be given to the selection of an appropriate material and damage model and determination of their respective material constants while performing the FE simulations. Various parametric studies are performed to fine–tune the input parameters with the aim of producing results closer to the experimental results. FE based analysis provides detailed qualitative and quantitative insight to the chip formation process that is very much required for profound understanding of the influence of machining parameters and their optimization.

Furthermore, a methodology is developed that makes use of a hybrid approach to determine the optimal cutting parameters while machining WHAs with minimum possible experimental tests. The developed FE model is used for the generation of full factorial data required for performing multi-objective optimization. The current research work makes use of Grey relational analysis (GRA) and Non-dominating sorting genetic algorithm (NSGA-II) as benchmarks and proposes two hybrid algorithms namely, Hybrid artificial bee colony algorithm (HABC) and Hybrid cuckoo search algorithm (HCS), for performing multi-objective optimization.

Chapter2 LITERATURE REVIEW

Metal cutting or machining is the most important mechanical process in the industry through which almost all the products get their final shape and size, either directly or indirectly. The technique by which the metal is cut or removed is complex not merely because it involves high straining and heating but also because the conditions of operation are most varied in the machining process as compared to other manufacturing processes (Modern metal cutting : a practical handbook 1997). The type of input parameters selected during the machining process decides the output variables. The critical output variables are cutting force and power, surface finish, tool wear and tool failure, the size and properties of the finished product. A small change in input variables say, cutting parameters, tool geometry and workpiece or tool material may alter these output variables to a great extent (Akdemir, et al. 2012, Astakhov 2006). A large number of input variables leads to a significant number of combinations and consequently, understanding the interrelationship between the input and output variables, becomes an arduous task. Therefore, researchers have always been fascinated by the area of metal cutting both for its obvious technical and economic importance and the complexities associated with the process. Efforts are being made continuously to understand the complex mechanism of cutting in a simple and an effective way. The age-old technique of trial and error experiments has contributed significantly and is still widely used in metal cutting research. Various mathematical models have also been developed which form the core of the metal cutting theory. These models range from simplified analytical models to complex, computer-based numerical models.

WHA has emerged as one of the superior materials for high-density applications, especially in armour-piercing (AP) ammunition (Kiran, et al. 2015) because of its additional unique properties like high elastic modulus, toughness, corrosion resistance, and hardness. However, such properties pose challenges while machining during manufacture of KEPs. To overcome such challenges, there is a need for a proper understanding of machinability aspects of these alloys. Hence, a detailed literature review is presented in this chapter that gives a better insight of the recent developments and achievements in the area of conventional machining. The chapter also discusses the mechanical behavior of WHAs and the probable challenges

faced during machining of such alloys. Finally, based on the literature survey, research gaps are addressed and objectives are stated to overcome the identified gaps.

2.1 Characterization studies on WHAs

In general, WHAs are processed by three different methods, namely, liquid phase sintering (LPS), spark plasma sintering (SPS), and extrusion. Further to compact these alloys, swaging is performed. Material properties vary based on tungsten content and its alloying elements. The density, thermal conductivity, yield strength, and hardness tend to increase with the increase in tungsten content (Gero, Borukhin and Pikus 2001). Islam, et al. (2007) performed microstructural analysis on three grades of WHA (88, 93 and 95 WHA). The observations showed that an increase in tungsten content increases the grain size, solid volume fraction, contiguity, and connectivity. The tensile test and fractography study revealed that the tensile properties of these alloys are affected by the matrix volume fraction and contiguity. Kiran, et al. (2013) found that with the increase in tungsten content, there was a decrease in elongation and impact properties due to increased contiguity and reduced volume fraction of the matrix phase.

Similarly, Das, et al. (2010) found that different alloying elements like copper and iron in the matrix affected tensile behavior. The WHA containing iron exhibited superior tensile properties at room temperature because W-grain undergoes cleavage fracture due to a stronger matrix phase. In contrast, WHA containing copper exhibited inferior tensile properties as the matrix suffered interface fracture due to a relatively weaker matrix phase. On performing high-temperature tensile tests on WHA (Gong, Fan and Ding 2015), it was observed that the mechanical properties such as ultimate tensile strength, yield strength and fracture strength decreased with an increase in temperature. The findings were supported by scanning electron microscope (SEM) fractographic observations, which showed that the W cleavage and ductile rupture of matrix phase was dominant at room temperature, whereas at elevated temperatures (400-1100 °C) fracture was purely because of W/M and W/W interfacial debonding. Similarly, the effect of cyclic heat treatment was investigated (Kiran, Kumar, et al. 2016) wherein it was found that the increase in the number of heat treatment cycles increased the solubility of tungsten in the matrix and the matrix volume fraction and

consequently, improved the fracture toughness. However, no change in work hardening exponent was observed.

Further, Zhou, et al.(2004) performed high strain rate tensile impact tests taking strain rates in the range of 100-1300 s^{-1} to analyze the effect of strain softening and fracture behavior of WHA. The observations showed that an increase in strain rate increased the tensile strength, but decreased the failure strain. The fractographic observations showed that the matrix developed dimples followed by void formation and void coalescence indicating ductile failure behavior of matrix. In contrast, tungsten grains failed predominantly due to trans-granular cleavage fracture.

The high strain rate torsion test on WHA was also performed (Kim, Lee and Noh 1998) on the torsional Klosky bar. The tests revealed that the shear stress increased, while the shear strain decreased due to adiabatic shear bandings formation at a point where shear strain was minimum and shear stress was maximum. The compression tests performed on 90 WHA by (Coates and Ramesh 1991) taking strain rates in the range of 10^{-4} to 7×10^{3} s^{-1} found that the material exhibited little strain hardening. However, flow stress increased up to 25% with an increase in strain rate as more significant hardening was observed in the matrix phase than that of tungsten grains.

Similarly, Kim, et al. (1998) conducted a high strain rate compression tests for 93 WHA grade with strain rate in the range of 3000 to 5000 s^{-1} and performed controlled barreling test for temperature in the range of 25 to 725 °C for analyzing the shear band formation. SEM analysis showed that when the tests were conducted at room temperature, the shear band and fracture initiation were observed. Whereas at higher temperatures, thermal softening suppressed the shear band formation. Along the similar lines, Lee, et al. (1998) observed that flow stress increased with the increase in strain rate, but decreased with the increase in temperature. Also, work hardening decreased considerably with the increase in strain rate and temperature. Hence, it could be concluded that there exists a strong relationship between strain rate and temperature, flow stress and micro hardness. Woodward, et al. (1985) also studied the effect of strain rates on 90, 95, and 97 WHA at room temperature and

analyzed the compression flow stress behavior. The results showed that softening occurred at the higher strain rates due to cracking and self-heating of the specimens. Similarly, Gero, et al. (2001) performed tensile and compression tests at lower strain rates for 90, 93, and 95 WHA grades. From fractography studies, it was found that the failure under tension occurred due to W-W interface separation, producing cleaved tungsten grains after strain hardening in the matrix phase. In contrast, failure under compression mode occurred after deeper deformation of tungsten grains and matrix phase. From this behavior, it could be concluded that the failure mode in compression completely differed from that of tension mode due to the absence of W-W interface separation. It was also observed that with the decrease in tungsten content, there was an increase in plasticity of the alloy due to the ductile behavior of the matrix phase.

Hence, from the above literature survey, it was observed that tungsten content, and the test conditions such as strain rate, type of loading and temperature significantly affect the material properties and mechanical behavior of WHAs. The detailed literature review on manufacturing aspects and associated mechanical properties of WHAs, so presented, would help in understanding the machining behavior of WHAs and addressing the concerns related to machining of WHAs which is a requisite during manufacture of KEPs.

2.2 Manufacturing of KEPs

WHAs are gaining popularity in defense applications for the development of KEPs owing to their high density, strength, and ductility (McLaughlin, et al. 2003). Adiabatic shear localization is an important deformation and failure mechanism of materials for penetrations at high strain rates, as observed in case of KEPs. Adiabatic shear bandings when formed on penetrator head keep the penetrator head in acute shape and reduce the diameter of the penetration tunnel, thus leading to self-sharpening phenomenon (MagnessJr. 1994). But, WHAs are found to be resistant to such phenomena due to their high strain rate sensitivity. WHAs usually form mushroom-like heads, resulting in inferior penetration performance (Jinxu, et al. 2008). Thus, creating WHAs with a high susceptibility to adiabatic shear bandings has been a goal for many years. The manufacturing of KEPs involves either LPS,

SPS or extrusion followed by swaging as primary operation (Jinxu, et al. 2008, Xiaoqing, et al. 2010). WHA with 90W sintered by LPS in vacuum environment showed even grain distribution with dispersed coarse tungsten grains (Vettivel, Selvakumar and Leema 2013), whereas, SPS could produce fine grains with lesser W-W contiguity in WHA (Li, et al. 2014). Extrusion is one of the preferred methods for the generation of homogenous cylindrical specimens for WHAs (Essam, et al. 2019).

However, it was found that the hot-hydrostatic extrusion resulted in the poor susceptibility of WHA rod to adiabatic shear bandings on the axial direction (Jinxu, et al. 2008). One of the recent works stated that the self-sharpening ability can be enhanced by making improvements on the type of operations used such as hot extrusion, hot torsion, swaging (Xiaoqing, et al. 2010) and cyclic heat treatment processes (Kiran, Kumar, et al. 2016). Cury, et al. (2013) had investigated the performance of cobalt free WHA by long term vacuum heat treatment process to achieve mechanical properties close to cobalt containing WHA. The heat treatment process had improved grain refinement and solubility of tungsten grains in the matrix phase. This led to improved strength and ductility of cobalt free WHA with improved adiabatic shear bandings formation during penetration. Similarly, Luo, et al. (2016) compared the self-sharpening behavior of fine-grained WHA and conventional WHA rod with 95 W. It was observed that fine grained WHA had a 10.5% increased penetration depth compared to that of conventional WHA. This was due to W-W debonding, which was the main fracture mode for fine-grained WHA, and higher dynamic compression strength. Further, by grain refinement of higher grades of WHA using controlled heat treatment process, penetrator efficiency and adiabatic shear band formation were improved (Kim, et al. 1998).

Employing extrusion followed by swaging as the only process, it is not possible to manufacture KEPs completely. Generally, the swaged tungsten alloy bars may develop non-uniform cross-section with poor surface finish. Therefore, in order to get the desired finish/shape as well as precise dimension, machining is necessary as a secondary operation. Smooth surface finish while machining is a must since the WHAs are highly notch sensitive and any stress concentration at the surface will lead to catastrophic failure during applications, especially in case of KEPs. But precision

machining with desired surface finish can be challenging and uneconomical owing to higher values of strength, hardness and elastic modulus of the alloys (Vladimir and Leonid 1997). Machining of hard materials involves significant challenges like tool wear, high co-efficient friction, poor surface finish, segmented or discontinuous chip formation and longer machining time (A. Pramanik 2013). Hard materials can be machined by two techniques i.e., grinding and turning. Grinding is suggested for small dimensional changes because grinding involves multiple cutting edges that are randomly scattered over grinding wheel and effective rake angles vary over a large area. This would form longer contact time and cause thermal damage to workpiece material (Ruzzi, et al. 2020). Hence, grinding is not much preferred for machining WHA (Sahin 2014). On the contrary, turning operation imparts greater precision, especially with regards to features such as concentricity, roundness and thread details/dimension. However, there are only a few research articles available related to the turning of WHAs.

Although, significant efforts have been made to improve the primary processing techniques and mechanical behavior of WHAs (Das, Rao and Pabi 2010, Kiran, Kumar, et al. 2016), there are limited studies that address the challenges faced during machining of difficult to cut WHAs. Hence, the next section focuses on the machining aspects of various difficult to machine material that would help in performing machinability assessment on WHAs while exploring the alloys as prospective materials for KEPs.

2.3 Machinability aspects

The metal cutting process involves various independent and dependent variables. Independent variables are the input variables over which the machinist has direct control, as shown in Figure 2.1. The type of input parameters selected during the machining process decides the dependent variables. The important dependent or output variables are cutting force and power, surface finish, tool wear and tool failure, and the size and properties of the finished product. Machinability assessment is carried out by considering any of these output variables as one of the limiting criterion (Zimmerman , Boppana and Katbi 1989, Akdemir, et al. 2012, El-Hossainy, et al. 2010, Zheng and Liu 2014), as discussed in the subsequent sections. It is a common

practice to perform turning experiments on a lathe equipped with a dynamometer for the measurement of cutting forces that are easier to analyze and directly related to the mechanics of the cutting process (Modern metal cutting : a practical handbook 1997). Extensive efforts have been made to evaluate the machining behavior of metallic materials. The present section reviews extensively the machinability of some of the difficult to machine materials such as titanium alloys, nickel-based alloys, tungsten copper composite, and copper infiltrated tungsten to discuss and present the effect of machining parameters on cutting force, heat generation, chip formation, tool wear, surface integrity and mechanical properties (hardness, residual stress, and fatigue).

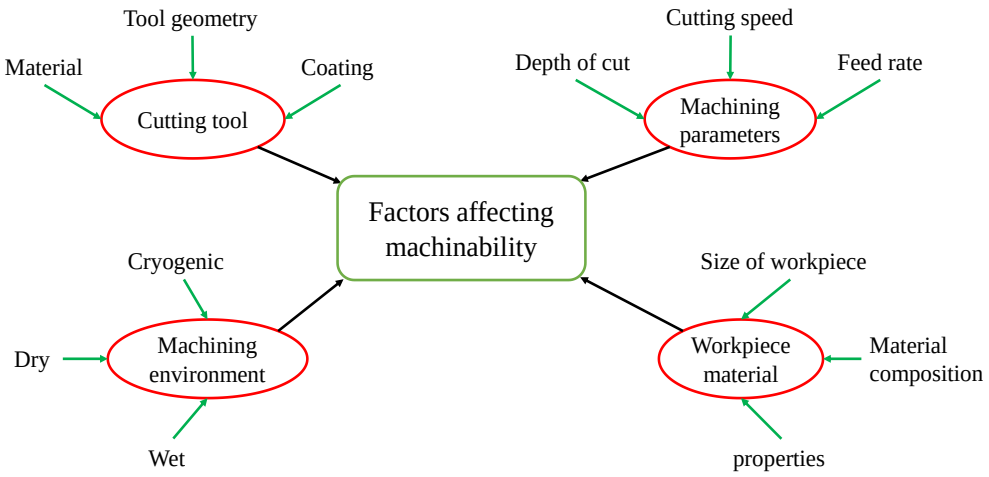

Figure 2.1 Factors affecting machinability

The machinability of titanium alloys was reviewed and possible solutions were suggested to improve the machining efficiency of the same (A. Pramanik 2013, Pramanik and Littlefair 2015). From the study, it was observed that machining of titanium alloy was a complex process and had significant challenges like saw tooth chips, high temperature, high tool wear, residual stress, high-pressure loads, and undercut parts. Hence, the use of following methods like vibration analysis kit, high-pressure coolant, cryogenic cooling, thermally enhanced machining, hybrid machining and high conductive cutting tool were suggested to overcome these challenges and improve the machinability of titanium alloy. Similarly, Thakur, et al. (2009) investigated the machinability of Inconel 718 alloy for high speed turning using cemented tungsten carbide tools. It was observed that machinability indices such as chip compression ratio were higher in Inconel 718 alloy due to work hardening during machining. A higher shear angle was observed as thin chips were

formed with reduced cutting force and friction at high speed turning. Also, flank wear and micro-chipping came out to be predominant failure modes which affected tool performance and tool life greatly.

Further, a comparative study was performed (Parida and Maity 2018) on three nickel-based alloys, namely, Inconel 718, Inconel 625, and Monel-400 during hot turning process. The investigations showed that the type of workpiece material being machined greatly affected all the output variables. Higher cutting forces and better surface finish values were found while machining Inconel 718 as compared to that of the other two alloys. Notch wear was found to be the significant for Inconel 625, whereas diffusion and crater wear were predominant for Inconel 718 and Monel-400, respectively. Similarly, machinability studies were performed on infiltrated tungsten copper alloy and tungsten copper composite, respectively using the tungsten carbide tools (Das, Chakraborty, et al. 2008). The studies showed that the cutting force components were affected by feed rate for any value of cutting speed. The surface roughness increased with feed rate and decreased with an increase in cutting speed. From the response surface method (RSM) and analysis of variance (ANOVA), it was observed that a combination of higher cutting speed followed by a medium to low feed rate was advantageous in reducing cutting forces and surface roughness values (Gaitonde, et al. 2010).

2.3.1 Cutting Forces and MRR

The cutting forces in machining is a result of the extreme conditions at the tool-workpiece interface. This interaction can be directly related to many other output variables such as the generation of heat, tool wear and quality of machined surface as well as the chip morphology (Bartarya and Choudhury 2012, Saini, Ahuja and Sharma 2012). Moreover, the estimation of cutting forces is essential for the determination of the cutting power consumption, structural design of the machine–fixture-tool system as well as condition monitoring of both the cutting and machine tools (Chen, et al. 2019). The cutting force is generally measured using a piezoelectric tool dynamometer during machining that captures the deflections or the strains in the elements supporting the cutting tool. A significant number of investigations were directed towards the prediction and measurement of cutting forces, of which few recent and most relevant ones are discussed below.

The effect of feed rate on cutting forces while machining St 44 steel. The results showed that cutting force decreased with increasing cutting speed and increased with an increase in feed rate at a constant depth of cut (Seker, Kurt and Ciftci 2004). Further, Filho, et al. (2019) investigated the effect of cutting speed, feed rate, and depth of cut on cutting force for Ti-6Al-4V and Ti-6Al-7Nb alloys under dry condition. The lowest cutting force was found when the depth of cut and feed rate was low and cutting speed was high. Further, it was observed that the depth of cut was the most significant factor affecting cutting force. Similarly, Wyen and Wegener (2010) studied the effect of cutting-edge radius on cutting forces while machining Ti-6Al-4V with changing cutting speeds and feeds. From machining tests, it was found that, as compared to cutting force, feed force was more sensitive to change in cutting edge radius. The influence of cutting speed on feed force was nonlinear and was dependent on cutting edge radius. Similar investigations were performed on AISI52100 alloy steel (Shihab, Khan and Siddiquee 2013), AISI 1050 steel (Rao, Rao and Srihari 2013) and AISI D3 steel (Ravi and Gurusamy 2020).

MRR is defined as the amount of material removed during machining from the workpiece per unit time. Experimental MRR is measured by taking the difference between initial weight of the workpiece before machining and final weight of the workpiece after machining for a specific period of time, as shown in equation (2.1). While equation (2.2) shows the analytical expression providing the relationship between cutting parameters and MRR.

$$MRR_{Exp} = \left(\frac{W_i - W_f}{t_m}\right) \tag{2.1}$$

$$MRR_{Th} = V_c f d \tag{2.2}$$

The dry turning was performed on Al6061 and the effect of process parameters were studied. It was observed that the feed rate had major influence on MRR followed by the depth of cut and cutting speed. Further, optimum process parameters were determined for finding desired MRR using ANOVA considering depth of cut of 0.15 mm and cutting speed of 429 m/min (Rajendra and Deepak 2016). Similarly, Thakur, et al. (2020) investigated the effect of cutting parameters on MRR for AISI1018 low carbon steel and plastic mould steel (P20) during turning operation on CNC lathe using tungsten carbide tools. From the Taguchi analysis, the results revealed that

cutting speed had the most significant effects on MRR, followed by the depth of cut and feed rate for both the materials. Similar kind of findings were obtained in other works as well (Nguyen and Hsu 2017, A. Thakur, et al. 2020). However, based on the available literature, it is difficult to draw a general conclusion regarding cutting force and MRR with respect to various workpiece materials, thus instigating further investigations.

2.3.2 Surface roughness

Surface roughness is measured as the average deviation from nominal surface. This is a widely used index of product quality and, in most cases, a technical requirement for mechanical products (Khare, Agarwal and Srivastava 2018). Achieving the desired surface quality is of great importance for the functional behavior of a part. However, surface roughness is dependent on numerous uncontrollable factors that influence pertinent phenomena, thus making it almost impossible to find a straightforward solution. Hascalik and Caydas (2007) studied the effect of machining parameters on surface roughness while turning Ti-6Al-4V using uncoated tungsten carbide cutting tool. The ANOVA test revealed that feed rate had a major effect on surface roughness followed by the depth of cut. Further, Taguchi analysis using S/N ratios showed that velocity of 90 m/min, a feed rate of 0.15 mm/rev and depth of cut of 0.5 mm had predicted lowest surface roughness values. Similarly, Singh, et al. (2016) studied the effect of nose radius on surface roughness while CNC turning of Aluminum 6061 under dry conditions. The ANOVA and RSM method exhibited that the nose radius followed by feed rate was the most significant parameters that affect surface roughness. Increasing the cutting speed and depth of cut increased surface roughness to a small extent. Whereas, increasing the nose radius resulted in decrease in surface roughness. Similar observations were also found while machining AISI4140 hardened steel and 300M high strength steel (Asilturk and Akkus 2011, Zheng, et al. 2018).

2.3.3 Cutting temperature

Temperature is one of the limiting factors in metal cutting operations that affect several parameters during cutting, such as tool life, mechanics of chip

formation, cutting forces, process efficiency, surface quality, etc. (Bartarya and Choudhury 2012, Liu, et al. 2020). The precise measurement of cutting temperature is not as straight forward as that of cutting forces. There is no simple equivalent device like a cutting tool dynamometer that exists for measuring the cutting temperature. Instead, several alternate methods have been proposed in the literature to measure cutting temperature during machining (Diaz-Alvarez, et al. 2017). Some of those methods are thermocouples, application of thermal paints, infrared radiation pyrometer, infrared photography, fine powder technique and metallographic methods (Goyal, et al. 2014). Most of the techniques provide limited information on complete temperature distribution during machining.

Tool work thermocouples are the most practical and economic methods. However, these are not without limitations (Kuczmaszewski and Zagorski 2013) as these measure the mean temperature over the entire contact area and is incapable of determining high local or flash temperatures, which may occur for short periods (Stephenson 1991, Michalski, Strąk and Piasecka 2017). There are also risks of obtaining inaccurate results if a built-up edge (BUE) is formed. This technique has limited application in high speed machining because of the electrical resistance properties of the cutting tools used (Buruaga, et al. 2018). Even there exists a great challenge while machining hard materials such as WHAs as they are known to form discontinuous chips (Nandam, Ravikiran and Rao 2014). This adds further discrepancy in the temperature measurement. Hence, in the past few years, vast developments in sensors, high range measuring devices and image capturing techniques have been made (Diaz-Alvarez, et al. 2017).

The radiation techniques are non–contact thermographic methods to measure the surface temperature of the body based on its emitted thermal energy. It is used for both temperature field measurement (infrared thermography) and point measurement (pyrometer or infrared thermometer). Infrared thermography includes the use of photo cameras with films sensitive to infrared radiation or the infrared cameras. These techniques are superior to thermocouples in many aspects. The advantages include fast response, no physical contact with the heat source and no interference with heat flows. This makes it even suitable for high speed machining applications

where high temperatures can be captured easily due to no direct contact with the heat source. The radiation techniques has been used by many of the researchers in the past, (J. Heigel, E. Whitenton, et al. 2017, Masoudi, et al. 2017, Lauro, Brandao and Filho 2013), just to name a few. Kus, et al. (2015) performed dry machining experiments on heat-treated AISI 4140 alloy steel using coated tungsten carbide inserts and measured experimental cutting temperature using K-type thermocouple and infrared radiation pyrometers. The investigations showed that infrared radiation pyrometer was able to capture better insight of chip tool interface temperature than K-type thermocouple due to lower thermal conductivity of coated inserts. The experimental cutting temperature was then validated with developed 3D FE machining simulation model at the tool chip contact area, and the results showed good agreement with experimentally measured temperatures. In pyrometer, the possible source of error in temperature measurement is related to the uncertainty of the surface emissivity. Knowing the exact surface emissivity is extremely difficult because it varies with surface temperature, surface roughness and possible phase transitions (Sutter and Ranc 2007). On the contrary, infrared photography has come up as one efficient technique that can overcome most of the above mentioned challenges and provide better accuracy in temperature measurement during machining. Kuczmaszewski and Zagorski (2013) used infrared camera while face milling of magnesium alloys. It was observed that temperature measured by the infrared camera was the most suitable method in terms of temperature measurement in unstable areas as compared to the thermocouple method. Further, Cotterell, et al. (2013) used infrared thermal imaging while machining Ti-6Al-4V alloy during the milling process at low speed and feed rates. The measured experimental cutting temperatures were validated with the Ernst-Merchant thermal model by video analysis technique.

2.3.4 Chip morphology

Chip morphology is one of the important parameters to determine the machinability of any material. Different types of chips are formed under various cutting conditions and are known to affect output variables such as cutting forces, temperature, tool wear, and surface finish (Buruaga, et al. 2018). Generally, four types of chips are formed during machining, namely, continuous type, continuous with BUE, discontinuous type and serrated type. From the available literature, it was

observed that the machining of hard materials usually formed serrated or discontinuous chips due to their high strength, hardness and lower thermal conductivity (Cotterell, et al. 2013, Parida and Maity 2018). Zang, et al. (2018) investigated serrated chip formation during machining Ti-6Al-4V alloy for various cutting speeds and developed FE model to identify the effect of thermal conductivity on the degree of segmentation and the adiabatic shear localization. The results of simulation and experimental SEM analysis of chips showed that with the increase in cutting speed and decrease in thermal conductivity, the tendency of chip segmentation increased. The high-temperature zones, as predicted in simulations, illustrated the adiabatic shear due to material softening and deformation.

While machining Inconel 718 alloy (Pawade and Joshi 2011, Rakesh and Datta 2019), it was observed that the serrated chips were formed at higher cutting speeds. In contrast, continuous helical chips were observed at lower cutting speeds. Chip serration at higher cutting speeds was attributed to the shear instability and intense localized deformation in the primary deformation zone. While at lower cutting speeds, the dominance of strain hardening and thermal softening led to continuous helical chips. Further, Das, et al. (2008) found discontinuous chips almost powder form with serrated edges while machining infiltrated copper tungsten alloy. Similar kind of chips were found when tungsten carbide was machined using CBN tools (Liu and Li 2001). Nandam, et al. (2014) also observed discontinuous chip while machining 90, 93 and 95 WHA grades under cryogenic conditions.

2.3.5 Tool wear

WHAs are one of the difficult to machine materials that cause rapid tool wear because of its high yield strength and hardness (Lim, et al. 1993, Young 1996). It is well known that cutting tool wear profoundly affects the parts productivity, production costs, dimensional accuracy, and workpiece surface integrity. Hence, a better understanding of the wear mechanisms during machining operation remains essential. In general, the distinct wear mechanisms that are predominant under various cutting conditions are as follows: abrasion, adhesion, plastic deformation, oxidation, diffusion, and chipping or notching (Mativenga and Hon 2005, Najar and Butt 2018, Kuram 2016). Machining of hard materials, as in the case of WHAs involves discontinuous chip formation, which possibly leads to formation of abrasive

or adhesive wear on the flank surface with BUE (Dargusch, et al. 2018, Jahan, et al. 2019, Venugopal, Paul and Chattopadhyay 2007). Chen, et al. (2018) evaluated abrasiveness index and observed diffusion, chemical, abrasive, and microchipping as the significant cause for rapid crater wear while dry machining high chromium cast iron using PCBN inserts. Similarly, Kagnaya, et al. (2014) observed severe abrasion and pullout phenomena during dry machining on AISI 1045 steel using WC-6Co uncoated carbide tools near chip/tool contact. Zhang, et al. (2014) also evaluated tool failure for TC21 alloy under dry machining using coated carbide tools, and from SEM analysis it was found that adhesion and chipping were significant factors responsible for tool failure. Tang, et al. (2019) found the predominant wear mechanism had changed as the hardness of the work material changed for PCBN tool during dry machining of AISI D2 hardened steel by varying the hardness in the range of 40-60 HRC under similar cutting conditions. Wu, et al. (2018) performed tool wear studies on PCD tools by micro end milling operation on tungsten carbide and found the occurrence of brittle fracture and generation of micro defects on the milled surface.

Once the tool wear mechanism has been identified, the prediction of tool wear by analytical method plays a significant role in avoiding a large number of trial and error experiments. Usui, Shirakashi and Kitagawa (1984) developed an analytical tool wear model that was able to capture crater and flank wear for tungsten carbide tools for a wide variety of tool shapes and cutting conditions. Similarly, Zhao, Barber and Zou (2002) modified Usui wear model by incorporating temperature-dependent hardness constants, which in turn captured thermal softening effects of the cutting tool. Luo, et al. (2005) developed a new flank wear model that captured the relative sliding velocity between tool and workpiece, the hardness of tool, and temperature effects on tool flank wear reasonably well. In a few of the recent works, FE models have been used in conjunction with user-defined subroutines for deriving tool wear model constants to predict the tool wear growth (Zanger and Schulze 2013, Attanasio, et al. 2008, Yen, et al. 2004). Likewise, Li, et al. (2019) developed a meta-learning tool wear rate model to predict tool wear for the dynamic process control system for changing machining conditions. Considering the fact that prediction of tool life using tool life equations is very tedious, there is always a need for an accurate tool wear

rate model that is able to capture tool wear mechanism efficiently, mainly, for difficult to cut materials such as WHAs.

2.4 Application of FEM in machining

The focus, nowadays, is mainly to simulate the real machining operation by FEM, which may substitute the expensive cutting experiments to a great extent. These methods not only aid in better understanding of machining behavior of emerging alloys but also lead to optimization of cutting parameters with lesser experimental tests data (Arrazola, et al. 2013). Numerous FE codes such as DEFORM, FORGE2, ABAQUS/Explicit, Ansys/LS-DYNA, MSC Marc, and Thirdwave AdvantEdge have come up that are being used by the researchers. ABAQUS/Explicit and Thirdwave systems' AdvantEdge were used for simulation and compared the results with experimental test results (Dali, Ghani and CheHaron 2017). It was found that there were hardly any research papers available related to the FE simulations of machining WHAs. But similar researches were found related to machining simulations of other hard materials which can be correlated with machining behavior of WHA.

In one of the recent works, the ALE-FEM model was developed to understand the tool edge geometries while hard turning of AISI 4340 using coated PCBN tools (Coelho, Ng and Elbestawi 2007, Jiang and Wang 2019). Effect of different tool wear models and friction models on the parameters affecting the wear process for cemented carbide tools while machining alloy 718 were analyzed using MSC Marc (Diaz-Alvarez, et al. 2014). 3D numerical predictions of tool wear based on modified Takeyama and Murata wear model was simulated using SFTC Deform 3D software (Ozel, et al. 2011). Similarly, a 3D model was developed to predict the cutting forces for various cutting speeds and feed rates using a modified Zerilli-Armstrong model for Co-Cr-Mo alloy using Deform 3D software (Trimble, et al. 2020). The effect of tool geometry on chip segmentation was analyzed using the FE model by incorporating stress triaxiality factor in the damage model for AISI1045 steel during machining (Devotta, et al. 2017).

It is well known that the chip formation in machining operation involves high strain-rates and temperatures, large plastic deformations, localization of failure of target material, etc. This predominantly adds complications in modelling the material

behavior accurately undergoing deformation during FE simulations. The inherent strain rates experienced during machining are usually in the order of 10^4 ~10^6 s^{-1} which is 6 to 7 orders of magnitude higher than typical values used in quasi-static tension tests (Zhou, et al. 2017, Oxley 1963, Frueh, et al. 2016). This predominantly adds complications in modeling the material behavior undergoing deformation during FE simulations. Hence, the selection of an appropriate material constitutive model and the damage model, as well as the determination of respective material constants, are vital concerns to develop realistic FE models for machining.

2.4.1 Material model

Several classical plasticity models have been widely employed that represent, with varying degrees of accuracy, the material flow stresses as a function of strain, strain rate and temperature. These models include the Oxley model, the Johnson-cook model, Zerilli-Armstrong model, Mechanical Threshold stress (MTS) model, Litonski-Batra model, Maekawa model, etc. (Arrazola, et al. 2013). The Johnson-Cook (JC) plasticity model has been successfully used by many researchers because of availability, as an in-built model, in most of the commercial FE codes (Bosetti , Bort and Bruschi 2013). Machining outputs such as temperature distributions, cutting forces, residual stresses in the machined surface, strain in the deformation zones and chip formation characteristics were simulated for a continuous and segmented chip (Palanisamy, et al. 2020, Trimble, et al. 2020) using JC model. Mabrouki, et al. (2016) found that JC model predicted chip thickness better than that of other models and gave better insight.

Besides selecting a suitable material constitutive model, there is also a need to determine the material model constants, precisely for obtaining accurate results using FE models. In the past, researchers have developed different methods to derive the JC constants for various materials, namely, experimental, analytical, and numerical techniques. The experimental technique includes performing high strain testing and then making use of the obtained stress strain data in conjunction with conventional optimization techniques to determine the JC constants (Zhou, et al. 2017). Taylor's impact tests and Split Hopkinson Pressure Bar (SHPB) are typically categorized as high strain rate tests. These tests are capable of undergoing very high strain rates closer to what is expected in machining or ballistics for certain materials.

But the availability of this advanced equipment is very limited because of the extremely high cost and need of skilled operator. Moreover, conducting high strain rate tests for materials like WHAs is highly challenging because of their higher hardness and increased work hardening effects at higher strain rates (Gong, Fan and Ding 2015). An advancement over standard optimization methods in experimental approach is the use of evolutionary computational algorithms which identify material parameters through a fine grain search technique and state superiority over classical data fitting techniques (G. Chen, et al. 2012, Gupta, et al. 2013). The numerical approaches use FE analysis to simulate the machining process in which the predicted outputs (chip morphology, machining force, temperature, etc.) are compared to that of experiments and JC constants are fine-tuned using an inverse approach (Bosetti , Bort and Bruschi 2013, Sagar, Priyadarshini , et al. 2018). The analytical approach includes the use of inverse identification algorithms in conjunction with either SHPB tests or machining tests to determine material characterization and predict the flow stress behavior of the material (J. C. Filho 2017). Table 2.1 shows a summary of some of the relevant works related, especially to the analytical approach for the identification of JC constants.

Table 2.1 Summary of analytical approach for determination of JC model constants

Experimental tests	Strain rates	Method	Material	% Error
SHPB	10^4 s^{-1}	FEM orthogonal simulation	Steel (Aviral Shrota* 2012), 51CrV4 steel (Zabel, Rödder and Tiffe 2017)	10
		Levenberg–Marquardt Algorithm using orthogonal turning model	AISI 52100 (Aviral and Martin 2011), AA2024-T351 (Saleem, et al. 2017)	10
		Descriptors and proxies using press forge model	Hyperfoam (Martin Bäker 2013)	15
		Extended Oxley's shear zone theory	AISI 1045 (Lalwani, Mehta and Jain 2009)	15
		Response surface method	Inconel 718 (Amir Malakizadi 2016), 95 WHA (Sagar, Kumar, et al. 2019)	16
Impact	10^6 s^{-1}	Impact on flat-ended	AISI 4340 (Chakraborty , Shaw and Banerjee 2015)	15

		cylindrical rod using Axisymmetric model		
		Computational modeling of Taylor impact test	OFHC copper (Campagne-Lambert, et al. 2008)	18
Machining	10^6 s^{-1}	Inverse Oxley's predictive theory and optimization of cutting forces by PSO and iterative gradient method	AISI 1045 (J. C. Filho 2017), AL 6082-T6 (Ning and Liang 2019)	5
		Kalman filter using orthogonal turning model	AISI 4140 (Mathias, Aylin and Jan-Eric 2014), Rene-108 (Niaki, Ulutan and Mears 2015)	1.64

The literature survey indicates that there is limited data available related to high strain testing of WHAs and as a result, JC constants for the same are also unavailable. The possible reason could be the difficulties and limitations associated with carrying out of the high strain rate tests for different grades of WHA using drop weight or SHPB tests because of their high hardness and strain hardening effects. Furthermore, it also is noted that inverse analysis showed higher accuracy over other approaches. Though many works are available based on inverse analysis, none has considered WHA as the work material.

2.4.2 Damage model

The damage models describe failure in the material as a function of the mechanical variables such as stress, strain, temperature, strain rate, etc., such that if the prescribed function reaches a critical value, failure is expected in the material. Such a state is called the damage initiation criterion. Further, the failure or element deletion occurs due to the accumulation of strain at the onset of damage. The process of element deletion is controlled by damage initiation criteria and damage evolution process (Abaqus, User's manual Version 6.14-1 2014). The use of a damage model in FE modeling in machining is necessary to simulate both the realistic tool penetration into the workpiece as well as to predict discontinuous chips during the metal cutting process. The elements at the chip-tool interface undergo severe plastic deformation in the form of progressive degradation of material stiffness leading to

skewing of elements. These skewed elements have reached the damage initiation criterion threshold and have lost completely load-bearing capacity leading to element deletion (Hibbitt, and Karlsson & Sorensen 2007). This process of damage is most successively governed by the JC damage model and has been commonly used among other damage models during FE machining simulations (Palanisamy, et al. 2020). Jomaa, et al. (2017) applied the JC material and the damage model to simulate the high-speed machining of AA7075-T651 alloy for analysis of serrated chip formation. Chen, et al. (2014) calculated fracture initiation strain in the chip layer using JC plastic and damage models by simulating the cutting process of aluminum alloy and found that the fracture strain had an effect on predicted cutting force and deformation at high strain rate conditions. Hence, the failure model and the determination of failure parameters are crucial to the deformation at high strain rate conditions.

The failure parameters of the JC damage model are calculated according to the failure strain measured from the flow curves at various loading conditions such as quasi-static and dynamic split Hopkinson bar tests. Johnson and Cook (1985) determined the fracture constants of the JC damage model according to the fracture strain measured using the tensile Hopkinson bar test. The fracture strain was identified by measuring the cross-sectional area of post-tested fractured specimens and the maximum stress point in the flow curves was considered as the initiation of localized instabilities. Majzoobi and Dehgolan (2011) derived JC damage model constants by performing low strain rate quasi-static tensile test to high strain rate tests on flying wedge apparatus and combined experimental deformation with numerical simulations using LS-Dyna and then determined the constants using a genetic optimization algorithm. Similarly, Murugesan and Jung (2019) identified JC damage model constants for AISI 1045 medium carbon steel by performing low strain rate tensile test on flat, smooth round and pre-notched specimens at room and high temperature using numerical and graphical validations methods. Chen, et al. (2018) used high strain rate compression test at various strain rates (2500-10000 s^{-1}) and temperatures (20 to 300 °C) for Ti-6Al-4V alloy. The failure initial strains for flow stress were calculated at the transition from stable plastic to damage evolution stage using a combined experimental-numerical approach and fitted JC damage model by GA optimization method.

2.5 Multi-objective optimization

The main focus of the machinability study is to improve the quality of machined products and reduce the manufacturing cost. This summons optimization problem which seeks identification of the best parametric combination for the machining process. However, machining is a complex process involving numerous input cutting parameters and multiple output variables that are conflicting in nature (material removal rate and surface roughness). Hence, the optimization of machining parameters has to be necessarily a multi-objective optimization task (Serra, Chibane and Duchosal 2018). Though much work has been reported in the literature to improve the process performance, proper selection of process parameters remains a challenge. There are several multi-objective optimization techniques for the same as goal programming, simulated annealing (SA), grey relation, and genetic algorithms (GA), and so on. Generally, optimization of the machining process requires a large number of experimental tests to be performed, which is time-consuming and expensive. As a result, experimental test arrays are usually chosen based on a compromise between the cost of the experiments (cost includes the time required to run the experiments) and the required accuracy of the results. Orthogonal arrays in terms of Taguchi's design come up as a fair compromise between cost and accuracy (A. Thakur, et al. 2020). Taguchi's design is a method that includes a plan of experiments to acquire data in a controlled manner and subsequently, execute these experiments, and analyze data for obtaining information about the behavior of the given process (Pandey, Goyal and Meghvanshi 2017).

Further, many researchers in the past have used orthogonal array along with GRA to optimize multiple responses in the machining process (Raykar, D'Addona and Mane 2015, Prakash, Gopal and Karthik 2020). The main advantage of GRA is that it requires a minimum number of experimental data set for optimization of multi-response outputs. While, the drawback is that it normalizes the output responses, and mean of normalized values are converted to Grey relational grades (GRG). The highest GRG is considered as an optimum combination, but these optimum combinations are highly localized optimum values which are deviated from global optima of output responses. To overcome such problem, many evolutionary algorithms like Nondominated sorting genetic algorithm (NSGA II), artificial bee

colony algorithm (ABC), cuckoo search algorithm (CS), differential evolution (DE), SA and particle swarm optimization (PSO) were proposed. Based on the versatility, efficiency, and accuracy of the results, NSGA II, ABC, and CS have gained a lot of popularity.

NSGA II algorithm was proposed by (Deb, et al. 2002) with fast computation, elitist multi-objective evolutionary algorithm based on the nondominated sorting approach and efficient constraint handling method. The algorithm was able to converge the optimal solution with minimum iteration. Single pass dry turning tests were performed on EN24 steel using tungsten carbide tool to minimize tool wear and maximize the MRR using NSGA II (Yang and Natarajan 2010). The electro-chemical machining was optimized using L27 orthogonal array for EN19 using NSGA II to achieve desired MRR and surface roughness (Twari, Mandal and Kumar 2015). It was observed that NSGA II could handle only two objective functions at a time for the optimization process, and the third objective function was considered as dummy function and predicted the value of the latter based on optimum combination derived (Ciro, et al. 2016). In addition to this, during the formulation of crowding distance in NSGA II, an instability was produced when the front F_i was used to restrict the population size. Consequently, the algorithm could lose some closely packed pareto optimal solutions and give place to other non-pareto optimal solution, thus leading to loss in convergence property (Deb, et al. 2002). This was solved by introducing ABC and CS algorithms which could handle more than two objective functions.

ABC algorithm was proposed by (Karaboga and Basturk 2008) and the performance of the former was compared with DE, PSO, and evolutionary algorithm. It was observed that the ABC algorithm performed better than the mentioned algorithms and was able to solve multimodal engineering problems with high dimensionality. The cutting parameters in rough turning were optimized of AISI 1045 steel using ABC algorithm for minimizing specific cutting energy and maximizing MRR using L27 orthogonal array test data (Sredanovic , et al. 2019). Das, et al. (2014) optimized surface roughness and MRR using ABC algorithm for EN31 steel for electro-discharge machining. Similarly, Hossain and Liao (2017) performed optimization on end mill operation for hot die steel for minimizing machining time and surface roughness using HABC algorithm. Further, Yildiz (2013) performed

multi-pass turning and combined Taguchi's method and ABC algorithm for optimization. Yang and Deb (2013) developed a CS algorithm for solving multi-objective optimization of complex nonlinear engineering design problems. Qiang, et al. (2018) optimized outlet power and wear rate of abrasive waterjet machining using CS algorithm for L18 orthogonal array test data. Further, Senthilkumar, et al. (2014) combined other methods like Taguchi's DOE, GRA and developed hybrid Taguchi-Grey relational and CS while hard turning AISI D3 using coated inserts to achieve minimum tool wear and surface roughness and maximum MRR. Ding, et al. (2019) developed a hybrid method by combining PSO and CS algorithm for two different engineering problems and observed that hybrid method was capable of handling nonlinear optimization problems with multi-constraints and, consequently, predicting local optimal with better performance than PSO and CS algorithms.

Based on the literature survey presented, it is clear that GRA and NSGA II optimization methods could predict optimal solutions with normalized and compromised local minima whereas ABC and CS algorithm could handle more number of response outputs with a better search strategy. To add further, the hybrid methods, so developed, showed significant improvements over these algorithms. But, most of the literature work related to machining had utilized orthogonal array design for optimization. Such an approach may end up in predicting local optima and, subsequently, fail to give priority to response parameters based on their effectiveness on the process. Hence, this demands further improvements in the existing algorithms. Research gap Table 2.2 presents the overall summary of the literature review presented in the previous sections highlighting the research gaps.

Table 2.2 Summary of literature survey

Topics	Methods	WHA
Manufacturing of KEPs	SPS method	(Li, et al. 2014, Senthilnathan, Annamalai and Venkatachalam 2018)
	liquid phase sintered	(Kiran, Venkat, et al. 2013, Das, Chakraborty, et al. 2008),

	Extrusion	(Xiaoqing, et al. 2010)
	Grinding	----------
	Turning	(Nandam, Ravikiran and Rao 2014)
Machinability aspects	Cutting forces and MRR	(Das, Chakraborty, et al. 2008, Gaitonde, et al. 2010, Nandam, Ravikiran and Rao 2014)
	Cutting temperature	
	Surface finish	
	Chip morphology	
	Tool wear analysis	**Research Gap**
Machining simulations	Material model constants	(Rohr, et al. 2008, Lee, Xiea and Lin 1998)
	Damage model constants	**Research Gap**
	Prediction of output variables	**Research Gap**
Optimization	Single-objective optimization	(Gaitonde, et al. 2010)
	Multi-objective optimization	**Research Gap**

Based on the research gaps identified from the existing literature survey, the possible solutions are proposed in Table 2.3.

Table 2.3 Research gaps and proposed solutions

Gaps	Proposed solution
Gap-1: No detailed machinability study of WHA has been reported in the literature. Only a limited study on machining of WHA has been reported.	*Sol-1:* A detailed machinability studies need to be carried out using turning experiments for different grades of WHA and need to analyze the effect of cutting parameters on response outputs
Gap-2: Limited studies have been observed related to experimental and analytical tool wear analysis of hard materials and limited discussions has been observed related to WHA.	*Sol-2:* The effect of tool geometry on tool wear and type of wear mechanism need to be identified and the development of new tool wear rate model for WHA.

Gap-3: Though extensive studies pertaining to FE machining simulations of hard materials are found in literature, no work related to WHAs have been reported so far.	*Sol-3:* There is a need to develop the FE machining simulation model, identify the effect of strain rate on the material model, and analyze chip morphology. Validation of the FE model with machining test results need to be performed.
Gap-4: Limited research work has been reported for the multi objective optimization of hard material machining and no studies have been reported related to the optimization of machining WHA.	*Sol-4:* A new hybrid multi-objective optimization model needs to be developed and validate with the existing optimization model for identifying optimum cutting parameters for machining.

2.6 Objectives of the current research work

Based on the above discussion, the following have been laid down as the objectives of the present work:

- Determination of the mechanical properties and machinability analysis of WHAs;
- Determination of the material model constants of WHAs for high deformation rates;
- FE Analysis of the chip formation process during turning of WHAs under different cutting conditions to predict cutting forces, temperatures, chip morphology, and stress;
- Experimental validation of the simulation results;
- Optimization of Machining performance measures (cutting forces, surface roughness, temperature, tool wear, etc.) while machining WHAs.

2.7 Overall work plan

This section presents the overall work plan adopted for the detailed machinability studies of WHAs and their correlation with mechanical properties, FE

modelling of chip formation and determination of optimum cutting parameters for higher productivity. Figure 2.2 illustrates the schematic representation of the overall work plan adopted in the present work.

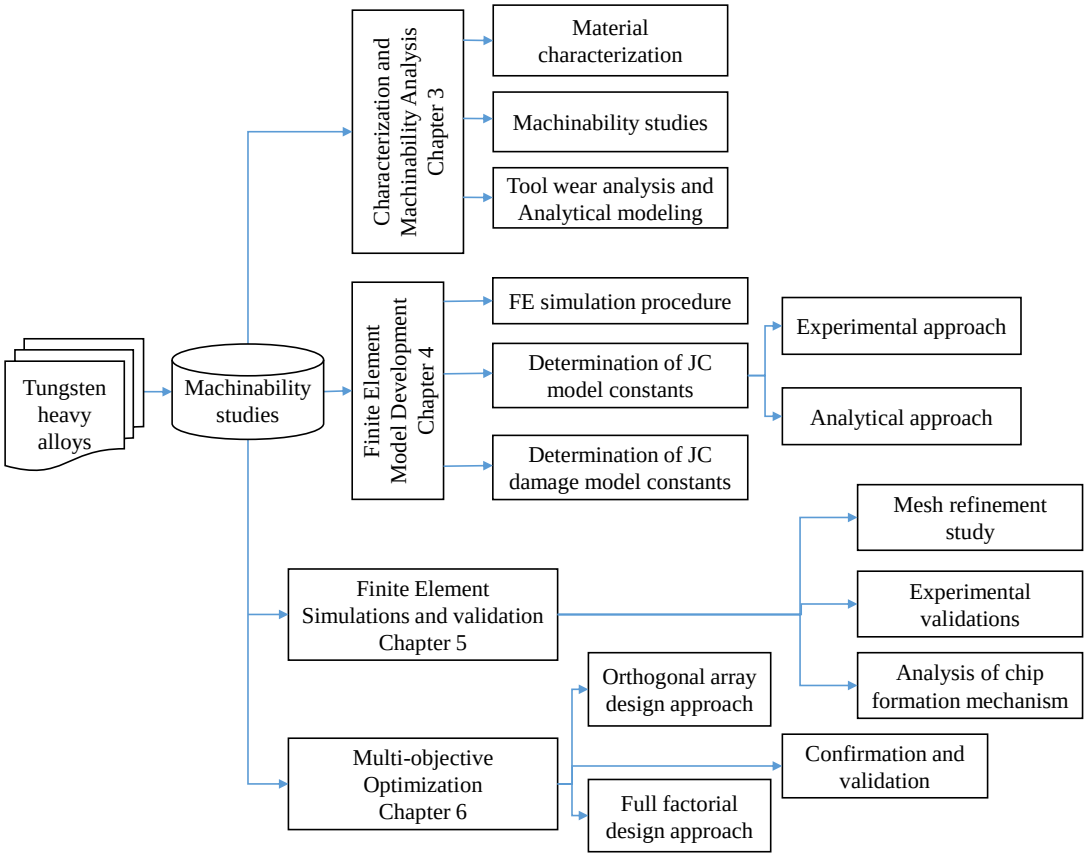

Figure 2.2 Overall work plan adopted

2.8 Thesis outline

This thesis includes seven chapters as a whole. These chapters can be summarized as follows:

Chapter 1 Provides a basic introduction to the topic chosen and briefly discusses the problem definition and research motivation.

Chapter 2 Includes a comprehensive literature review that gives a better insight of the recent developments and achievements in the area of conventional machining. Literature reviews are arranged under different headings that discuss the material characterization of WHAs and the probable challenges faced during machining of difficult to machine alloys. Finally, based on the literature survey,

research gaps are highlighted and objectives are proposed to overcome the identified gaps.

Chapter 3 Focuses on the material characterization and machinability analysis of WHA grades. A detailed microstructural analysis of the given WHA grades along with experimental studies related to machinability assessments, tool wear analysis and analytical modeling of tool wear growth during machining with varying tungsten content. This chapter attempts to explain the complex interrelationship between material properties such as hardness, ductility/brittleness and tungsten content with that of machining outputs such as cutting forces, temperature, surface roughness and tool wear.

Chapter 4 Provides a detailed description of the formulation of the 2D FE model for orthogonal cutting. This chapter presents a methodology to determine both the material and damage model constants that are used as FE inputs.

Chapter 5 Focus on mesh refinement study of 2D FE simulation model and the predicted results are compared with the experimental ones under similar cutting conditions to validate the developed FE simulation model.

Chapter 6 Explores the capability of two approaches used in multi-objective optimization, namely, orthogonal array design and full factorial design. This chapter focuses on formulating a strategy that utilizes a hybrid approach to reduce the number of experimental trials by combining the developed FE model with the evolutionary algorithms to be used for full factorial design.

Chapter 7 Concludes this thesis and suggests directions for future research.

Summary

This chapter presents an overview of the various types of studies carried out in the analysis of the metal cutting process. There has been a considerable amount of research work devoted to the development of experimental, analytical and numerical methods for providing a detailed insight into the chip formation process. Experimental methods, though an indispensable part of the metal cutting studies, are generally time-consuming and expensive. The focus is mainly to develop a robust model that would enable evaluation of machining performance, i.e., prediction of various output variables such as cutting force, temperature, chip thickness and so on

without the need for expensive machining tests. With the advent of powerful computers, FE models are gaining much of the popularity for predicting the output responses. However, there are certain key aspects in FEM which needs to be addressed adequately. Thereupon, some of the critical numerical aspects as well as the prediction capabilities of FE simulations have been discussed. Finally, recent most developments in multi objective optimization and its relevance in machining has been conferred. Based on the comprehensive literature review presented, research gaps are identified and objectives are proposed to overcome the identified gaps. Finally, the thesis outline is presented.

Chapter3 CHARACTERIZATION AND MACHINABILITY ANALYSIS

This chapter focuses on material characterization techniques and analysis of three different grades of WHAs with varying tungsten content. Besides, experimental studies related to machinability assessments, tool wear analysis and analytical modelling of tool wear growth during machining of WHAs are performed and results are discussed in much details. Machinability assessment is somewhat complicated because there is no single unique criterion based on which it can be decided. This is often evaluated through several criteria such as tool life, cutting force, surface finish, dimensional accuracy, and chip controllability. The material properties of the work material (composition, microstructure, hardness, strength, etc.) and operating conditions (cutting speed, feed, depth of cut and tool geometry) have a direct influence on the machinability of a work material. WHAs are one of the difficult to machine material that causes rapid tool wear because of its high yield strength and hardness (Lim, et al. 1993, Young 1996). It is well known that cutting tool wear highly affects the parts productivity, production costs, dimensional accuracy and work piece surface integrity. Hence, a better understanding of the wear mechanisms and prediction of tool wear growth during machining operation are equally essential. The present chapter makes an attempt to assess the material properties and machinability of these alloys as a potential material for high density applications. Such analysis may help in understanding and resolving critical issues, such as process-related problems during manufacturing and causes of failure when put in service.

3.1 Material characterization

Material characterization is the process of measuring and determining the physical, chemical, mechanical and microstructural properties of materials. The specific techniques, associated instruments and detailed analysis of various material properties of WHAs are presented in the following sections.

The goal of chemical characterization is to identify and quantify the chemical constituents of a material. It is the chemical composition that determines the density, hardness, strength and other properties of a particular material and hence, is

considered as the most crucial factor for analyzing the material behavior. Chemical composition tests were performed using X-ray fluorescence spectrometry (XRF), as shown in Figure 3.1. XRF is a non-destructive analytical technique used to determine the elemental composition of materials. Cylindrical samples of specific dimensions were prepared for the analysis. The samples were placed in X-ray chamber wherein they are bombarded with short-wavelength X-rays. These X-rays ionize the work material and result in the emission of radiation from work material. Since these emitted radiations have different energy levels and are unique for a specific element, individual atoms can be detected, allowing for a complete breakdown of chemical composition.

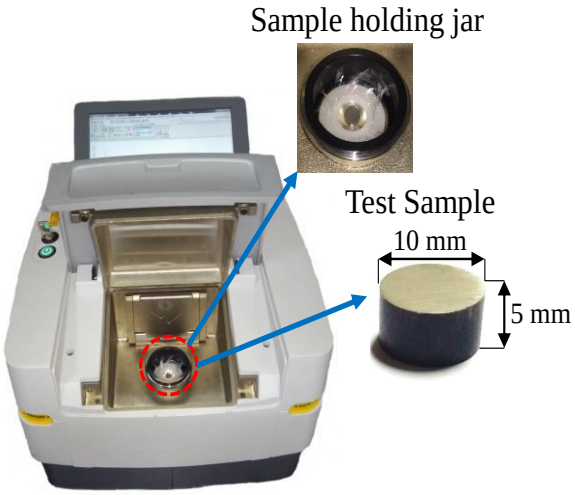

Figure 3.1 X-ray fluorescence spectrometry composition test setup (make: Panalytical EPSILON 3)

The resulting chemical compositions for the selected materials are shown in Table 3.1. The results showed that tungsten content was the major element followed by nickel and ferrous in all the three grades. However, in 90 WHA cobalt was also identified along with other alloying elements.

Table 3.1 composition of WHAs

	Composition			
Grade	Fe	Ni	Co	W
90WHA	2.5	5	2	90.5
95WHA	1.5	3	-	95.5
97WHA	1.5	2	-	96.5

3.1.1 Physical and mechanical properties

Equipment details

The knowledge of physical and mechanical properties is requisite for finding the suitability of a material for different applications. Physical properties denote the physical state of materials that are exclusive of their chemical or mechanical components. While mechanical properties determine a material's behavior when subjected to mechanical stresses. The subsequent section presents the details of the equipment used and methods adopted, followed by the results of a few of the significant properties concerning the selected work materials.

- ***Density***

The density of all the three grades of WHAs was measured using Mettler Toledo Density Kit, as shown in Figure 3.2. The density measurement was based on the buoyancy technique which utilizes Archimedes' principle. The method included measuring the mass or weight of the work sample of specific dimensions in the air M_{air} as well as in water M_{water} and then calculating the density ρ using Equation (3.1).

$$\rho = \frac{M_{air}}{M_{air} - M_{water}} \times \rho_{water} \tag{3.1}$$

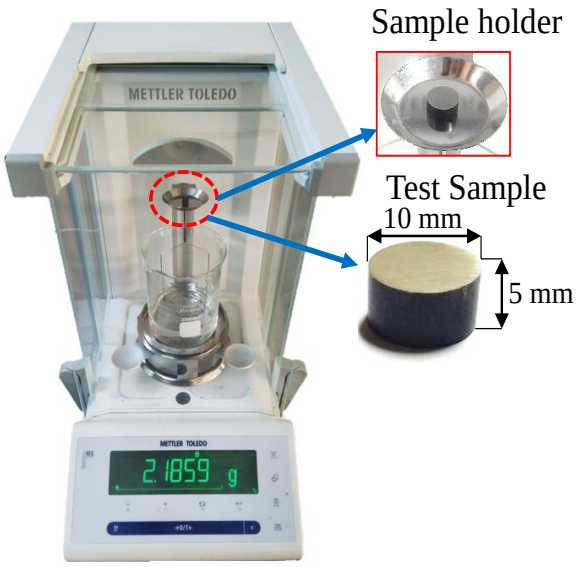

Figure 3.2 Density tester (make: MS-DNY-54)

❖ ***Hardness***

The hardness was measured on the given work materials using Micro Vickers Hardness Tester, as shown in Figure 3.3. The Vickers method is based on an optical measurement system. A square base pyramid shaped diamond was used in the Vickers scale by applying an indentation load of 1 kgf with a dwell time of 30 s for each test. The hardness value was estimated and the same process is repeated three to four times at different locations for each of the samples to confirm the average hardness values.

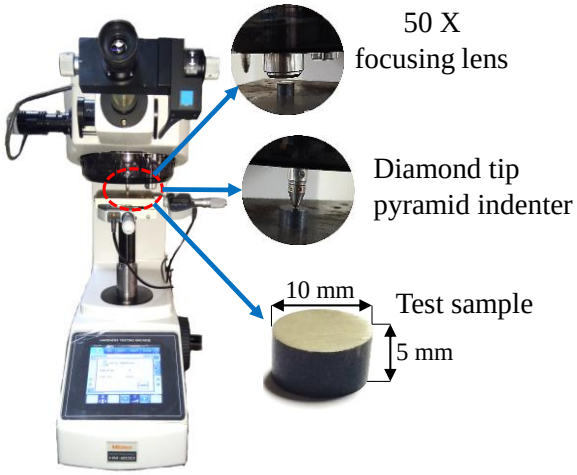

Figure 3.3 Micro-Vickers hardness tester (Mitutoyo HM-200 Series 810)

❖ ***Thermal conductivity and specific heat***

The thermal conductivity and specific heat were measured using the transient plane source method using Hot disk TPS 500 S tester, as shown in Figure 3.4. Work samples of particular dimensions were held in die with 5501 kapton sensor. The sensor was electrically connected to a power supply and sensing circuit. As the current was supplied to the sensor, an increase in temperature was observed, which was recorded over time. The heat generated was diffused into the sample at a rate dependent on the thermal transport characteristics of the material. Consequently, thermal conductivity and specific heat values for the given alloys were calculated.

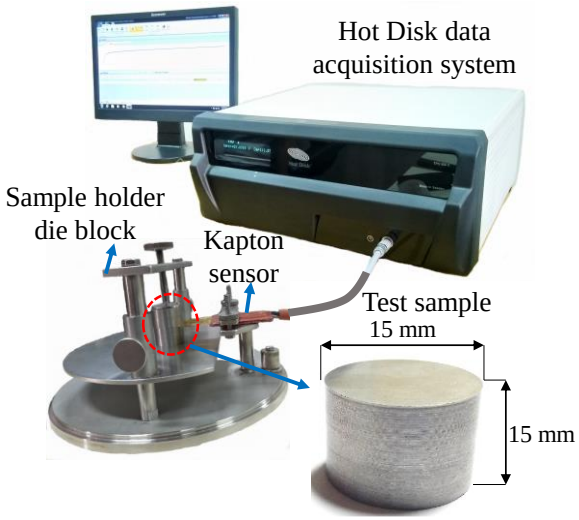

Figure 3.4 Thermal constant analyzer test setup

❖ ***Elasticity and strength***

Young's modulus, Poisson's ratio, yield strength and ultimate tensile strength were determined by conducting uniaxial tension tests on universal tensile testing machine using a contact type extensometer, as shown in Figure 3.5. The tests were performed on all three grades keeping strain rate at 0.01 s^{-1}. The samples were prepared in the form of round bars following ASTM-E8 sub size standard with specific dimensions. The force-displacement responses obtained from the tests were re-plotted in terms of engineering stress and strain (refer Figure 3.6) to calculate Young's Modulus, yield strength and ultimate tensile strength.

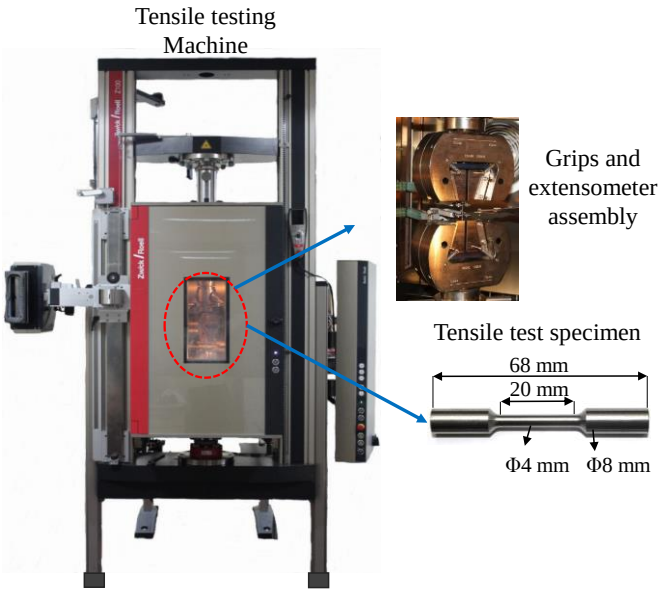

Figure 3.5 Universal tensile testing machine (make: Zwick/Roell Z100)

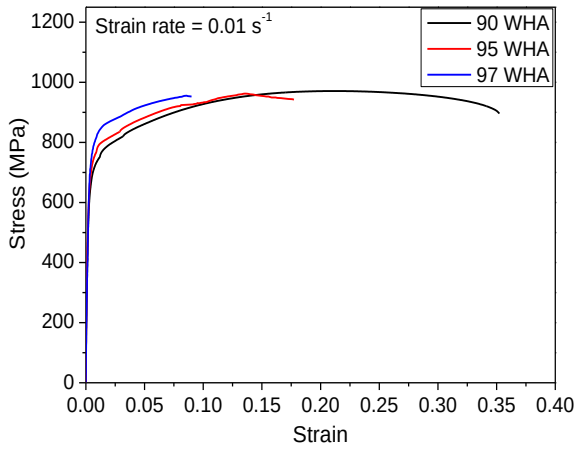

Figure 3.6 Engineering stress versus strain plot for three grades of WHAs

Analysis of material properties

The physical and mechanical properties of WHAs obtained from the tests discussed in the previous section are listed in Table 3.2.

Table 3.2 Physical and mechanical properties of WHAs

Sl.No.	Property	Grade		
		90	95	97
1	Density (g/cc)	17.0	17.5	18.1
2	Hardness (HV)	294	321	330
3	Specific heat (J/kg °C)	320	307.37	293.10

4	Thermal conductivity (W/m °C)	56.92	57.43	58.30
5	Young's Modulus (GPa)	213.91	267.59	309.36
6	Poisson's ratio	0.24	0.22	0.19
7	Yield strength (MPa)	653.64	658.88	743.03
8	Ultimate tensile strength (MPa)	955.11	962.99	971.08

The data presented in Table 3.2 clearly showed the effect of tungsten content on both the physical and mechanical properties of WHAs. It was observed that both the density and hardness increased as the tungsten content increased. In addition, Young's modulus, yield strength and ultimate strength also tend to increase with the increasing tungsten content. Poison's ratio was measured from uniaxial tensile test as shown in Table 3.2 using methodology followed by (Kenji and Hideo 1961). Lateral strain was calculated by measuring the initial diameter at gauge length and final diameter at fracture using digital micro-meter and stereo microscope, respectively. The Poisson's ratio measured by extensometer and calculated using the above method were almost same and mean values of three experimental trials were presented in Table 3.2. Poisson's ratio values were found to be relatively lower for all three grades and show a decreasing trend with the increase in tungsten content. Furthermore, a decrease in the values of specific heat and an increase in thermal conductivity is observed with the increase in tungsten content.

3.1.2 Microstructural properties

Standard procedures were followed in preparing the samples by cutting, mounting, grinding and polishing for microstructural evaluation using inverted metallurgical microscope (make: Meiji IM7200). The sample surfaces were etched with Murakami's reagent for a time period of 30-60 seconds. The size of the tungsten particles, grain number, contiguity and volume fraction of the matrix phase of the WHAs were determined from images recorded using Scanning Electron Microscope (SEM), as shown in Figure 3.7.

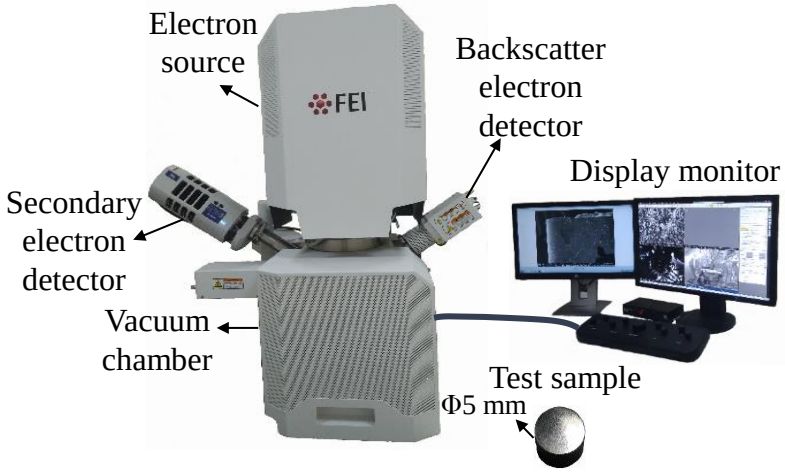

Figure 3.7 Scanning Electron Microscope (make: FE-SEM, Apero S, FEI)

The use of mean chord intercept length, point-counting method and counting W-W and W-M mean chord intercept line technique, average grain size, contiguity and matrix volume fraction were calculated using Equation (3.2), (3.3) and (3.4).

$$\bar{G} = \frac{2\,V_W}{2\,N_{WW} + N_{WM}} \tag{3.2}$$

$$C_C = \frac{2N_{WW}}{2N_{WW} + N_{WM}} \times 100 \tag{3.3}$$

$$V_M = \frac{N_M}{N_M + N_W} \times 100 \tag{3.4}$$

Figure 3.8 shows SEM images of 90, 95 and 97 WHA alloys along with arrows showing the planar surface. Different phases are labeled in the micrograph. In 90 WHA, the W grains appeared smaller and relatively more round in shape as compared to those in 95 WHA and 97 WHA. The particle size increased from 90 to 97 WHA. The difference in grain size could be attributed to decreasing volume fraction of matrix phase with increasing W. Also, as W increased, the grains tend to become more angular. As the volume fraction of the matrix phase decreases and that of W increases, there is a process called shape accommodation to ensure maximum packing that leads to planar interfaces and thereby, angular particles (J. Das , A. G. Rao , et al. 2014).

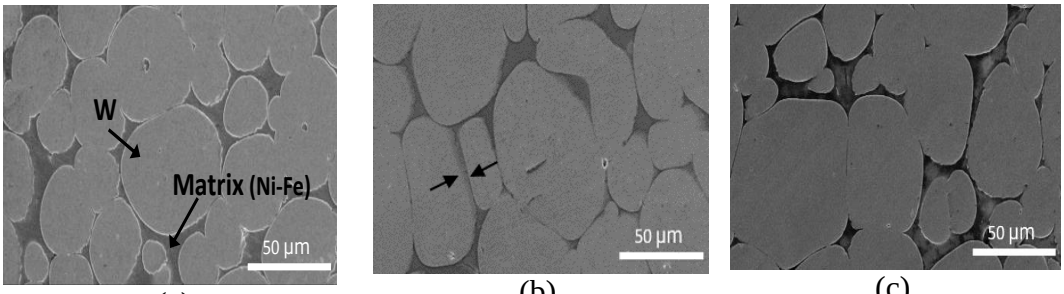

(a) (b) (c)

Figure 3.8 Micrographs of (a) 90 WHA (b) 95 WHA and (c) 97 WHA

The contact area of the tungsten-matrix interface decreases and tungsten-tungsten interface increases with increasing W. A similar trend was observed by (Islam, et al. 2007) when the tungsten content was increased from 88 WHA to 95 WHA. Figure 3.9 clearly shows the increase of grain size, W-W contiguity and decrease in matrix volume fraction with increase in W content. The data points from the literature were superimposed (Islam, et al. 2007).

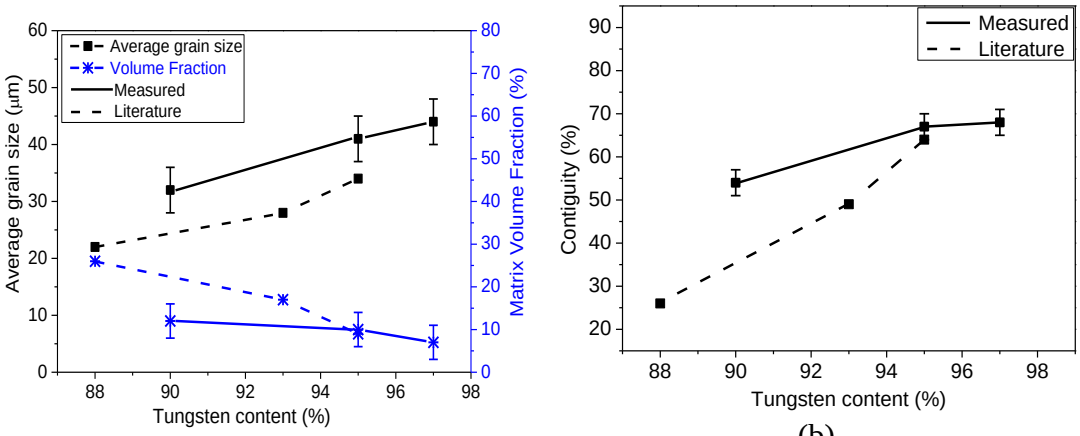

(a) (b)

Figure 3.9 Variation of (a) average grain size, matrix volume fraction and (b) contiguity as a function of tungsten content

There was a reduction of 25 - 34% in the grain size of 90 WHA as compared to those of 95 WHA and 97 WHA. Consequently, the volume fraction of the matrix phase decreased from 12% to 7%, whereas the contiguity values increased from 50 to 65 % as the W content increased. Higher contiguity indeed leads to an increase in hardness with the increase in tungsten content that will have significant implications on material behavior.

3.2 Machinability studies

Turning tests were performed on WHAs to study the machining behavior in terms of various machining outputs such as cutting forces, MRR, surface roughness and chip morphology. This section discusses the experimental techniques used, followed by the results obtained during the turning tests. An in-depth analysis is presented showing the correlation between the material properties and cutting conditions with the measured outputs during machining of WHAs

3.2.1 Sample preparation and experimental details

WHA samples were manufactured through sintering followed by swaging. The sample selected for machining was around 130 mm length and 11 mm diameter. Each of the work samples were heat-treated for stress relieving to reduce the internal stresses that might have developed in the work materials due to the originating manufacturing process. The specimens were heated to temperature of 550 °C and held for about 4 hours in order to attain uniform temperature on the entire specimen. Inert atmosphere was maintained during the entire heat treatment process by passing argon gas through tubular furnace until the cycle gets completed (J. Das , A. G. Rao , et al. 2014). Figure 3.10 (a) and (b) show the set up for heat treatment and heating-cooling curves for WHAs, respectively.

Turning tests were conducted using uncoated cemented carbide tools with varying rake angles on a CNC lathe. In these tests, cutting speed, feed rate and depth of cut were varied while the length of cut is kept constant. The tangential and feed cutting force components acting on the tool holder were measured using a three-component piezoelectric force dynamometer. Surface roughness values were measured on the machined surface using a profilometer of 4 mm sampling length, 1 mm/sec traverse speed, cut off 0.8 mm and 5 μm diamond tip to measure arithmetic mean deviation (R_a) using Gaussian filter method. Three readings were taken in the middle of the machined surface at 90° angle on each sample.

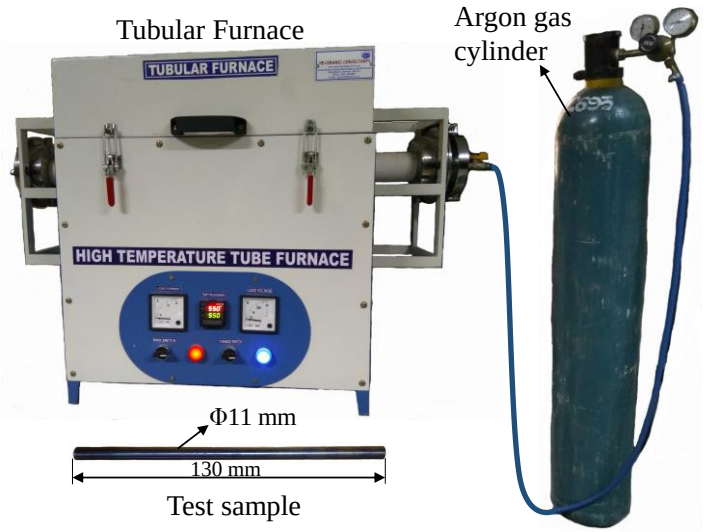

(a)

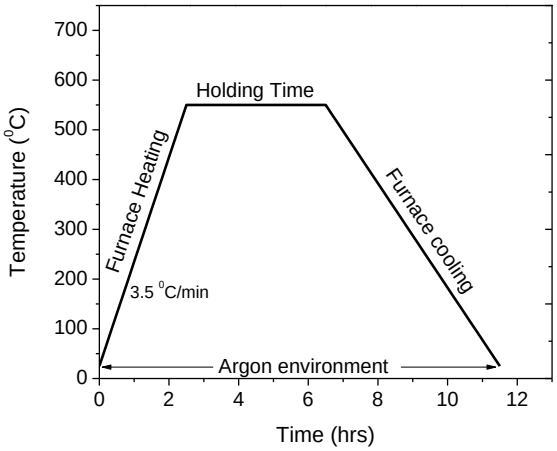

(b)

Figure 3.10 (a) Heat treatment tubular furnace setup (b) Heating and cooling curve for WHA samples

The machined chips were collected to measure the chip thickness and study the chip morphology with the help of a tool maker's microscope. The machining time was recorded for machining 15 mm length by a stopwatch. The chips obtained after every cut were collected and weights of the same were measured in grams by a precision digital weight balance to calculate MRR in gram/minute. The tests were conducted in dry conditions. The experimental setup and the equipment used are shown in Figure 3.11, while test conditions and equipment specifications are listed in Table 3.3.

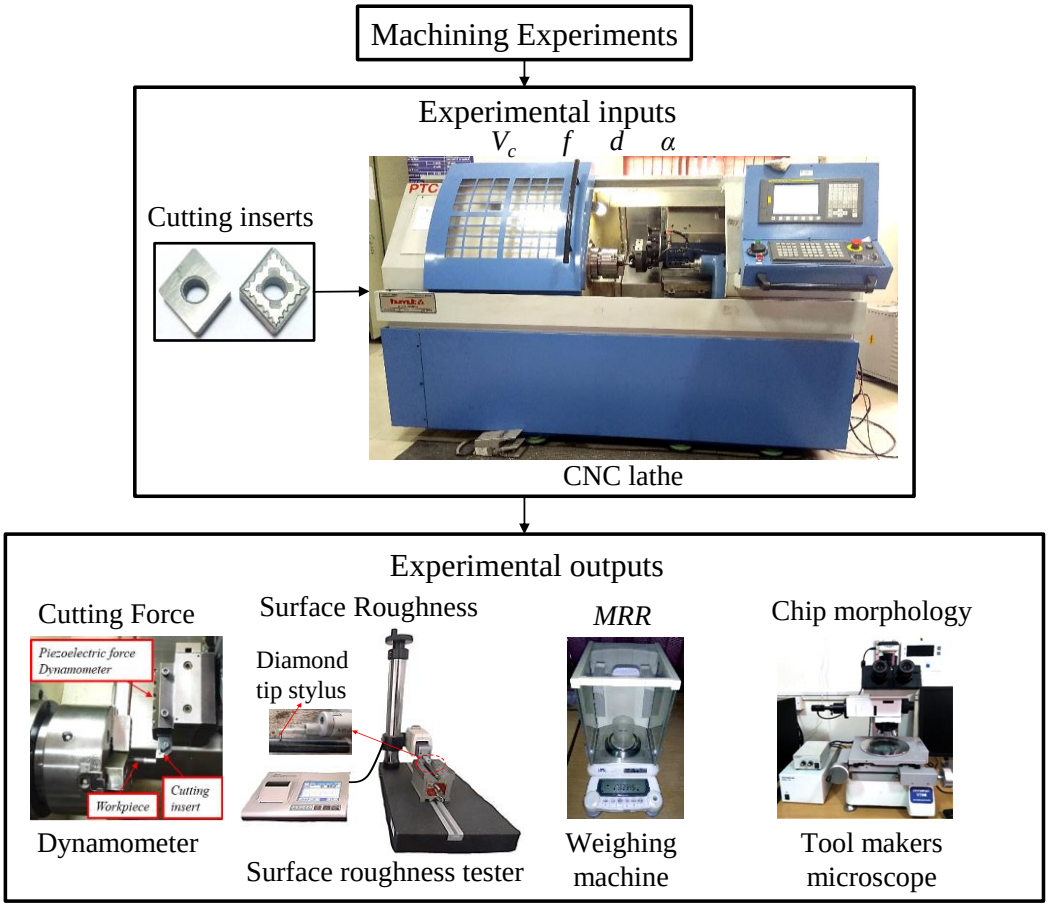

Figure 3.11 Experimental machining test setup

Table 3.3 Experimental details of the machining tests

Machine tool	CNC Lathe HMT PTC200
Tool holder	MCLNL2020K12, MSSNL2020K12
Tool Insert	CNMG120408, CNMA120408
Tool rake angles (˚)	2, -5
Nose radius (mm)	0.8
Cutting parameters	
Cutting speed (m/min)	70, 50, 30
Feed (mm/rev)	0.05, 0.1. 0.15
Depth of cut (mm)	0.10, 0.15, 0.2
Length of cut (mm)	15
Tool cutting edge angles (˚)	80
Cutting condition	Dry
Cutting force measurement	3- axis Piezoelectric lathe tool dynamometer

Surface roughness tester	Mitutoyo SJ410 surface roughness tester
Microscope	Tool Maker's microscope Olympus-STM6
Weighing machine	Shimadzu AUW220 Analytical Balance

3.2.2 Analysis of machining outputs

The effect of tungsten percentage on the machinability of WHAs is investigated under different cutting conditions and cutting tool geometry. The machinability assessment includes chip morphology, MRR, cutting forces and surface roughness. In order to ensure the reliability of these measured parameters, each test was repeated three times with the same cutting parameters.

Chip morphology and chip thickness

The chip morphology during the machining of WHAs at cutting speeds of 30, 50 and 70 m/min, feed of 0.1 mm/rev and depth of cut of 0.15 mm for rake angles -5º and 2° are shown in Figure 3.12 (a) and (b), respectively.

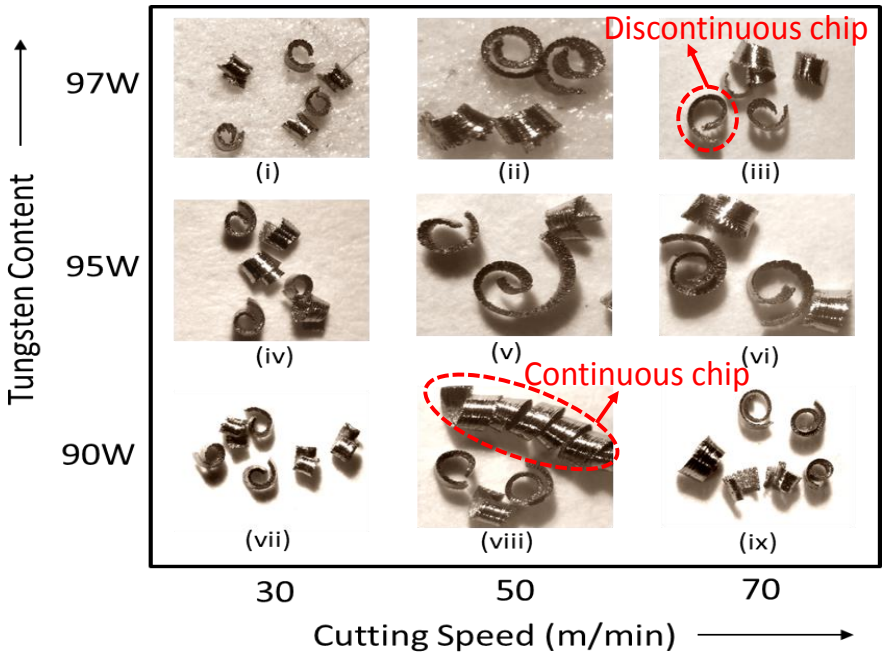

(a)

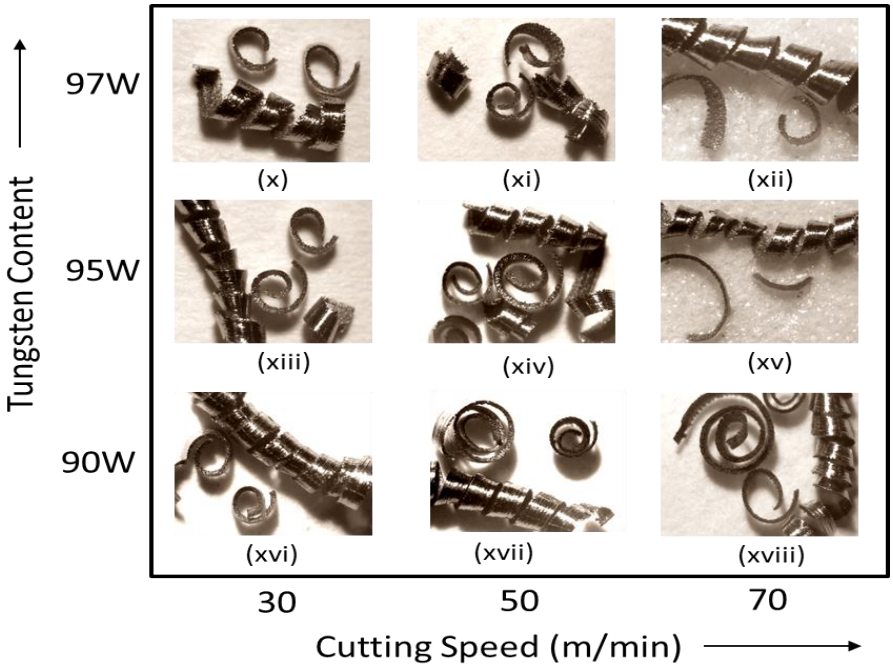

(b)

Figure 3.12 Chip morphology while machining WHAs using rake angle of (a) -5º and (b) 2º at cutting speeds of 30, 50 and 70 m/min, feed 0.1 mm/rev and depth of cut 0.15 mm

Tool rake angle, tungsten content, and cutting velocity have a significant effect on the chip morphology. Machining with positive rake angle yields mixed type chips that are discontinuous chips along with continuous type as compared to negative rake angle wherein the chips are the discontinuous type with only one exception that is in case of 90% W (Figure 3.12 (a). viii). The difference is basically attributed to the material flow of work-piece in the vicinity of the tool rake face. In general, when the rake angle is negative, the material flow becomes unsteady, resulting in cracks, especially in a brittle material. In contrast, when the rake angle is positive, shear deformation occurs leading to longer chips (Piispanen 1948). Since WHAs exhibit limited ductility, work-piece material undergoes limited plastic deformation with negative rake angle resulting in fragmented chips. Hence, as the tungsten content increases, the tendency of chip fragmentation increases, an indication of increase in brittleness of material resulting in smaller chips. This may also be attributed to increasing contiguity that results in increasing brittleness as W-W interface is a potential crack nucleation site (Rabin and German 1988). In the case of positive rake angle, a mixture of ductile and brittle failure gives rise to a mixed chip morphology.

Figure 3.13(a) and (b) shows the variation in chip thickness, (c) and (d) shows the variation in chip reduction coefficient as a function of cutting speed and feed for the three grades of WHAs. The chip thickness varies from 70-100 μm. In the chip thickness and chip reduction coefficient versus cutting velocity plot, the trends are again not very definitive for negative rake angle. It is mentioned earlier that a negative rake angle promotes brittle failure that leads to scatter in data. However, for positive angle, the thickness decreases with increase in cutting velocity. This may be due to temperature rise during machining. Also, with the increase in temperature the ductility of the material increases giving rise to thicker chips. Besides temperature effect, the decrease in chip thickness could also be because of change in shear plane angle which certainly has an effect on chip thickening. Higher is the shear angle, lower is the chip thickness. However, at higher cutting speed, the ductility may decrease because of high strain effects.

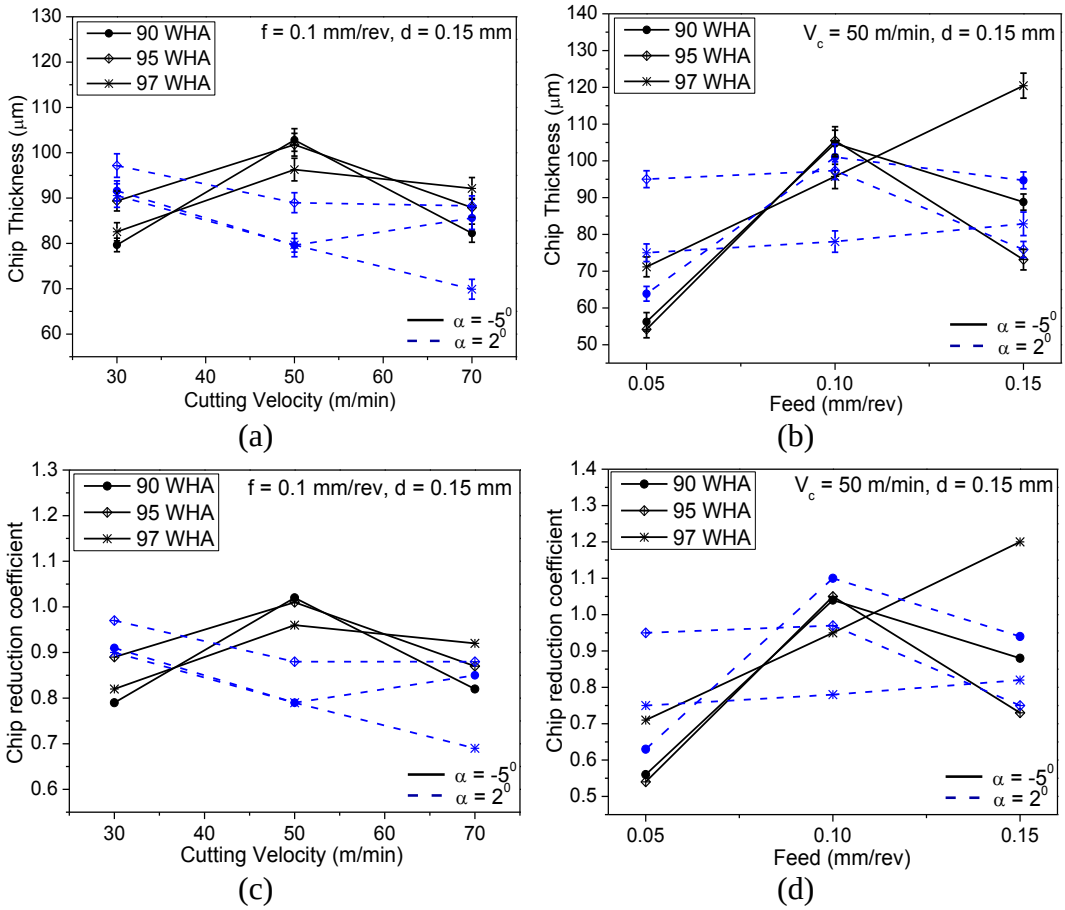

Figure 3.13 Effect of cutting velocity on (a) chip thickness, (c) chip reduction coefficient and effect of feed on (b) chip thickness, (d) chip reduction coefficient at depth cut 0.15 mm.

Material Removal Rate

MRR is calculated experimentally using Equation (2.1), while Equation (2.2) depicts the analytical expression explaining the relation between cutting parameters and MRR.

Figure 3.14 (a) and (b) show the effect of cutting speed and feed on MRR for the selected grades of WHA using two different cutting tool geometries (2° and -5°).

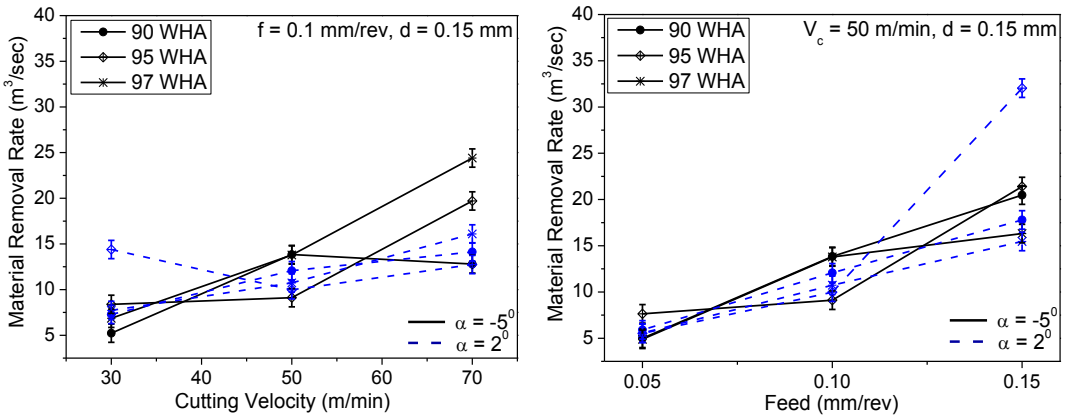

Figure 3.14 Effect of MRR on (a) cutting velocity and (b) feed at depth cut 0.15 mm

It can be seen that all three grades of WHA show an increasing trend with the increase in cutting speed and feed for both the type of rake angles. This is expected because cutting speed, feed and depth of cut are directly proportional to MRR (refer Equation (6)). It is noted that when the cutting speed is highest (i.e., at 70 m/min), 97 WHA (Figure 3.14 (a)) at constant feed rate shows maximum MRR both for positive and negative rake angles. On the contrary, 97 WHA shows lowest MRR at highest value of feed and 95 WHA showed the maximum one, especially when rake angle is 2°, at constant cutting speed. These variations may be explained by looking at the type of chip morphology obtained for the respective cutting conditions in Figure 3.12. It is inferred that higher chip fragmentation and lower chip thickness ensure better chip flow and hence, higher MRR.

Cutting forces

The experimentally measured cutting force signature and its variation with respect to cutting velocity and feed are shown in Figure 3.15 (a), (b) and (c), respectively.

The measured cutting forces with varying cutting speeds at a constant feed for all grades show different trends for positive and negative rake angles, as shown in Figure 3.15 (b). For the positive rake angle, the force decreases with increasing speed. But, it does not show any consistent trend for the negative rake angle. For the lower cutting speeds, the values of cutting forces are higher with positive rake as compared to that of negative rake angle. However, a cross over occurs at the highest speed (70 m/min.). This phenomenon could be correlated well with the type of chips being produced in the respective cutting conditions. The chips obtained using negative rake angle are discontinuous producing small fragments due to brittle fracture; whereas, in case of positive rake angle chips are partly continuous type undergoing shear deformation. Since less force is required for removing smaller fragments, values of cutting force are lower in case of negative rake angle.

The crossover at the highest speed may be due to additional parameter that is increasing temperature that may lead to material softening. When the rake angle is -5°, the cutting force appears to go through minimum at 50 m/min for 95 WHA and 97 WHA, whereas for 90 WHA there is a hint of maximum at 50 m/min. Thus, the trends are not consistent and this may be a result of brittle fragmentation, which is statistical in nature and may be prone to scatter. The radius of curvature of chip curl could also be one probable factor for such trend. It is observed that smaller is the radius of curvature, more constricted is the curling of chips, thus increasing the compressive load on the negative rake face of the tool while removing the chip. As far as the effect of feed rate is concerned, the force increases with the increase in feed rate (Figure 3.15(c)), an expected trend as the thickness of the chips increases with increasing feed.

It is noted that higher values of cutting forces are exhibited by 97 WHA for positive rake angle with respect to both cutting speed and feed. This may be attributed to higher hardness because of the higher tungsten content in 97 WHA. Owing to predominant brittle failure of the chips for negative rake angle, the hardness does not

play a role and with scatter dominating the trends are inconsistent for negative rake angle.

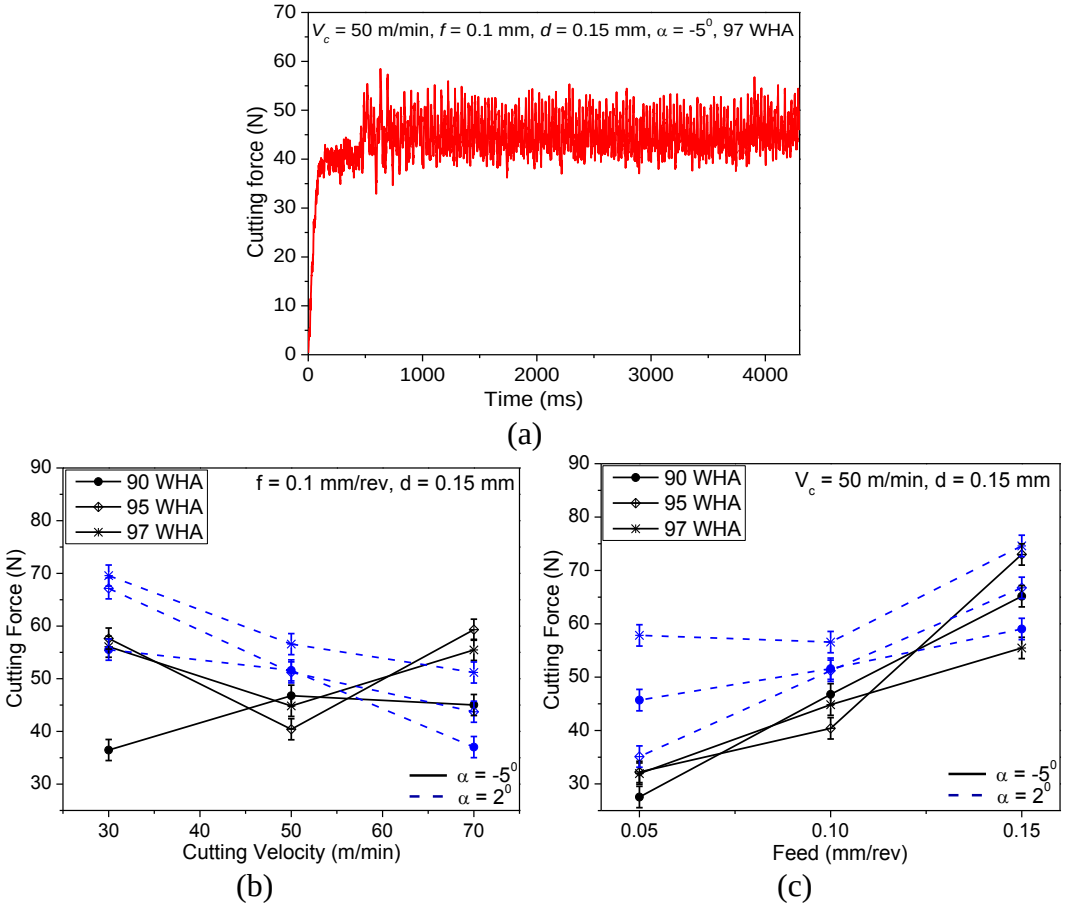

Figure 3.15 (a) Cutting force signature with respect to time, the effect of (b) cutting velocity and (c) feed on cutting forces at a depth of cut 0.15 mm.

Surface roughness

The measured surface roughness profile for a distance of 4 mm as shown in Figure 3.16 (a). While Figure 3.16 (b) and (c) show the effect of cutting speed and feed on surface finish using both positive and negative rake angles for the investigated alloys. While for the positive rake angle, the surface roughness does not change much or at most exhibits a marginal decrease, no particular trend is seen for the negative rake angle. In the surface roughness versus feed plot, as the feed rate increases, surface roughness increases. For the positive rake angle, despite the presence of minima, a hint of positive trend is observed. 90 WHA appears to give a better surface finish (lower surface roughness values). This is expected since this alloy has higher ductility that will promote mixed chip formation. 97WHA, at least

in one case, shows higher surface roughness which is possibly a result of its limited ductility.

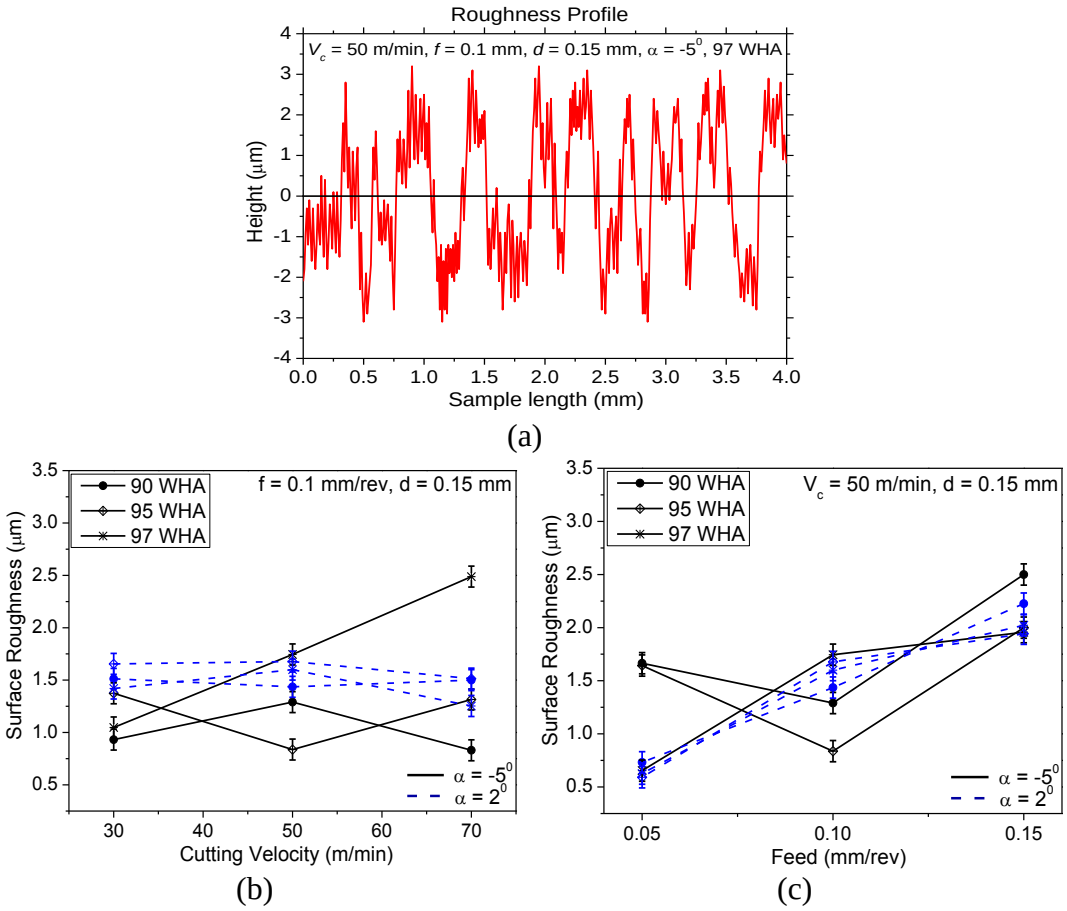

Figure 3.16 (a) Surface roughness profile with respect to sample length, the effect of (b) cutting velocity and (c) feed on surface roughness at a depth of cut 0.15 mm.

The variation of surface roughness as a function of cutting force for all three grades of WHA at different cutting speeds are shown in Figure 3.17.

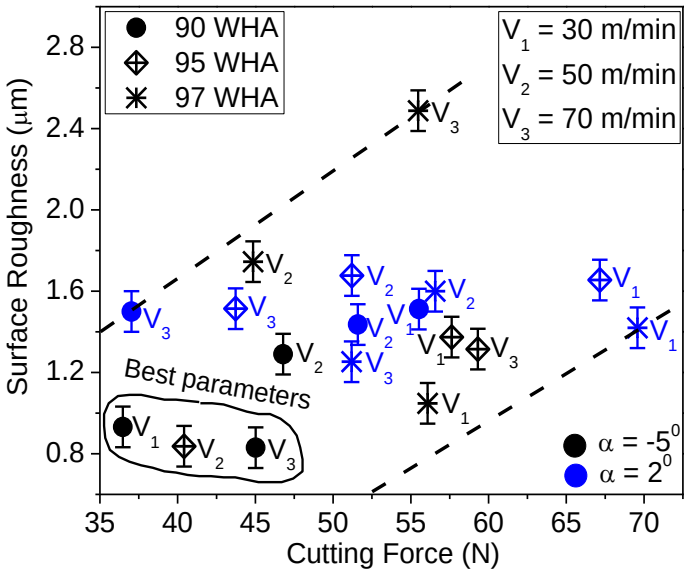

Figure 3.17 Variation of surface roughness versus cutting force for different grades of WHA at feed = 0.1 mm/rev and rake angles -5° and 2°

While the data are spread all over, a general trend is discernible that is, for negative and positive rake angle, the surface roughness increases with an increase in cutting force. The positive rake showed overall higher values for both cutting force and surface roughness as compared to that of negative rake angle. It is observed that 90 WHA and 95 WHA at relatively lower cutting velocities showed the best possible values of cutting force and surface roughness, together, whereas, 97 WHA showed the worst of all.

Tungsten content effect

With increasing tungsten content, the volume fraction of the matrix phase decreases and the contiguity of W increases. This results in increasing hardness, which has implications on surface roughness, MRR and cutting force. On the whole, it can be concluded that with the increase in tungsten content, there is an increase in MRR and cutting force for different cutting speeds, feed rates and tool rake angles (see Figure 3.18 (a) and (b)). Surface roughness against tungsten content does not change significantly, exhibiting a flat trend.

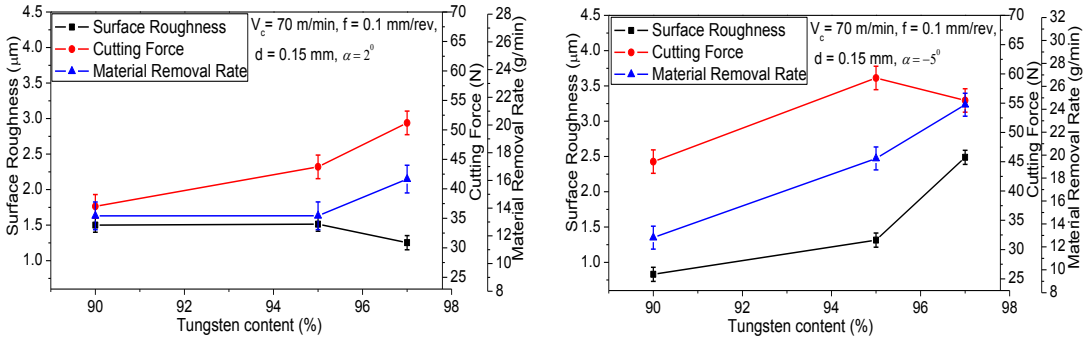

Figure 3.18 Effect of tungsten content on surface roughness, cutting force, material removal rate for (a) positive and (b) negative rake angle

3.3 Tool wear analysis and analytical modeling

Tool wear is of foremost importance in machining operation. Owing to its direct impact on the surface quality and machining economics, tool wear is typically used to evaluate the overall productivity of the machining process. From the preceding section, it is inferred that 90 WHA showed relatively better machinability attributes as compared to other two grades. Hence, 90 WHA is considered as the work material for tool wear analysis. The present section is divided into two parts. First part deals with the experimental approach for analysis of flank wear, estimation of tool life and identification of predominant wear mechanism. While the second part focuses on the analytical approach for prediction of flank wear growth and tool life.

3.3.1 Experimental analysis of tool wear

In this study, machining tests were conducted by turning of 90 WHA under dry conditions. Firstly, the growth of flank wear is studied and tool life is determined for different tool geometries as well as its effect on other machining variables is investigated. Secondly, the predominant tool wear mechanism is identified using SEM analysis.

Test procedure

Uncoated carbide inserts (make: WIDIA) with two different rake angles i.e., -5º and 2º, were used with the following specifications: CNMA120408-THMF and CNMG120408MS-W10HT, respectively. Both the inserts were mounted using a tool holder with specification MCLNL2020K12 (make: WIDIA). Flank wear tests were performed at constant velocity of 50 m/min, feed rate of 0.1 mm/rev and depth of cut of 0.15 mm using two different types of cutting inserts. The turning operations were continued until the failure criterion is achieved i.e., tool flank wear of 600 µm is reached. Measured flank wear progressions for both the tool geometries are plotted as a function of cutting time to determine the tool life. During the flank wear tests, cutting force components, temperatures as well as surface roughness values were also measured simultaneously at specific time intervals. Minimum of three readings are taken at different locations of the work piece and average of the same are taken as the final value. Flank wear was measured by METZER M optical microscope at 40 X magnification. The worn surfaces were analyzed using SEM as well as Energy-dispersive X-ray spectroscopy (EDS) at successive machining time intervals. Figure 3.19 depicts the methodology adopted for performing the experimental studies and analytical approach.

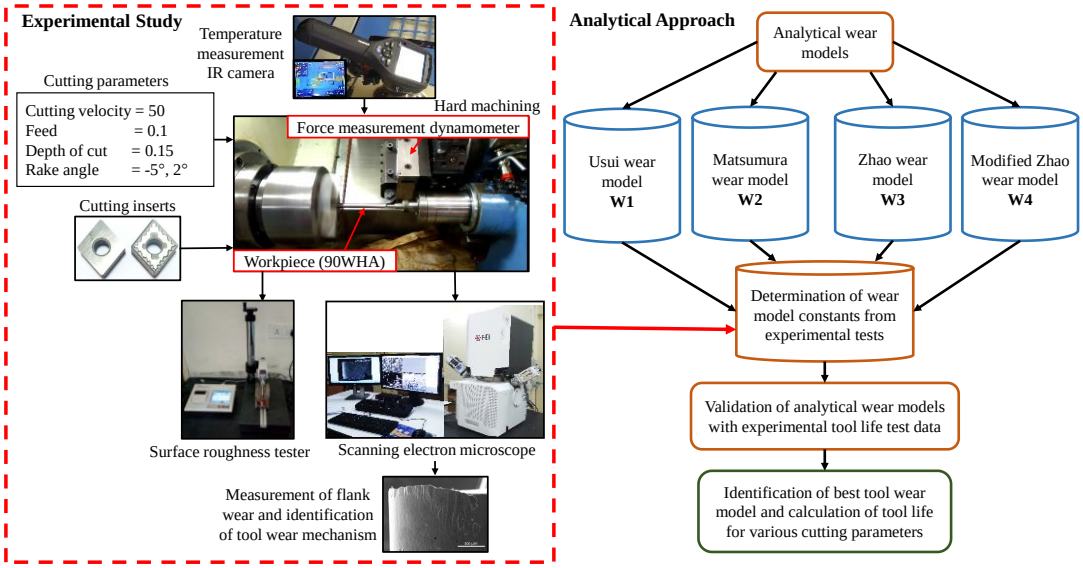

Figure 3.19 Flowchart showing the overall methodology adopted

Tool life estimation

Tool flank wear progression along with SEM images and built up edge measurements for two different tool geometries (-5º and 2º rake angle) has been shown in Figure 3.20 (a) and (b). The images were taken at regular time intervals as the wear progressed and presented according to three distinct regions of the wear growth curve, namely, initial or rapid growth region, steady state region and catastrophic failure region.

The tool lives for both the cutting tools were estimated from the flank wear growth curve by considering the time taken to reach the failure criterion (i.e., 600 µm of flank wear). As presented in Figure 3.20 (a) and (b), tool life comes out to be 18 minutes and 14.82 minutes for -5º and 2º rake angles, respectively. Though the difference in the values of estimated tool life was not much with respect to the given tool geometries, SEM images showed certain amount of difference in flank wear growth pattern. The development of BUE on fresh cutting edge was observed during the initial and steady state region for both the cases. Based on the measured tool life values, it can be stated that the cutting tool with negative rake angle performed reasonably well as compared to that of positive rake angle for machining 90 WHA under similar cutting conditions. This is expected because the negative rake angle leads to higher wedge angle which results in increased strength of tool tip, thus making the cutting tool more sustainable under severe cutting conditions.

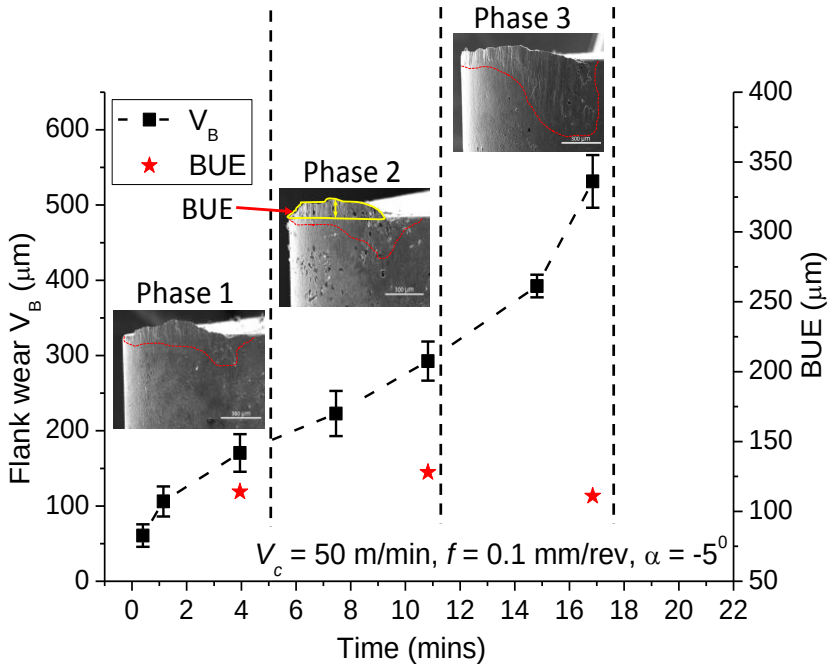

(a)

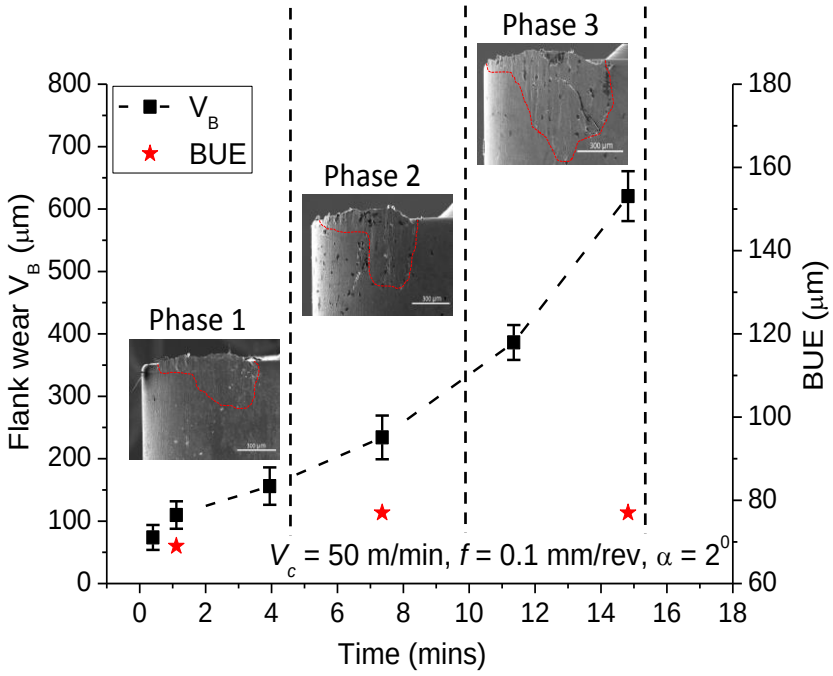

(b)

Figure 3.20 Flank wear measurements, SEM micrographs and BUE measurement for (a) -5º, (b) 2º rake angles

Figure 3.20 (a) and (b) shows the development of BUE with respect to three regions of flank wear growth. The graph clearly shows the difference in values of BUE formation for -5º and 2º angles. The BUE measured in case of 2º rake angle is fairly

low as compared to that of -5º. The BUE size for the rake angle -5º reduced in the catastrophic failure region, thus confirming to the cause of change in chip morphology as the machining progressed. Whereas for 2º rake angle, BUE size slightly increased and became stable as it reached steady state region.

Figure 3.21 shows the variation in chip morphology as the flank wear progressed. As expected, discontinuous chips are observed during machining using negative rake angle (-5º). The chips became highly fragmented in the catastrophic failure region for -5º rake angle. It was observed that there is a prominent BUE in the first two regions. The presence of BUE on the tool tip possibly change the effective rake angle from negative to near positive. Consequently, in the initial and steady state regions, chips obtained were slightly continuous. Nevertheless, as the BUE reduces, chips produced were highly fragmented or discontinuous. Whereas, for 2º rake angle, chips were not as fragmented as observed in case of -5º rake angle. Furthermore, not much change in chip morphology is observed with respect to the flank wear progress. Also, BUE formation for 2º rake angle is not as prominent as in case of -5º.

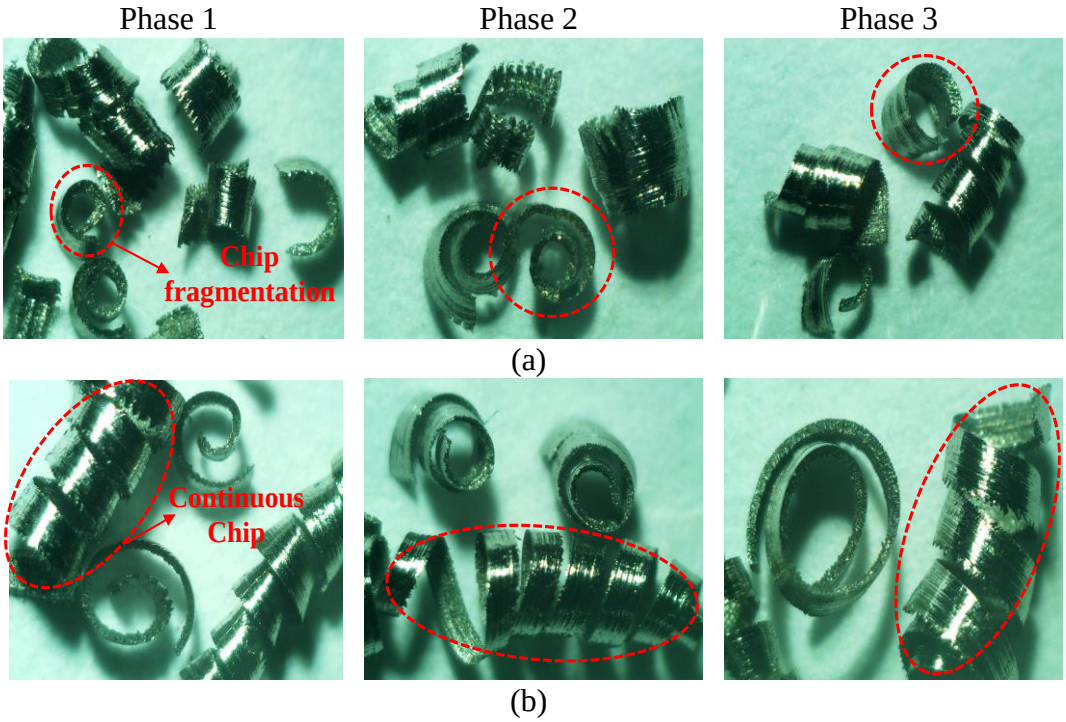

Figure 3.21 Variation of chip morphology with the flank wear progress for (a) -5º and (b) 2º rake angles.

Effect of flank wear on machining outputs

The correlation between flank wear and cutting force components with respect to time for the rake angles -5º and 2º are shown in Figure 3.22 (a) and (b), respectively.

The graphs in Figure 3.22 show a strong relationship between force components and the flank wear. The trend for force components and that of flank wear closely match, especially for -5º rake angle, showing three distinct regions similar to that of flank wear. A steep increase in force components was observed for both the tool geometries. This sudden increase in cutting force may be attributed to the development of BUE on tool tip as shown in SEM images (Figure 3.20(a) and (b)). Beyond this point, it is observed that the forces reached a steady state. For -5º rake angle, the steady state is followed by a sudden increase in the forces. The point at which the cutting forces abruptly increased coincided with the catastrophic failure region of the flank wear growth.

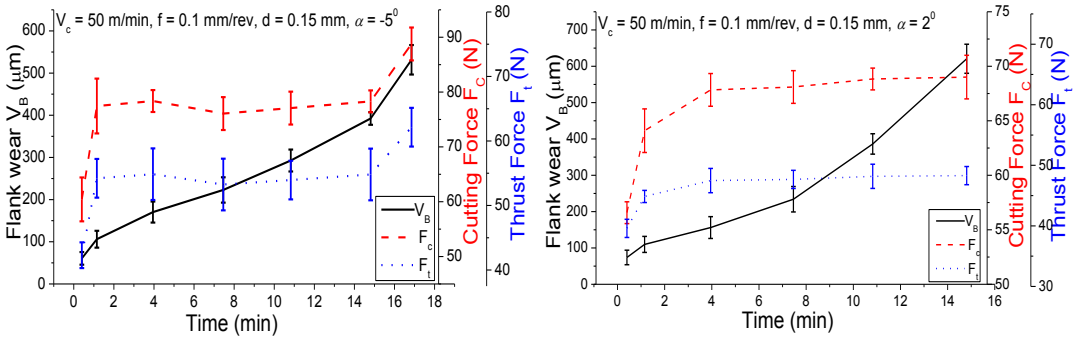

(a) (b)

Figure 3.22 Variation of flank wear, cutting force and thrust force with respect to time for rake angles (a) -5º and (b) 2º.

However, for 2º rake angle, the forces increased gradually reaching a maximum value, nearly same as that obtained in case of -5º rake angle. Hence, it can be inferred cutting force and thrust force trends are different for positive and negative rake angles. A similar pattern is observed for the temperature measured as the flank wear progressed. Figure 3.23 (a) and (b) show the correlation between flank wear and cutting temperature with respect to time for the rake angles -5º and 2º, respectively. In Figure 3.23 (a), the sharp increase in cutting temperature can be attributed to the development of prominent BUE on the tool tip in initial as well as steady region of flank wear growth, as shown in Figure 3.20 (a). Because of such a steep increase in cutting temperature, thermal softening became the dominant factor over strain

hardening and consequently cutting force components achieved a steady state. In the catastrophic failure region, BUE reduced considerably, thereby reducing the cutting temperature. However, further reduction in cutting temperature could be possibly because of the formation of highly fragmented chips with the flank wear progression. It is noted that there could be possible chances of getting error while measuring the cutting temperatures experimentally for highly fragmented chips. In Figure 3.23 (b), for positive rake angle, a gradual increase in cutting temperature is observed as the flank wear progressed. This suggests that the gradual increase in cutting temperature resulted in increase of flank wear.

Figure 3.23 (c) and (d) show the effect of flank wear on surface roughness with respect to time for the rake angles -5º and 2º, respectively. In both the cases, it is evident that with the increase in flank wear, surface roughness increased. The surface roughness value reached a maximum value in the catastrophic failure region. It is observed that surface roughness values are lower in case of negative rake angle with a maximum value not exceeding 2.2 μm. Whereas for the positive rake angle, the maximum value of surface roughness is closer to 3.7 μm.

Thus, overall, it can be inferred that as the cutting temperature increases flank wear increases and as the flank wear increases there is a considerable increase in forces. The increase in forces could possibly lead to vibrations which in turn would prove detrimental to the surface finish of the workpiece, thus leading to higher surface roughness values. Hence, this shows machining is such a complex process in which not merely the input parameters affect the machining outputs but also the machining outputs are interdependent on each other. The basic understanding of the tool wear growth and its mechanism is not only challenging but also equally important to perform machining operations effectively and economically.

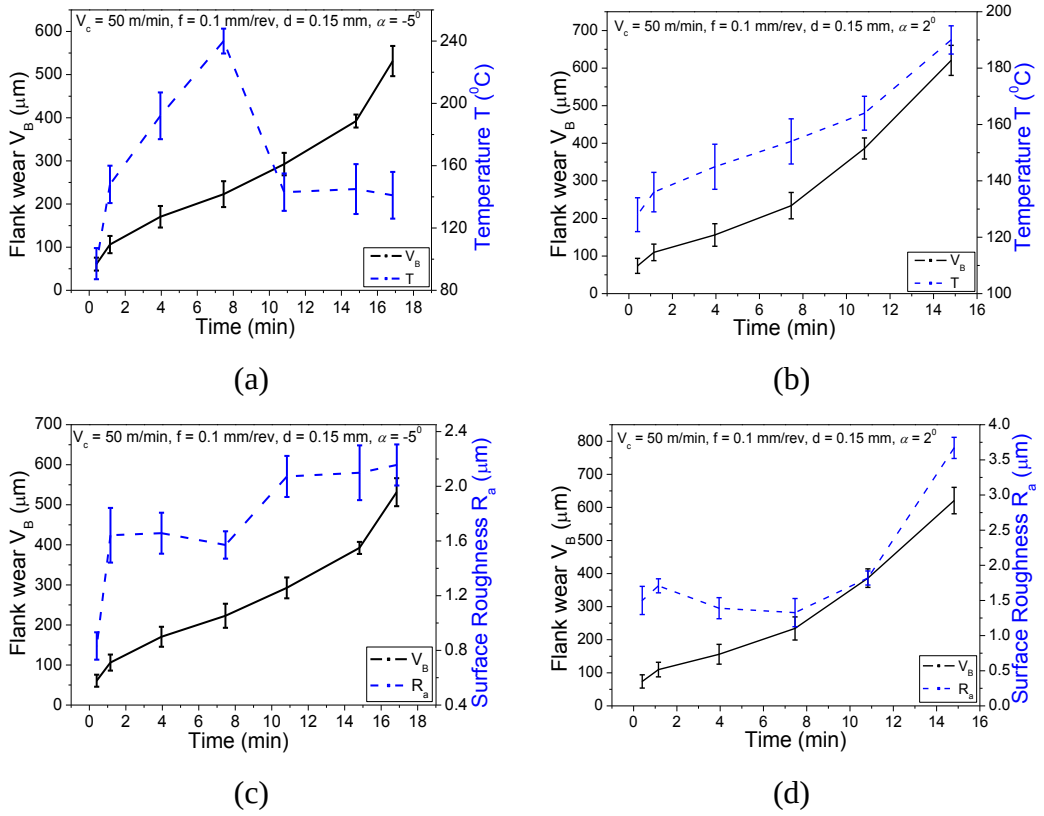

Figure 3.23 Variation of flank wear and cutting temperature with respect to time for rake angles (a) -5º and (b) 2º. Variation of flank wear and surface roughness with respect to time for rake angles (c) -5º and (d) 2º.

SEM analysis and identification of wear mechanism

Identification of the predominant wear mechanism plays a vital role in understanding the tool wear growth. Figure 3.24 shows the SEM micrograph of the flank surface of unworn cutting tool and the corresponding EDS analysis of the surface. The micrograph showed the arrangement of WC-Co microstructure on the surface of the unworn surface. While EDS analysis confirmed the chemical composition of the uncoated carbide inserts. These results would suffice as a reference for studying the worn surfaces of the given carbide inserts.

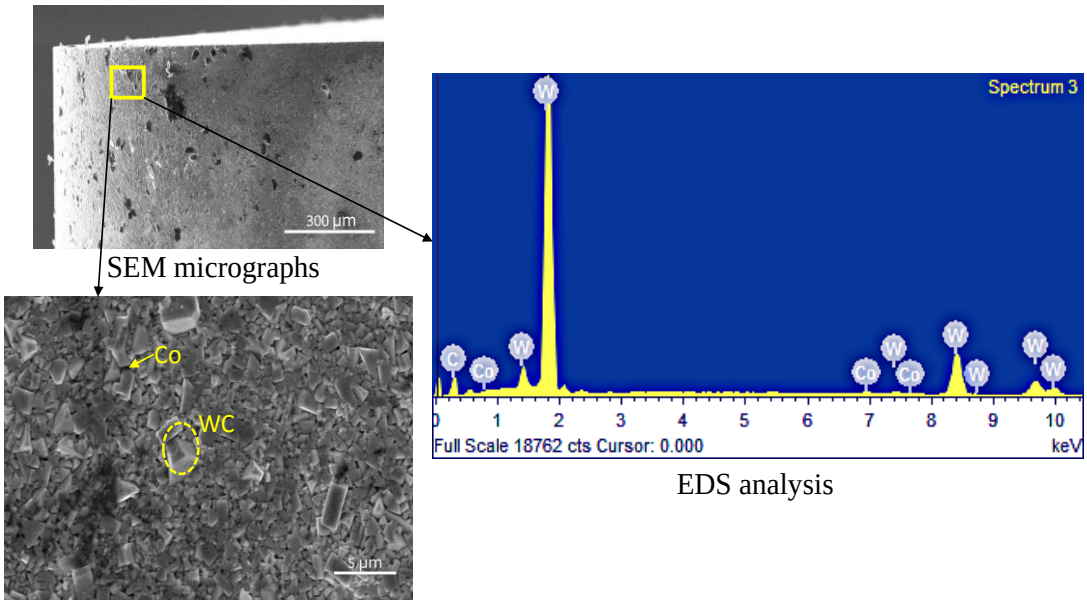

Figure 3.24 SEM micrographs, microstructure and EDS analysis of the unworn surface for the uncoated carbide inserts

Figure 3.25 shows the SEM micrographs and the corresponding EDS analysis of the worn surface for the uncoated carbide inserts in the catastrophic failure region for rake angles -5º and 2º, respectively. In Figure 3.25 (a) and (b), the microstructural arrangements in the SEM micrographs appear disorganized as compared to the initial one (see Figure 3.24). Such disarrangement could be due to abrasion that would lead to micro-cracks at WC/WC or at WC/Co interfaces or chipping due to the alternative stress (Kagnaya, et al. 2014, Najar and Butt 2018). Consequently, few deep grooves or slip line traces on the surface of WC grains on the worn flank surface are observed.

In addition, a prominent adhesion layer is also observed. This may be attributed to a combination of high friction forces between the tool and the chip and high cutting temperatures in the catastrophic failure region. The EDS analysis in Figure 3.25 (a) and (b) shows the presence of W-Ni-Fe elements. This indicated that the elements present in the adhesion layer are same as that of the workpiece material, thus confirming adhesion as one of the predominant mechanism. Furthermore, it is observed that Co and W elements have not diffused into the adhesion layer. Hence, the SEM micrographs show the occurrence of both abrasion and adhesion. However, the accumulation of workpiece elements as adhesion layers is more prominent for both the tool geometries as compared to that of abrasive micro-scratches on the worn

surface. Hence, in the present work, adhesion is considered as the dominant mechanism while machining 90 WHA using uncoated carbide for both -5º and 2º rake angles.

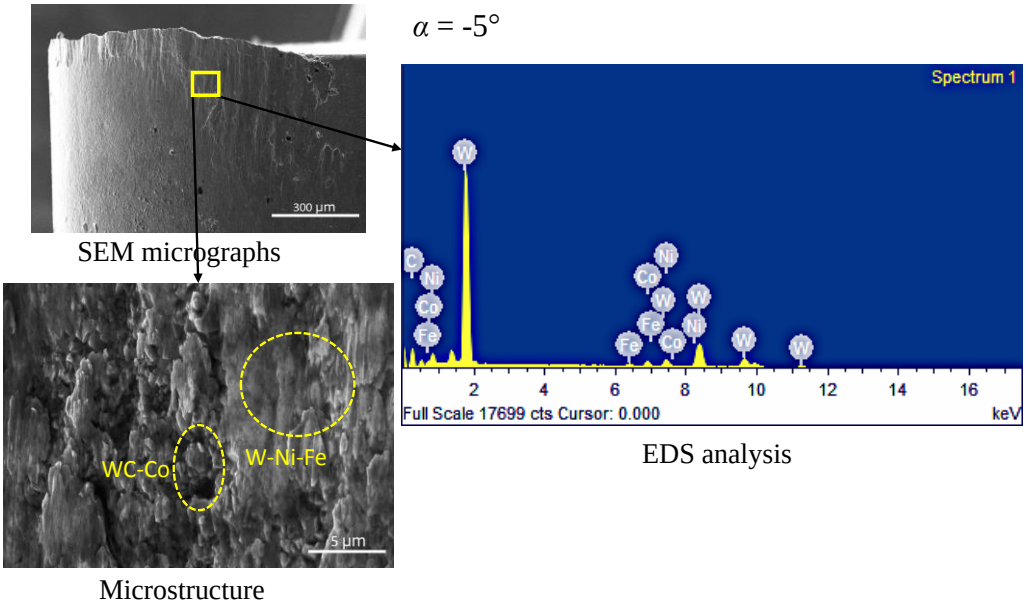

(a)

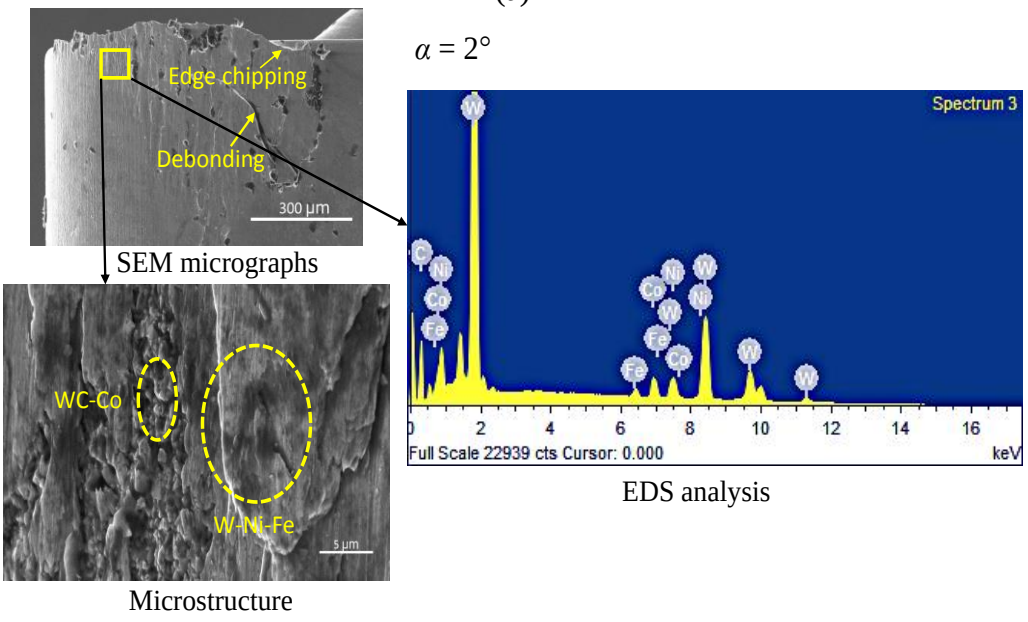

(b)

Figure 3.25 SEM micrographs, microstructure and EDS analysis of the worn surface for the uncoated carbide insert (a) -5º and (b) 2º rake angle in the catastrophic failure region.

In the case of 2º rake angle (Figure 3.25 (b)), deep scars appeared similar to the micrographs obtained by (Kagnaya, et al. 2014). It is also reported that the adhesive

layer at the tool–chip separation zone is formed according to a "formation–stacking–pulling out" process, which may get removed periodically by the chip. Such removal can be further amplified by the debonding of WC fragments. In order to confirm debonding, further investigations are performed on cutting insert with 2º rake angle by etching the worn surface in ultrasonic cleaner for 1 hour using methanol solution and then observing at higher magnification using SEM.

Figure 3.26 (a) shows the deep scars before etching, which appeared similar to debonding phenomenon, while Figure 3.26 (b) shows the wear scars after etching. It can be seen that the adhered layer on the tool disappeared after etching, leaving few abrasion marks on the flank surface. This confirms that it is an accumulation of workpiece material elements in the form of the adhesive layer that got dissolved when etching is done. However, further use of this cutting tool would have led to debonding and, consequently, complete damage of the tool tip.

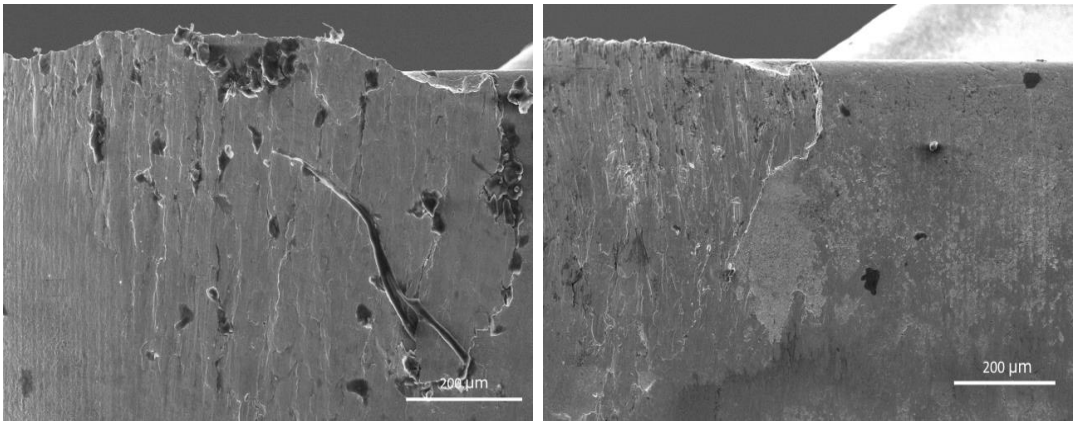

(a) (b)

Figure 3.26 SEM micrograph of worn flank surface for 2º rake angle (a) before etching (b) after etching

3.3.2 Analytical tool wear rate models

Once the tool wear mechanism is identified, the prediction of tool wear by analytical method plays a major role in avoiding large number of trial and error experiments. Analytical approach includes utilization of tool wear rate models. These models describe the wear growth rate, i.e., the rate of volume loss at the tool face (rake or flank) per unit contact area per unit time, as a function of various cutting process variables (Arsecularatne, Zhang and Montross 2006).

The analytical approach requires experimental tests to be continued until the tool wear criterion is reached. The minimum number of trials that must be performed is determined by the number of constants included in the given model. The tool wear rate models are derived from one or several wear mechanisms, namely, adhesion, abrasion, diffusion, etc. In the present work, worn surfaces are carefully examined and dominant wear mechanism is identified. Depending upon the obtained results, suitable tool wear rate models are taken into consideration. Four models, based on adhesion as dominant wear mechanism, are selected; out of which, three models are developed by the researchers in the past and one is newly proposed. The basic intention is to test the efficiency of the selected tool wear models by comparing the predicted results with the experimental ones and come up with the best tool wear rate model. The identified best tool wear rate model would be used further to predict tool life for different cutting velocities and feed rates.

Tool wear rate models

Four tool wear rate models used based on adhesion are: (1) W1: Usui model, (2) W2: Matsumura model, (3) W3: Zhao model and (4) W4: modified Zhao model.

W1: Usui model (Usui, Shirakashi and Kitagawa 1984)

In this model, wear rate is dependent on σ_n normal stress, v_c cutting velocity and θ_f cutting temperature variation. The model is based on the following assumptions:

- Rake angle is assumed to be zero degrees
- Hardness of cutting tool remains constant
- Coefficient of friction is equal to the wear land
- Temperature increases logarithmically

The predicted wear rate, in terms of adhesive wear volume per unit time, is given as follows:

$$\frac{dW}{d\ t_m} = B_e\ \sigma_n\ v_c\ e^{\left(\frac{-C_d}{\theta_f}\right)} \tag{3.5}$$

where, B_e is experiment wear rate constant, C_d is constant of element diffused layer at contact surface. The constants are not taken straight away from the literature, instead, the values are derived using the methodology given in the literature (Usui, Shirakashi and Kitagawa 1984). Incidentally, the derived values came out to be closer to the ones given in the literature and t_m machining time

Equation(3.5) was further integrated and represented as follows:

$$W = B_e\ \sigma_n\ v_c\ e^{\left(\frac{-C_d}{\theta_f}\right)}\ t_m \tag{3.6}$$

Since rake angle was assumed as zero degree and volume of wear was almost equal to flank wear. It was assumed that volume of wear W is equal to flank wear V_B.

$$W = V_B \tag{3.7}$$

Equation (3.5) has been modified further using Equation (3.7) and represented in following from.

$$V_B = B_e\ \sigma_n\ v_c\ e^{\left(\frac{-C_d}{\theta_f}\right)}\ t_m \tag{3.8}$$

where, B_e = 7.9x10^{-9} and C_d = 5301.8, $\sigma_n = \frac{F_t}{A_t}$, $A_t = bV_B$. Since thrust force increases with tool wear, a time dependent thrust force polynomial equation is developed for -5° and 2° rake angles using Figure 3.22 (a) and (b). This is achieved by taking initial thrust force F_{ti} for every new cutting parameter combination during turning operation for a single pass. Equations (3.9) and (3.10) shows the developed polynomial equations for the rake angles -5^o and 2^o, respectively

$$F_t = F_{ti} \times t_m^{0.0556} \tag{3.9}$$

$$F_t = F_{ti} \times t_m^{0.0295} \tag{3.10}$$

Similarly, cutting temperature θ_f is determined by measuring the initial temperature θ_{fi} and calculating the average temperature rise $\Delta\theta_{Exp}$ from the experimental cutting temperature versus time graph during turning operation for single pass under varied cutting conditions. The expression is as follows:

$$\theta_f = \theta_{fi} + increment(\Delta\theta_{Exp}) \tag{3.11}$$

W2: Matsumura model

(Matsumura, Shirakashi and Usui 2008) is the modified version of Usui wear rate model which considers the variation of normal stress, cutting velocity, cutting temperature as well as tool geometry (in terms of rake angle α and relief angle β) with respect to time. The model is based on the following assumptions:

- Frictional stress is equal to normal stress
- Temperature increases logarithmically
- Hardness of cutting tool remains constant

The tool flank wear is shown in Equation (3.12).

$$\frac{dV_B}{d\ t_m} = B_e\ \sigma_n\ v_c\ e^{\left(\frac{-C_d}{\theta_f}\right)}\left(\frac{1}{tan\beta} - tan\alpha\right) \tag{3.12}$$

Equation (3.12) is further integrated and represented as follows:

$$V_B = B_e\ \sigma_n\ v_c\ e^{\left(\frac{-C_d}{\theta_f}\right)}\left(\frac{1}{tan\beta} - tan\alpha\right)\ t_m \tag{3.13}$$

where, B_e, C_d are the constants taken from W1 model, σ_n is calculated using thrust force similar to W1 model using Equation (3.8), (3.9) and θ_f values are calculated using the Equation (3.11). β is taken as 5º and α is taken as per experimental settings.

W3: Zhao model (Zhao, Barber and Zou 2002)

The W1 and W2 wear models consider tool hardness, indirectly, in terms of wear constants. This indicates that the tool hardness would remain constant for any variation of temperature, which is not true. In order to overcome this limitation, (Zhao, Barber and Zou 2002) introduced the effect of tool hardness concerning the change in temperature, cutting velocity, relief angle and normal stress with time progression during machining which is expressed as follows:

$$V_B = D_t\left(\frac{2\ v_c}{d^2\ tan\beta}\right)^{\frac{1}{3}}\left(\frac{F_t\ \ t_m}{Z_t}\right)^{\frac{1}{3}} \tag{3.14}$$

$$Z_t(\theta_f) = A_1{\theta_f}^3 + A_2{\theta_f}^2 + A_3\theta_f + A_4 \tag{3.15}$$

where, D_t depends on tool wear experiments, Z_t is temperature dependent tool hardness as shown in Equation (3.15), hardness constants A_1 = 0.000006, A_2 = -0.054, A_3 = 0.5853 *and* A_4= 1517 (Zhao, Barber and Zou 2002) and F_t, θ_f were calculated using Equations (3.9) to (3.11) by similar procedure. The model is based on the following assumptions:

- Rake angle is assumed to be zero degrees
- Frictional stress is equal to normal stress
- Temperature increases logarithmically

W4: Modified Zhao model

The proposed model is a modified form of Zhao model which includes rake angle as an additional input parameter along with other factors considered in Zhao model.

Besides, the modified Zhao model altered the temperature expression used in Zhao model by incorporating non-linear temperature variation to capture temperature rise during flank wear growth more precisely. Note that all the three models considered temperature variation to be linear which is not valid. The basic objective is to develop a robust wear rate model that fits well for varied rake angles and capture non-linear temperature behaviour. The proposed model is based on the following assumptions:

- Frictional stress is equal to normal stress
- Endurance limit of workpiece material remains constant

The underlying relation between flank wear and various input parameters is shown below (Luo, et al. 2005):

$$W = D_t \left(\frac{F_t L_m}{d V_B Z_t} \right) \tag{3.16}$$

Figure 3.27 presents the schematic diagram of a cutting tool showing the wear land and cutting tool angles. Wear volume is converted to wear land measurement V_B in Equation (3.17) according to Stephenson analysis (Stephenson and Agapiou 2016).

$$W = \frac{1}{2} d V_B MN \tag{3.17}$$

Wear land is measured in terms of rake angle and relief angle (see Figure 3.27) and hence, expressed in Equation (3.18).

$$\frac{V_B}{MN} = cot\beta - tan\alpha \tag{3.18}$$

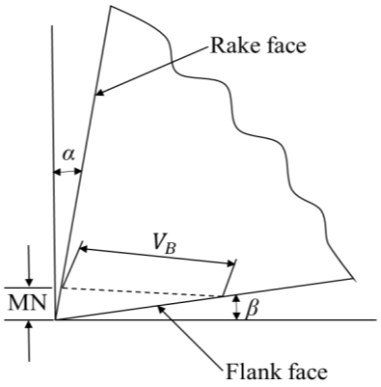

Figure 3.27 Schematic diagram of cutting tool with rake angle α and relief angle β

Further wear land *MN* from Equation (3.18) has been substituted in Equation (3.17) and expressed as follows:

$$W = \frac{dV_B{}^2}{2(cot\beta - tan\alpha)} \tag{3.19}$$

V_B is a variable which increases with the development of flank wear. By substituting Equation (3.19) in Equation (3.16), flank wear is expressed as follows:

$$V_B = D_t \left(\frac{2\,(cot\beta - tan\alpha)}{d^2}\right)^{\frac{1}{3}} \left(\frac{F_t\, L_m}{Z_t}\right)^{\frac{1}{3}} \tag{3.20}$$

Since $L_m = V_C\, t_m$, Equation (3.20) can further be expressed as:

$$V_B = D_t \left(\frac{2\,(cot\beta - tan\alpha)v_c}{d^2}\right)^{\frac{1}{3}} \left(\frac{F_t\, t_m}{Z_t}\right)^{\frac{1}{3}} \tag{3.21}$$

where, D_t depends on tool wear experiments, F_t thrust force, d depth of cut, Z_t are calculated using Equations (3.9), (3.10) and (3.15). But as mentioned earlier, the above three wear rate models could not capture nonlinear temperature rise behaviour as these models assumed temperature rise as linear increment parameter with time. So, in order to capture nonlinear temperature rise behavior, a time-dependent temperature polynomial equation for -5° and 2° tool geometries is derived as shown in Equations (3.22) and (3.23) from experimental temperature measured graph as shown in Figure 3.23 (a) and (b).

$$\theta_f = 3.5 \times 10^{-6} t_m^2 + 4.1 \times 10^{-2}\, t_m + \theta_{fi} + \Delta\theta_{At} \tag{3.22}$$

$$\theta_f = 4 \times 10^{-5} t_m^2 + 3.57 \times 10^{-2}\, t_m + \theta_{fi} + \Delta\theta_{At} \tag{3.23}$$

Equations (3.22) and (3.23) require measurement of θ_{fi} during turning operation for single pass at varied cutting conditions, as done for the other three models. But instead of considering the average temperature increase ($\Delta\theta_{Exp}$), proposed model incorporates analytical temperature rise $\Delta\theta_{At}$ which is calculated analytically. The analytical expression for temperature variation is taken from (Luo, et al. 2005), as shown in Equation (3.24).

$$\Delta\theta_{At} = \frac{2Q l_c}{k_w \sqrt{\pi(1.27 S_{ei} + P_{ei})}} \tag{3.24}$$

where $\Delta\theta_{At}$ is calculated by determining tool flank workpiece contact length l_c near tool flank face of workpiece, $Q = \frac{K_w \times \Delta\theta_f}{f}$ with the rate of heat generated in primary shear deformation zone with respect to Peclet number P_{ei} and endurance limit S_{ei}

equal to 425 MPa (Lorenzo, et al. 2013) and thermal conductivity k_w of workpiece material to carry away the heat from tool flank–workpiece zone.

P_{ei} depends on the rate of material removal per unit depth of cut and the thermal diffusivity of material and is expressed in Equation (3.25).

$$P_{ei} = \frac{v_c d \rho c_p}{k_w} \tag{3.25}$$

Length of contact l_c near tool flank face is taken as a function of depth of cut and rake angle (Iqbal, Mativenga and Sheikh 2009) and expressed as shown in Equation (3.26)

$$l_c = 2d(\xi(1 - tan\alpha) + sec\alpha) \tag{3.26}$$

Figure 3.28 shows the stepwise approach for calculating the flank wear growth analytically using the four tool wear rate models.

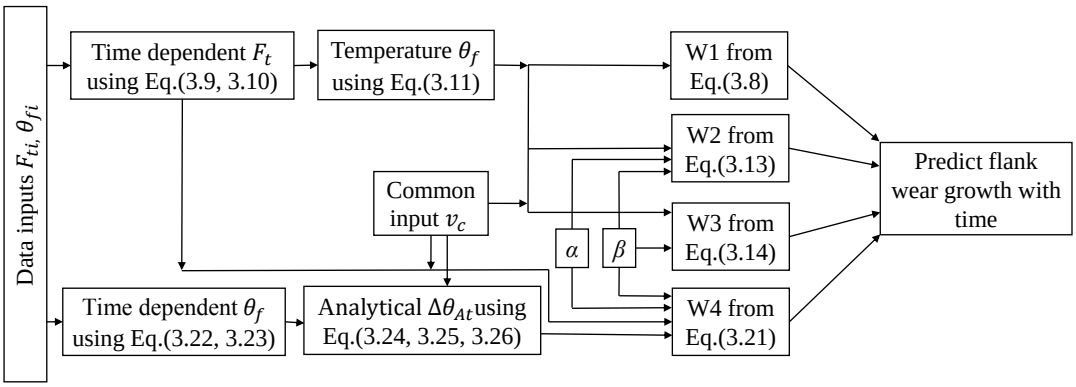

Figure 3.28 Step wise approach for flank wear growth prediction analytically

3.3.3 Experimental validation of tool wear rate models

This section compares the flank wear growth curves predicted analytically using the selected tool wear rate models with the experimental ones under similar cutting conditions. Figure 3.29 (a) and (b) show the predicted flank wear growth using the selected analytical models and their validation with the experimentally measured ones for rakes angles -5º and 2º, respectively.

In Figure 3.29 (a) for -5° rake angle, it is observed that all the four models are able to predict flank wear growth with respect to machining time. But, W1 and W2 models could not capture the steady state wear region satisfactorily. This could be due to the incapability of the models to capture the temperature dependent tool hardness. On the contrary, flank wear growth curves predicted by W3 and W4 models

could show the three regions of flank wear growth distinctly. However, a larger deviation is observed for the model W3, particularly in the catastrophic failure region, as compared to that of W4. It is known that during the flank wear growth, until the steady growth region, temperature is not that sensitive. Nevertheless, as the flank wear enters catastrophic failure region, temperature plays a major role in accelerating the wear. Since W4 is the only model that considered non-linear temperature variations, it could show better results as compared to others. Figure 3.29 (b) for -5° rake angle, shows the percentage error of the predicted flank wear as the flank wear progressed with respect to the experimental ones. The newly proposed model W4 showed the least percentage error amongst all with error percentage as low as 0.003%.

Similarly, in the case of 2º rake angle (Figure 3.29), all the models could predict the flank wear growth reasonably well, including W1 and W2, which had failed to replicate the steady region satisfactorily for -5º rake angle. Figure 3.29 (b) for 2º rake angle showed the estimated error percentage of the predicted flank wear for all the models. Again, W4 showed the least error as compared to others.

Overall, it is observed that the newly proposed model came out to be the best model for predicting flank wear growth for both the positive as well as negative rake angles. It is noted that one of the most commonly used model W1 i.e., Usui model showed larger deviations, especially for the negative rake angle. This was obvious because the model included neither the rake angle effect nor the tool hardness factor. On the other hand, W2 considered both rake angle and relief angle effect but did not consider tool hardness variation. Such a phenomenon indicates that the commonly used models such as W1 and W2 could not predict the flank wear growth satisfactorily.

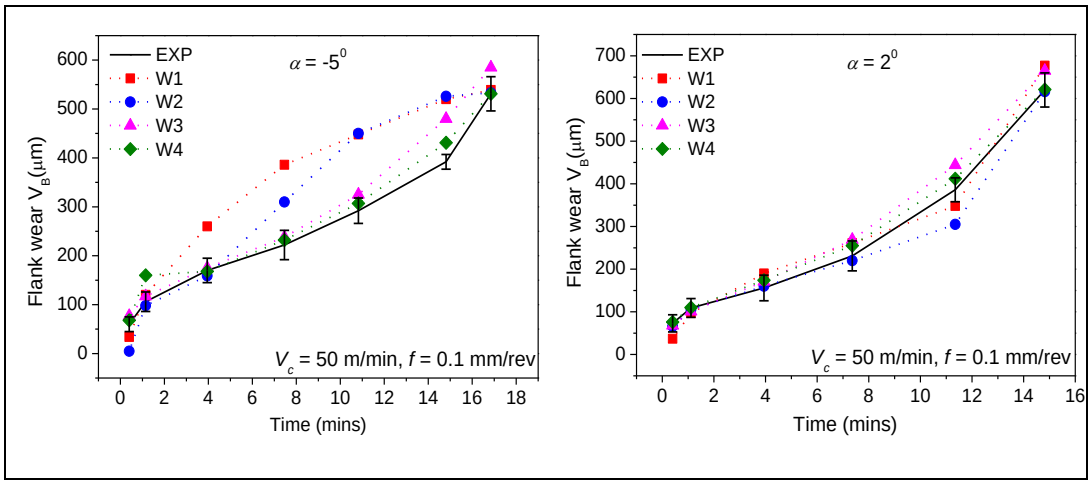

(a)

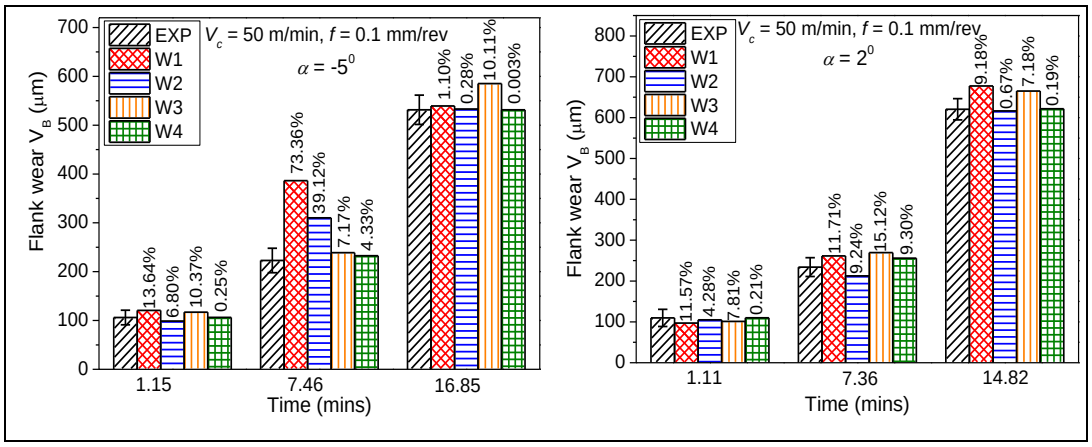

(b)

Figure 3.29 Comparison of tool life with respect to experimental and predicted tool wear models for -5° and 2° rake angle (a) tool life plot (b) bar chart and error percentage with experiment

Similarly, for W3, higher deviations are observed in the catastrophic region, especially for negative rake angle. This may be because temperature dependent tool hardness (in case of W1 and W2), rake angle effect and nonlinear temperature behavior are not considered as input to these models. Moreover, in theory of machining, most of the analyses are based upon ideal conditions i.e., assuming rake angle as positive. Whereas, in the case of newly proposed model W4 rake angle is included explicitly as one of the key inputs, in addition to temperature dependent tool hardness and relief angle, to include the overall effect of tool geometry on flank wear. Consequently, W4 could show the best results for both positive and negative rake angles. Further, W4 is the only model that considered non-linear temperature variations and thus, showed better results as compared to others.

3.3.4 Analytical prediction of tool life

The model which showed the best results, i.e., W4 (modified Zhao model), is used for predicting tool life at varying cutting speeds. Experimental tool life tests are also conducted under similar cutting conditions and measured values of tool life are compared with the predicted ones. The primary objective is to check the robustness of the proposed model under varied cutting conditions. Figure 3.30 presents the predicted values of tool life using W4 at different cutting speeds for -5º rake angle as well as the error percentages with respect to that of measured values. It is observed that W4 could replicate the effect of the cutting speeds on tool life fairly well, i.e., as the cutting speed increased, there was a decrease in tool life. Such observation is in accordance with Taylor's tool life equation. Also, this is much expected considering the fact that higher cutting speeds lead to higher material removal rate and, consequently, higher cutting temperatures and thermal softening of tool (Hoier, et al. 2019). Furthermore, the predicted values of tool life closely matched the experimental ones with error percentage well within 7%.

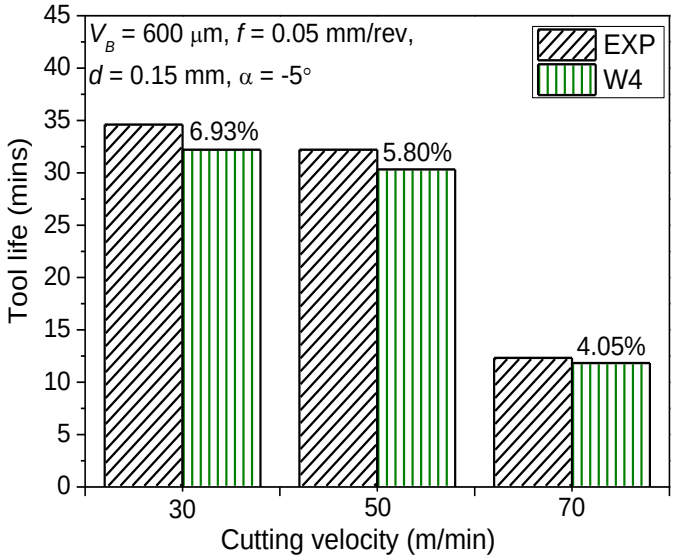

Figure 3.30 Comparison of experimental and W4 predicted tool life for varying cutting velocity at -5° rake angle.

As a whole, it can be stated that the proposed model W4 came out to be a good choice when compared with the tool wear models that are commonly being used to predict tool life analytically under varied cutting conditions. It is to be noted that the same model can also be extended not only for predicting the tool life for different grades

of WHAs but also for cooling or lubrication conditions. Although the mathematical equations did not consider any parameters that are directly related to lubrication conditions, it considers the effect of cooling and lubrication indirectly in the form of outputs such as cutting forces and temperatures. Since these outputs are affected by cooling or lubrication conditions considerably, the effect of the latter on tool wear growth gets captured inevitably.

It is also observed that approaches based on artificial intelligence techniques like fuzzy logic, neural networks and meta-learning models have emerged in the recent past for monitoring and prediction of tool wear (Li, et al. 2019). There is no doubt that such approaches have shown substantial improvements in the accuracy of predicting tool wear. However, the drawback of such an approach is that it is based on an empirical model which generally needs extensive experimental data (Salimiasl 2017). In addition, these empirical models fail to explain the physical meaning. Whereas, the proposed model in the current work includes mathematical equations representing the corresponding physical laws, thus, giving a better insight of tool wear growth with respect to input and other output parameters. Hence, one feasible way could be to combine these approaches, if possible, to get the benefit of both.

Summary

The present chapter attempts to assess a comprehensive analysis of material properties for three different grades of WHAs with varying tungsten content. There exists a strong relationship between tungsten content, material properties and microstructural parameters. Such a phenomenon is further analyzed by machinability of WHAs with varying tungsten content in terms of different machining characteristics such as chip morphology, material removal rate, cutting force and surface roughness. Besides, experimental analysis and analytical prediction of the tool wear growth under varied cutting conditions are performed. From the machinability tests, it is found that the dependence of chip morphology, MRR, cutting force and surface roughness on feed rate, tungsten content and tool geometry show a clear trend but not in the case of cutting velocity. A complex interplay of different variables such as hardness, ductility/brittleness, and temperature rise during machining appears to be responsible for such behavior. Similarly, experimental tool

wear results show there exists a strong relationship between flank wear and other machining outputs, namely, force components, cutting temperature, chip morphology and surface roughness. Overall, it can be stated that machining is a complex process in which not merely the input parameters affect the machining outputs, but also the machining outputs affect each other adversely. This instigates for a comprehensive understanding of the physics underlying the chip formation mechanism during machining of difficult to machine WHAs. Hence, the next chapter focuses on the FE modelling of the chip formation process to simulate difficult to measure variables such as the distribution of stress, strain and temperatures in the cutting zone.

Chapter4 FINITE ELEMENT MODEL DEVELOPMENT

The metal cutting is considered as a thermo–mechanical process involving numerous complexities. An adequate quantitative understanding of the mechanics governing the metal cutting process is essential to carry the metal removal process efficiently and economically. With advances in computational techniques, numerical methods such as FE method are one of the popular tools for analysis of the cutting process. This approach substitutes the expensive trial and error experimental techniques to a great extent. However, the selection of suitable material and damage models and subsequently the determination of precise material model constants are one of the prime concerns in FEM. The present work focuses on formulating a methodology to calculate and fine-tune the material as well as damage model constants. Hence, a 2D FE model of the orthogonal cutting process is developed considering the computed material and damage model constants as material inputs.

4.1 FE simulation procedure

The present work focuses on the development of a 2D FE model of chip formation under orthogonal cutting conditions. Although 2D analysis is a restrictive approach from a practical point of view, it reduces the computational time considerably and provides satisfactory results regarding the details of the chip formation. A plane strain condition is assumed because the feed value is generally very less as compared to the depth of cut. A fully coupled temperature displacement analysis is performed using ABAQUS/Explicit version 6.14 to simulate the chip formation process.

4.1.1 Geometric details, boundary conditions and material properties

The 2D model comprises a portion of the cutting tool and a rectangular block representing the workpiece. The cutting tool is considered to be perfectly sharp based on the fact that the effect of the tool edge radius hardly plays any role once a steady state is reached in cutting (Priyadarshini, Pal and Samantaray 2012). The cutting tool used in the model is uncoated tungsten carbide with rake angles -8°, -5° and 2° and clearance angle 7°. Both the workpiece and the tool are considered as deformable bodies and discretized with four-noded plane strain thermally coupled quadrilateral,

bilinear displacement and temperature (CPE4RT) with reduced integration and hourglass control element type.

As boundary conditions, the cutting tool movement is constrained in the vertical direction by fixing the top edge in Y-axis and velocity equal to the cutting speed (in m/sec) is given in negative X-direction. The bottom of the workpiece is fixed in Y-axis and the left edge of the workpiece is fixed in X-axis. By this, it not only restricts the workpiece movement but also aids in calculating the cutting and feed force in X and Y directions, respectively. As thermal boundary conditions, the tool and the workpiece are kept initially at room temperature. The geometric details with boundary conditions and meshing are shown in Figure 4.1. The material properties of both the workpiece and cutting tool used in the simulation of the chip formation process are listed in Table 4.1.

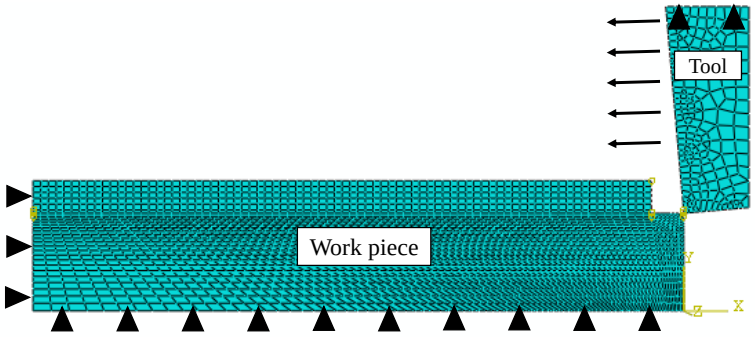

Figure 4.1 Geometric model, meshing and boundary conditions in the FE model

Table 4.1 Material properties of workpiece and cutting tool (Priyadarshini, Pal and Samantaray 2012) for FE simulations

Property	Workpiece			Tool (Tungsten carbide)
	90WHA	95WHA	97WHA	
Density (kg/m^3)	17013	17500	18106	11900
Young's Modulus (N/m^2)	213 x 10^9	267 x 10^9	309x 10^9	534 x 10^9
Poisson's ratio	0.24	0.22	0.2	0.22
Specific heat (J/kg °C)	320	307.37	293.1	400
Thermal Conductivity (W/m °C)	56.92	57.43	58.30	50
Coefficient of thermal Expansion (m/m °C)	4.4 x 10^{-6}	4.2 x 10^{-6}	4.0 x 10^{-6}	---
Fracture Toughness (MPa m$^{1/2}$)	36	41	44	---

ABAQUS procedure

4.1.2 Material constitutive equation

Constitutive equations capture the thermo-mechanical properties of a material experiencing deformation. These constitutive equations could be one or a group of equations that would depend on the complexity of the material behavior and expresses the deformation of the material in terms of flow stresses.

Deformation of material is distinguished as elastic and inelastic response based on the assumption that there exists an additive relationship between the strain rates such that:

$$\dot{\varepsilon} = \dot{\varepsilon_e} + \dot{\varepsilon_p} \tag{4.1}$$

where $\dot{\varepsilon}$ is total strain rate of material, $\dot{\varepsilon_e}$ is elastic strain rate and $\dot{\varepsilon_p}$ is inelastic strain rate. Equation (4.1) specifies that material initially undergoes elastic deformation, and when the flow stress is beyond the elastic limit, plastic deformation takes place. The elastic deformation can be simply expressed by linear elastic relationship as:

$$\sigma = D_e : \varepsilon_e \tag{4.2}$$

where D_e is the elastic stress tensor and ε_e is the elastic strain.

The plastic deformation is usually expressed in terms of constitutive equations and it contains yield criterion, flow rule and strain hardening rule. The yield criteria define the state of stress at yielding, the flow rule describes increment of plastic strain during yielding and the strain hardening rule defines how the material strain hardened as the plastic strain increases. The machining process usually comes under the category of large deformation problems were the Von Mises yield criterion and Prandtl-Reuss flow rule are generally used to describe the isotropic yielding and hardening (Rodriguez, Jonsen and Svoboda 2017).

These criteria make machining a complex process of plastic deformation since the workpiece material is subjected to very high levels of strain, strain rate and temperature, which significantly affects flow stress. So, an accurate and reliable rate-dependent constitutive model is required to define stress-strain response in terms of strain rate, temperature and work hardening such that the physics of metal cutting is represented adequately. Johnson-Cook constitutive model (Johnson and Cook 1983) is one such model that considers the flow stress behavior of the work material in

terms of strain, strain rate and temperature. This model is most widely used and regarded as numerically robust. The equivalent flow stress is expressed as:

$$\sigma = (A + B\varepsilon^{n})(1 + Cln\dot{\varepsilon_p}^{*})(1 - T^{*m}) \quad (4.3)$$

$$\dot{\varepsilon}_p^{*} = \frac{\dot{\varepsilon}_p}{\dot{\varepsilon}_{po}} \text{ and } T^{*} = \left(\frac{T - T_r}{T_m - T_r}\right) \quad (4.4)$$

where T_r is the room temperature taken as 25°C, T_m is the melting temperature of the workpiece material, *A* is the initial yield stress at reference strain rate (MPa), *B* the hardening modulus at reference strain rate, *n* the work-hardening exponent, *C* the strain rate dependency coefficient, and *m* the thermal softening coefficient. *A*, *B*, *C*, *n* and *m* are empirical material model constants derived from different mechanical tests. Since the machining process involves strain rate in the range of 10^4 to 10^6 s^{-1}, the evaluation of these material property data accurately is a very challenging task. SHPB test is one of the alternatives which enables material testing in the range of 10^4 s^{-1} and it can be used up to reasonable strains and for elevated temperatures (Zabel, Rodder and Tiffe 2017). Hence, this method is widely used to determine the materials constants required as inputs in modeling of FE machining simulations (Xie, et al. 2019, Ozel and Karpat 2007). The present work determines the JC model constants experimentally by utilizing the high strain rate test data available in literature as well as analytically by using machining data.

4.1.3 Damage model

A ductile failure model is additionally incorporated both for chip separation and simulation of discontinuous chips as expected in case of machining WHAs. The use of the damage model as chip separation criterion aids in a smoother movement of the cutting tool into workpiece without any mesh distortion near the tool tip. Material failure refers to the complete loss of load carrying capacity which results from progressive degradation of material stiffness. Specifications for the damage model include a material response (undamaged), damage initiation criterion, damage evolution and choice of element deletion (Abaqus, User's manual Version 6.14-1 2014).

Damage initiation criterion

Damage initiation criterion refers to the commencement of damage for a given state of a material. This damage initiation criteria for the fracture of metals includes ductile

and shear failure. In the present case, this damage initiation has been taken care of by the Johnson-Cook damage model. This model makes use of damage parameter ω_d which is defined as the sum of the ratio of initial equivalent plastic strain ε_0^p and summation of increment of the equivalent plastic strain $\Delta\varepsilon^p$ to the fracture strain ε_f (Abaqus, User's manual Version 6.14-1 2014), given as follows:

$$\omega_d = \frac{\varepsilon_0^p + \sum \Delta\varepsilon^p}{\varepsilon_f} \tag{4.5}$$

The fracture strain ε_f is expressed as follows (Johnson and Cook 1983):

$$\varepsilon_f = [D_1 + D_2 \exp(D_3\sigma^*)]\left[1 + D_3\, ln\left(\frac{\dot{\varepsilon}}{\dot{\varepsilon}_0}\right)\right][1 - D_5 T^*] \tag{4.6}$$

$$\sigma^* = \frac{\sigma_h}{\bar{\sigma}} \tag{4.7}$$

where, σ_h is the hydrostatic stress and D_1 to D_5 are experimentally determined damage constants. The expression in the first set of the bracket in Equation (4.6) refers to the decrease in fracture strain as the hydrostatic stress increases and the yield stress decreases. The second and third terms in the bracket show the effect of strain rate and temperature on fracture strain. The damage initiation criteria are met when the value of ω_d (Equation (4.5)) reaches one. In machining, it is known that the maximum stress and strain occur in front of the cutting tool. With the advancement of the cutting tool, the plastic strain increases within the workpiece material near the tool tip. Hence, as the plastic strain increases ω_d of the element gradually reaches the damage initiation criterion threshold.

Damage evolution

The damage evolution occurs when progressive degradation of material stiffness takes place, leading to material failure by following the process of damage initiation criterion. By this the stress tensor in the material at any given time during analysis, is presented by (Hibbitt, and Karlsson & Sorensen 2007):

$$\sigma = (1 - D)\bar{\sigma} \tag{4.8}$$

where $\bar{\sigma}$ is the equivalent stress tensor computed in the current increment. When the overall damage variable D reaches a value 1, at this point, failure occurs and the concerned elements are deleted from the computation. By this, the material has lost its load-bearing capacity and it has been explained with the help of Figure 4.2, which

describes the characteristic stress-strain curve for the material undergoing damage (Hibbitt, and Karlsson & Sorensen 2007). The solid curve represents the damaged stress-strain response, while the dashed curve is the response in the absence of damage. In Figure 4.2 σ_{y0} and ε_0^p are the yield stress and equivalent plastic strain at the onset of damage and ε_f^p is the equivalent plastic strain at failure (i.e., D = 1).

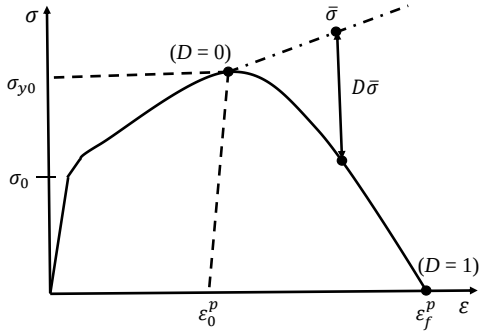

Figure 4.2 Stress-strain curve with damage evolution

The effective plastic displacement, after the damage initiation criterion is met can be defined with evolution law, i.e., If a linear evolution of the damage variable with plastic displacement is assumed, then the damage variable increases as follows:

$$D = \frac{L_e \varepsilon^p}{u_f^p} = \frac{u^p}{u_f^p}$$
$$u_f^p = \frac{2G_f}{\sigma_{yo}} \tag{4.9}$$

where L_e is the typical length of a line across an element for a first-order element, known as characteristic length of the element, u_f^p is the plastic displacement at failure and G_f is the fracture energy per unit area.

The above model ensures that the energy dissipated during the damage evolution process is equal to G_f only if the effective response of the material is perfectly plastic (constant yield stress) beyond the onset of damage. In this work, G_f is given as an input parameter which is a function of fracture toughness K_{IC}, Young's modulus E and Poisson's ratio ν as follows (Mabrouki, et al. 2008).

$$G_f = \left(\frac{1-\nu^2}{E}\right) K_{IC}^2 \tag{4.10}$$

Element deletion

The ELEMENT DELETION = YES module in ABAQUS 6.14 software along with the Johnson-Cook damage model of the software are used to delete the elements that fail.

4.1.4 Interfacial contact and heat generation

A contact constraint has been enforced by applying a kinematic contact algorithm in a master-slave contact pair, where the rake surface of the cutting tool is defined as the master surface and chip as the salve surface. Through this process, momentum is conserved between the contacting bodies. The kinematic contact algorithm works in two steps. It firstly identifies which slave nodes in the predicted configuration penetrate the surface and then estimates the resisting force required to oppose the penetration based on the depth of penetration of slave nodes, mass associated with it and the time increment. The contact algorithm calculates the total internal mass of the contacting interfaces and the acceleration correction for the master surface nodes. The acceleration correction for the slave nodes is then determined by using the predicted penetration of each node for a time increment and the acceleration correction for the master surface nodes. By this, a corrected configuration can be obtained in which the contact constraints are enforced. Modeling of tool-chip friction is based on Coulomb's law with the mean value of coefficient of friction taken as 0.2 which came out to be the best compromise between computational efficiency and cutting force accuracy (Aviral and Martin 2011).

During the machining, heat is generated in the primary shear deformation zone and the secondary shear deformation zone due to severe plastic deformation and the friction in the tool-chip interface. It is formulated by steady-state energy equation for orthogonal machining process as:

$$\bar{q} = \bar{q}_p + \bar{q}_f \tag{4.11}$$

$$\bar{q}_p = \eta_p \sigma \dot{\varepsilon}^p \tag{4.12}$$

$$\bar{q}_f = \eta_f J \tau \dot{\gamma} \tag{4.13}$$

where $\bar{q}_p$ is the heat generation rate due to plastic deformation, η_p the fraction of the inelastic heat, $\bar{q}_f$ is the volumetric heat flux due to frictional work, $\dot{\gamma}$ the slip rate, η_f

the frictional work conversion factor considered as 1, *J* the fractional of the thermal energy conducted into the chip and τ is frictional stress.

The factor η_p defines the heat generation caused by shear deformation (plastic strain) of the workpiece due to cutting tool movement. This term is introduced as a source of temperature stress coupling for coupled temperature displacement analysis and the thermal solution is obtained only at nodes were thermal degrees of freedom have been activated. Thus, the value of η_p is assumed to be 0.9 (Mabrouki, et al. 2008). By this chip retains 90% of the heat generated due to shear deformation, while 10% is lost to the environment. The fraction of dissipated energy caused by friction η_f is assumed to be 1. From the fraction η_f there is an amount of heat *J* remaining in the chip and a heat fraction (1-*J*), conducted into the cutting tool. In the present work, the value of *J* is assumed to be 0.8. Thus, the chip carries away a part of the heat is taken care by Equation (4.11) to (4.13) which combine both the heat fractions, i.e., *J* and η_p giving an average within a range of 70-80% of the total heat.

4.1.5 Solution procedure

In the present study, FE machining simulations is formulated using the explicit dynamic analysis with ALE technique.

ALE formulation

The ALE technique combines the features of pure Lagrangian and Eulerian analysis. The ALE approach allows flow boundary technique without altering elements and connectivity of the mesh using the adaptive meshing technique in ABAQUS/Explicit. The idea is to apply features of the Eulerian approach for modeling the area around the tooltip, while Lagrangian form can be applied to the free surface of the chip. By this method, severe element distortion and entanglement can be avoided in the cutting zone without the use of a re-meshing criterion.

Explicit dynamic analysis

The explicit dynamic ALE formulation is mainly used to solve highly non-linear problems involving large deformations and changing contact, as observed in machining. It is known that the mechanical solution response is obtained using the explicit central difference integration rule with a lumped mass matrix. Since both the

forward difference and central difference integrations are explicit, the heat transfer and mechanical solutions are obtained simultaneously by an explicit coupling. Therefore, no iteration or tangent stiffness matrices are required.

The explicit procedure integrates through time by using many small time increments. Both the central difference and forward difference operators are conditionally stable.

FE software: ABAQUS

The selection of software plays a significant role in FE machining simulation for determining the quality and scope of analysis that can be performed. Presently there are many commercial software packages available for solving various engineering problems that might be static, dynamic, linear, or non-linear. Some of the dominant general-purpose FE software packages are ABAQUS, ANSYS, MSC/NASTRAN, SRDC-IDEAS, MSC Marc, COMSOL Multiphysics, etc. These different software packages would offer different capabilities, and this makes it critical to select a suitable software package with appropriate features required for performing a given analysis successfully. In the present study, ABAQUS/Explicit software package has been used because of its several unique features.

The software like Deform and AdvantEdge with specific modules that are explicitly designed for machining simulations and the solvers are optimized specifically for metal cutting processes. This feature makes it effective where a quick, easy to set up machining simulation is needed. By this, it may lead to limited use of a program, thus giving not much flexibility in configuring the control of the solver. On the contrary, ABAQUS is a general-purpose, highly sophisticated simulation program based on FEM that can solve problems ranging from relatively simple linear analyses to the highly complex non-linear simulations. From this, it clear that more skill, effort and time is required to set up simulations as no preset controls and assumptions are available. But this is the feature that takes modeling to a very high level of detail and ensures a thorough analysis by allowing precise control on the boundary conditions, mesh attributes, element type, solver type and so on. A complete ABAQUS program consists of three stages, namely pre-processing, analysis and post-processing. The input file and output file link these stages. The subsequent sub-sections would discuss various modules of ABAQUS/CAE in brief.

❖ **Part module**

Individual parts are created in the part module either by sketching their geometry directly in Abaqus/CAE or by importing their geometry from other geometric modeling programs. Depending upon the analysis, the parts can be 2D or 3D deformable, discrete rigid, analytical rigid parts. In the present study, both the cutting tool and the workpiece are considered as 2D deformable bodies. The part tools contained in this module allow editing and manipulating the existing parts defined in the current model.

❖ **Property module**

Property modules allow us to assign various material properties to the part instance. A material definition specifies all the property data relevant to a particular analysis. For a coupled temperature displacement analysis, both the mechanical strength properties and heat transfer properties must be given as inputs. Various plasticity models and damage models are also contained in the property module. As an input, the material constants of the selected plastic model and damage model, such as the Johnson-Cook material model and Johnson-Cook damage model respectively, are defined in a tabular form.

❖ **Assembly module**

The individual parts that are created in part module exist in their coordinate system. It is in the assembly module that these parts are assembled by relative positioning for each other in a global coordinate system.

❖ **Step module**

In the present study, coupled temperature displacement explicit dynamic analysis has been used for the machining simulation process. Further step module provides a convenient way to capture changes that occur in the model during analysis. Step module helps us to specify specific output requests with region-specific. The general solution controls and solver controls can also be customized. Furthermore, adaptive mesh regions and the controls for adaptive meshing in selected areas can be specified in this module. So in the present case, ABAQUS/Explicit is used to implement ALE adaptive meshing.

- **Interaction module**

The interaction module allows us to specify mechanical and thermal interactions between regions of a model or between a region of a model and its surroundings. Surface-to-surface contact interaction has been used to describe contact between tool and workpiece in the present study. The interaction between contacting bodies is defined by assigning a contact property model to a contact interaction that defines tangential behavior and normal behavior. Further kinematic contact algorithm has been used to enforce contact constraints in master-slave contact pairs, where the rake surface of the cutting tool is assigned as master surface and chip as the slave surface. Both the frictional conditions and the friction-generated heat are included in the kinematic contact algorithm through TANGENTIAL BEHAVIOUR and GAP HEAT GENERATION modules of the software.

- **Load module**

The load module is used to assign loads, boundary conditions and predefined fields on geometric model surfaces and edges.

- **Mesh module**

The mesh module allows generating mesh on parts and assemblies created within ABAQUS/CAE. In the present case, the CPE4RT element type was selected for meshing. An advancing front algorithm was used while free meshing the parts to avoid large differences in element size and make the numerical procedure more efficient.

- **Job**

The job module allows us to create a job, to submit it to ABAQUS/explicit for analysis and to monitor its progress.

- **Visualization**

The visualization module provides graphical display of FE models and results. It extracts the information of the model and results from the output database.

In the analysis, the stage solver solves the numerical problem defined in the model. In the present case, ABAQUS/Explicit has been used as a solver to simulate the machining model.

- **Solution strategy**

Since the machining process involves nonlinear dynamic response, a direct integration system needs to be used. ABAQUS/Explicit solver is beneficial since no convergence criteria are considered, non-linear contact simulations proceed smoothly.

4.2 Determination of JC model constants

The JC model constants for various materials can be determined using experimental, analytical, and numerical techniques. The experimental technique includes performing high strain testing and then making use of the obtained stress-strain data in conjunction with conventional optimization techniques to determine the JC constants (Zhou, et al. 2017). An advancement over standard optimization methods in experimental approach is the use of evolutionary computational algorithms that identify material parameters through a fine grain search technique and state superiority over classical data fitting techniques (Bosetti , Bort and Bruschi 2013, Gupta, et al. 2013). The analytical approach includes the use of inverse identification algorithms in conjunction with either high strain rate tests or machining tests to determine material characterization and predict the flow stress behavior of the material (Frueh, et al. 2016). The numerical approaches use FE analysis to simulate the machining process in which the predicted outputs (chip morphology, machining force, temperature, etc.) are compared to that of experiments (Woodward, et al. 1985) and JC constants are fine-tuned using an inverse approach (Kiran, et al.2018).

The present section discusses the methodology to identify the JC model constants for WHAs using four different approaches, out of which three were experimental based (M1, M2 and M3) and one analytical (M4). The details are as follows:

M1: M1 is based on the experimental approach, as discussed earlier, wherein the stress-strain data using high strain rate test is taken from the literature (Woodward, et al. 1985) and JC constants are derived using the conventional optimization technique.

M2 and M3: M2 and M3 are also based on the experimental approach similar to M1, with the only exception that JC constants are further fine-tuned using evolutionary algorithms, namely, GA and ABC, respectively (Bosetti , Bort and Bruschi 2013).

M4: M4 is based on analytical approach such that JC constants are calculated using inverse identification algorithm in conjunction with machining tests and Oxley's model (Ning, et al. 2019).

The schematics of the overall methodology adopted to determine JC constants is present in Figure 4.3.

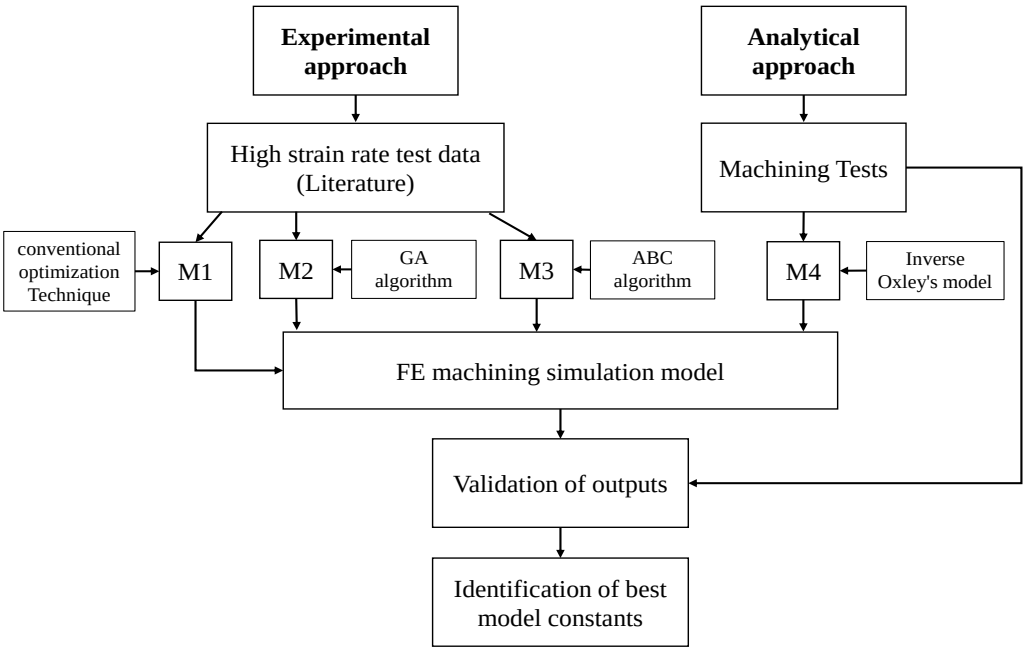

Figure 4.3 Overall methodology adopted to determine JC constants

4.2.1 Experimental approach

The experimental approach makes use of stress-strain data obtained using high strain rate test from the available literature in conjunction with conventional optimization techniques or evolutionary algorithms to determine the JC model constants.

- **M1**

The true stress-strain data are calculated from the stress-strain data obtained from the literature. The data points are then considered in the plastic region until Ultimate Tensile Strength (UTS). The computed stress-strain data are used further to determine M1, as discussed below.

At reference strain rate and temperature:

Constant *A* is yield stress at room temperature was considered

$$\sigma = (A + B\varepsilon^{n}) \tag{4.14}$$

Equation (4.14) was further modified and the graph was plotted in terms of $\ln(\sigma - A)\ vs\ ln\varepsilon$, where *n* is slope and *B* is an intercept of the plot.

At fixed plastic strain and reference temperature:

$$\sigma = (A + B\varepsilon^n)(1 + Cln\varepsilon^*) \tag{4.15}$$

From Equation (4.15) graphs was plotted in terms of $\left(\frac{\sigma}{(A+B\varepsilon^n)} - 1\right) vs\ \ln(\varepsilon^*)$ from the slope of the graph, a value of *C* is calculated.

At fixed plastic strain and reference strain rate:

$$\sigma = (A + B\varepsilon^n)(1 - T^{*m}) \tag{4.16}$$

From Equation (4.16) graphs was plotted in terms of $\ln\left(1 - \frac{\sigma}{(A+B\varepsilon^n)}\right) vs\ \ln(T^*)$. From the slope of the graph, the value of *m* is calculated. For each plastic strain value, one set of *C* and *m* values is derived. Thus, there exist many sets of *C* and *m* constants. Thereby considering minimum average absolute error $(\Delta)$from Equation (4.17) and maximum correlation coefficient from Equation (4.18), an optimum *C* and *m* values were determined.

$$\Delta = \frac{1}{N}\sum_{i=1}^{i=N}\left|\frac{\sigma_{exp}^i - \sigma_{pre}^i}{\sigma_{exp}^i}\right| \times 100 \tag{4.17}$$

$$R = \frac{\sum_{i=1}^{i=N}(\sigma_{exp}^i - \bar{\sigma}_{exp})(\sigma_{pre}^i - \bar{\sigma}_{pre})}{\sqrt{\sum_{i=1}^{i=N}(\sigma_{exp}^i - \bar{\sigma}_{exp})^2 \sum_{i=1}^{i=N}(\sigma_{pre}^i - \bar{\sigma}_{exp})^2}} \tag{4.18}$$

- **M2**

GA is the process derived from biological evolution. This algorithm modifies the individual solution repeatedly. At each stage, GA selects individual parents randomly from the current population and children are produced for the next generation by mutation process. The population evolves. An optimal solution over a successive generation is obtained (Addona and Teti 2013).

The constants *B, C, n* and *m,* were considered as design variables. The initial population is created by a random selection of each design variable from the corresponding defined range.

Once the initial population is formed, three members are selected randomly and the one which satisfies the fitness function $\Delta(x)$ is chosen as a parent. Similarly, a set of

ten parents are selected. Fitness function, in this case, is the difference between experimental and calculated data of true stress-strain curve, as given below in Equation (4.19) where $\Delta(x)$ is absolute error functions at i^{th} strain rates. The objective of the fitness function is to minimize $\Delta(x)$, i.e.,

$$x(B, n, C, m) = Min\{\Delta(x)\} \tag{4.19}$$

The selected ten parents are encoded to binary strings and considered as chromosomes. Then the recombination of chromosomes is done by the crossover of the binary strings of two randomly selected chromosomes. During crossover between two parents, a probability of 0.1 is considered as a mutation factor and one of its bit is flipped to form children. The children's chromosomes are then decoded to obtain design variables. This procedure has been repeated for 250 generations. The solution converged at around the 230^{th} generation. After that, there is not much change in absolute error and hence, the process is terminated. Figure 4.4 shows the flow chart of the implemented strategy for GA to determine JC Model constants.

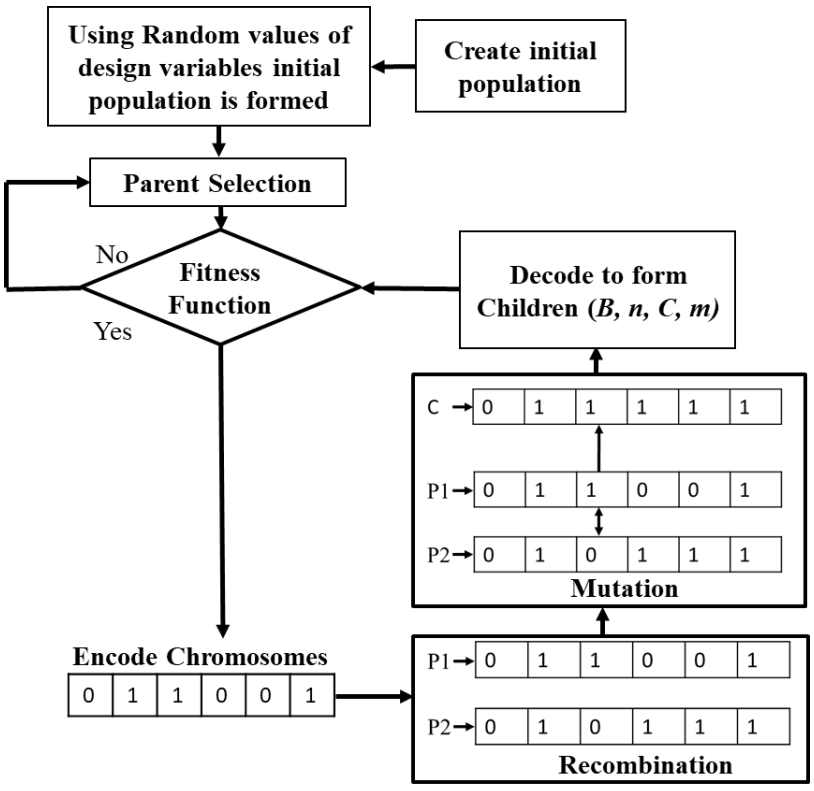

Figure 4.4 Flow chart of the implemented strategy for GA

❖ **M3**

ABC Algorithm is a naturally inspired algorithm based on the intelligent behavior of foraging honey bee swarms. The foraging behavior, learning, memorizing and information sharing characteristics of honey bees are used in solving multi-objective optimization problems (R.Yildiz 2013).

Firstly, the constants *B*, *C*, *n* & *m* are considered as design variables. The range of each design variable is divided into different solution sets, i.e., food sources. At the same time, the initial population of a swarm is taken based on the number of food sources. The process starts with scout bees, which identifies food source and converts it to employed bee and transports one combination of the solution, i.e., nectar to the hive. The onlooker bees at hive check the nectar amount using fitness function $\Delta(x)$. The fitness function defined in this algorithm is the same as the one taken for GA in Equation (4.19). Next onlooker bees compare the nectar amount and stores P as the best solution, using objective function $x(B, n, C, m)$ in its memory using Equation (4.19)

If the solution representing food source does not improve after a number of trials, then the food source is abandoned and employed bee gets converted to scout and again, a new search for new food source begins. After a certain number of trials onlooker bees memorize the P best solution stored in the memory using an objective function. If there is no further improvement in the solution for all desired sets of food sources, then the process terminates and overall best design variable combination is displayed as an optimal solution. Figure 4.5 shows the flow chart of the implemented strategy for ABC algorithm to determine JC model constants

Both of these optimization algorithms are coded in python using libraries NumPy, SciPy and pandas.

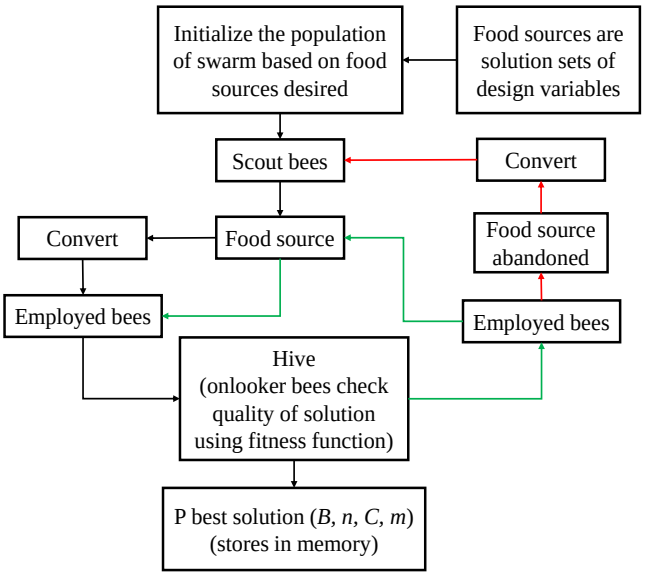

Figure 4.5 Flow chart of the implemented strategy for ABC algorithm

4.2.2 Analytical approach (M4)

The analytical approach makes use of PSO (Particle swarm optimization) as inverse identification algorithm in conjunction with machining tests and Oxley's model to determine the JC model constants for WHAs.

Extended Oxley's machining theory

This model uses extended Oxley's machining theory to predict the JC model constants. The exponent n_{eq} was calculated using the JC model constants *A, B* & *n* using the following Equation (A.1):

The shear zone model for orthogonal cutting based on the parallel-sided theory by Lalwani and his co-workers (Lalwani, Mehta and Jain 2009) is shown in Figure A.1. The values of ϕ, C_0 and ζ from a given set of input parameters such as feed, depth of cut, cutting speed and rake angle are evaluated using Oxley's machining model using an iterative loop-based computer program. The error between shear stress (τ_{int}) and shear flow stress (q_{chip}) in the chip at the interface is used to estimate the final value of the shear angle. Similarly, C_0 was approximated by determining the minimum difference between normal stress at the tool-chip interface and the stress derived using the stress boundary condition at point B (σ'_N). The value of ζ is determined by finding the minimum force value. These parameters are calculated using Equations (A.1)-(A.31), detailed in Appendix.

PSO algorithm

PSO is an evolutionary computational technique developed based on the social behavior of bird flocks. It was first proposed by Kennedy and Eberhart (1995). In PSO, each particle is considered as *i*, move in search space of the optimization problem of *j* solution space. The particle with the best fitness value is considered as the leader of the swarm and guides other particles to move in the best search areas. Each particle is influenced by its search direction by intellectual information (its own best position found so far called $y_{g\ best}$). The leader of the swarm is updated on each interaction or generation.

The extended Oxley's model has been formulated as follows:

$$\text{Min } f(\vec{y}),\ \vec{y} \in S, g_i(\vec{y}) \leq 0, i = 1, \ldots\ldots, m, L_j \leq y_j \leq U_j, j = 1, \ldots\ldots, n \quad (4.20)$$

where $f(\vec{y})$ is the function to be optimized, $\vec{y}$ is the vector of solutions, $g_i(\vec{y})$ is the constraint function. $L_j$and $U_j$are the lower and upper limits of solution space.

The two elements, $y_{p\ best}$ and $y_{g\ best}$, besides the current position of the particle y_i, were used to calculate its new velocity $v_i(t+1)$based on its current velocity $v_i(t)$ using the following equation:

$$v_i(t+1) = v_i + P_1 rand(y_{p\ best} - y_i) + P_2 rand(y_{g\ best} - y_i) \quad (4.21)$$

where P_1 and P_2 are acceleration constants to control the influence of the intellectual and social information concerning random real numbers between 0 and 1 generated with a uniform distribution.

After each particle updated its analogous velocity, the following equation is used to update its position:

$$y_i(t+1) = y_i(t) + v_i(t+1) \quad (4.22)$$

where, $y_i(t)$is the current position of the particle and $y_i(t+1)$ is its new position.

In order to start the optimization process, an initial population is created. To each particle of the initial population, a random boundary constraint value is chosen as (a_i, b_i) of the i^{th} variable is assigned using the following equation:

$$y_i(t=0) = a_i + rand_i(b_i - a_i) \quad (4.23)$$

where, $rand_i$ denotes a uniformly distributed number between 0 and 1, generating a new value for each parameter. Each particle uses Oxley's model to predict cutting forces for the new random position of the JC model constants in the define solution

space and measures error between experiments cutting forces using the following equation:

$$E_r = \sqrt{\frac{F_{C\,pre} - F_{C\,exp}}{{F_{C\,exp}}^2 + \left(\frac{F_{t\,pre} - F_{t\,exp}}{F_{t\,exp}}\right)^2}} \tag{4.24}$$

From the least error value of F_C predicted from Oxley's model using PSO JC model constants are derived as M4.

The flow chart in Figure 4.6 explains the procedure to evaluate the desired output parameters. Table 4.2 shows the various predicted optimum output from M4 approach for three grades of WHA based on PSO optimization technique for machining test data.

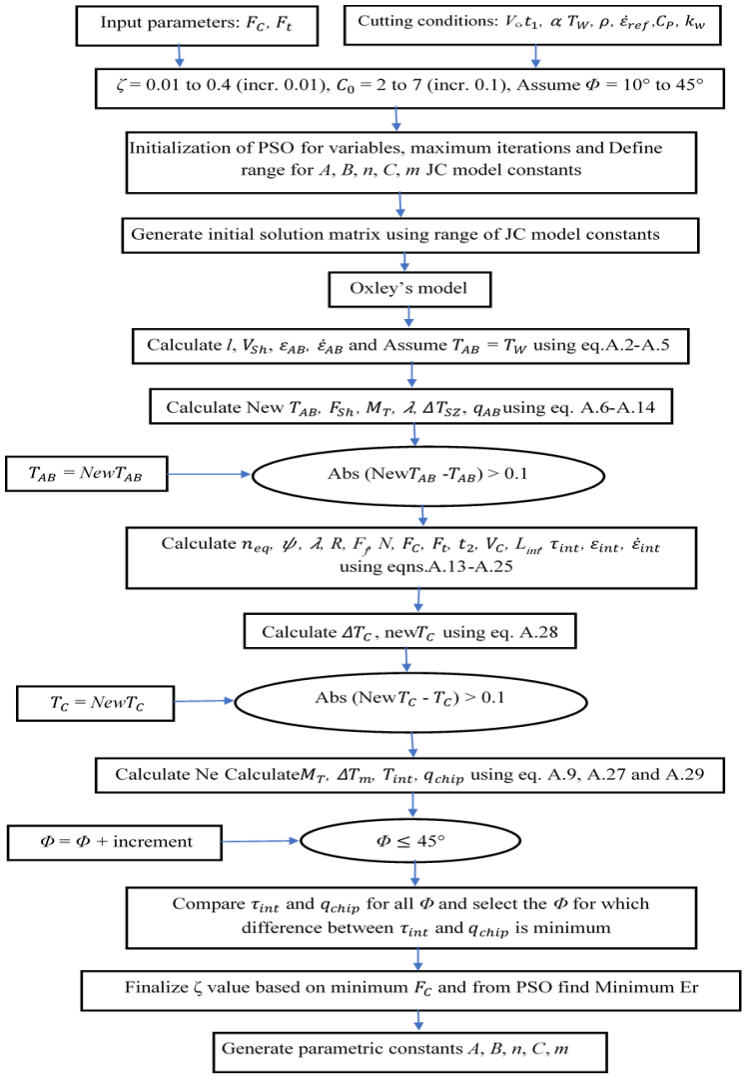

Figure 4.6 Flow chart for predicting JC model constants using analytical approach

Table 4.2 Predicted outputs from M4 approach for three grades of WHA

90 WHA																
Test No.	ζ	C_0	ϕ	t_2	ε_{AB}	$\dot{\varepsilon}_{AB}$	ε_{int}	$\dot{\varepsilon}_{int}$	T_{AB}	T_{int}	q_{AB}	n_{eq}	ψ	L_{int}	F_C	F_t
1	0.12	7	20.2	0.27	0.87	17118	4.52	7408	278.76	571.06	704.33	0.0844	51	0.31	42.18	28.03
2	0.14	7	19.4	0.28	0.91	11709	4.23	4159	269.05	527.01	712.15	0.0847	52	0.33	44.23	30.77
3	0.2	7	18.2	0.30	0.96	6564	3.65	1525	252.65	457.13	725.96	0.0851	53	0.36	47.72	33.48
4	0.23	7	17.8	0.15	0.98	21375	3.48	4218	248.47	437.39	739.65	0.0852	54	0.19	24.78	17.82
5	0.1	7	20.4	0.40	0.87	8238	5.04	4323	278.86	589.16	698.63	0.0844	51	0.46	62.21	37.87
95 WHA																
Test No.	ζ	C_0	ϕ	t_2	ε_{AB}	$\dot{\varepsilon}_{AB}$	ε_{int}	$\dot{\varepsilon}_{int}$	T_{AB}	T_{int}	q_{AB}	n_{eq}	ψ	L_{int}	F_C	F_t
1	0.12	7	20.0	0.27	0.88	16936	4.58	7251	308.02	651.10	775.34	0.0762	53	0.32	47.53	31.16
2	0.16	7	19.0	0.29	0.92	11452	4.00	3481	297.68	587.37	780.53	0.0764	53	0.35	50.08	34.95
3	0.18	7	17.8	0.31	0.98	6412	3.93	1616	277.58	522.93	790.37	0.0768	54	0.38	56.67	40.28
4	0.22	7	17.4	0.16	1.00	20869	3.62	4203	272.44	494.22	803.80	0.0769	54	0.19	27.83	21.38
5	0.1	7	20.2	0.41	0.87	8151	5.11	4233	308.16	672.59	769.13	0.0761	53	0.48	70.10	45.37
97 WHA																
Test No.	ζ	C_0	ϕ	t_2	ε_{AB}	$\dot{\varepsilon}_{AB}$	ε_{int}	$\dot{\varepsilon}_{int}$	T_{AB}	T_{int}	q_{AB}	n_{eq}	ψ	L_{int}	F_C	F_t
1	0.09	6	20.6	0.25	0.90	15698	5.53	11378	405.66	848.69	958.15	0.0548	56	0.29	56.19	39.86
2	0.14	6	19.6	0.27	0.94	10603	4.31	4672	389.32	798.61	963.02	0.0549	57	0.31	57.07	42.72
3	0.22	6	18.4	0.29	0.99	5931	3.55	1550	358.67	671.06	970.88	0.0551	57	0.34	61.06	49.39
4	0.29	6	18	0.15	1.01	19297	3.22	3735	347.40	617.32	976.32	0.0551	58	0.17	39.34	33.99
5	0.09	6	20.8	0.38	0.89	7557	5.51	5537	408.35	899.57	955.76	0.0548	56	0.44	63.22	43.32

4.3 Determination of JC damage model constants

The JC damage model is effective to define the failure state for high strain rate conditions, such as impact compression/tension (Chakraborty , Shaw and Banerjee 2015, Campagne-Lambert, et al. 2008) and machining (Martin Bäker 2013, Sagar, Kumar, et al. 2019), by taking into account the eff ects of the stress state, strain rate and temperature on the initiation of fracture strain (IFS). Normally, the damage parameters are calculated according to the failure strain measured from the flow curves at various loading conditions, such as high strain rate tests. The present section discusses the approach adopted to determine the JC damage constants of WHAs for high strain rate compression deformation. The failure initiation parameters of JC damage model are obtained by optimization using a combined experimental–numerical approach, as presented in one of the recent works (G. Chen, C. Ren and L. Lu, et al. 2018). The experimental data i.e., high strain rate testing data required for

the calculations are taken from the available literature (Woodward, et al. 1985, J. Das, G. Rao, et al. 2011).

4.3.1 Overall approach

In this work, to determine the JC damage constants for high strain rate deformation, stress-strain data from high strain rate tests from the available literature (Woodward, et al. 1985) for the given grades of WHAs are considered. In the given literature, a series of high strain rate tests were performed for a strain rate in the range of 11 to 775 s^{-1} and temperature in the range of 25 to 500 °C for all the three grades of WHA. An FE model for high strain rate test is developed without a damage model under similar experimental conditions. The predicted stress strain from the developed model is then validated with that of the experimental ones under various strain rates. The damage parameters are further optimized according to the measured IFS and the simulated stress triaxiality, equivalent strains, stresses and temperatures. In the present work, it is assumed that the fracture in the compression test samples occur at the point where the stress drops off. Therefore, the flow stresses at the conditions with cracks are used to calculate the IFS.

Generally, the damage behavior in high strain rate compression samples occurs in three stages. In the first stage, the strain hardening dominates in the stable plastic region of the flow stress curve. In the second stage, a drop in flow stress due to damage initiation occurs and leads to the start of instability. In the third stage, damage evolution occurs wherein the flow stress decreases gradually and leads to crack propagation. The IFS is identified from experimental stress strain curves by drawing a tangent line to the stable plastic region and damage evolution region of flow stress curve. The intersection point of these tangent lines is considered as IFS. Five loading conditions are taken into considerations to determine the IFS and the measured values are listed in Table 4.3. The derived IFS from the compression deformation process is taken as reference, and simulated results are fitted with specific equations in terms of equivalent plastic strain versus time. The fitted coefficients from the derived expressions, as shown in Equation (5.1) to (5.4) corresponding to the five conditions are determined to calculate IFS for the given grades of WHA. Using the measured IFS at five conditions for each grade and the predicted stress, strain and temperature

from the high strain rate simulations, the parameters D_1 to D_5 are determined by optimization using GA. Figure 4.7 illustrates the overall methodology adopted schematically to determine the JC damage constants.

Table 4.3 Identification of IFS for high strain rate tests on three grades of WHA

WHA grade	Test condition	Strain rate (s^{-1})	Temperature (°C)	Initiation of failure strain (IFS)
90 WHA	1	11.5	20	0.32
	2	370	20	0.26
	3	685	20	0.23
	4	11.5	400	0.41
	5	11.5	500	0.43
95 WHA	1	27	20	0.31
	2	350	20	0.25
	3	775	20	0.22
	4	27	400	0.40
	5	27	500	0.42
97 WHA	1	12.4	20	0.28
	2	340	20	0.24
	3	600	20	0.19
	4	12.4	400	0.36
	5	12.4	500	0.38

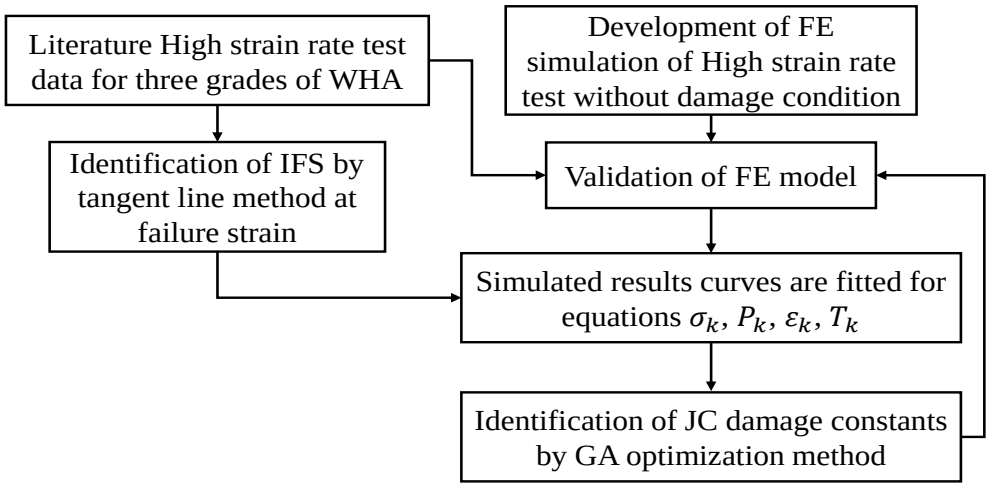

Figure 4.7 Overall methodology to derive JC damage model constants

4.3.2 FE simulations for high strain rate tests

A series of high strain rate simulations with plastic but without damage model has been considered, as followed in the literature (Chen, Ke, et al. 2016). This is based

on following assumptions. Firstly, the stress, strain field, and stress state are assumed to be unaffected by damage in the uncoupled approach (Borvik, Hopperstad and Berstad 2003). Secondly, it is presumed that the influence of plastic deformation on damage is negligible (Khan and Liu 2012). Figure 4.8 shows a 3D FE geometric model with meshing and boundary conditions using FE software ABAQUS/Explicit (version 6.14). It is noted that in the 3D high strain rate deformation model, the specimen is supported by the transmission bar and incident bar. The strain rate is applied in terms of velocity (m/sec) in the X-axis at the free end of the transmission bar. The specimen is supported by the incident bar which absorbs and resists the transmission velocity through the specimen. The free end of the incident bar is constrained in all directions. Since the yield strength of both transmission and incident bar is higher than the specimen, deformation will occur in the specimen. The lengths of the incident and transmission bars are the same as used in experiments. All the geometric parts, i.e., transmission, incident bar, and specimen, are modeled as deformable bodies and discretized with eight-noded thermally coupled brick, trilinear displacement, and temperature (C3D8RT) with reduced integration and hourglass control element type. The total number of elements on the specimen is 258240 and 69084 on transmission and incident bar. Mesh distortion is controlled by ALE mesh control, and interaction is defined using the general contact method. In the simulation, the temperature is set at ambient conditions on bars. While the temperature on the specimen is set as per experimental conditions. The physical properties of the WHA specimens and tungsten carbide bars as are listed in Table 4.1.

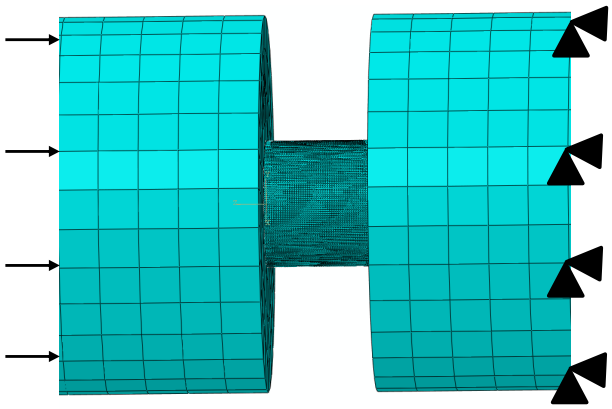

Figure 4.8 High strain rate 3D geometric model with meshing and boundary condition

The JC material model constants as well as damage model constants, so obtained, are presented in the following chapter. The derived constants are used to develop the FE simulation model to simulate the chip formation during machining of WHAs. The predicted outputs are then compared with the experimental ones under similar conditions for validation of the developed model.

Summary

This chapter deals with the methodology adapted for numerical simulation of FE based 2D orthogonal cutting model. Three different grades of workpiece material are selected, namely 90, 95 and 97 WHA grade to carry out machining simulations. Further this chapter presents a methodology to determine the JC constants of WHAs under high strain rate conditions using machining tests in conjunction with Oxley's predictive model and PSO algorithm. Currently, availability of the high strain rate data for stated grades of WHA is limited and consequently, JC constants for the same are not readily available. The overall methodology includes the determination of four sets of JC constants, namely, M1, M2 and M3 from the high strain rate test data available in literature by using conventional optimization technique, GA and ABC algorithm, respectively. Whereas M4 is determined from machining tests using the inverse identification method. Besides, damage model constants are also determined for the given grades of WHAs by GA optimization using a combined experimental–numerical approach. The results obtained from the developed model are discussed in the next chapter.

Chapter5 FINITE ELEMENT SIMULATIONS AND VALIDATION

Validation is the final and mandatory stage of any model development. No digital simulation can ever completely replace the experimental tests. However, simulations can greatly reduce the number of experiments that are required in certain cases such as optimization of cutting parameters, thus saving enormous amount of workpiece material. This chapter presents the computed values of JC material and damage model constants that are used as FE inputs in the developed FE model. The adequacy of the developed model is investigated by simulating the model for varied cutting parameters and comparing the obtained results such as cutting force, thrust force, chip morphology and temperature with that of the experimental ones.

5.1 Computed values of JC model constants

Table 5.1 lists the JC model constants determined using M1, M2, M3 and M4 for all the three grades of WHA. It is noted that the value of A and n, i.e., initial yield strength and strain hardening exponent predicted by M4 is comparatively lower in case of all three grades of WHA. This could be because of the determination of M4 constants at temperatures encountered during machining in contrast to M1, M2 and M3 wherein constants are calculated taking the high strain rate stress-strain data at room temperature (Woodward, et al. 1985). Lower values are expected for M4 because as the temperature increases, yield strength and strain hardening effect reduce. A similar trend has been reported in the literature (Jaspers and Dautzenberg 2002). The value of *m* is determined by following a trial and error approach using FE machining simulations similar to the one reported in the literature (Ning and Liang 2018). It is to be noted that temperature rise during turning tests varied in the range of 100 to 200^{o} C. But, thermal softening effect in WHAs is observed when the temperature exceeds 500^{o}C (Das, Sarkar, et al. 2012). This implies that the effect of *m* has the least effect on machining simulation outputs.

Table 5.1 Values of JC model constants derived using M1, M2, M3 and M4 approach for three grades of WHA.

WHA Grade	Models	*A* (MPa)	*B* (MPa)	*C*	*n*	*m*
90 WHA	**M1**	1100	1221	0.03	0.87	1.913
	M2	1100	758.62	0.06	0.203	0.921
	M3	1100	766.66	0.019	0.294	1.323
	M4	1030	1040	0.01	0.17	0.449
95 WHA	**M1**	1300	1281.8	0.02	0.85	1.980
	M2	1300	1084.3	0.02	0.59	1.830
	M3	1300	1166.7	0.06	0.42	1.940
	M4	800	842	0.01	0.15	0.91
97 WHA	**M1**	1066	1217	0.043	0.48	1.903
	M2	1066	879.76	0.078	0.29	1.950
	M3	1066	1140	0.022	0.59	1.812
	M4	821	1020	0.01	0.14	1.265

Figure 5.1 shows the comparison of predicted flow stress behavior using M1, M2, M3 and M4 with measured ones with different strain rates at room temperature for three grades of WHA. It is observed that M4 followed by M3, showed better results as compared to M1 and M2 for all grades of WHA. The possible reason for M4 to outperform others could be because of the fact that the JC model constants are calculated for the strain rates that are encountered during the machining operation. Whereas for the remaining models, material constants are determined from the stress-strain data using high strain rate test (Woodward, et al. 1985). However, fine-tuning of the material constants using ABC algorithm (Sagar, et al. 2018) showed considerable improvement over M2 and M1.

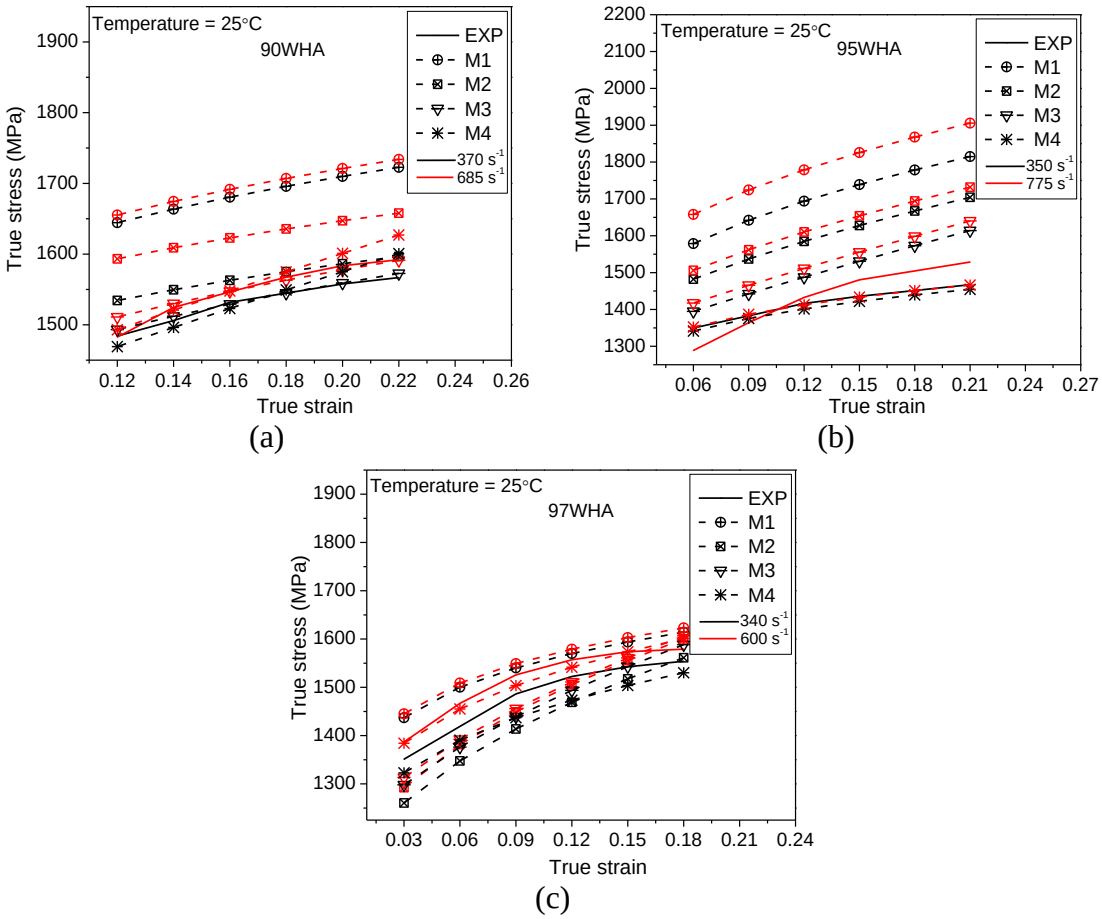

Figure 5.1 Comparison of predicted flow stress behavior using M1, M2, M3 and M4 with experimental varied strain rates (a) 90WHA, (b) 95WHA, (c) 97WHA.

5.2 Computed values of JC damage constants

To determine the damage parameters D_1 to D_5 the triaxial stress σ^*, loading strain rate $\dot{\varepsilon}$, temperature T and fracture strain ε_f needs to be identified. In present work σ^*, $\dot{\varepsilon}$, T is calculated by high strain rate simulation without damage model, and the measured IFS is used to determine the damage parameters as stated by (G. Chen, C. Ren and L. Lu, et al. 2018).

Figure 5.2 shows the experimental and simulated flow stresses for deformed specimen at five different conditions for 90 WHA. The IFS is measured from the experimental flow stress curve drawing tangent lines at stable plastic region and in damage evolution region. The intersection point of these two tangent lines is IFS. Similar procedure is followed for 95 and 97 WHA.

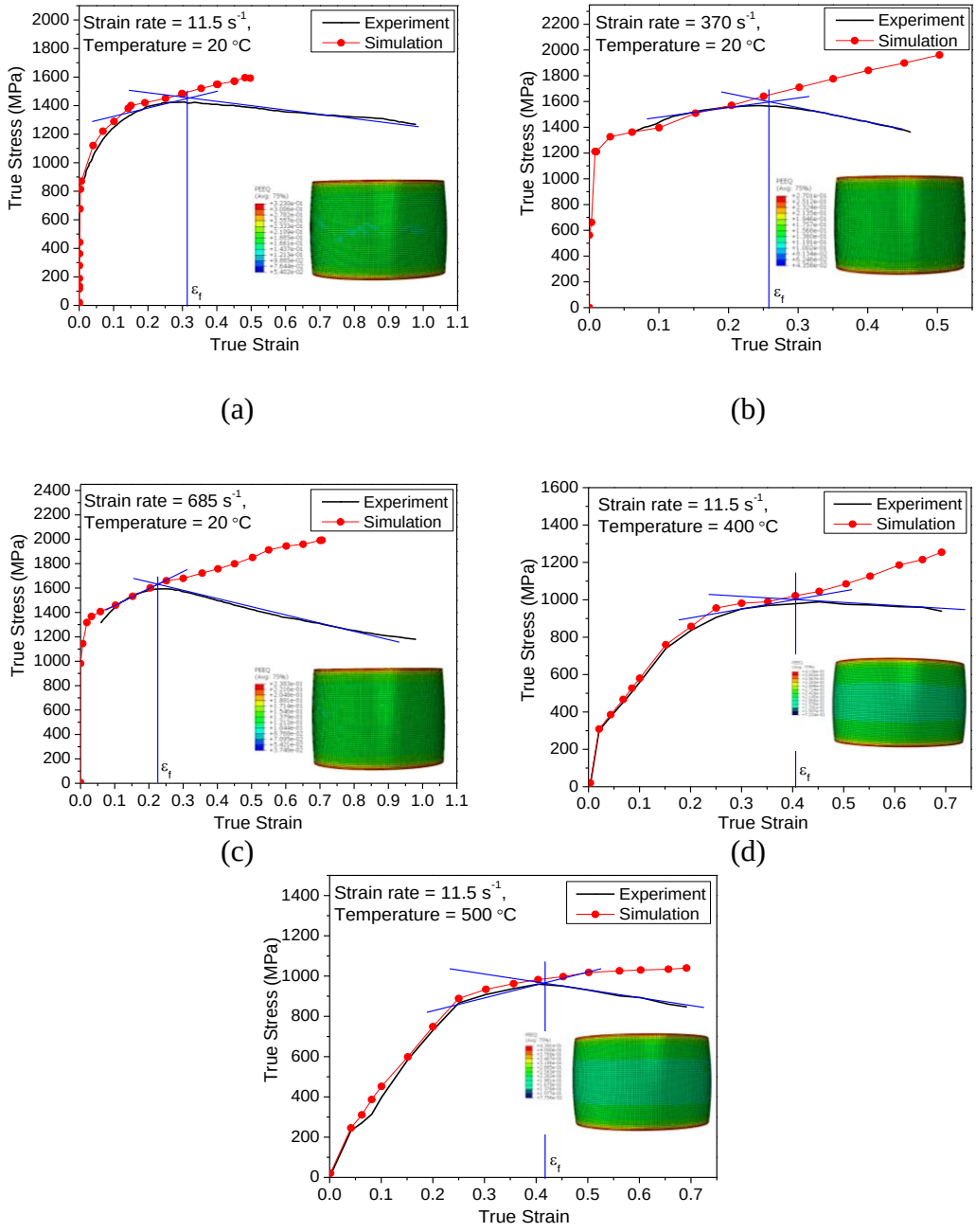

Figure 5.2 Determination of IFS and comparison of experimental with simulated flow stress without JC damage constants at (a) Sim.1: 11.5 s^{-1}, 20°C; (b) Sim.2: 370 s^{-1}, 20°C; (c) Sim.3: 685 s^{-1}, 20°C; (d) Sim.4: 11.5 s^{-1}, 400°C; (e) Sim.5: 11.5 s^{-1}, 500°C.

The Equations (5.1) to (5.4) are used to fit the measured IFS, as given below:

$$\sigma_k = R_1 \ln(\varepsilon_k) + S_1 \tag{5.1}$$

$$P_k = R_2 \ln(\varepsilon_k) + S_2 \tag{5.2}$$

$$\varepsilon_k = R_3 t + S_3 \tag{5.3}$$

$$T_k = R_4 \varepsilon_k + S_4 \tag{5.4}$$

where *k* represents a specific loading condition. Then substituting these equations into Equation (4.6), the IFS at specific condition *k* can be calculated by Equation (5.5).

$$\varepsilon_{fk} = \left[D_1 + D_2 \exp\left(D_3 \frac{-P_k}{\sigma_k}\right)\right]\left[1 + D_3\, ln\left(\frac{\dot{\varepsilon}_k}{\dot{\varepsilon}_0}\right)\right]\left[1 - D_5\left(\frac{T_k - T_r}{T_m - T_r}\right)\right] \tag{5.5}$$

where $\varepsilon_{fk}$is the IFS at the specific condition *k*. In the present work, the strain rate of compression test $\dot{\varepsilon}_k$ is calculated by the slope of the fitted curve of equivalent plastic strain versus time. Further, to increase the prediction accuracy of triaxial stress, a ratio of simulated pressure to Von Mises stress is calculated.

Figure 5.3 show the simulated and fitted curves of von Mises stress, positive value of pressure, strain and temperature of one node in the cross-section of the specimen at the strain rate 370 s^{-1} and temperature 20 °C (Sim.2) for 90WHA. Similar procedure is followed to measure fitted coefficients for other two grades of WHA. The fitted coefficients corresponding to the conditions 1-5 which are used to calculate IFS are shown in Table 5.2.

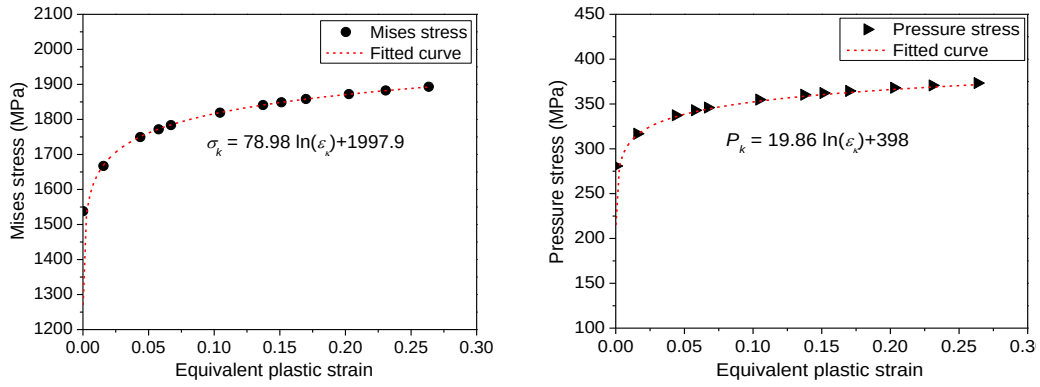

(a) (b)

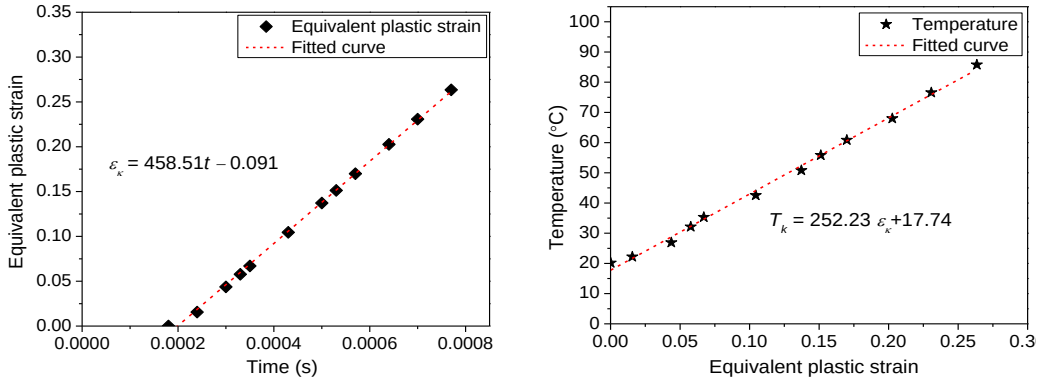

(c) (d)

Figure 5.3 Simulated and fitted curves of Von Mises stress, the positive value of pressure, equivalent plastic strain, and temperature at one node in the cross-section of the specimen at 370 s^{-1} and 20°C (Sim.2) for 90WHA.

Table 5.2 Fitted parameters for Equation (5.1) to (5.4) by high strain rate simulation without damage model for three grades of WHA.

WHA Grade	Test	R_1	S_1	R_2	S_2	R_3	S_3	R_4	S_4
90	Sim.1	94.36	2468.5	22.13	425	701.10	-0.124	386.94	17.12
	Sim.2	78.98	1997.9	19.86	398	458.51	-0.091	252.23	17.74
	Sim.3	61.23	1994.7	14.52	324	780.06	-0.083	187.79	13.57
	Sim.4	88.36	2212.8	21.86	405	685.42	-0.148	371.35	16.87
	Sim.5	82.67	2108.6	20.74	384	672.13	-0.152	351.28	16.42
95	Sim.1	92.42	1990.2	11.32	514	356.45	-0.093	382.53	20.62
	Sim.2	96.52	1998.3	8.96	501	373.66	-0.105	364.42	18.49
	Sim.3	89.73	1893.6	14.52	526	384.72	-0.132	403.68	22.41
	Sim.4	74.62	1991.8	13.56	506	413.74	-0.231	410.73	15.82
	Sim.5	72.83	1987.2	14.61	498	426.51	-0.226	413.62	16.24
97	Sim.1	63.42	1997.5	39.47	346	512.47	-0.116	378.46	24.51
	Sim.2	59.62	1992.4	37.25	326	448.66	-0.085	245.01	19.28
	Sim.3	68.53	1995.7	22.58	312	696.96	-0.066	242.71	19.55
	Sim.4	60.83	1982.6	32.62	335	558.62	-0.142	354.53	22.82
	Sim.5	58.41	1973.1	41.84	328	523.48	-0.167	314.78	21.72

Table 5.3 shows the computed values of JC damage model constants from the FE high strain simulation model by the GA optimization method for 90, 95, and 97WHA.

Finally, the constants D_1 to D_5 are identified by the GA optimization method using both the predicted stress, strain, and temperature from simulations and the measured IFS. The objective function of GA optimization is set as the minimum value of the accumulated square error function $\Delta(x)$, aiming to minimize the total relative errors between the calculated and measured IFS.

$$f(D_1, D_2, D_3, D_4, D_5) = min\{\Delta(x)\} \tag{5.6}$$

The optimized damage constants for all the three grades are presented in Table 5.3. Further the high strain rate simulation with optimized damage constants is validated with experimental flow stresses at two different conditions for 90 WHA as shown in Figure 5.4. The results predicted by the high strain rate simulation with damage constants closely matched with the experimental flow stress curves. From this it can be confirmed that the derived damage constants could predict damage initiation and damage evolution successfully under similar experimental conditions.

Table 5.3 JC damage model constants for three grades of WHA

Grade	D_1	D_2	D_3	D_4	D_5
90WHA	-0.953	-2.443	-4.785	0.019	0.623
95WHA	-1.225	-2.134	-3.679	0.023	0.768
97WHA	-1.312	-1.897	-2.893	0.036	0.853

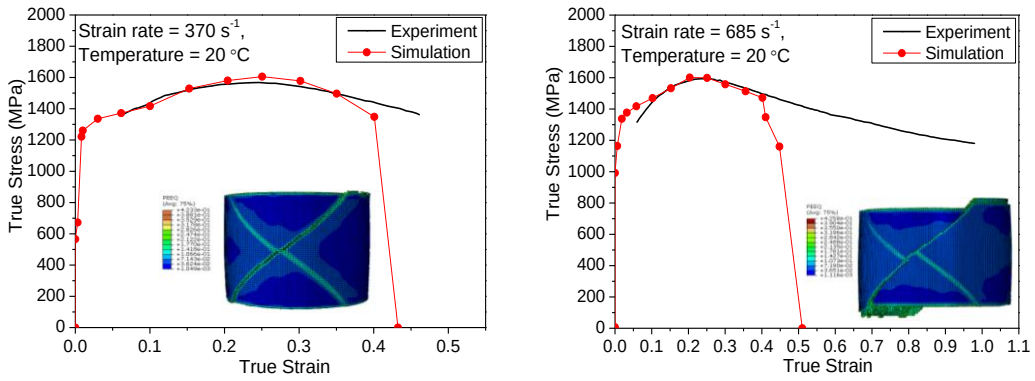

(a) (b)

Figure 5.4 Comparison of experimental with simulated flow stress using JC damage constants at (a) Sim.2: 370 s^{-1}, 20°C; (b) Sim.3: 685 s^{-1}, 20°C

The appropriate FE inputs along with damage constants are used to develop the FE model and the adequacy of the same is investigated by simulating the model under varied cutting conditions and comparing the obtained results such as cutting forces, chip morphology, etc. with that of the experimental ones. Various parametric studies such as the effect of mesh size, JC material model constants and cutting parameters are performed while simulating the chip formation process for 90, 95 and 97 WHA.

5.3 Mesh refinement study

The selection of proper mesh size plays a critical role in defining the accuracy and computational time of the FE simulation model. It is even well known that finer mesh leads to greater accuracy but at the cost of higher computational time. So, the best way of meshing a model is to get results closer to the experimental ones on the one hand and consumes relatively less computational time, on the other hand. Even it should be noted that refining mesh beyond a limit leads to increase in CPU time and no significant changes in numerical results can be observed. Thus, a mesh sensitivity analysis is performed to identify optimum meshing condition that yields consistent and accurate results with relatively lesser computational time.

In the present work three different varied meshing conditions have been considered in chip region by varying mesh size of 29 × 29 μm, 19 × 19 μm, 15 × 15 μm and 11 × 11 μm in the chip thickness direction as shown in Figure 5.5.

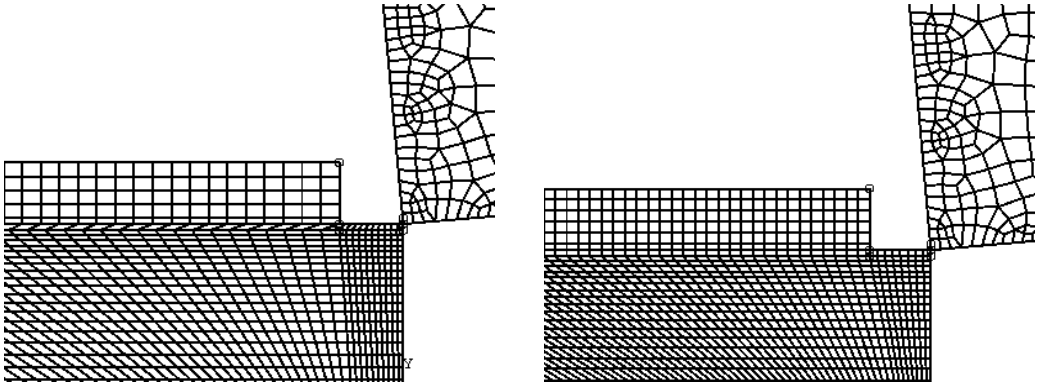

(a) (b)

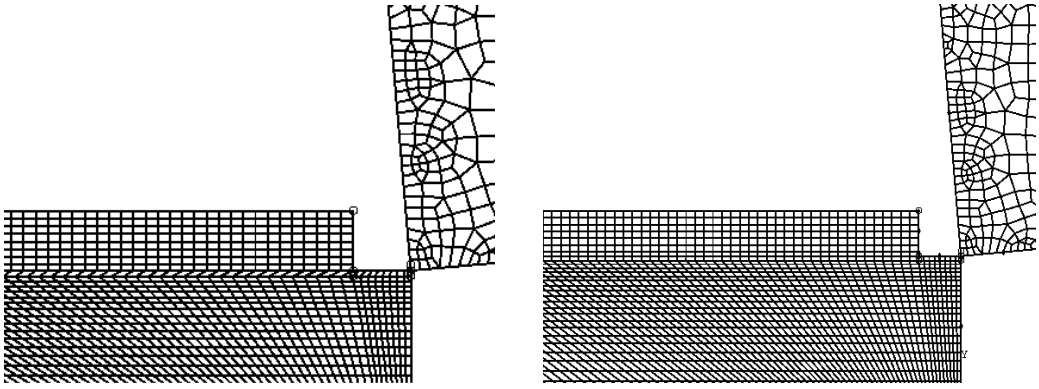

(c) (d)

Figure 5.5 Mesh configuration for (a) 29 × 29 μm, (b) 19 × 19 μm, (c) 15 × 15 μm and (d) 11 × 11 μm

Table 5.4 summarizes the effect of mesh size on FE outputs and CPU time. Not much variation in average values of stress, strain and temperature in the shear zone is observed for mesh size beyond 19 × 19 μm. This implies that further mesh refinement may not be required as far consistency of the result is concerned. Moreover, there is a limitation to the reduction of element size from the software point of view. Since the time step in ABAQUS/Explicit is controlled by the smallest element size, reduction of element size beyond a certain point leads to termination of the analysis in the first time step itself. Hence, mesh size 15 × 15 μm is considered as a fair choice for the subsequent simulations.

Table 5.4 Mesh sensitivity analysis for a simulation time of 1 ms

Mesh size	Stress (GPa)	Strain	Temperature (°C)	CPU time (hr:min:s) for 1ms
29 × 29 μm	1.58	0.68	486	30:96
19 × 19 μm	1.29	0.56	284	0:58:32
15 × 15 μm	**1.27**	**0.54**	**280**	**1:19:48**
11 × 11 μm	1.27	0.54	280	1:56:30

5.4 Experimental validations

FE simulations taking M1, M2, M3 and M4 as input are run under similar cutting conditions as that of the experimental ones and the predicted results were compared with the ones measured experimentally.

5.4.1 Chip morphology

Machining tests showed that the type of chip obtained during machining of all three grades of WHA are purely discontinuous chips. Figure 5.6 (a), (b) and (c) shows the chip morphology and equivalent plastic strain distribution for a specific cutting parameter combination ((V_c = 50 m/min, f = 0.1 mm, d = 0.15 mm and α = -5^0) using M1, M2, M3 and M4 for 90, 95 and 97 WHA, respectively. It is evident from the experimentally obtained chips that chips tend to be more fragmented with the increase in the tungsten content. All the four models could replicate such phenomena satisfactorily. Although, the chips predicted using M1, M2 and M3 are discontinuous in nature, but the fragments appear scattered and triangular shaped. It is clearly observed that M4 could simulate discontinuous chips fairly well as compared to that of other two models when compared with experimental chip morphology. It can be inferred that as the JC constants vary, not just the maximum value of equivalent plastic strain but the distribution pattern of equivalent plastic strain near the shear plane also change; consequently, affecting the chip morphology. This clearly showed the interdependence of FE simulations on JC constants.

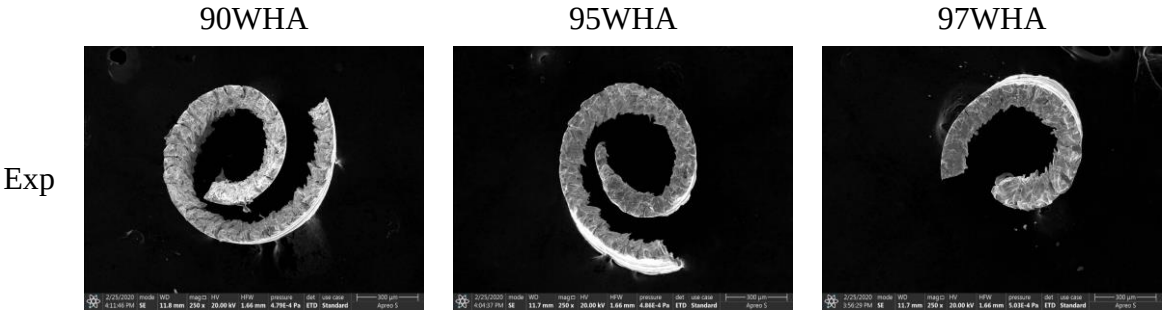

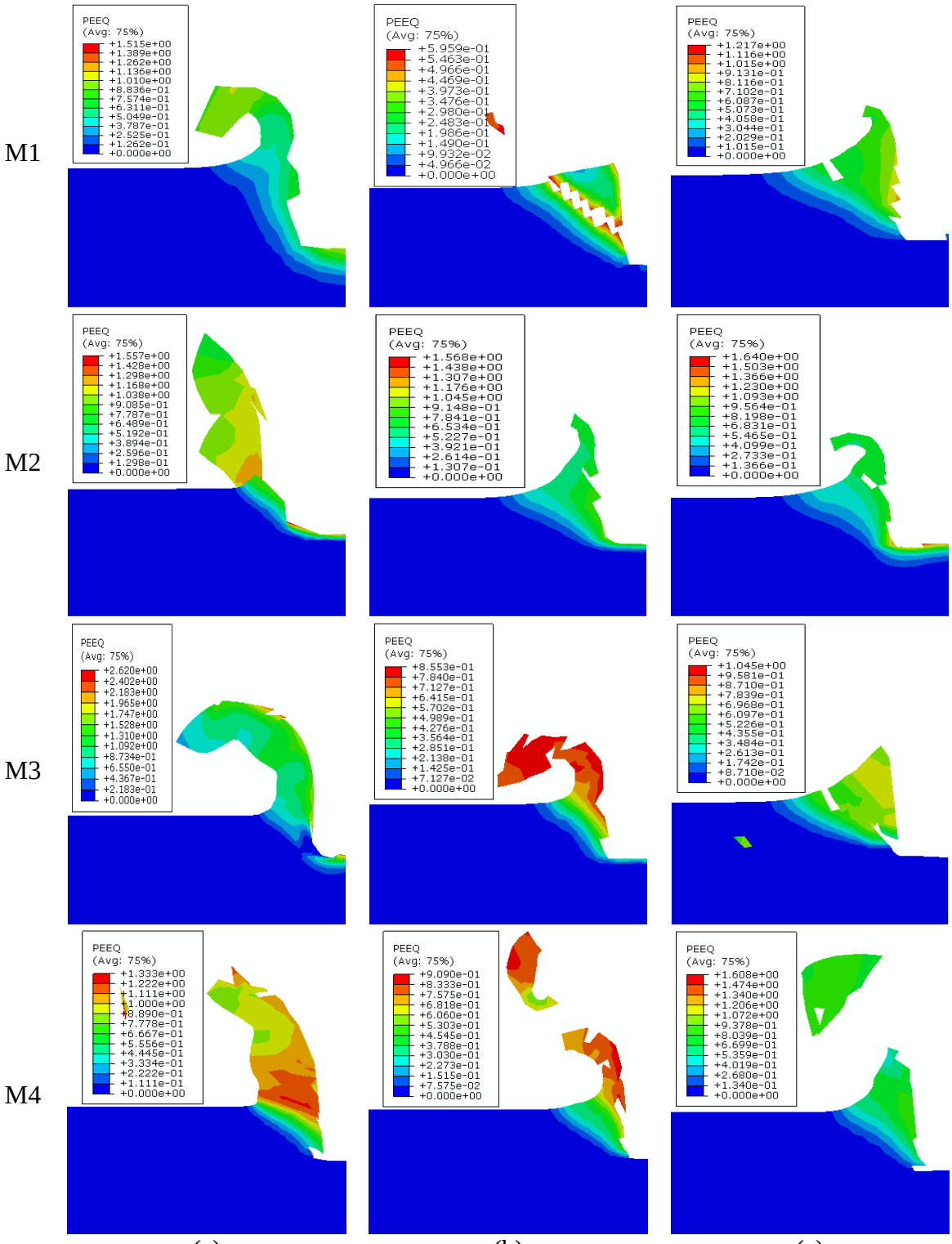

Figure 5.6 Comparison of predicted chip morphology and equivalent plastic shear strain distribution using M1, M2, M3 and M4 for (a) 90 WHA (b) 95 WHA and (c) 97 WHA

Furthermore, Figure 5.7 (a) and (b) show chips obtained experimentally as well as predicted using M4 for -5° and 2° rake angles, respectively while machining 97

WHA. As expected, chip curling is more prominent for a positive rake angle as compared to that of negative one. A similar trend is observed for the predicted chips as the rake angle changed from negative to positive. It can be stated that M4 could simulate chip formation satisfactorily for both positive and negative rake angle.

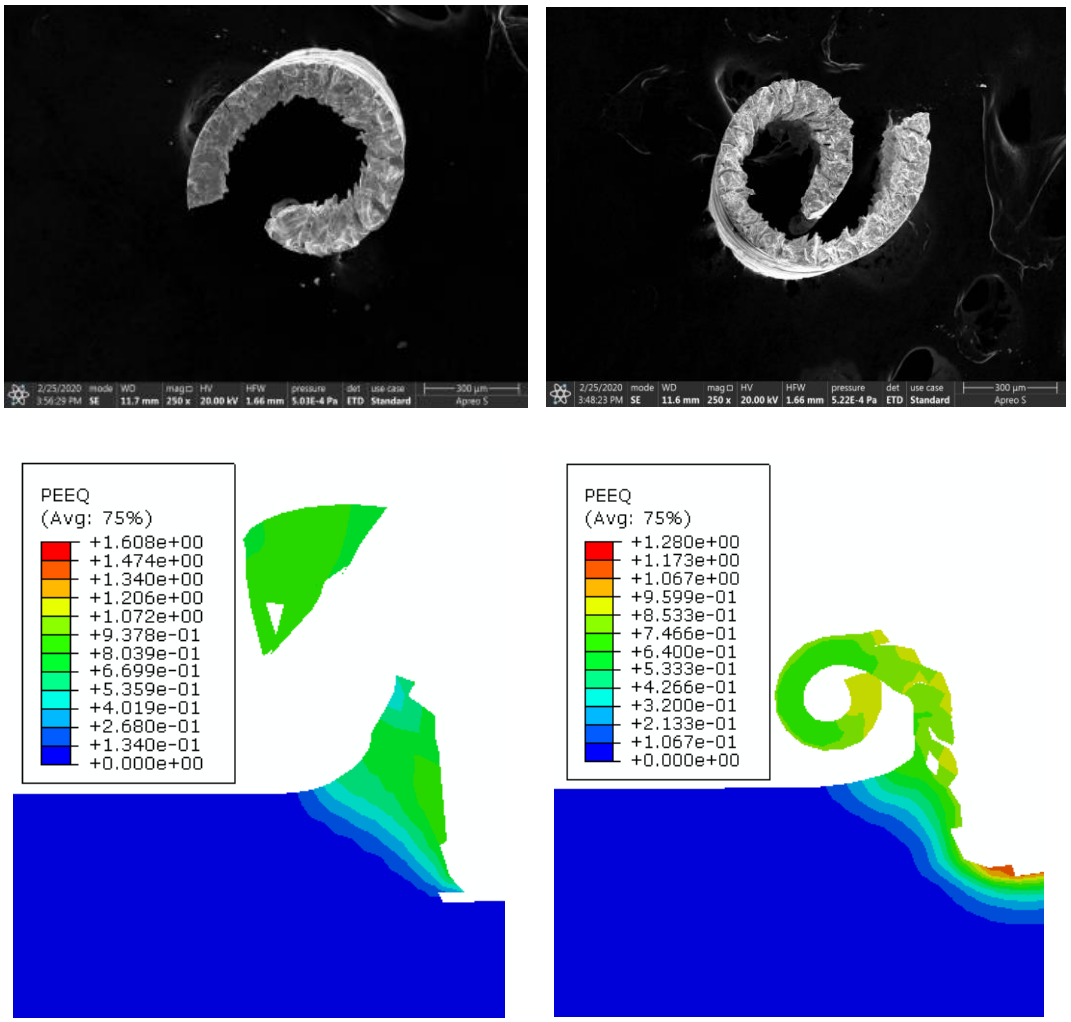

(a) (b)

Figure 5.7 Experimental and predicted chip morphology while machining 97WHA using (a) -5° and (b) 2° rake angles

5.4.2 Cutting forces

To give a clear picture of how the force varies concerning JC constants, a force signature (both measured and predicted) while machining 97WHA under specific cutting conditions has been presented in Figure 5.8

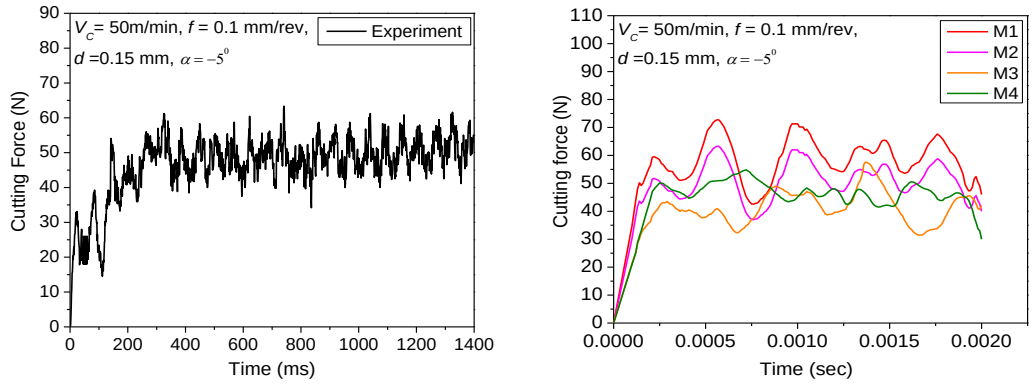

(a) (b)

Figure 5.8 Comparison of cutting force signature (a) Experimental, (b) change in the JC model constants from predicted FE machining simulations.

It can be observed that the force signatures of respective models correspond to the type of chips simulated. The force signature of M4 is found to be relatively smoother and closer to the experimental cutting force signature as compared to M1, M2 and M3. The lower values of cutting forces look reasonable and are expected because of the discontinuous chips being formed during the cutting operation.

Figure 5.9 and Figure 5.10 show the predicted values of cutting force and thrust force with respect to that of experimental ones as a function of cutting velocity and feed rate, respectively for two different rake angles and three WHA grades. Models M3 and M4 could replicate the trend observed for both cutting force and thrust force with respect to cutting velocity, feed, grade and rake angle. Whereas M1 showed incapability in showing the trend, especially concerning cutting velocity and feed rate. Moreover, M1 showed maximum deviation with error percentage exceeding 23% both for cutting force as well as thrust force. However, M2 and M3 showed a slight improvement over M1. It is in the case of M4 wherein predicted values of both cutting force and thrust force completely coincided with the experimental ones except for one specific combination of cutting parameters where the maximum deviation is close to 15%.

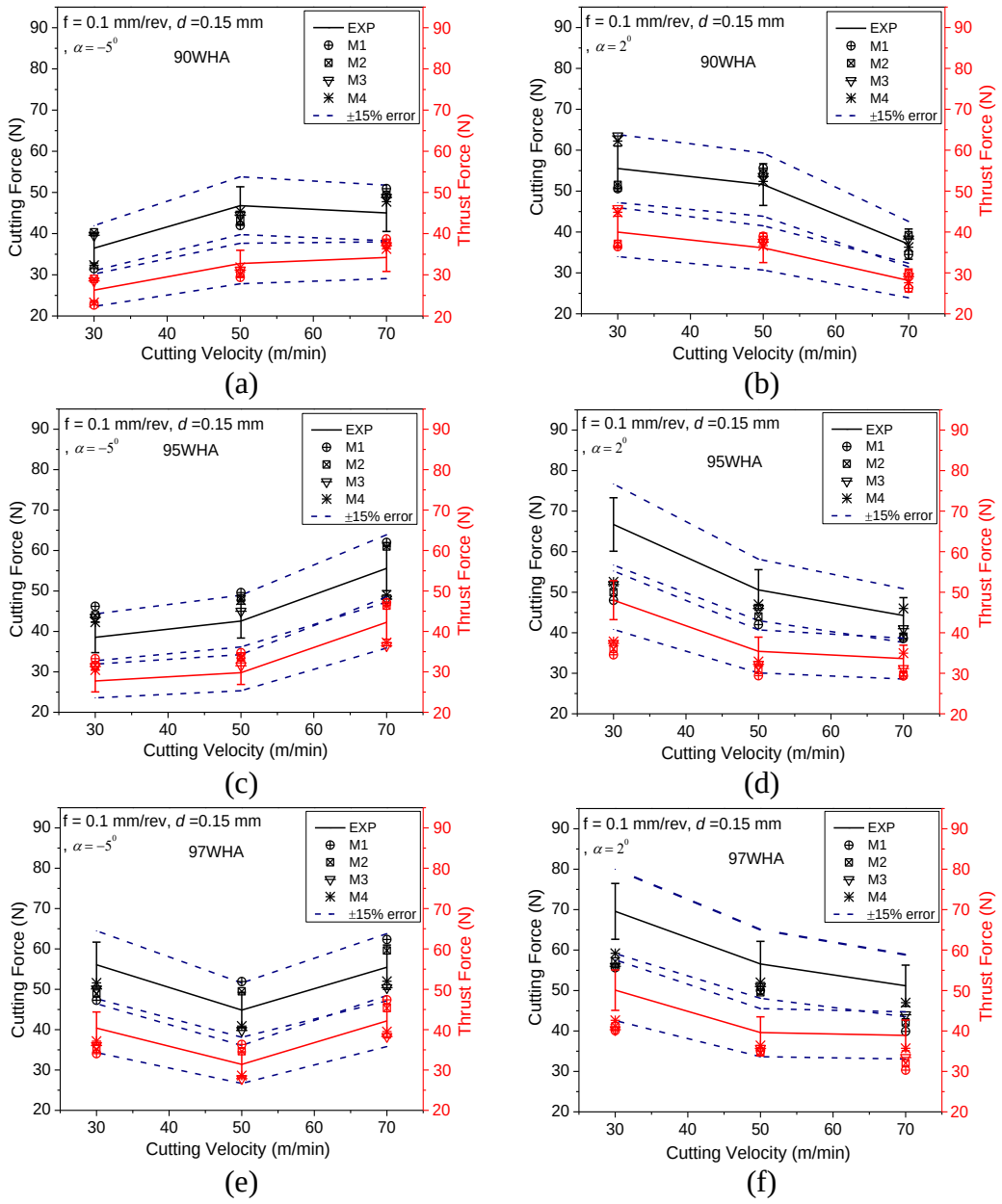

Figure 5.9 Comparison of experimental and predicted cutting force, thrust force as a function of cutting velocity and rake angle for (a) & (b) 90 WHA, (c) & (d) 95 WHA, (e) & (f) 97 WHA.

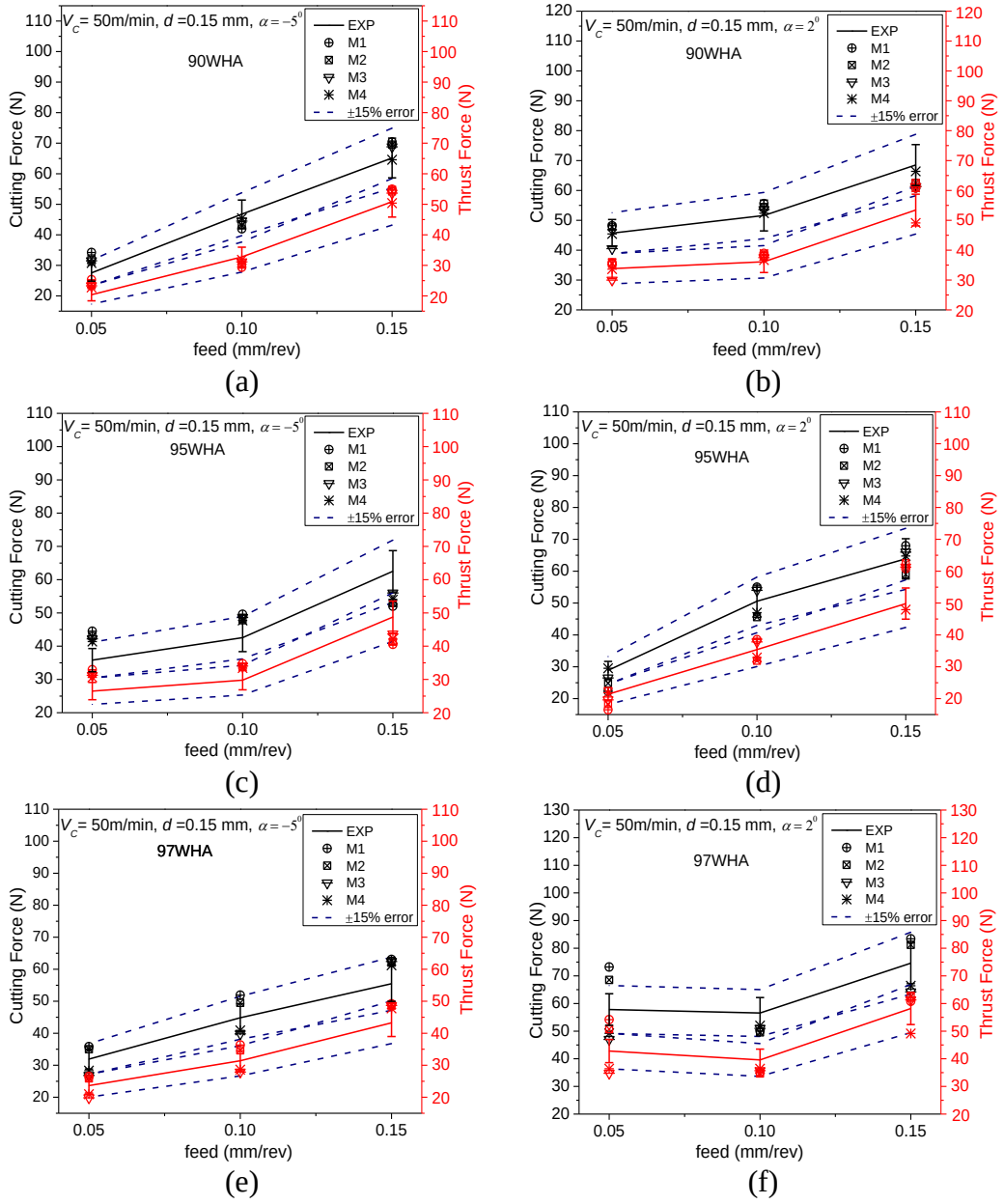

Figure 5.10 Comparison of experimental and predicted cutting force, thrust force as a function of feed and rake angle for (a) & (b) 90 WHA, (c) & (d) 95 WHA, (e) & (f) 97 WHA.

5.4.3 Temperatures

Besides cutting forces is measured, another significant parameter that affects the machining process is cutting temperature. The measurement of cutting temperature by the experimental techniques is challenging. In the past, many researchers have used different techniques to measure cutting temperature (Silva et al. 1999, Goyal et al. 2014). But in the present study, the temperature is measured using thermal imaging camera FLIR E60 with temperature measuring range of -20° to 650 °C. IR camera is

calibrated by placing WHA and tungsten carbide samples in a muffle furnace for different steady-state temperatures.

The emissivity is found to be 0.85, which lies well within the range documented in the literature (Sassi and Ghmari 2009). Figure 5.11 (a) shows the average temperature measured by IR camera for one particular combination of cutting parameters. While Figure 5.11 (b) and (c) show the temperature distribution predicted along the tool chip interface and primary shear zone for a specific cutting condition as a sample. The average temperature is then predicted by taking into consideration the temperature at shear zone and the chip tool interface.

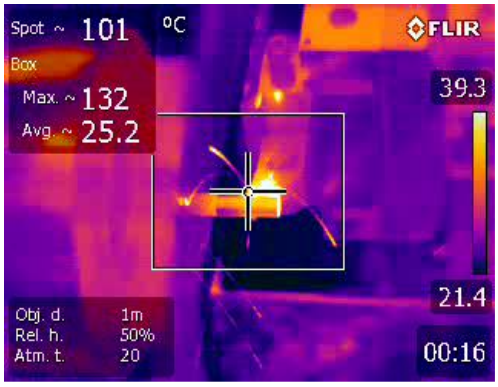

(a)

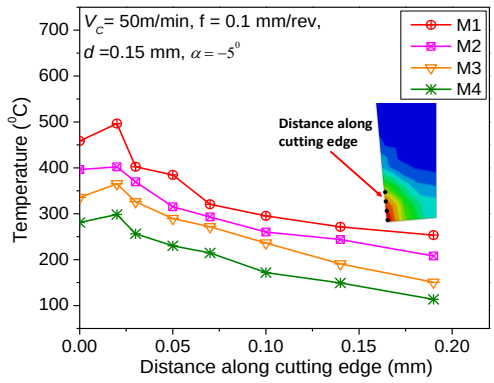

(b)

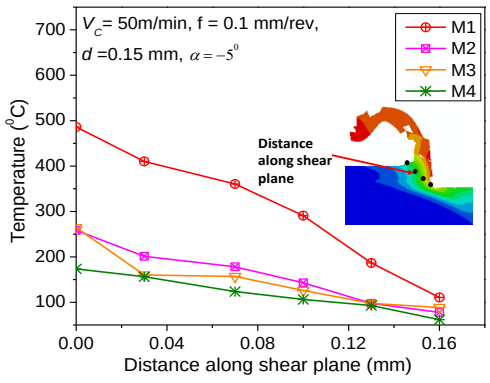

(c)

Figure 5.11 (a) Measured temperature using IR camera and temperature distribution predicted along (b) shear zone and (c) tool chip interface

Figure 5.12 shows the simulated temperature at chip tool interface for variation of JC model constants. It is observed that the M4 model had the least maximum temperature as compared to that of M1, M2 and M3.

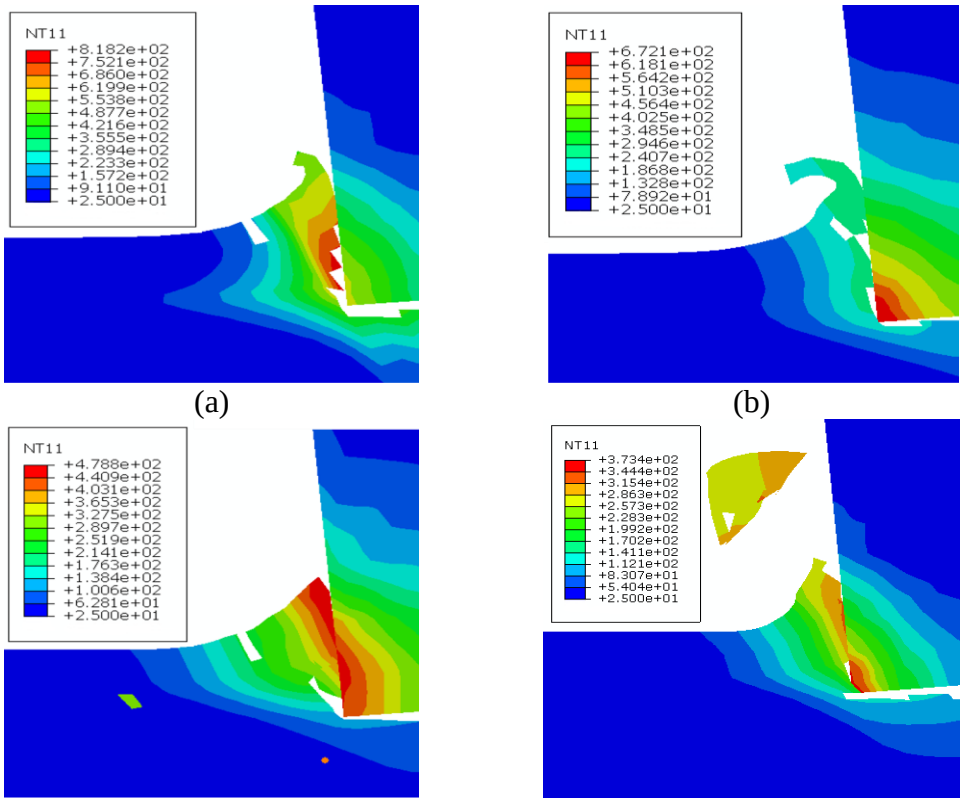

Figure 5.12 Comparison of simulated temperature distribution at chip tool interface for (a) M1, (b) M2, (c) M3 and (d) M4.

Figure 5.13 and Figure 5.14 show the variation of temperature with respect to cutting velocity and feed rate, respectively for different WHA grades and rake angles. Overall, it can be stated that the measured values of temperatures were lower than that of the predicted ones. This is much expected as the IR camera could only capture the average temperature of the chip, which was continuously in motion while machining.

Another reason could be because of the fact that orthogonal cutting conditions are considered in simulations for simplification. Orthogonal cutting conditions tend to give a higher value of temperatures as compared to that of oblique cutting. However, similar approach has been adopted for experimental validations in quite a few of number of literature (Ning, et al. 2019). Furthermore, the differences in the values predicted by three of the models are much evident from the graphs presented. The deviation in average temperature values is fairly large both for M1, M2 and M3. On the other hand, M4 is able to replicate the material behavior undergoing

deformation during the chip formation process perfectly with predicted cutting temperatures closely matching with that of the experimental ones.

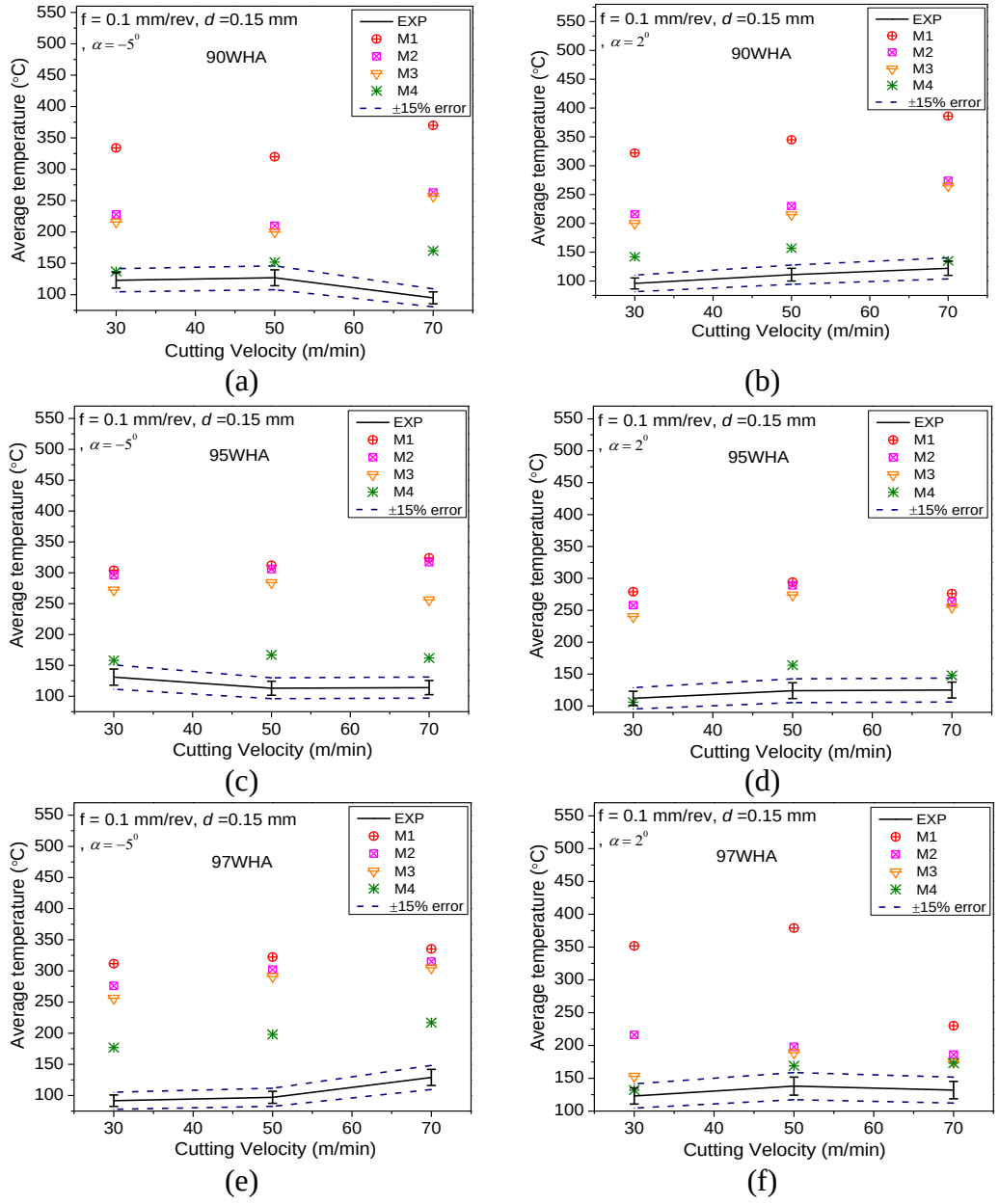

Figure 5.13 Comparison of experimental and predicted average temperature as a function of cutting velocity and rake angle for (a) & (b) 90 WHA, (c) & (d) 95 WHA, (e) & (f) 97 WHA.

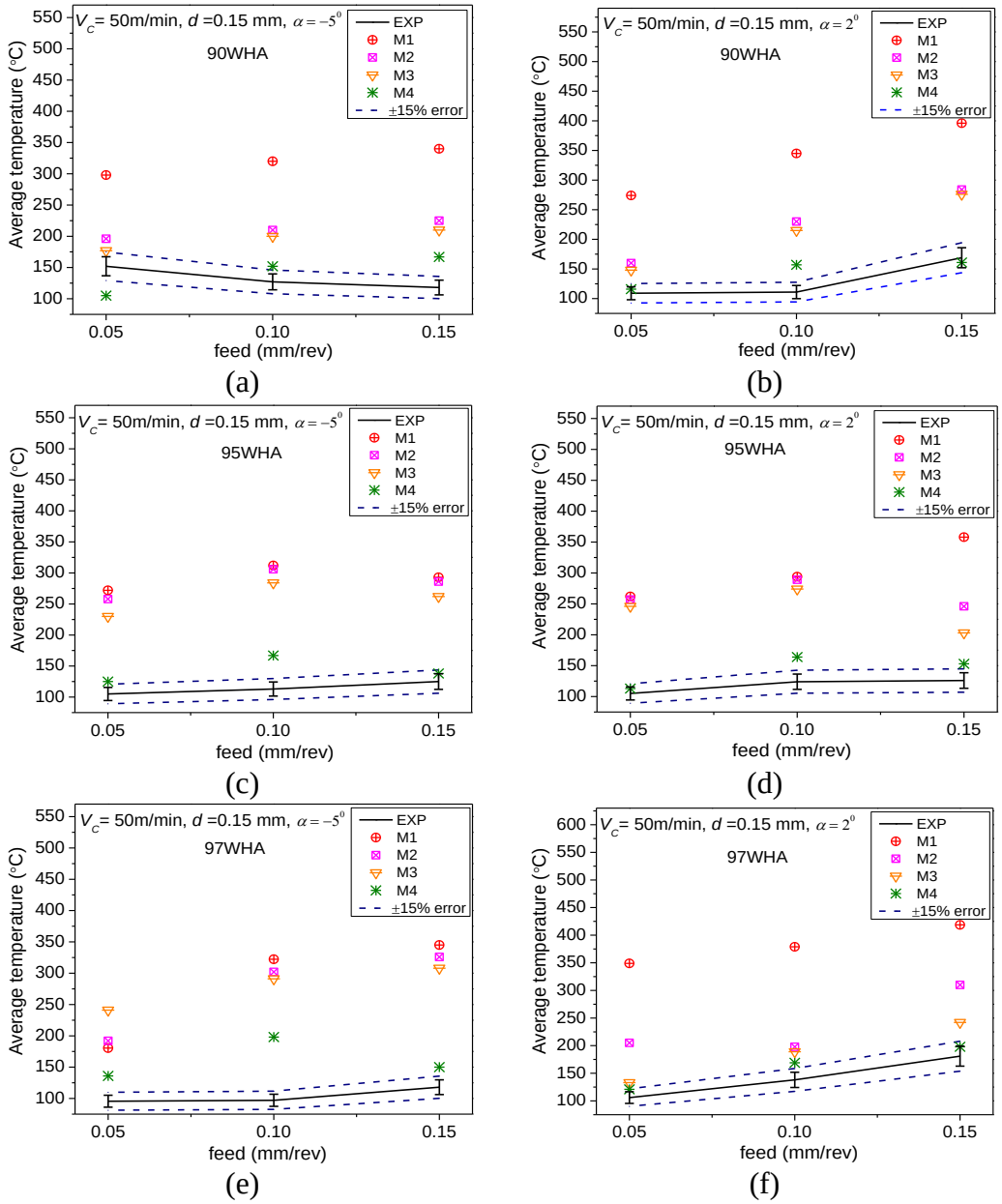

Figure 5.14 Comparison of experimental and predicted average temperature as a function of feed and rake angle for (a) & (b) 90 WHA, (c) & (d) 95 WHA, (e) & (f) 97 WHA.

Likewise, Figure 5.15 and Figure 5.16 show the predicted values of equivalent shear strain with respect to that of experimental ones under varying cutting velocities and feed rates, respectively. Note that the determination of experimental equivalent shear strain, which is a function of shear angle and rake angle, was calculated using Equation (A.4). The measured value of chip thickness and consequently chip thickness ratio were utilized for determination of shear angle as given in Equation (5.7).

$$\varphi = tan^{-1}\left(\frac{r_t cos\alpha}{1 - r_t sin\alpha}\right) \quad (5.7)$$

Further, shear strain values predicted using M4 showed minimum deviation when compared with that of experiments.

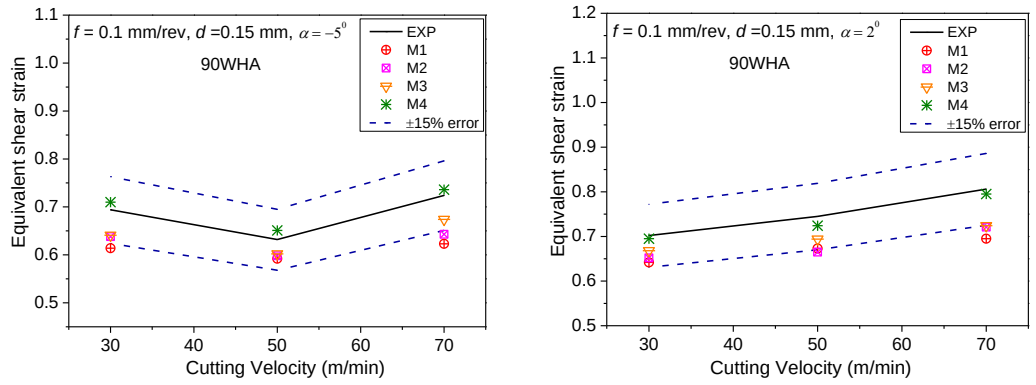

(a)

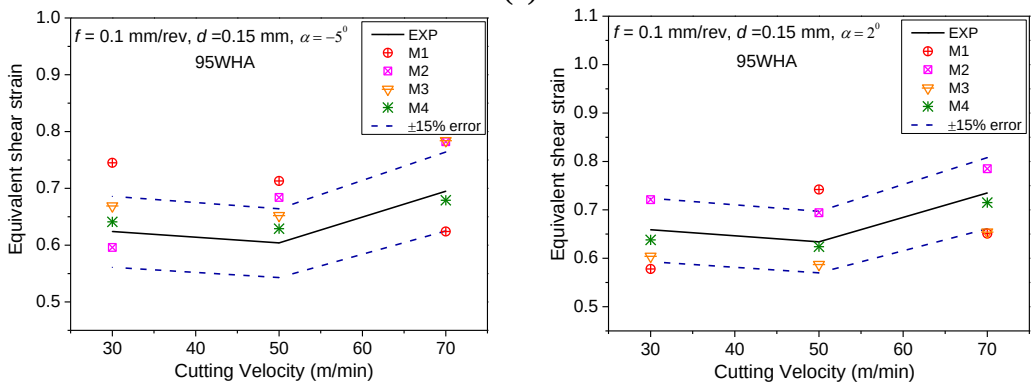

(b)

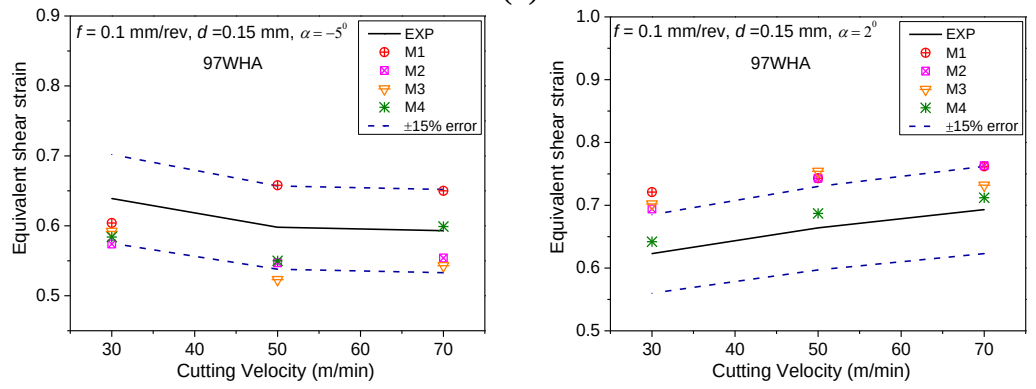

(c)

Figure 5.15 Comparison of experimental and predicted equivalent shear strain as a function of cutting velocity and rake angle for (a) 90 WHA, (b) 95 WHA and (c) 97 WHA

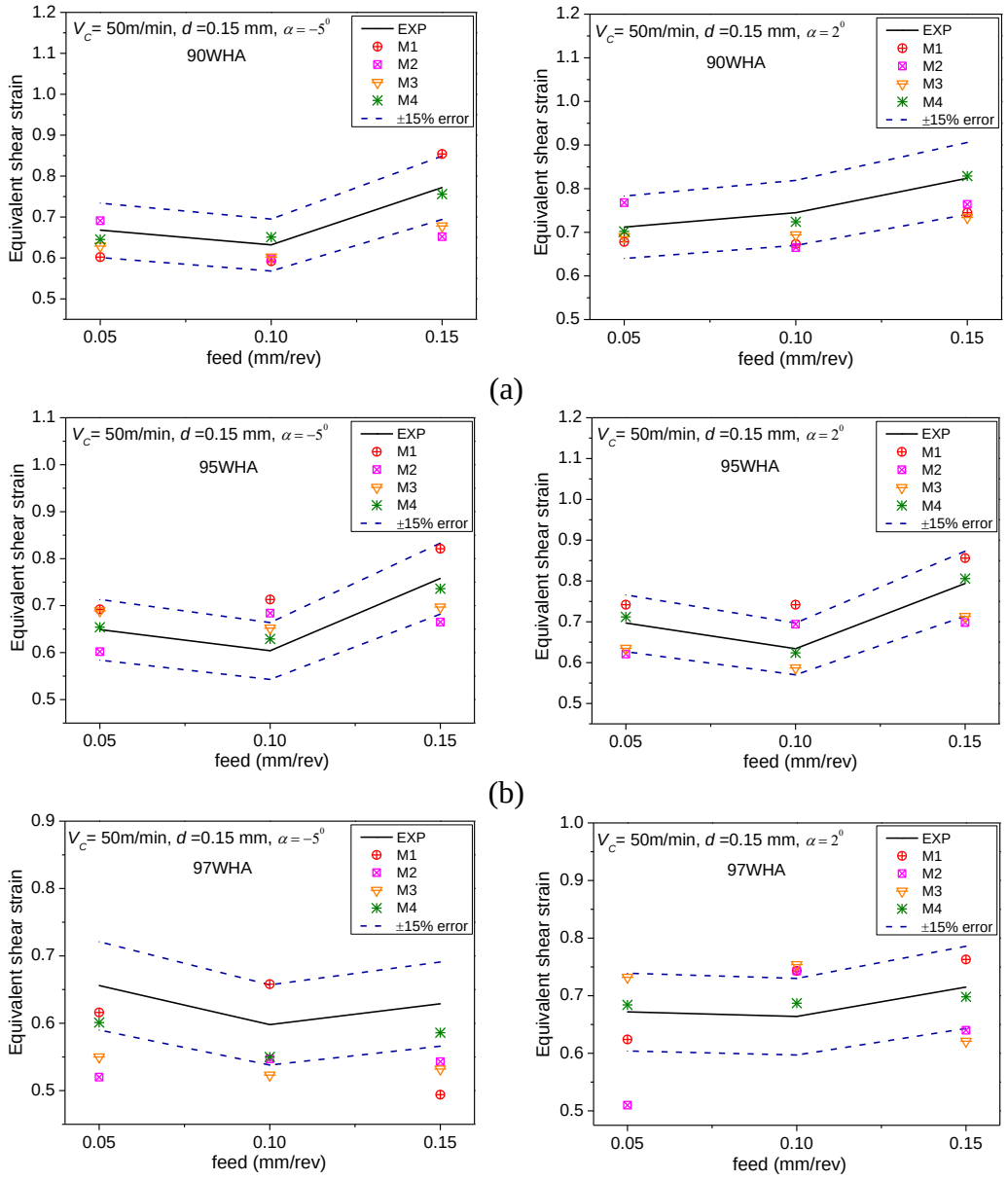

Figure 5.16 Comparison of experimental and predicted equivalent shear strain as a function of feed and rake angle for (a) 90 WHA, (b) 95 WHA and (c) 97 WHA

As a whole, M4 came out to be the best choice for machining simulations. Such observation is very much clear from values presented in Table 5.5.

Table 5.5 comparison of overall adequacy of model M1, M2, M3 and M4

Predicted Output	M1		M2		M3		M4	
	Mean of error %	Mean STD	Mean of error %	Mean STD	Mean of error %	Mean STD	Mean of error %	Mean STD
Cutting force	16.30	4.59	12.34	3.13	11.54	2.98	5.49	1.25
Thrust force	22.59	4.44	17.31	3.42	15.64	3.12	7.35	1.44
Temperature	56.63	32.18	41.04	22.38	38.98	21.86	24.55	13.03
Shear strain	14.44	3.95	11.29	3.10	10.86	2.98	7.12	2.80

The graphic representations provided in Figure 5.17 shows a better insight into the capability of M4 to predict the machining outputs using FE model.

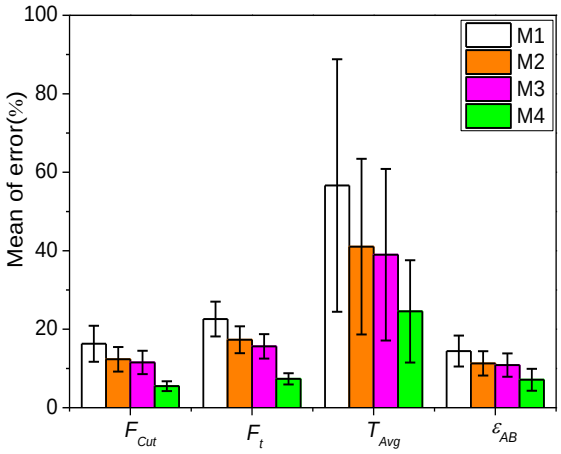

Figure 5.17 Mean error percentages of M1, M2, M3 and M4 for cutting force, thrust force, average temperature and equivalent shear strain.

Since M4 values are derived under similar strain rates and temperatures that are actually exhibited during machining, it could successfully predict all the outputs closer to that of experimental ones. Whereas, in M1 the constants are derived for strain rates in the range of 11-775 s^{-1} at room temperature. As a result, it could not replicate the material behavior precisely during the machining process as these strain rates are much lower than the ones that are experienced during machining.

It is observed that M2 and M3 showed some amount of improvement over M1 because of the fine-tuning of the constants, using GA and ABC algorithm. As a whole, when the results of current work are compared to that of the similar works available in the literature (Sagar, et al. 2018), it is observed that the other models

could achieve the error percentages in the range of 15-20 %. While M4 could achieve a mean error percentage as low as 6%. Such improvement could be because of the modifications made in the error expression (see Equation (4.24)) as well as refinement done to typical ranges selected for ζ, C_0 and Φ in the PSO algorithm as compared to that of Filho's (J. C. Filho 2017).

5.5 Analysis of chip formation mechanism

A detailed analysis is performed using the model M4 under varied cutting conditions for understanding of the physics underlying the chip formation mechanism during machining of WHAs. Hence, an attempt is made to explain the phenomenon with the help of predicted variables that are difficult to measure such as the distribution of stress, strain and temperatures in the cutting zone.

5.5.1 Effect of tungsten content

Figure 5.18 and Figure 5.19 present the distribution of stress and temperature, respectively for rake while machining 90 WHA, 95 WHA and 97 WHA under varied cutting velocities keeping other cutting parameters constant.

Cutting velocity	90 WHA	95 WHA	97 WHA
30	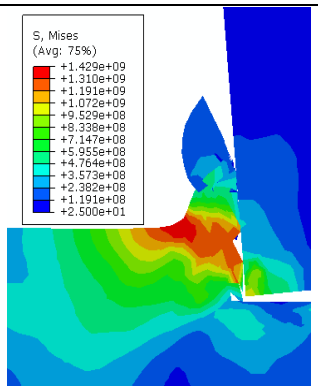	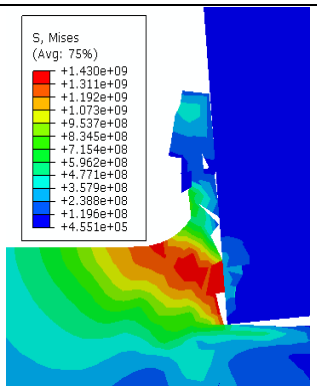	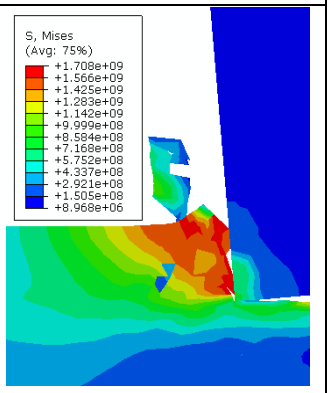

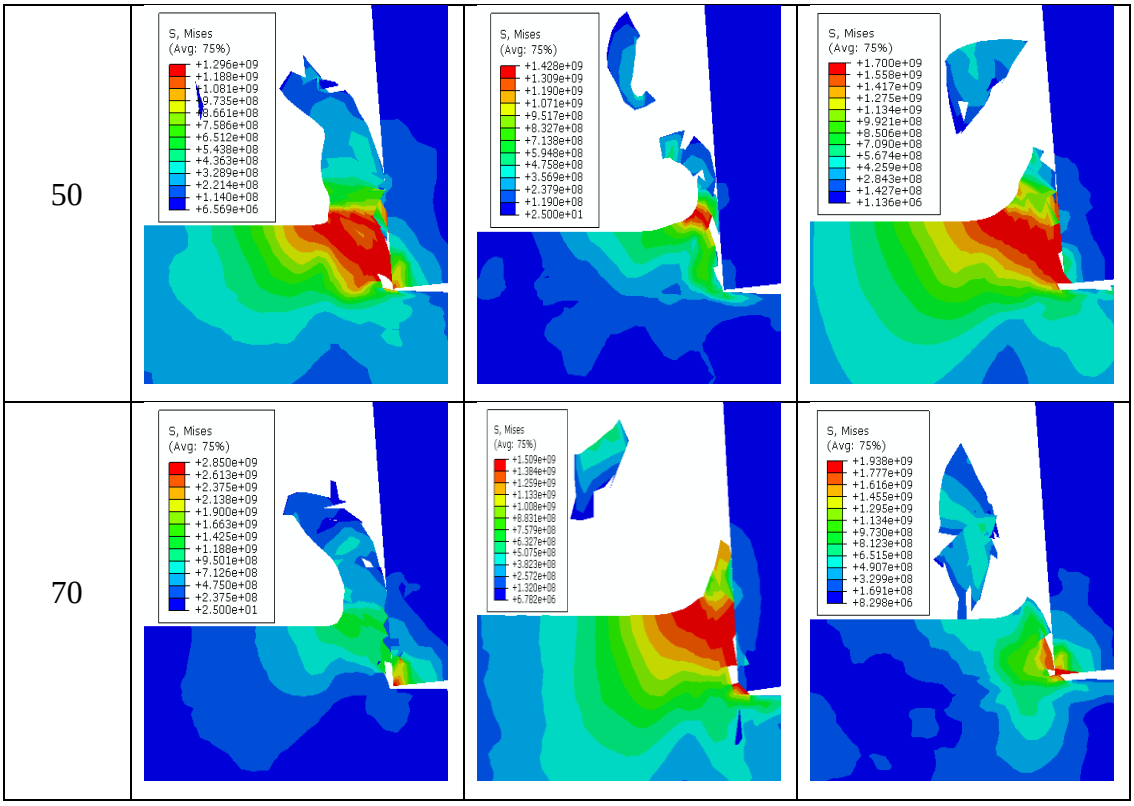

Figure 5.18 Distribution of stresses while machining 90, 95 and 97 WHA at varied cutting velocities

It is observed that as the tungsten content increases, the stresses in the primary shear zone increase for the given cutting velocities, which in turn causes higher straining in the primary shear zone. Such a phenomenon increases the chance of occurrence of fragmentations in chips. A similar trend in chip morphology is observed during machinability studies, as presented in Chapter 4 (see Figure 3.12). Favorably, the predicted stress distributions could give a better insight into the mechanism responsible for the resulting chip morphologies during the machining of WHAs. It is interesting to note that the temperature at primary shear zone follows a similar pattern like that of the stresses as the tungsten content varies under varied cutting velocities, as shown in Figure 5.19 As far as cutting tool temperatures are concerned, 97 WHA tend to have higher maximum temperatures on the rake face for the given cutting velocities. Generally, higher cutting temperatures accelerate the tool wear, which consequently deteriorates the machined surface. This could be one of the reasons for getting higher surface roughness values while machining 97 WHA under varied cutting conditions during machinability studies (see Figure 3.16).

Cutting velocity	90W HA	95 WHA	97 WHA
30	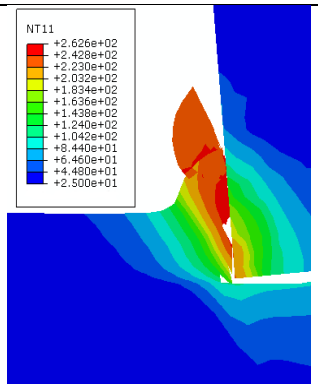	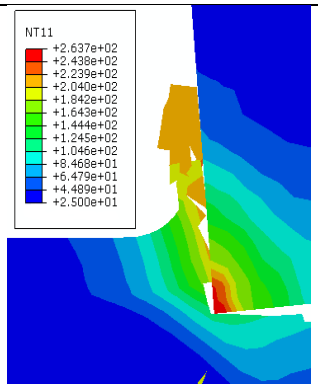	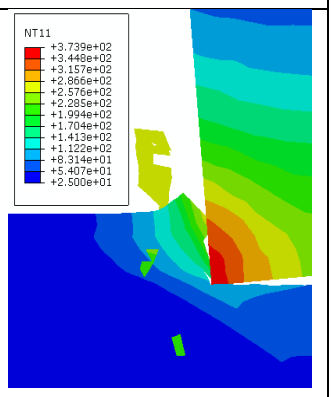
50	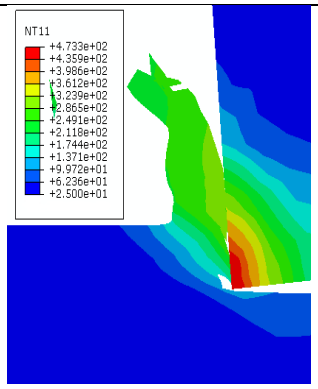	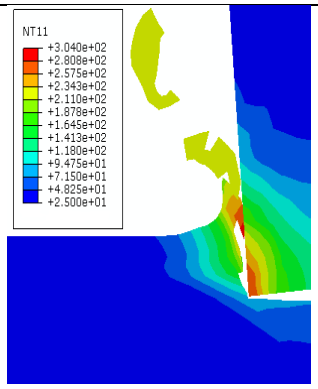	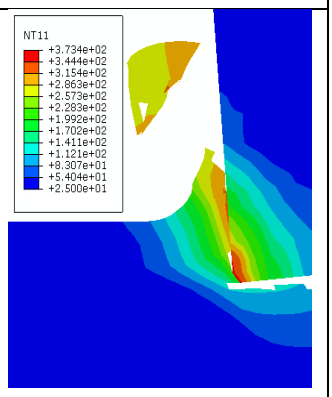
70	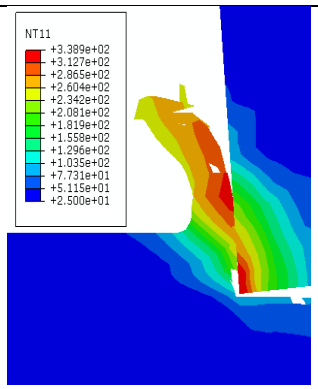	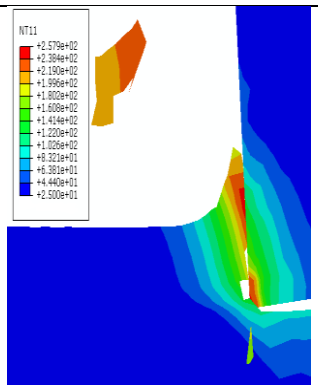	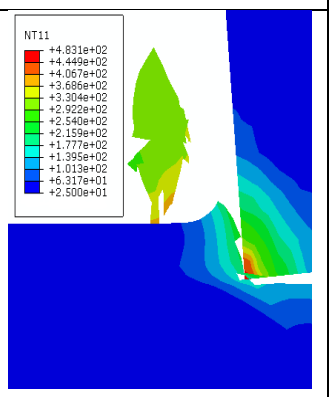

Figure 5.19 Distribution of temperature while machining 90, 95 and 97 WHA at varied cutting velocities

5.5.2 Effect of rake angle

Figure 5.20 (a), (b) and (c) present the distribution of stress, strain and temperature, respectively for rake angles, -5° and 2°, under a specific cutting condition while machining 90 WHA.

Figure 5.20 shows that the rake angle plays a crucial role in determining the type of chip produced. The negative rake angle resulted in a decrease in shear plane angle

and higher compression on chip, which in turn in led to the increase of stress in the primary shear zone from 0.9 GPa to 1.29 GPa (see Figure 5.20 (a)). Consequently, the strain in the primary shear zone increased from 0.8 to 1.3 and as the material strength is decreased with increasing straining, ultimate fracture occurs when the predefined damage evolution criterion is satisfied. Hence, the tendency to obtain discontinuous chips increases as the rake angle changes from a positive value to negative one.

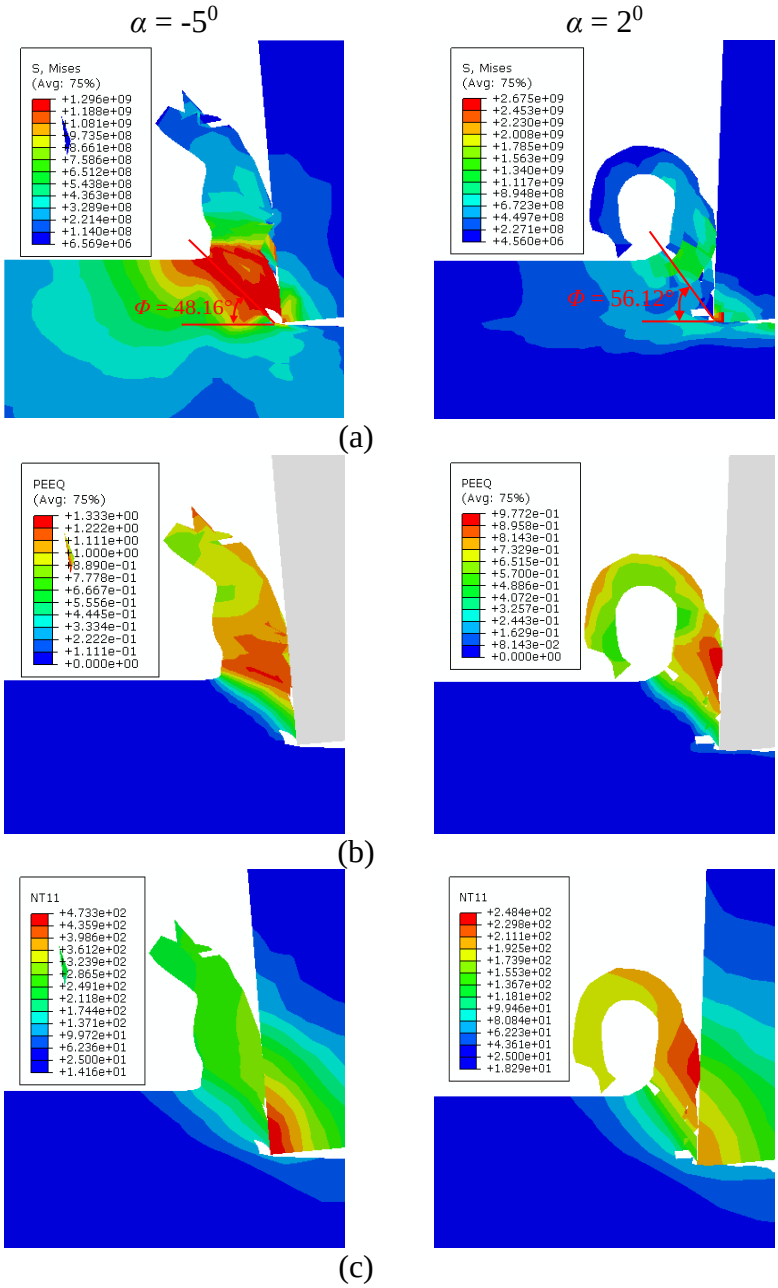

Figure 5.20 Distribution of (a) stress, (b) strain and (c) temperature for -5° and 2° rake angles while machining 90 WHA

From Figure 5.20 (c), it is observed that temperature rises mainly in the chip region, with maximum values localized along with the tool-chip interface for both the rake angles. However, a higher value of temperature is found for negative rake angle which is expected because of the lower value of shear plane angle that leads to higher shear plane area and increased chip thickness. It can be seen that the maximum temperature on the rake face of the cutting tool with -5° rake angle is above 450°C; whereas maximum temperature achieved in case of 2° rake angle is below 300°C. The higher temperature value in case of -5° rake angle explains the development of prominent BUE, which was found during experimental measurement of flank wear in Chapter 4 (see Figure 3.20) under similar cutting conditions. Since the maximum temperatures on the rake for both the tool geometries are above 300°C, it essentially validates the experimental findings stating that the dominant wear mechanism is adhesion for both the cases.

Summary

This chapter deals with the analysis and validation of results obtained from the developed FE model using computed values of JC material and damage model constants. The adequacy of the developed model is investigated by simulating the model for varied cutting parameters and comparing the obtained results with that of the experimental ones. To validate the identified material and damage constants, machining outputs (cutting forces, temperature and shear strain) are predicted considering M1, M2, M3 and M4 along with the damage constants as input under different cutting conditions and compared with the corresponding experimental values. The predicted outputs obtained using M4 closely matched with that of the experimental ones with error percentage well within 10%. Furthermore, the developed FE model with M4 as material input is used as a substitute for the experimental test for developing full factorial data that are requisite for performing multi-objective optimization in the following chapter.

Chapter6 MULTIOBJECTIVE OPTIMIZATION

Multi-objective optimization is a method that determines a unique optimal solution for a process involving multiple input parameters and has more than one objective function. Machining is one such process that involves many input cutting parameters and has multiple output responses (cutting force, surface roughness, MRR and tool wear) that have interdependent correlations. A broad understanding of the machining behavior and the chip formation mechanism of WHAs under different cutting conditions have been arrived at. But, in order to find the optimal cutting parameters and tool geometry that gives the best possible values of machining variables for all the three grades of WHAs, it requires optimization. However, the optimization of the machining process involves a large number of experimental tests to be performed which is time consuming and expensive. As a result, experimental test arrays are usually chosen based on a compromise between the cost of the experiments (cost includes the time required to run the experiments) and the required accuracy of the results. Orthogonal arrays are the most common type of Taguchi DOE that come up as a fair compromise between cost and accuracy. However, precise machining of WHAs, especially for critical applications, may require a higher degree of accuracy during the identification of optimum parameters. On that account, a full factorial design approach could be an alternate solution for such cases. Hence, the present chapter explores the capability of both the approaches, namely, orthogonal array and full factorial design, in multi objective optimization.

6.1 Overall methodology

In the present study, five input parameters, namely, Vc, f, d, α and g with three levels are considered for optimization, as shown in Table 6.1. The first approach, i.e., the orthogonal array design, uses L27 orthogonal array for conducting the experimental tests. The machining tests for 90, 95 and 97 WHA are performed on CNC lathe (HMT PTC 200) and the output responses such as cutting forces, cutting temperature and flank wear are measured using piezoelectric lathe tool dynamometer, FLIR E60 thermal image camera and METZER M stereo microscope, respectively. The test data, so obtained, is used for multi-objective optimization using GRA.

In the second approach, a full factorial design with total of 81 test data is considered. Since conducting these many tests would be time consuming and expensive, the developed FE model, as discussed in Chapter 5, is used for generating the full factorial data required for multi objective optimization. The developed FE model is used to predict the cutting force and average cutting temperature for the 81 test combinations. Further, tool flank wear is calculated for a machining time of 10 minutes using modified Zhao model, as presented in Chapter 4, by considering the predicted cutting forces and temperatures. Subsequently, the full factorial data is used for multi-objective optimization using three evolutionary algorithms, namely, NSGA-II, Hybrid ABC, and Hybrid CS. Out of the three algorithms, NSGA II is one of the commonly used algorithms for multi objective optimization, while the remaining two are newly proposed ones.

The basic idea of considering NSGA II in the current analysis is to use it as a benchmark for comparison with HABC and HCS algorithms. Finally, the optimal solutions predicted by all the four methods are compared and validated. The confirmation tests are performed based on the differences between the values predicted by optimization models and that of the experimentally measured ones. The method having the least error difference is considered as the best model, out of the four, for predicting optimal solutions for machining WHAs. The overall methodology is shown schematically in Figure 6.1.

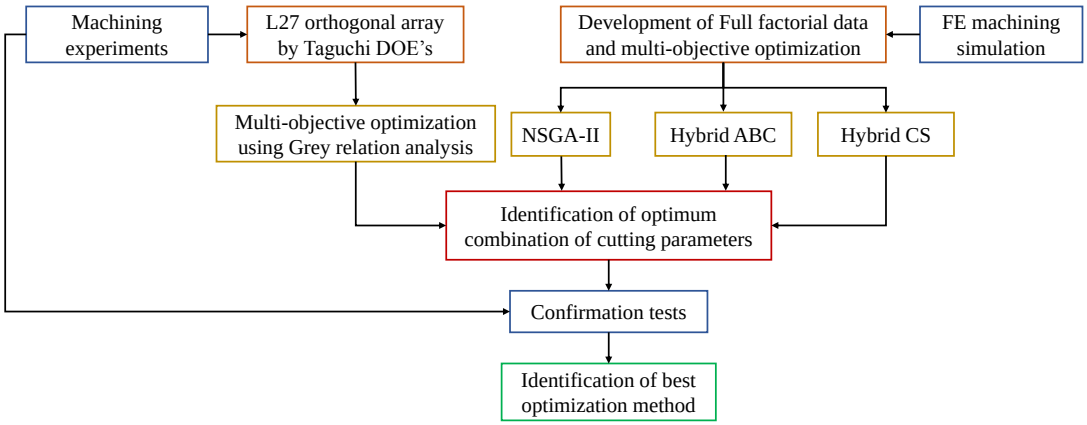

Figure 6.1 Overall methodology for multi-objective optimization

6.2 Orthogonal Array design approach

Turning tests are performed employing the Taguchi L27 orthogonal array based on the process parameters presented in Table 6.1. Table 6.2 shows the experimental design considered for performing Taguchi analysis and GRA based optimization. The machining tests are repeated three times and average values of the output responses, namely, cutting force, temperature and tool flank wear are also presented in Table 6.2. The selection of input parameters and their corresponding ranges are based on few critical factors such as the limiting cutting conditions on CNC lathe for vibration free machining under dry cutting conditions, tool manufacturer's catalog and the range of values taken by researchers in the literature (Nandam, Ravikiran and Rao 2014).

Table 6.1 Process parameters and their levels

Factors	Level 1	Level 2	Level 3
Cutting velocity (V_c)	30	50	70
Feed (f)	0.05	0.10	0.15
Depth of cut (d)	0.10	0.15	0.20
Rake angle (α)	-8	-5	2
Grade (g)	90	95	97

Table 6.2 L27 orthogonal array and measured output responses

Exp. No.	V_c m/min	f mm/rev	d mm	α deg	g	F_c N	T °C	V_B µm
1	30	0.05	0.2	-5	90	46.40	85.25	204.71
2	30	0.05	0.2	-5	95	45.11	82.70	193.00
3	30	0.05	0.2	-5	97	47.32	70.83	203.20
4	30	0.1	0.1	2	90	33.23	96.65	389.62
5	30	0.1	0.1	2	95	34.42	85.30	377.69
6	30	0.1	0.1	2	97	32.33	129.00	392.70
7	30	0.15	0.15	-8	90	68.80	88.30	239.65
8	30	0.15	0.15	-8	95	71.00	125.50	240.49
9	30	0.15	0.15	-8	97	68.43	104.40	246.99
10	50	0.05	0.15	2	90	44.58	108.00	366.90
11	50	0.05	0.15	2	95	32.88	105.00	328.67

12	50	0.05	0.15	2	97	45.91	106.00	363.73
13	50	0.1	0.2	-8	90	57.26	163.00	246.04
14	50	0.1	0.2	-8	95	55.02	127.00	234.76
15	50	0.1	0.2	-8	97	60.05	214.50	240.13
16	50	0.15	0.1	-5	90	76.61	94.75	451.12
17	50	0.15	0.1	-5	95	79.45	86.00	467.45
18	50	0.15	0.1	-5	97	69.82	87.20	448.82
19	70	0.05	0.1	-8	90	21.02	79.23	316.82
20	70	0.05	0.1	-8	95	23.36	70.50	322.84
21	70	0.05	0.1	-8	97	22.62	74.00	310.61
22	70	0.1	0.15	-5	90	44.97	87.60	290.39
23	70	0.1	0.15	-5	95	51.81	102.00	319.61
24	70	0.1	0.15	-5	97	55.71	127.00	326.02
25	70	0.15	0.2	2	90	86.17	112.70	406.56
26	70	0.15	0.2	2	95	86.20	125.50	394.99
27	70	0.15	0.2	2	97	92.63	111.53	408.19

6.2.1 Taguchi Analysis and ANOVA

The data presented in Table 6.2 is used for calculation of Signal to Noise (S/N) ratios for each output parameter and the S/N ratios is used to identify the constituency of results. Further by calculating mean for each output response combinations, a mean effect plot and percentage contribution of input variables are identified by Analysis of Variance (ANOVA) method (13). Detailed Taguchi's DOE approach followed in the present work has been shown in Figure 6.2.

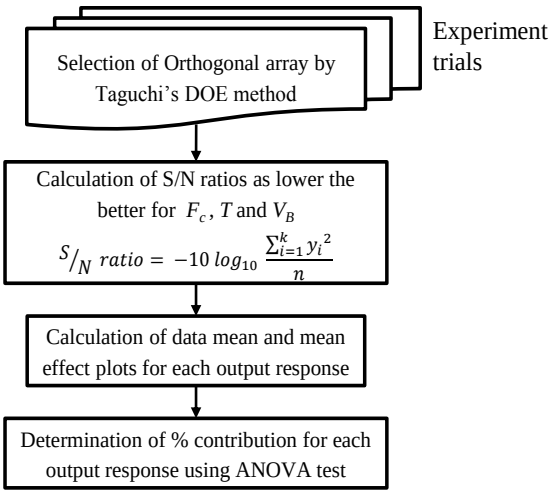

Figure 6.2 Flow chart for analysis of L27 orthogonal array

Table 6.3 presents the S/N ratios of the selected output responses for the analysis.

Table 6.3 S/N ratios of each output responses

Exp. No.	F_c S/N ratio	T S/N ratio	V_B S/N ratio
1	-33.33	-38.62	-46.22
2	-33.11	-38.36	-45.71
3	-33.53	-37.05	-46.16
4	-30.43	-39.77	-51.81
5	-30.75	-38.63	-51.54
6	-30.20	-42.33	-51.88
7	-36.76	-38.94	-47.59
8	-37.03	-42.03	-47.62
9	-36.71	-40.40	-47.85
10	-32.99	-40.67	-51.29
11	-30.36	-40.42	-50.34
12	-33.43	-40.51	-51.22
13	-35.19	-44.24	-47.82
14	-34.81	-42.33	-47.41
15	-35.57	-46.69	-47.61
16	-37.69	-38.78	-53.09
17	-38.00	-38.69	-53.40
18	-36.89	-38.81	-53.04
19	-26.50	-38.10	-50.02
20	-27.37	-36.98	-50.18
21	-27.13	-37.40	-49.84
22	-33.06	-38.88	-49.26
23	-34.35	-40.21	-50.09
24	-34.92	-42.08	-50.27
25	-38.71	-41.24	-52.18
26	-38.71	-41.98	-51.93
27	-39.37	-40.99	-52.22

Cutting forces

The calculated mean and effect of each input parameter on cutting forces are estimated. Figure 6.3 shows the mean effect, percentage contribution of cutting parameters and interaction plots for high contributing cutting parameters on cutting forces.

The mean effect plots in Figure 6.3 (a) clearly show that with the increase in feed rate, there is a considerable increase in cutting forces. This is very much expected because as the feed rate increases, the uncut chip thickness increases, thereby

increasing the amount of force required for removing the chip layer. A similar trend is observed in the case of depth of cut. No such trend is observed for cutting force with respect to cutting velocity, grade and rake angle.

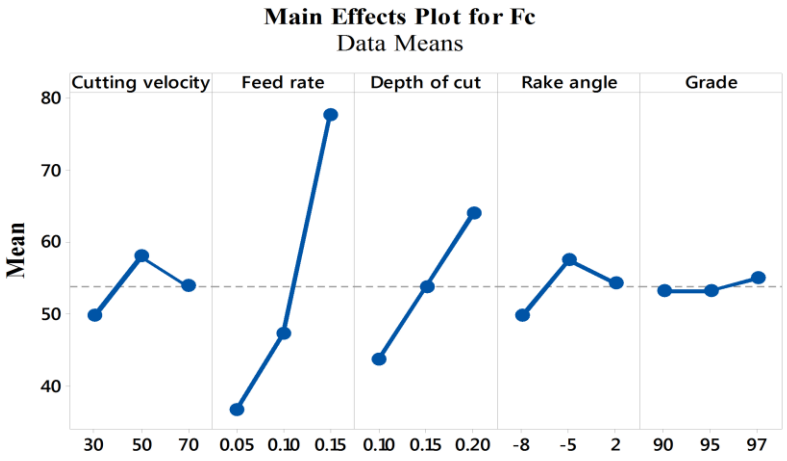

(a)

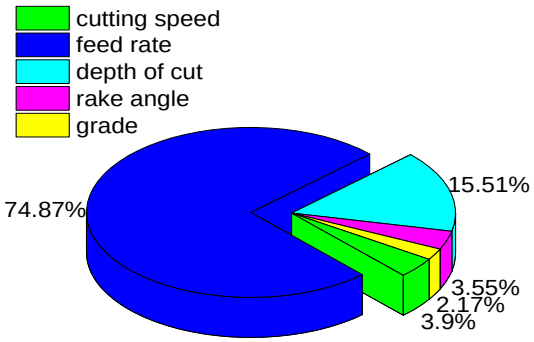

(b)

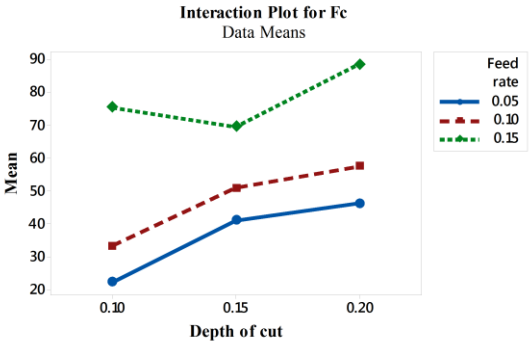

(c)

Figure 6.3 (a) Mean effect plots (b) Percentage contribution of cutting parameters and (c) Interaction plot for major contributing cutting parameters for cutting forces

In Figure 6.3 (b), it is found that feed rate has major contribution with value as high as 75% followed by the depth of cut; whereas WHA grade followed by rake angle and cutting speed have the least effect on cutting forces. This implies that a small variation in feed rate would lead to a significant change in cutting forces. While no considerable change in forces would be observed with the variation in WHA grades.

Further interaction plots are drawn for major contributing factors in Figure 6.3 (c). It is observed that as the feed rate and depth of cut increase, cutting force increases almost linearly for the feed rates 0.05 and 0.1 mm/rev. However, with further increase in feed rate, cutting force values increase as a whole, showing lesser interaction effect of depth of cut on feed rate.

Cutting temperature

The calculated mean and effect of each input parameter on cutting temperatures are estimated. Figure 6.4 shows the mean effect, percentage contribution of cutting parameters and interaction plots for high contributing cutting parameters on cutting temperatures.

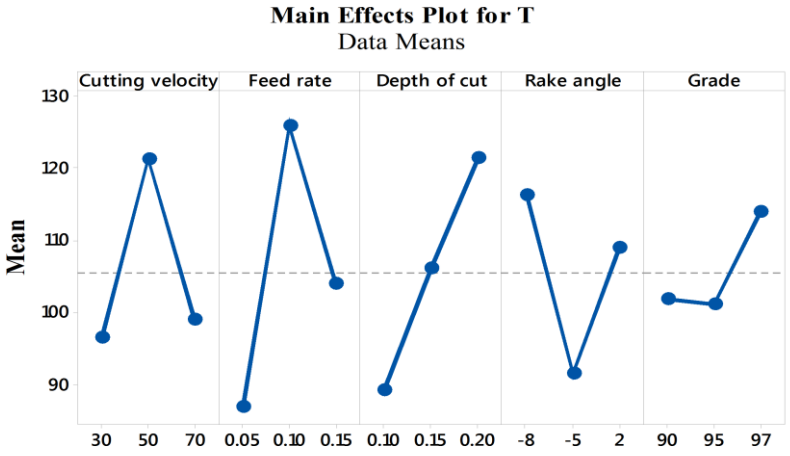

(a)

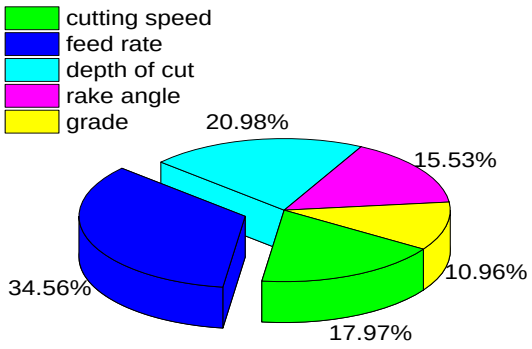

(b)

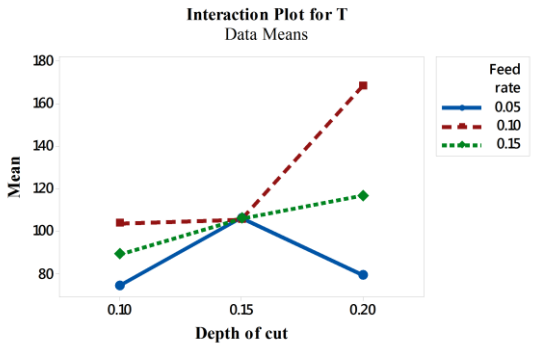

(c)

Figure 6.4 (a) Mean effect plot (b) Percentage contribution of cutting parameters (c) Interaction plot for major contributing cutting parameters for cutting temperatures

The mean effect plots in Figure 6.4 (a) clearly show that all the input parameters significantly affect the cutting temperature. However, the effect of depth of cut on cutting temperature is quite straight forward, i.e., with the increase in depth of cut, cutting temperature increases. In Figure 6.4 (b), it is found that feed rate followed by the depth of cut have comparatively higher contributions with values 35% and 21%, respectively; whereas percentage contributions of the remaining input parameters together comes out to be nearly 50% with individual values falling in the range of 11-18 %. Consequently, the interaction effects between feed rate and depth of cut, as

shown in Figure 6.4 (c), do not follow any proper trend. This implies that the temperature effects in machining process are a complex phenomenon.

Flank wear

Flank wear is another significant response parameter that affects both cutting force and cutting temperature, as discussed in chapter 4. Flank wear is measured for 10 mins of machining. Figure 6.5 shows the mean effect, percentage contribution of cutting parameters and interaction plots for high contributing cutting parameters on flank wear.

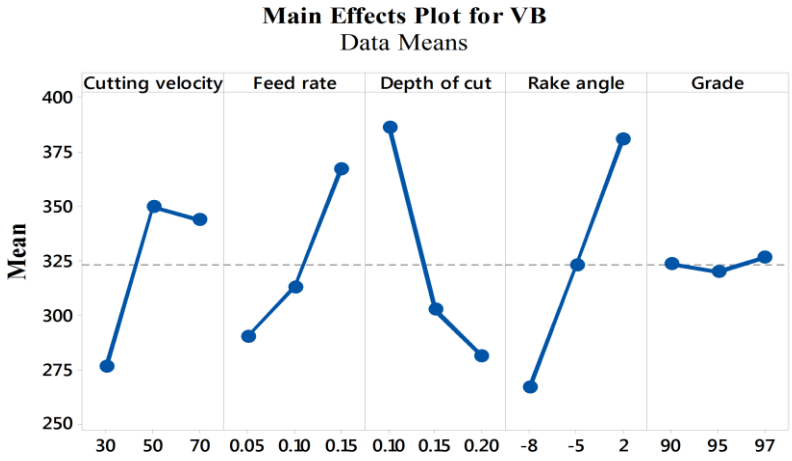

(a)

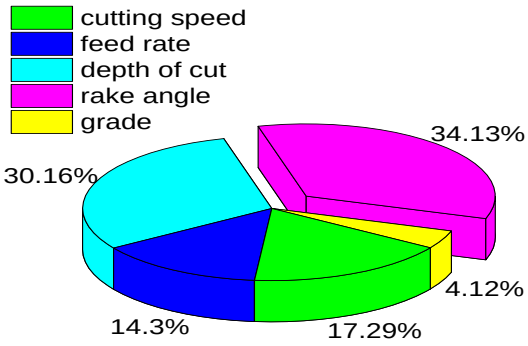

(b)

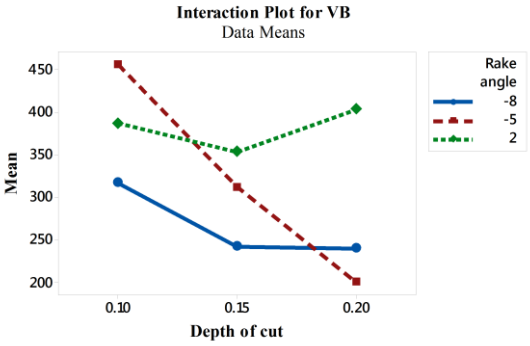

(c)

Figure 6.5 (a) Mean effect plots (b) Percentage contributions of cutting parameters (c) Interaction plot for major contributing cutting parameters on flank wear

The mean effects plots in Figure 6.5 (a) show that all the input parameters, except WHA grade significantly affect the flank wear. It is observed that as the rake angle changes from a negative to positive value, there is a drastic increase in flank wear. In Figure 6.5 (b), it can be seen that the rake angle followed by the depth of cut have the most significant contributions in the variation of flank wear with 34% and 30%,

respectively, as percentage contributions. WHA grade is found to have very little effect on the flank wear. Similarly, Figure 6.5 (c) shows the interaction effects between the major contributing cutting parameter. The interaction effect between rake angle and depth of cut is highly prominent for the rake angle -5° as compared to that of 2° and -8°, as far as flank wear is concerned.

6.2.2 Grey relational analysis

GRA is one of the most widely used multi-objective optimization models for solving real-world problems (Pawade and Joshi 2011) GRA divides problem information into three stages. In the first stage, the problem variables having no information is considered a black region. In the second stage, problem variables having complete information is considered as the white region. In the third stage, the problem variables having incomplete information are considered a grey region (Caydas and Hascalik 2008). It is well known that in complex processes such as machining, the relationship between various factors has interdependence that are difficult to interpret. Such a system that gives inadequate, incomplete, and uncertain information is often called grey. GRA is one commonly used technique to solve such kind of problems (Raykar, D'Addona and Mane 2015). GRA converts complicated multiple performance characteristics to a single solution level in terms of grey relational grades. This section focuses on developing a multi objective optimization model, using GRA, that would predict right combinations of cutting parameters to achieve optimum machining variables, namely cutting force, cutting temperature, and flank wear (Ghetiya, Patel and Kavar 2016, Prakash, Gopal and Karthik 2020) based on the data presented in Table 6.1 and Table 6.2.

The experimental values, normalized mean, Grey relational coefficient, and Grey relational grades (GRG) of response outputs F_c, T, and V_B are presented in Table 6.4. The response outputs are normalized and converted to Grey relation coefficients as per steps 1, 2, and 3. GRG is computed by taking the mean of the Grey relational coefficients corresponding to each experiment combination as per step 4, as shown in Figure 6.5. Since the larger value of GRG indicates better performance of the process, Experiment 3 in Table 6.4 with the highest GRG is considered as an optimum combination within the L27 response table.

Figure 6.6 shows the flowchart depicting the major steps that have been followed to achieve the optimum output variables (Ghetiya, Patel and Kavar 2016, Prakash, Gopal and Karthik 2020).

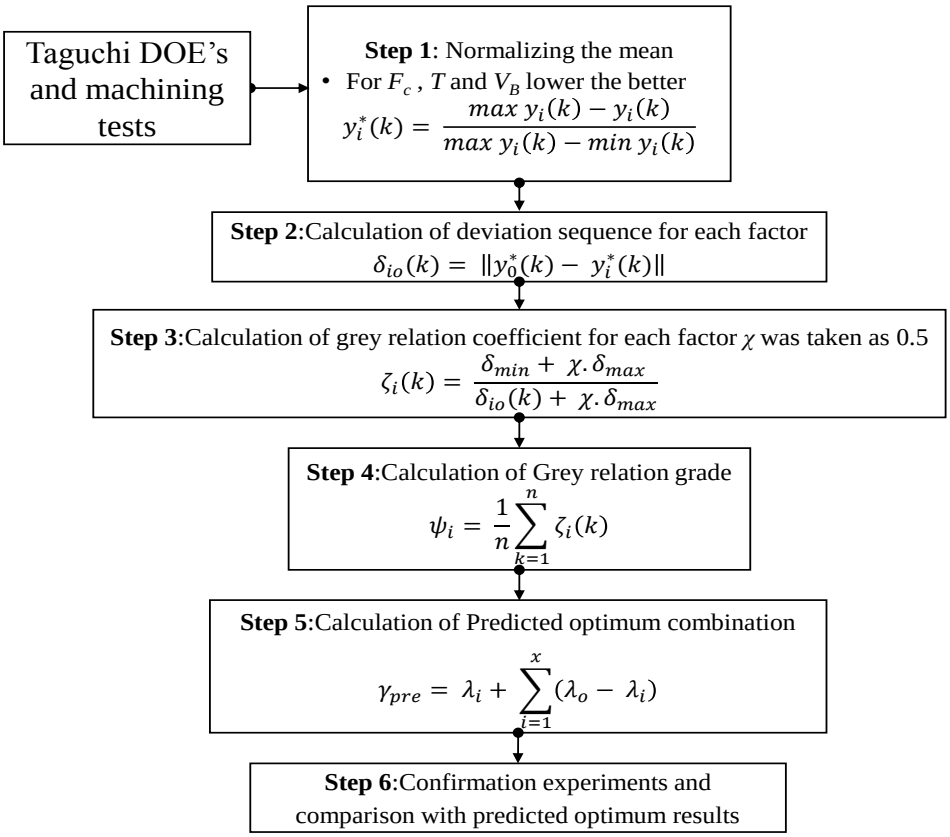

Figure 6.6 Flow chart for Grey relation analysis

Table 6.4 Experimental results and Grey relation analysis

Exp. No.	Normalized mean			Grey relation co-efficient			*GRG*	*Rank*
	F_c	T	V_B	F_c	T	V_B		
1	0.646	0.898	0.957	0.585	0.830	0.921	0.779	6
2	0.664	0.915	1.000	0.598	0.855	1.000	0.818	2
3	0.633	0.998	0.963	0.577	0.995	0.931	0.834	1
4	0.829	0.818	0.284	0.746	0.734	0.411	0.630	11
5	0.813	0.897	0.327	0.728	0.829	0.426	0.661	8
6	0.842	0.594	0.272	0.760	0.552	0.407	0.573	16
7	0.333	0.876	0.830	0.428	0.802	0.746	0.659	9
8	0.302	0.618	0.827	0.417	0.567	0.743	0.576	15
9	0.338	0.765	0.803	0.430	0.680	0.718	0.609	13
10	0.671	0.740	0.366	0.603	0.658	0.441	0.567	18
11	0.834	0.760	0.506	0.751	0.676	0.503	0.643	10

12	0.652	0.753	0.378	0.590	0.670	0.446	0.568	17
13	0.494	0.358	0.807	0.497	0.438	0.721	0.552	19
14	0.525	0.608	0.848	0.513	0.560	0.767	0.613	12
15	0.455	0.000	0.828	0.478	0.333	0.744	0.519	22
16	0.224	0.832	0.060	0.392	0.748	0.347	0.496	24
17	0.184	0.892	0.000	0.380	0.823	0.333	0.512	23
18	0.319	0.884	0.068	0.423	0.812	0.349	0.528	20
19	1.000	0.939	0.549	1.000	0.892	0.526	0.806	5
20	0.967	1.000	0.527	0.939	1.000	0.514	0.817	3
21	0.978	0.976	0.571	0.957	0.954	0.538	0.816	4
22	0.666	0.881	0.645	0.599	0.808	0.585	0.664	7
23	0.570	0.781	0.539	0.538	0.696	0.520	0.584	14
24	0.516	0.608	0.515	0.508	0.560	0.508	0.525	21
25	0.090	0.707	0.222	0.355	0.630	0.391	0.459	25
26	0.090	0.618	0.264	0.355	0.567	0.405	0.442	27
27	0.000	0.715	0.216	0.333	0.637	0.389	0.453	26

Now, the GRG response is listed in Table 6.5. The values listed in the table are obtained by calculating the mean value of each input parameter at its corresponding level; for example, the mean of the GRG for V_c=30 m/min is calculated by averaging the GRG for the experiments 1-9. The optimum performance is then selected based on the highest value of GRG for each parameter in Table 6.5. It is noted that the optimal machining parameters can be predicted using the estimated GRG using step 5 (see Figure 6.5), even for the setting not available in the orthogonal array.

Table 6.5 Response table for predicted optimum level GRG

Symbol	Cutting parameters	Grey relation grade			Mean effect
		Level 1	Level 2	Level 3	
A	Cutting velocity	**0.623**	0.621	0.601	0.066
B	Feed	0.580	**0.621**	0.620	0.068
C	Depth of cut	0.629	0.574	**0.655**	0.072
D	Rake angle	**0.643**	0.642	0.571	0.063
E	Grade	0.479	0.569	**0.609**	0.067

The optimum cutting parameter combination are found to be A1B2C3D1E3, i.e., V_c = 30 m/min, f=0.1 *mm/rev*, d=0.2 *mm*, α=-8°and g=97 WHA. Furthermore, a comparison is made between the measured data from L27 orthogonal array and the

predicted ones. The corresponding output responses are listed in Table 6.6. These results indicated that the value of predicted GRG (0.852) is closer, but slightly higher, as compared to that of the experimental one (0.834). Lastly, the confirmation experiments are performed at the predicted optimum level of input parameters and compared with the ones obtained by evolutionary algorithms using the full factorial design approach in the following sections.

Table 6.6 Comparison of cutting parameters between measure data from L27 orthogonal array and predicted optimum level

Parameters	Optimum cutting parameters	
	Experiment	Predicted
Level	A1B1C3D2E3	A1B2C3D1E3
F_c	47.32	
T	70.83	
V_B	203.20	
GRG	0.834	0.852

6.3 Full factorial design approach

In the past, many researchers have used DOEs to reduce the number of experiments (Narayanan, Baskar and Ganesan 2018, Sagar, Priyadarshini and Gupta 2020) and utilized orthogonal array data for multi-objective optimization. These orthogonal arrays led to much redundancy in predicted optimum response from algorithms due to lack of proper training data. Moreover, the present section investigates the applicability of the evolutionary algorithms for the optimization of machining operations. But it is well known that evolutionary algorithms require a large amount of training data for accurate predictions of optimum responses (Serra, Chibane and Duchosal 2018). This motivates to consider the full factorial design for optimization in addition to L27 orthogonal design approach. In the full factorial approach, four input parameters, namely, Vc, *f*, α and *g* with three levels are considered, as shown in Table 6.7, thus making a total of 81 data sets. The output responses for the same are taken from the FE simulations using model M4, the details of which are listed in Table A1. Note that depth of cut has not been considered as one of the inputs based

on the fact that the effect of depth of cut on the output responses are straight forward and precise machining of WHAs require lower values of depth of cut.

Table 6.7 Process parameters and their levels for full factorial DOE

Factors	Level 1	Level 2	Level 3
Cutting velocity (V_c)	30	50	70
Feed (f)	0.05	0.10	0.15
Rake angle (α)	-8	-5	2
Grade (g)	90	95	97

6.3.1 Need for full factorial design

In order to check the prediction efficiency of full factorial design and compare the same with that of the L27 orthogonal array design, regression analysis is performed on the former to formulate a second-order polynomial regression equation, as shown:

$$F_C = 4498.594 - 5.967\,Vc + 929.592\,f + 24.503\,\alpha - 93.303\,g + 0.739\,Vc\,f - 0.031\,Vc\,\alpha + 0.061\,Vc\,g - 9.67\,f\,\alpha - 6.617\,f\,g - 0.212\,\alpha\,g - 666.222\,f^2 + 0.504\,\alpha^2 + 0.485\,g^2 \quad (6.1)$$

$$T = 17394.79 + 0.502\,Vc + 343.039\,f - 15.04\,\alpha - 374.238\,g - 6.944\,Vc\,f - 0.054\,Vc\,\alpha + 36.652\,f\,\alpha + 13.29\,f\,g + 0.095\,\alpha\,g - 3444.441\,f^2 - 0.860\,\alpha^2 + 2.011\,g^2 \quad (6.2)$$

$$V_B = 5877.67 - 3.466\,Vc + 1874.798\,f + 42.265\,\alpha - 120.774\,g + 1.291\,Vc\,f - 0.073\,Vc\,g - 6.471\,f\,\alpha - 14.302\,f\,g + 0.310\,\alpha\,g - 0.014\,Vc\,2 - 763.630\,f^2 + 1.076\,\alpha^2 + 0.633\,g^2 \quad (6.3)$$

It is to be noted that the coefficients with the least weightages in the regression equations are neglected to reduce the complexity of the equations. Lastly, a statistical analysis has been carried out to analyze the suitability of both the approaches.

Table 6.8 presents the significance levels predicted by both the approaches depicting how each of the input parameters affects the output responses. Both the approaches show similar results with few exceptions such as, for the inputs, namely, grade and rake angle in case of full factorial design. In order to find out the efficiency in the prediction of results, correlation coefficient R^2, predicted $R^{2,}$ and R^2 adjusted values are computed and are presented Table 6.9. An increase in the R^2 is observed for full factorial design, thus, implying that there is an improvement in the overall efficiency

over L27 data set. Since the value of the correlation coefficient R^2 lies in the range of 90-95%, the developed regression model is adequately significant. The regression model provides a good relationship between the input parameters and the output responses.

Table 6.8 Comparison of the Significance level of cutting parameters on machining performance attributes.

Cutting parameters	Cutting force (N)		Cutting temperature (°C)		Flank wear (μm)	
	L27	Full fact	L27	Full fact	L27	Full fact
Cutting velocity (m/min)	LS	LS	HS	HS	LS	HS
Feed rate (mm/rev)	HS	HS	HS	HS	HS	LS
Rake angle (°)	LS	HS	LS	LS	HS	HS
Grade	NS	NS	LS	HS	NS	NS

HS: High Significance; NS: No significance; LS: Low Significance

Table 6.9 Comparison of statistical interference of machining parameters

Response parameters	DOE	Correlation coefficient R^2	Pred R^2	Adj R^2
Cutting force (N)	L27	0.924	0.853	0.876
	Full fact	0.934	0.896	0.915
Cutting temperature (°C)	L27	0.896	0.832	0.857
	Full fact	0.929	0.867	0.882
Flank wear (μm)	L27	0.925	0.827	0.846
	Full fact	0.948	0.918	0.930

Similarly, a comparison is made regarding the normal probability versus residual plots for the predicted responses, as shown in Figure 6.7. The primary purpose of such a plot is to examine the standard deviation of predicted values with actual values such that the residuals fall on a straight line for normally distributed errors. The resulting plots in Figure 6.7 reveal that the full factorial design residuals are much closer to the straight line as compared to that of L27 in all cases. This signifies that the errors are normally distributed and the regression model is well fitted. Besides, it also explains that the regression model provides an excellent relationship between input parameters and output responses.

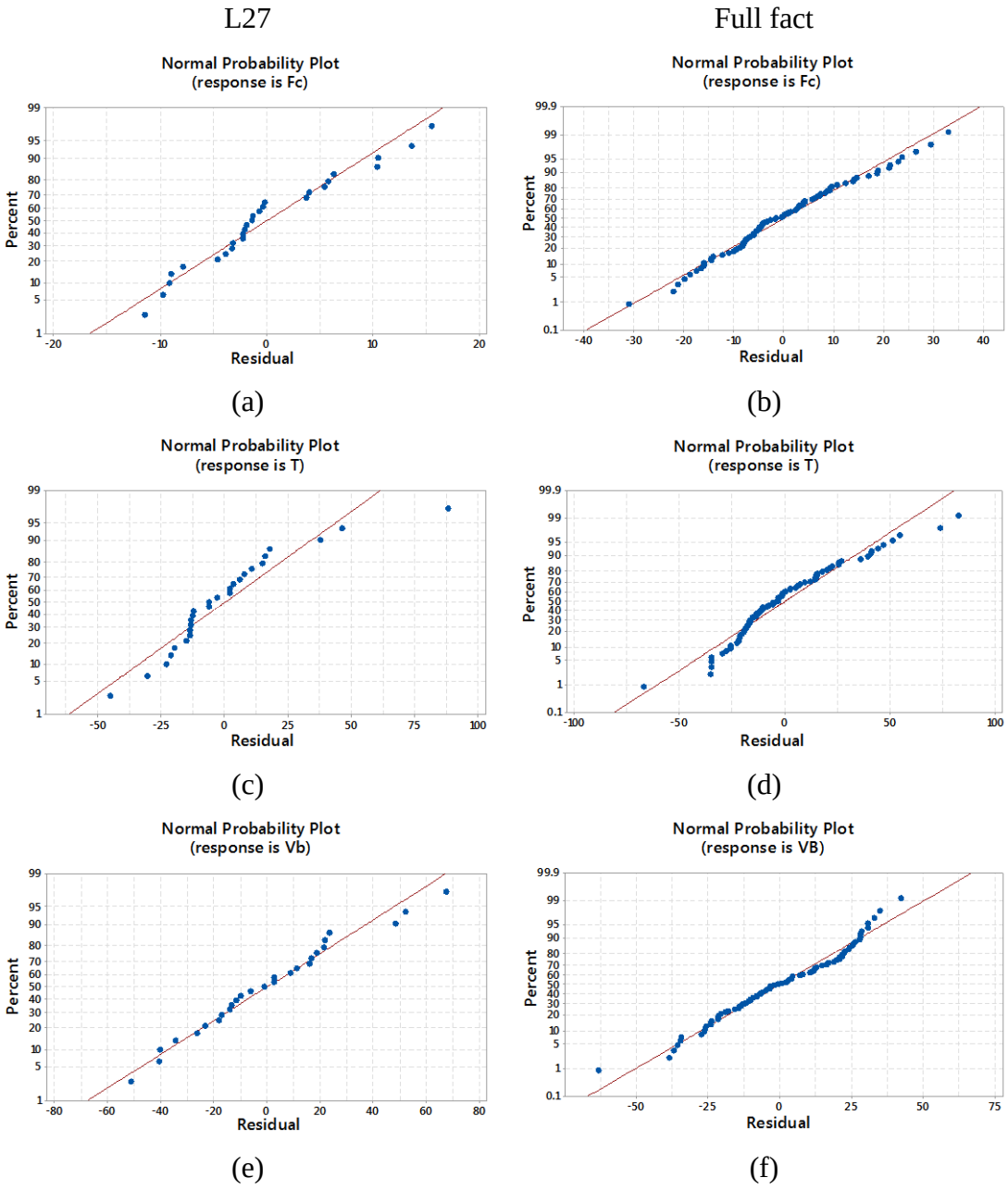

Figure 6.7 Comparison of normal probability versus residuals of predicted response between L27 and Full factorial design for (a), (b) Cutting force, (c), (d) Cutting temperature and (e), (f) Tool Flank wear

6.3.2 Evolutionary algorithms

Non-dominating sorting genetic algorithm

NSGA-II is a modified form of the genetic algorithm used for solving multi-objective optimization problems (Rao, et al. 2018). The key features of NSGA-II are fast nondominated sorting procedure along with an elitist preserving approach and a

parameterless niching operator with constraint handling method (Deb, et al. 2002). Further, NSGA II can handle only two objective functions at a time for the optimization process, and the third objective function is considered as dummy function and the value of the latter is predicted based on optimum combination derived (Ciro, et al. 2016).

Figure 6.8 shows the working and selection procedure of optimum solution from each population set. Figure 6.8 (a) shows average Pareto spread plots for change in distance measured by individuals with respect to previous generations and average solution spread for 240 generations. The data points concentrated on one side of average Pareto spread plots are the initial population derived by algorithm to start the optimization process. Whereas Figure 6.8 (b) shows the number of children formed after mutation and crossover process from a population size of 50. The more the effective contributing parent in each generation is identified by the histogram presented in Figure 6.8 (c) histogram that shows the average distance measured between each individual in population size of 50. Then the fractions of individuals are placed in each Pareto tier as rank 1 to rank 6 based on the effectiveness of the solution, as shown in Figure 6.8 (d). The ranking indicates that the rank 1 individuals are best and rank 2 individuals are dominated by rank 1 individuals only.

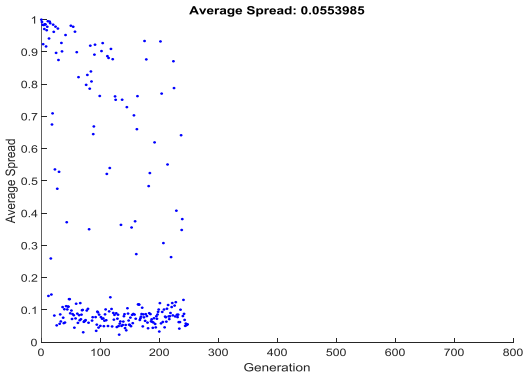

(a)

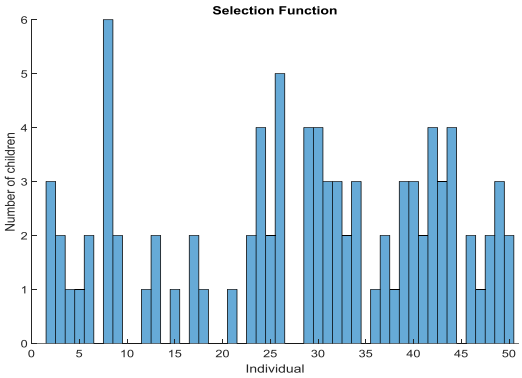

(b)

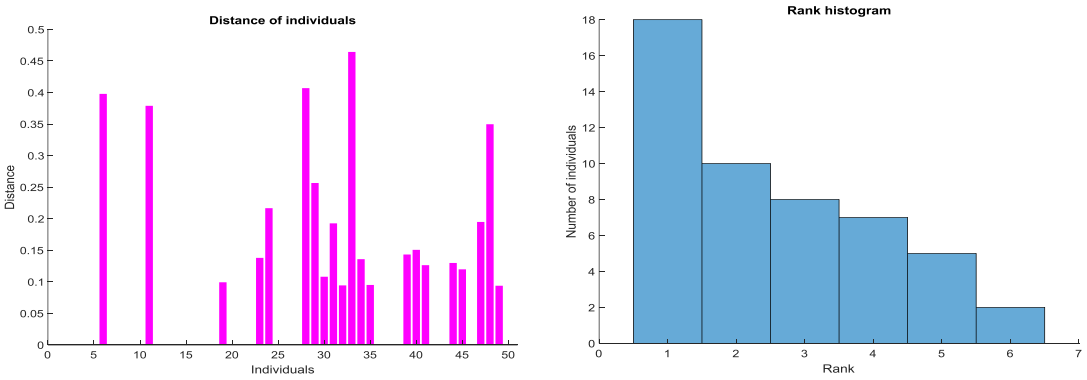

(c) (d)

Figure 6.8 (a) Average Pareto spread plot (b) Selection histogram for each population size (c) Average Pareto distance between an individual in a population (d) Ranking histogram of individuals

Note that few assumptions have been made while running NSGA II algorithm. Firstly, the initial population size is assumed to be 50 with tournament selection method. The population is then initialized with a tournament size of two between the parent population. In the next step, reproduction between the initial parent population is performed by crossover function, considering crossover fraction as 0.8. The constrained mutation function with forward migration strategy is taken into consideration at every 20 parent population with a maximum generation of 400. Finally, based upon these values, optimum responses are predicted, are shown in Table 6.10.

Table 6.10 Constants to run NSGA-II optimization and predicted optimum

Parameters	Functions and constants
Initial population size	50
Selection function	tournament
Tournament size	2
Reproduction	Crossover function
Crossover fraction	0.8
Mutation function	constraint dependent
Migration direction	Forward
Migration fraction	0.2
Migration interval	20
Maximum no of generations	400
Predicted optima F_c	23.64
Predicted optima T	107.6
Predicted optima V_B	190

Hybrid artificial bee colony algorithm (HABC)

The ABC algorithm is known to have a better solution search strategy and faster convergence. However, sometimes it may get trapped in local minima due to the repletion of search strategies, non-consistency in exploration and exploitation of solution space (X. S. Yang 2014). To overcome such problems, few hybrid methods have been adopted by a few researchers in the past (Hossain and Liao 2017, Das, et al. 2014). However, most of them have used experimental test data based on orthogonal array design. Such an approach, consequently, end up getting local minima as an optimum solution due to inconsistent training data. Hence, in the present work, a hybrid algorithm based on full factorial test data has been considered giving priority for each response parameter according to their effectiveness on the process.

In the present study, a single objective absolute minima technique is combined with ABC algorithm to determine global optima for each response output. Further, these global optima values are used as fitness function in ABC algorithm for multi-objective optimization. The following steps are used to perform the HABC algorithm.

Step1: Determination of absolute global minima

In this step, the input variables like cutting velocity (V_C), feed rate (f), rake angle (α), grade (g) are considered along with output responses like cutting force (F_c), cutting temperature (T), flank wear (V_B) in the form of following polynomial regression equations to initialize objective functions:

$$F_{min} = f_1(v_c, f, \alpha, g) \tag{6.4}$$

$$T_{min} = f_2(v_c, f, \alpha, g) \tag{6.5}$$

$$V_{Bmin} = f_3(v_c, f, \alpha, g) \tag{6.6}$$

f_1, f_2, f_3 are the function equations of polynomial regression equations (6.1) to (6.3) developed from full factorial DOE. From these three functions, the global minima of individual output responses are identified.

Step 2: Multi-objective optimization by ABC algorithm

In this step, the weightage is given to each of the response variables based on its effectiveness on the machining process. Among the three response variables, the highest rank (or effective) response variable is given more priority. Consequently,

global minima for this effective response variable is identified and a tolerance limit (a) is defined. It is noted that in the present case, F_c comes out to be an effective response variable. Hence, to minimize the other two response variables within the specified tolerance limit a of F_c global minima value ABC algorithm is used. The upper ($x_{g\,max}$) and lower ($x_{g\,min}$) bound values of input variables are identified for the allowable range of tolerance limit of F_c from the regression model using the following equations:

$$Z_{min}(x_{g\,min}) = (T(x_{g\,min}), (V_B(x_{g\,min}))$$
$$Z_{max}(x_{g\,max}) = (T(x_{g\,max}), (V_B(x_{g\,max})) \quad (6.7)$$
$$Z_{g\,min}(x_{g\,min}) \leq F_c(x_g),\ Z_{g\,max}(x_{g\,max}) \geq F_c(x_g)$$

$$x = (v_c, f, \alpha, g) \quad (6.8)$$

where, $x_{g\,max}$, x_g and $x_{g\,min}$ are maxima, best, and minima of global optima input variables, and x is the decision vector (input parameters).

Initialization:

For the dimensional e problem in the decision space, the main task is to generate food sources randomly in the corresponding search space during the initialization phase. The following equation initializes each food source:

$$x_{gi}^{e} = x_{gmin}^{e} + rand(0,1)(x_{gmax}^{e} - x_{gmin}^{e}) \quad (6.9)$$

where i is the nectar amount of food source in the position, e is the dimension index of food source range, rand (0, 1) is a random distribution of food source in search space over the interval (0, 1), x_{gmax}^{e} and x_{gmin}^{e} are the maximum and minimum limits of the e^{th} dimensional space for global optima food source, respectively. The next task is to assign a food source with a variable trial, i = 1,2,…n. The food source is said to be abounded if there is no further improvement in successive trials. Subsequently, the employed bee related to that particular food source gets converted to scout bee to find a new food source randomly.

Employed bees:

Each food source x_{gi} is explored by an employed bee. These employed bees explore a new temporary food source v_i around it. Therefore, for each food source, a corresponding employed bee uses one randomly selected neighbor k to generate a new position which is formulated as

$$v_i^e = x_{gi}^e + \varphi_i^e (x_{gi}^e - x_{gk}^e) \tag{6.10}$$

where k is a random neighbor different from i, φ_i^e is a randomly selected real number in the interval [-1,1]. After a new position for a food source is found, its fitness is evaluated at hive by onlooker bees using the expression:

$$P_i = \frac{\lim_{i \to a} Z_i}{Z_g} => \frac{T_i}{T_g} : \frac{V_{Bi}}{V_{Bg}} \tag{6.11}$$

where $P_i$is the probability associated with that food source, $Z_i$is the fitness value of the solution i (nectar amount of the food source in the position i), a is the user defined tolerance limit for global optima, T_i and V_{Bi} are other response functions fitness value of the solution i, Z_g, T_g, and V_{Bg} are other response functions at global optima. From the above equation, if the fitness of the new position is better than the old one, then a new food source replaces the old one. Otherwise, the trial for the old food source gets incremented to the next random position. The said procedure is repeated from the employed bees until 6000 specified iterations are reached or termination occurs provided there is no further improvement in the solution food source for 6000 trials. At the time of termination or 6000 iterations, the position of food source and its nectar amount are considered as the optimum values of the input variables and the response objective functions of the algorithm. Figure 6.9 shows the flow chart of the methodology adopted for the HABC algorithm.

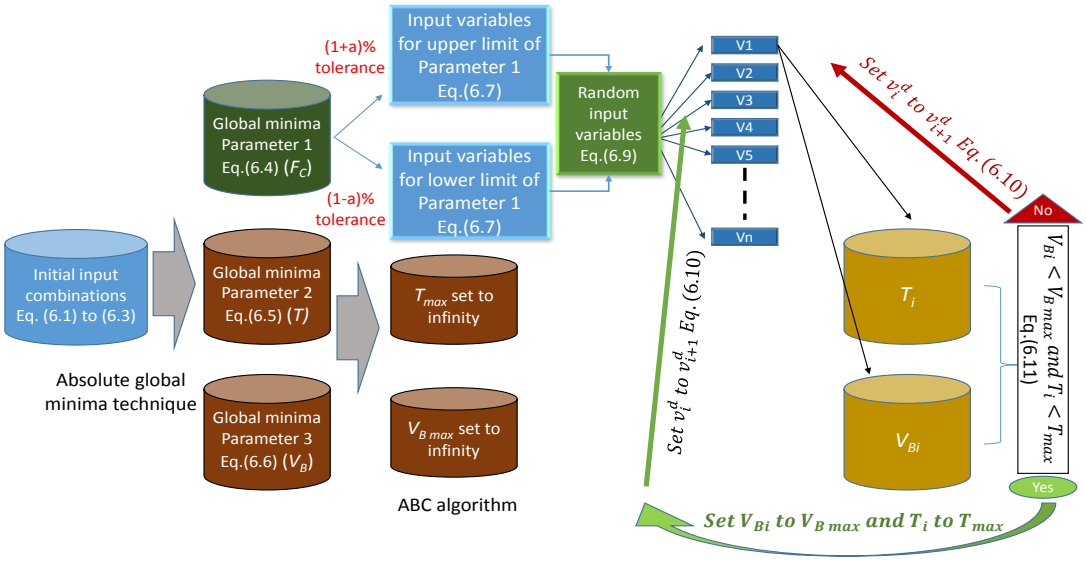

Figure 6.9 Flow chart for HABC

Table 6.11 shows the predicted global optima response values by absolute global minima technique considering the allowable input variables range $x_{g\,max}$ and $x_{g\,min}$ for tolerance limit of F_c. Further, a constant real number is assumed as 0.8 to identify temporary food source by employed bees, and finally, the optimum responses are predicted from the algorithm.

Table 6.11 Predicted outputs and constants to run HABC optimization

Global optima values by step1			a	$x_{g\,max}$				$x_{g\,min}$				φ_i^e	*Final optima predicted*		
$F_{c\,min}$ N	T_{min} °C	V_{Bmin} µm		V_c	f	α	g	V_c	f	α	g		$F_{c\,min}$ N	T_{min} °C	V_{Bmin} µm
17.32	83.34	153	25%	69.2	0.14	2	97	50	0.05	-8	90	0.8	26.29	101.3	196

Hybrid cuckoo search algorithm (HCS)

CS is a nature-inspired metaheuristic algorithm developed by (Yang and Deb 2013) which is further enhanced by the Levy's flight method by (Kaveh and Farhoudi 2013). From the available research works, it is found that the CS algorithm shows superior performance and better local search ability due to the use of Levy's flight mechanism as compared to traditional algorithms such as GA and PSO (Yang, et al. 2018). However, CS algorithm has poor global exploration performance and slow convergence speed due to the characteristic of random jumping in Levy's flight (Zhang, Ding and Jia 2019). For these reasons, it is necessary to explore some strategies to enhance the performance of CS algorithm. Hybrid approach is one such strategy where in the CS algorithm can be modified in a way that can overcome the limitations associated with it. Linearly decreasing inertia weight (Rani, AbdulMalek and Neoh 2012), individual guidance position update method and contemporary individuals with random generation method (Cheng, et al. 2019) etc. are some of the methods that have been successfully used in design and manufacturing layout management applications to improve the position update. Zhang, et al (2019) proposed a hybrid DE and CS algorithm to subgroup the cuckoo population by DE approach to increase population diversity between individuals in population iteration. Gmili, et al. (2019) modified the step function of cuckoo by combining Levy's flights random walk with PSO's particle movement strategy to improve the exploration and

exploitation of search space. Similarly, Chen and Wang (2019) proposed a HCS algorithm that uses a nonlinear decrement method to adjust the parameter *K* with increase in number of iterations. While Thirugnanasambandam, et al. (2019) proposed CS algorithm with adaptive parameter adjustment and applied it to multi-peak numerical optimization problems. In the improved algorithm, the parameter *K* is adaptively adjusted to linearly improve the optimal individual fitness value information in the contemporary population. Hence, it is felt that a similar approach can be used for the optimization of machining parameters. Senthilkumar, Tamizharasan and Anandakrishnan (2014) used Hybrid Taguchi-GRA and CS algorithm to optimize the performance of multilayered coated inserts for turning AISI D3 steel. However, results clearly showed that partial experimental test data based on orthogonal array design had again end up in getting local minima as optimum solution due to inconsistency in the training data. The major difference between the proposed algorithm and the existing ones is that the former directly identifies optimum response parameter by improved exploration and exploitation strategies of population search space and its diversity within the range of input parameters with ascending fitness function these hybrid methods has end up in either inconsistency in convergence of global optimal solutions or lack of input parameter data for training the algorithm. Thus, the present work explores the application of the hybrid approach and considers full factorial test data to improve the search space of the algorithm.

Based on the hybridization approaches used by researchers in the past, it addresses the improvement of CS algorithms exploration and exploitation strategies of population search space and its diversity. To enhance the optimization performance of CS, the HCS algorithm is proposed in this work. In the present study, a single objective absolute minima technique is combined with CS algorithm to determine global optima for each response output directly and adopts these global optima values as fitness function with tolerance limit. Further, the most effective response parameter in the process is identified and the effective response parameter is given highest priority among other response parameters. A controlled forward step size function is considered in Levy's flight method which greatly improves the exploration of search space and diversity of the population. Following are the steps adopted for HCS algorithm and are discussed in detail:

Step 1: Determination of absolute global minima

In this step, the input variables like cutting velocity (V_C), feed rate (f), rake angle (α), grade (g) are considered along with output responses like cutting force (F_c), cutting temperature (T), flank wear (V_B) in the form of polynomial regression equations to initialize objective functions using Equation (6.4) to (6.6) such that f_1, f_2, f_3 are the function equation of polynomial regression equations, (6.1) to (6.3), developed from full factorial design. From these three functions, the global minima of individual output responses are identified.

Step 2: Optimization

Initialization of population:

Nest = (V_c, f, α, g) a set of input variables.

Number of nests = 50

Initially, 50 nests are selected where cuckoo is going to lay eggs based on a step function such that

$$Nest = Lb + (Ub - Lb) * rand.(size(Lb)) \tag{6.12}$$

where Lb, Ub are the lower bound and upper bound limits of input parameters V_c, f, α, g and rand(size(Lb)) refers to the random lower bound vector movement in the range of 0 to 1.

Identification of best nest:

The function for best nest identification involves the following:

Nest = get cuckoos (nest, best nest, Lb, Ub)

The above function is used to replace the other bird eggs with cuckoo's egg using the Levy flight random step function method.

Levy flight function is expressed as:

$$\sigma_L = \left[\frac{\Gamma(1+\beta_w)sin\left(\frac{\pi\beta_w}{2}\right)}{\Gamma\left(\frac{1+\beta_w}{2}\right)\beta_w 2^{\frac{\beta_w-1}{2}}}\right]^{\frac{1}{\beta_w}} \tag{6.13}$$

where Γ is the standard gamma function. Since each cuckoo lays an egg in individual nest, β_w is taken as 1.5.

For the movement of a step function, solution vectors are defined as *u* and *v*. such that vector *u* is said to dominate over vector *v*. When $u_i \leq v_i$, then these vectors are expressed as:

$$u = rand.(s) \times \sigma_L$$
$$v = rand.(s) \tag{6.14}$$

The random movement taken by cuckoo to lay eggs as the step is expressed as:

$$step = \left(\frac{u}{abs(v)}\right)^{\frac{1}{\beta_w}} \tag{6.15}$$

The flights for next random nest by the step size is expressed as:

$$stepsize = 0.1 \times step \times (nest - bestnest) \tag{6.16}$$

The step size of flights is controlled by the typical length scale *L* and is taken as *L*/10. Otherwise, Levy flights may become too aggressive and make new solutions jump outside the design domain. Therefore, the actual random fights are expressed as:

$$s = s + stepsize \times randn(size(s)) \tag{6.17}$$

Using Equation (6.12) to (6.16), cuckoos randomly flights to the selected 50 nests and replaces the eggs (input variables) in some of the nests using a step function. Once the eggs are laid in the nest, the best nest is found using fitness function for each nest using the expression:

$$fitness = \frac{F_c}{F_{c\,min}} + \frac{T}{T_{min}} + \frac{V_B}{V_{B\,min}} \tag{6.18}$$

If there is further improvement in the solution using fitness function, then best nest is expressed as best nest = (V_c^*, f^*, α^*, g^*).

The probability of discovering the alien eggs (worst solution set) by considering P_a = 0.25 is expressed as:

$$K = rand(s) > P_a \tag{6.19}$$

where *K* is a Boolean value such that if *K* = 0, it is undiscovered, else if *K* = 1, it is discovered.

It means that cuckoos eggs should look very similar to the host bird eggs, so that it is undiscovered. Then, the fitness function has to be compared with the best solutions (global optima). So, in order to improve the solution finding efficiency, a random flight in a biased manner with the same random step size needs to be followed as nest1 = rand (s), nest 2 = rand(s) within 50 predefined nests and step size is expressed as:

$$stepsize = rand(s) \times (nest1 - nest2) \tag{6.20}$$

Further, in order to discard the discovered alien egg nests, Equation (6.20) is used.

$$nest = nest + (stepsize \times K) \tag{6.21}$$

Further, these alien nests are modified with new nests. The current best nest is compared with the fitness of already available best nest until the current iteration gets the best nest among these using the CS optimization process. The eggs of the best nest are considered as the desired optimized value. By following the above steps until the solution converges, the algorithm will run for n iterations, and the best possible converged solutions are obtained. A flow chart has been presented to explain the overall methodology followed in Figure 6.10.

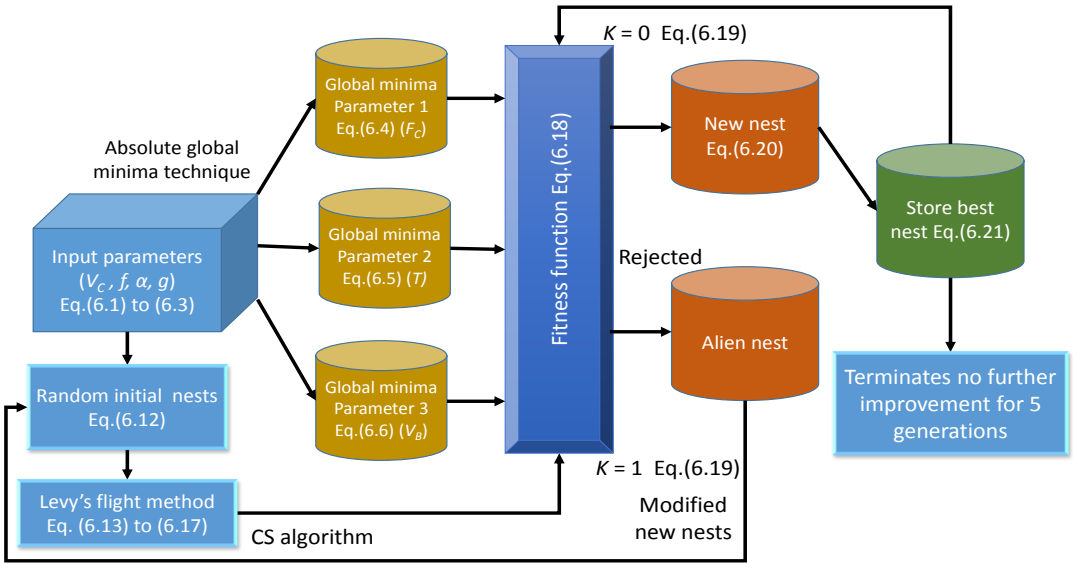

Figure 6.10 Flow chart for HCS algorithm

Table 6.12 shows the predicted global optima response values using the absolute global minima technique. Initially, 50 nests are assumed with Levy flight gamma function as 1and beta as 1.5. The length of step size is assumed as 0.1 and probability

to identify alien nest was taken as 0.25. By assuming these constant functions optimum responses are predicted.

Table 6.12 Predicted outputs and constants to run HCS optimization

Global optima values by step1			nest	B_w	r	L	P_a	*Final optima predicted*		
F_{min} N	T_{min} °C	V_{Bmin} μm						F_{min} N	T_{min} °C	V_{Bmin} μm
17.32	83.34	153	50	1.5	1	0.1	0.25	23.98	97	154

6.3.3 Comparison of performances

The present section compares the performance of all the three evolutionary algorithms elaborated in the previous section. The basic purpose of the comparison is to identify the best possible optimum cutting parameters for achieving the desired outputs. Figure 6.11 (a), (b) and (c) show the Pareto optimal plots drawn for NSAG-II, HABC and HCS algorithms, respectively. Note that a 2D plot is presented for NSGA II considering two objective functions. While the third objective function, i.e., flank wear, is considered as dummy function and is predicted based on optimum combination derived. While 3D plots are shown for HABC and HCS algorithms considering three objective functions. The predicted cutting force and the average temperature came out to be 23.64 N, 107.6°C and 190 μm, respectively for NSGA-II, as highlighted in a red circle in Figure 6.11 (a). Similarly, the respective values of optimum combination of cutting force, average temperature and flank wear predicted are 23.62 N, 101.3 °C and 196 μm for HABC algorithm and 25.55 N, 97 °C and 154 μm for HCS algorithm.

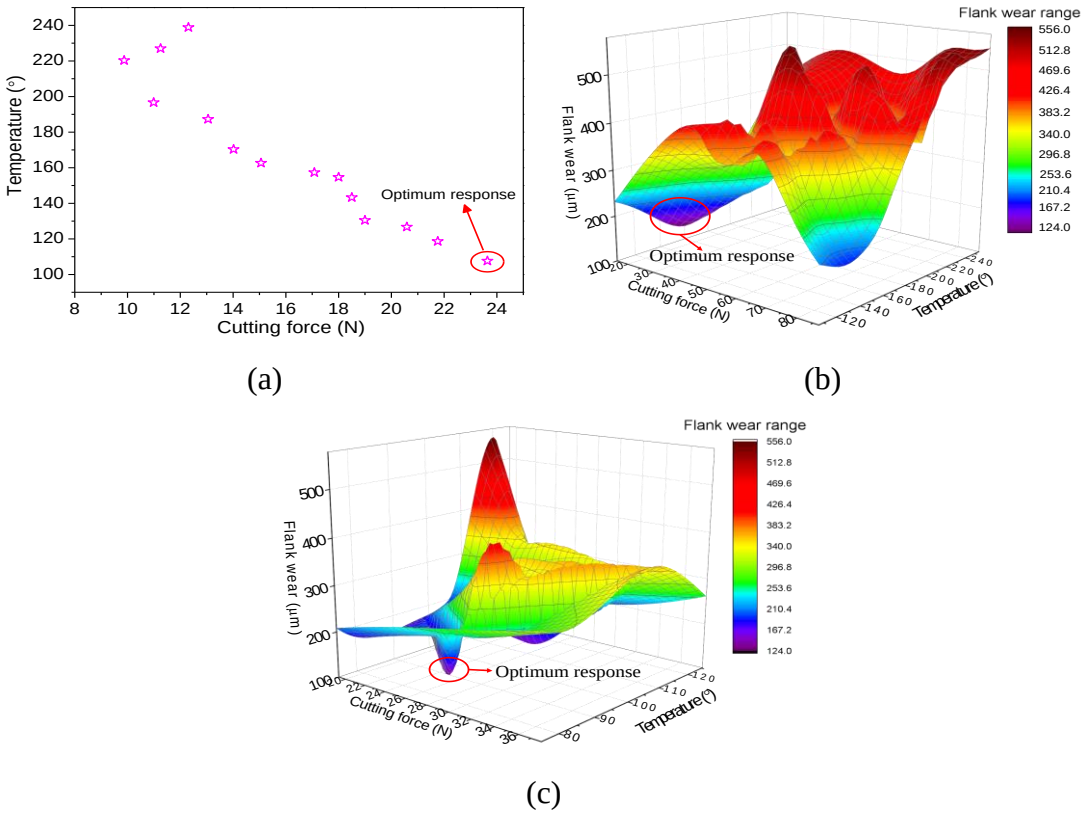

Figure 6.11 Comparison of pareto optimal front obtained for (a) NSGA-II, (b) HABC algorithm, (c) HCS algorithm

Figure 6.12 presents the comparison of optimum solution regions of the three algorithms with respect to iterations. In Figure 6.12 (a), crowding distance plot is drawn for average distance versus the number of generations. Crowding distance plot shows the spread of the solution in design space and the concerned diversity. It also specifics the number of generations required to converge the solution for given design space which came out to be around 240 for a set of Pareto optimal functions in the present case.

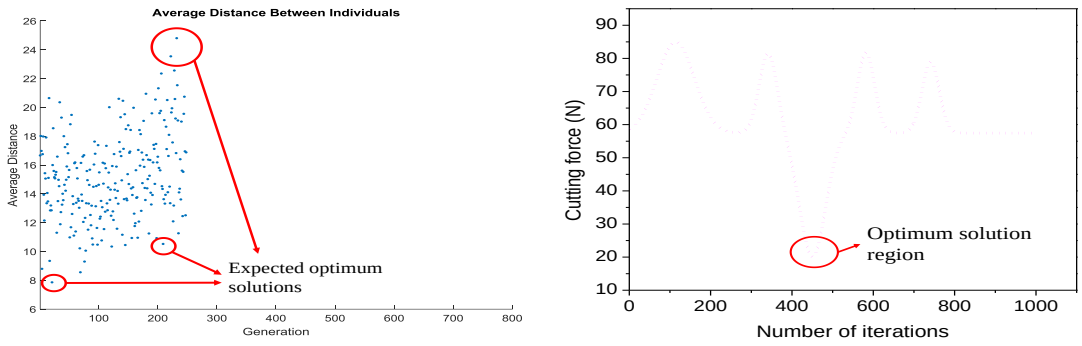

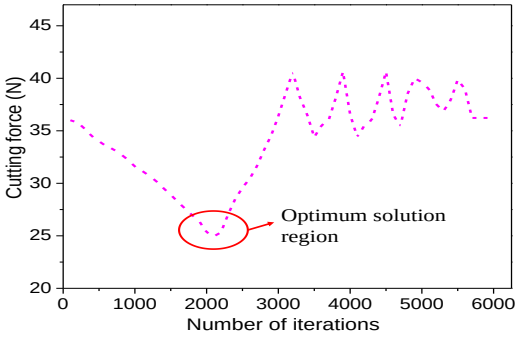

(c)

Figure 6.12 Comparison of optimum solution region with respect to iterations (a) NSGA-II, (b) HABC algorithm, (c) HCS algorithm

Similarly, in Figure 6.12 (b) and (c) cutting force versus number of iterations plots have been drawn for HABC and HCS, respectively. Since in both the algorithms cutting force is considered as an effective output response, plots are presented for cutting force only. In HABC algorithm, input variables are identified based on the tolerance limit range of cutting force initially and optimal solution of other output responses are computed. From Figure 6.12 (b), it is observed that there is no further improvement in solution beyond 990 iterations and as a result, the algorithm terminates. The optimal solution is found at 450^{th} iteration and consequently, optimal response at that particular solution set is considered as the final optimal parameters. While, in case of the HCS algorithm, only cutting force value is considered within the specified tolerance limit as fitness criteria and optimal solution is searched for the entire input variable range. In Figure 6.12 (c), it can be seen that the algorithm has run for 6000 iterations and beyond this, no further improvement is observed. Subsequently the algorithm gets terminated. The optimal solution from overall iterations is found at 2200^{th} iteration, and consequently, the optimal response and corresponding input variables at that particular solution are considered as the final optimal solution.

6.4 Confirmation and validation

In order to verify the obtained optimal results in the case multi-objective optimization problem of this process confirmation tests have been carried out. Table 6.13 lists the optimal input parameter combinations predicted by four different optimization methods.

Table 6.13 Computed optimal parameter settings

Model	V_c m/min	f mm/rev	d mm	α °	G
HCS	30	0.05	0.15	-5	95
HABC	56.4	0.05	0.15	-5	90
NSGA-2	58.82	0.061	0.15	-5	90
GRA	30	0.1	0.2	-8	97

Based on the predicted optimal parameter settings, confirmation experiments are performed and repeated three times for each case. Figure 6.13 (a), (b) and (c) show the comparison of values predicted by four multi objective optimization methods to that of experimentally measured ones for cutting forces, temperatures and flank wear, respectively. The optimum cutting parameters predicted by HCS algorithm could achieve the lowest values of all three output responses. Figure 6.13 (d) shows the experimentally measured values of two contradictory output responses, namely, MRR and surface roughness obtained while conducting the confirmatory tests considering optimum values of input parameters obtained from each of the four analyses. It is noted that the optimum cutting parameters predicted by HCS followed by HABC algorithm yield lower values of surface roughness as compared to NSGA II and GRA. It is understood that lower values of surface roughness are achieved at the cost of MRR. Since WHAs are mainly used in critical applications where precision is the prime concern, the cutting parameters predicted by HCS algorithm giving the best surface finish with a slight compromise with other outputs could be a fair choice.

As a whole, HCS seems to be the best choice for multi-objective optimization problem of the machining process. Such observation is very much clear from the values presented in Table 6.14. It is clearly observed that deviations in the predicted output responses from the measured ones are in the range of 15-51 % for NSGA-II, whereas, for HCS, it is well within 14 %.

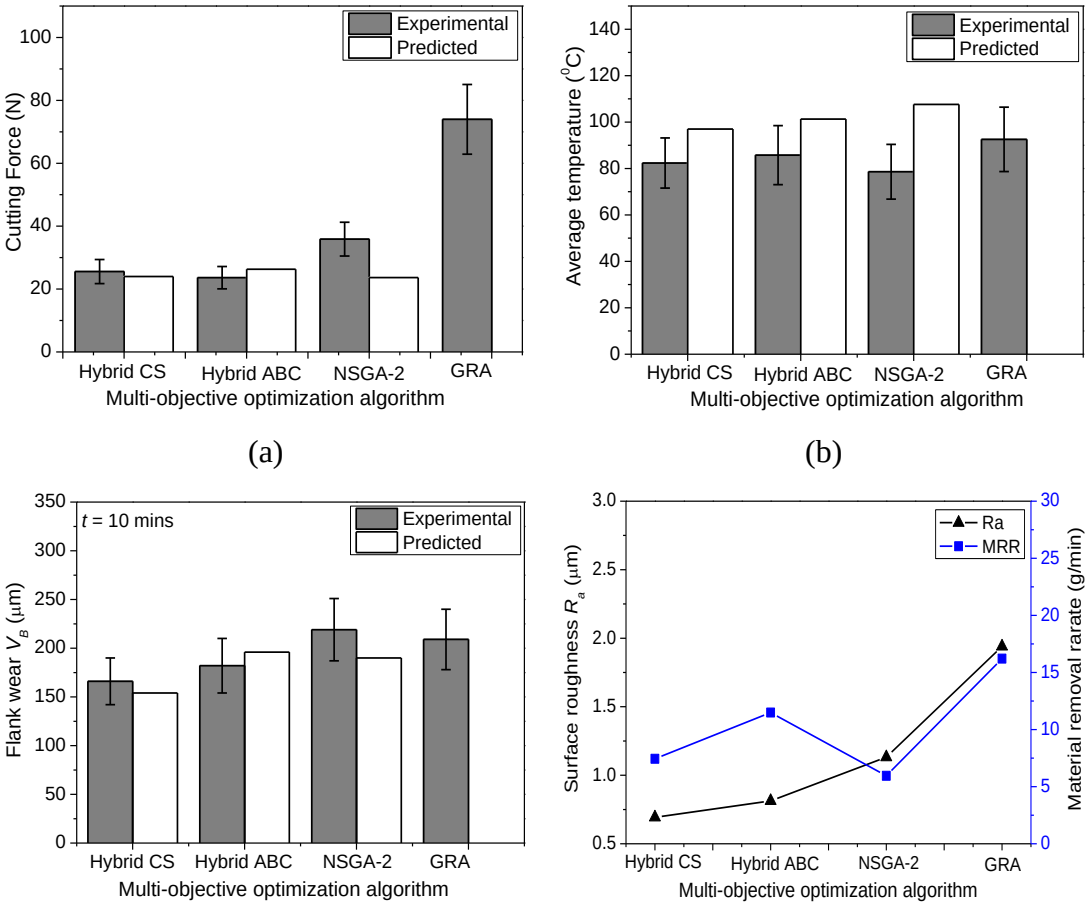

Figure 6.13 Comparison confirmation results of four optimization methods for (a) Cutting force, (b) Average temperature, (c) Flank wear, and (d) surface roughness and material removal rate.

Table 6.14 Comparison of the overall adequacy of multi objective optimization methods

Predicted Output	HCS		HABC		NSGA II	
	error %	STD	error %	STD	error %	STD
Cutting force	6.54	3.18	10.15	3.22	51.77	7.53
Cutting temp	14.74	11.46	15.35	12.96	26.95	15.69
Flank wear	4.79	20.49	7.14	23.90	15.26	25.47

The confirmation tests showed that HCS algorithm showed better performance as compared to the other three algorithms. This improvement may be due to the incorporation of the following strategies. Firstly, the effective use of absolute minima

technique and secondly, the improved exploration and exploitation search space by adopting controlled step size function in Levy's flight method. It is noted that few of the researchers in the recent past have also explored the application of hybrid approach by modifying the CS algorithm in complex engineering problems and found that the hybrid approach came out to be the best one as compared to other algorithms. Whereas, in NSGA II the major drawback is that, it could handle only two objective functions at a time for the optimization process, and the third objective function is considered as dummy function and in HABC use of constrained range of input parameters for predicted global optima by absolute minima technique has end up in deviation of global optimum solution.

Summary

Multi objective optimization problems are typically very difficult to solve. This chapter deals with formulation of four different approaches, namely, GRA based on L27 orthogonal array design and three evolutionary algorithms based on full factorial design. The data for GRA is derived from experimental tests based on L27 orthogonal array. While, FE simulations are performed for generating the full factorial data for the evolutionary algorithms. Out of the three algorithms, one is NSGA II which is one of the commonly used algorithms for multi objective optimization. The basic idea of considering NSGA II in the current analysis is to use it as a benchmark. While the other two algorithms are relatively new, namely, HCS and HABC. The experiments are performed with those optimum values of process parameters obtained from the analysis to confirm the results of the analysis. In comparison with other algorithms, HCS performs well for all the output responses. Such improvement may be due to the incorporation of controlled forward step size function in Levy's flight method, which greatly enhanced the exploration of search space and diversity of the population.

Chapter7 CONCLUSIONS AND FUTURE WORK

7.1 Summary

WHAs are one of the emerging alloys for a wide range of high density applications. The properties, such as high density, high strength, with no environmental effects, have made these alloys as one of the most preferred alloys for the manufacture of KEPs. Manufacturing of KEP requires machining as a secondary operation. But WHAs are generally considered as difficult to machine alloy. Machining of WHA requires optimum cutting parameters like feed, speed, depth of cut and tool geometry to achieve desired outputs and improve productivity. Hence, a detailed experimental analysis is carried out to understand the machining behavior of three different grades namely, 90, 95 and 97 WHA, in terms of cutting force, temperature, surface finish and tool wear.

In addition, an attempt was made to develop and analyze analytical tool wear rate models that can predict tool life accurately. The experimental findings showed that there exists a complex interrelationship between material properties, cutting conditions and machining outputs that are difficult to understand with limited number of machining tests. This demands to perform exhaustive experimental tests on trial and error basis for understanding the physics of chip formation mechanism. However, conducting these many tests on WHAs would be both expensive and time-consuming. Hence, to overcome this problem, a two-dimensional FE model is developed using commercially available software ABAQUS. Both the material and the damage models are appropriately selected, and the respective material constants are precisely determined.

Lastly, the developed FE model is used further to generate full factorial machining data required for performing multi-objective optimization. Three evolutionary algorithms, namely, NSGA II, HABC and HCS, are used to predict the optimal cutting parameters, in addition to GRA. The optimal parameters predicted by these algorithms are compared and the best parametric combination is presented that may be used while machining WHAs for improving the overall efficiency of the process and quality of KEPs at a relatively lower cost.

7.2 Conclusions

Following conclusions can be drawn from the current research work:

Material characterization and microstructural analysis

- Experimental findings showed that there is a significant effect of tungsten content on both the physical and mechanical properties of WHAs.
- Both the density and hardness increased as the tungsten content increased. Also, Young's modulus, yield strength and ultimate strength tend to increase with the increasing tungsten content
- A decrease in the values of specific heat and increase in thermal conductivity was observed with the increase in tungsten content.
- Microstructural analysis showed that there was a gradual increase in average grain size, decrease in matrix volume fraction and increase in contiguity with the increase in tungsten content, thus, leading to an increase in hardness with the increase in tungsten content.

Machinability studies of WHAs

- Chip morphology was found to be sensitive to tungsten content as well as cutting parameters, especially the tool geometry.
- For all three grades of WHA, MRR showed an increasing trend with the increase in cutting speed and feed for both the type of rake angles.
- 97 WHA exhibited higher values of cutting forces under all cutting conditions, typically for positive rake angle due to higher hardness because of the higher tungsten content.
- 90 WHA came up as a fair compromise among the three grades as far as machinability was concerned in terms of cutting force and surface finish.
- A complex interplay of different variables such as hardness, ductility/brittleness, and temperature rise during machining was observed.

Tool wear analysis and tool life predictions

- A strong relationship existed between flank wear and other machining response outputs, namely, force components, cutting temperature, chip morphology and surface roughness.
- The cutting tool with negative rake angle performed reasonably well as compared to that of a positive rake angle for machining 90 WHA under similar cutting conditions.
- SEM micrographs on the worn surface of the tool showed the occurrence of both abrasion and adhesion, the adhesion being the dominant one for both the tool geometries while machining 90 WHA.
- Out of four models, the newly proposed one, modified Zhao model, showed superior results with error percentage within 4-7%.

FE machining simulations

- A 2D plane strain FE model was developed by using simulation software ABAQUS/Explicit with computed JC material and damage models for machining three different grades of WHA.
- The JC material model constants derived from the experimental approach using high strain rate tests showed a much larger deviation in the predicted results, especially for cutting temperatures when compared with the experimental ones.
- The JC material model constants based on analytical approach could predict all the outputs with a mean error percentage well within 10% by using simple machining.
- The predicted temperature distributions could be correlated well with the experimentally measured surface roughness and tool wear under varied cutting conditions.

Multi-objective optimization

- Multi-objective optimization was performed using two different approaches, namely, L27 orthogonal array design using GRA and full factorial design using evolutionary algorithms, namely NSGA II, HABC and HCS to perform multi-objective optimization.

- The full factorial design showed improved R^2 value as compared to that of orthogonal array design.
- NSGA-II showed higher deviation in the predicted values as compared to that of HABC and HCS.
- As a whole, HCS came out to be the best choice for the multi-objective optimization model for the machining process.

  The fundamental objective of the proposed research work was to achieve higher productivity and better quality at a relatively lower cost while machining WHAs. Higher productivity in metal cutting generally implies higher MRRs. But higher MRR leads to faster tool wear. Again, the tool wear is directly related to the economics of machining and quality of the machined products. Thus, the prediction of tool wear rate is one of the prime factors during the optimization of the cutting process. Collectively, it can be concluded that the research outcomes achieved in the current work could address such concerns during the machining of WHAs. And hence, the proposed work would be helpful in both process parameter optimization and tool condition monitoring, thus, saving much of the production downtime.

7.3 Major contributions of this thesis

Based on the above conclusions, the proposed work could offer the following deliverables:

- Detailed machinability analysis of WHAs that show variations in different machining outputs with respect to the tungsten content;
- A tool wear rate model that predicts tool life accurately both for positive and negative rake angle;
- An FE model that predicts not only the cutting forces and chip morphology but also some of the difficult to measure variables like temperature, stress, strain, etc. under varied cutting conditions;
- An analytical model that determines JC material model constants at high strain rates using machining tests;

- A multi-objective optimization model that involves a unique approach by combining the FE model with evolutionary algorithms for the determination of optimal cutting parameters with minimum experimental tests.

Overall, it can be stated that a multi-objective optimization model based on combined FE–soft computing approach is developed that predicts optimum cutting parameters with respect to varied WHA grades with minimum possible experimental tests. For finish turning of KE penetrators (for diameters in the range of 10-15 mm), following cutting parameter range are found to be optimum: cutting velocity=30–50 m/min, feed rate=0.05 mm/rev, d= 0.15 mm and rake angle = -5° to achieve surface roughness in the range of 0.5–0.7 microns.

7.4 Limitations of the work

- In the present study, the machining tests were performed under dry cutting conditions.
- The newly proposed modified Zhao tool wear rate model can be extended for varied lubrication conditions.
- A more realistic 3D model can replace the developed 2D model wherein the effect of approach angle, tool nose radius and chip breakers can be analyzed.

7.5 Future scope

Despite the results achieved, there remains scope for further improvement. The following ideas can further broaden the scope of the current work:

- Taking into consideration a 3D FE model and incorporation of the novel techniques for lubrication and cooling would provide a more generalized approach.
- Since surface integrity has a direct impact on the fatigue life and tribological properties of machined parts, the machinability studies can further be extended to examine the machining-induced residual stresses during turning operation.
- The JC material model constants so determined under high strain rate conditions using machining tests can further be used in FE simulations of ballistic impact tests to understand the penetration mechanism of WHA armours.

REFERENCES

El-Hossainy, T M, A A El-Zoghby, M A Badr , K Y Maalawi, and M F Nasr. 2010. "Cutting Parameter Optimization when Machining Different Materials." *Materials and Manufacturing Processes* 25 (10): 1101-1114. doi:DOI: 10.1080/10426914.2010.480998 .

Kiran, U. Ravi, S. Venkat, B. Rishikesh, V.K. Iyer, M. Sankaranarayana, and T.K. Nandy. 2013. "Effect of tungsten content on microstructure and mechanical properties of swaged tungsten heavy alloys." *Materials Science and Engineering: A* 582: 389-396. doi:https://doi.org/10.1016/j.msea.2013.06.041.

Narayanan, N.Sathiya, N. Baskar, and M. Ganesan. 2018. "Multi Objective Optimization of machining parameters for Hard Turning OHNS/AISI H13 material, Using Genetic Algorithm." *Materialstoday Proceedings* 5 (2, Part2): 6897-6905. doi:https://doi.org/10.1016/j.matpr.2017.11.351.

Sagar, Chithajalu Kiran, Amrita Priyadarshini , Amit Kumar Gupta, and Sidharth Kumar Shukla. 2018. "Determination of Johnson Cook Material Model Constants and Their Influence on Machining Simulations of Tungsten Heavy Alloy." *ASME International Mechanical Engineering Congress and Exposition.* American Society of Mechanical Engineers. V001T03A010. doi:https://doi.org/10.1115/IMECE2018-88270.

Abaqus, User's manual Version 6.14-1. 2014. "Dassault Systems simulia corporation." Dassault Systemes Simulia, Inc. . http://wufengyun.com/v6.14/books/usb/default.htm?startat=pt05ch22s02abm03.html.

Addona, Doriana M.D., and Roberto Teti. 2013. "Genetic algorithm-based optimization of cutting parameters." *Procedia CIRP 7.* 323-328.

Akdemir, Ahmet, Şakir Yazman , Hacı Saglam, and Mesut Uyaner. 2012. "The Effects of Cutting Speed and Depth of Cut on Machinability Characteristics of Austempered Ductile Iron." *Journal of Manufacturing Science and Engineering* 134 (2). doi:doi:10.1115/1.4005805.

Amir Malakizadi, Stefan Cedergren, Ibrahim Sadik, Lars Nyborg. 2016. "Inverse identification of flow stress in metal cutting process using Response Surface Methodology." *Simulation Modelling Practice and Theory* 60: 40–53. doi:10.1016/j.simpat.2015.09.009.

Arrazola, P.J., T. Ozel, D. Umbrello, M. Davies, and I.S. Jawahir. 2013. "Recent advances in modelling of metal machining processes." *CIRP Annals* 62 (2): 695-718. doi:https://doi.org/10.1016/j.cirp.2013.05.006.

Arsecularatne, J.A, L.C Zhang, and C Montross. 2006. "Wear and tool life of tungsten carbide, PCBN and PCD cutting tools." *International Journal of Machine Tools & Manufacture* 46 (5): 482-491. https://doi.org/10.1016/j.ijmachtools.2005.07.015.

Asilturk, I, and H Akkus. 2011. "Determining the effect of cutting parameters on surface roughness in hard turning using the Taguchi method." *Measurement* 44 (9): 1697-1704. doi:https://doi.org/10.1016/j.measurement.2011.07.003.

Attanasio, A., E Ceretti, S Rizzuti, D Umberllo, and F Micari. 2008. "3D finite element analysis of tool wear in machining." *CIRP Annals* (Elsevier) 57 (1): 61-64. https://doi.org/10.1016/j.cirp.2008.03.123.

Aviral Shrota*, Martin Bäker. 2012. "A study of non-uniqueness during the inverse identification of material parameters." *Procedia CIRP 1* 72 – 77.

Aviral, Shrot, and Baker Martin. 2011. "How To Identify Johnson-Cook Parameters From Machining Simulations." *AIP Conference Proceedings.* 29-34. doi:10.1063/1.3589487.

Bartarya, G, and S.K Choudhury. 2012. "State of the art in hard turning." *International Journal of Machine Tools and Manufacture* 53 (1): 1-14. doi:https://doi.org/10.1016/j.ijmachtools.2011.08.019.

Becker, Steven , Hendrik Hotz , Benjamin Kirsch , Jan C. Aurich, Erik V. Harbou , and Ralf Muller. 2018. "A Finite Element Approach to Calculate Temperatures Arising During Cryogenic Turning of Metastable Austenitic Steel AISI 347." *Journal of Manufacturing Science and Engineering* (ASME) 140 (10): 101016(7 pages). doi:https://doi.org/10.1115/1.4040778.

Borvik, T, O.S Hopperstad, and T Berstad. 2003. "On the influence of stress triaxiality and strain rate on the behaviour of a structural steel. Part II. Numerical study." *European Journal of Mechanics - A/Solids* 22 (1): 15-32. doi:https://doi.org/10.1016/S0997-7538(02)00005-0.

Bosetti , Paolo , Carlos Maximiliano Giorgio Bort, and Stefania Bruschi. 2013. "Identification of Johnson–Cook and Tresca's Parameters for Numerical Modeling of AISI-304 Machining Processes." *Journal of Manufacturing Science and Engineering* (ASME) 135 (5): 051021(8 pages). doi:https://doi.org/10.1115/1.4025340.

Buruaga, M. S.D, D. Soler, P.X. Aristimuno, J.A. Esnaola, and P.J. Arrazola. 2018. "Determining tool/chip temperatures from thermography measurements in metal cutting." *Applied Thermal Engineering* 145: 305–314. doi:10.1016/j.applthermaleng.2018.09.051.

Campagne-Lambert, L. , Loic Daridon, Omar Oussouaddi, Said Ahzi, and X. Sun. 2008. "Simulation of the Taylor impact test and analysis of damage evolution using a nucleation and growth based approach." *Modeling, Measurement and Control* 77 (3-4): 19-35. https://hal.archives-ouvertes.fr/hal-00591015.

Caydas, Ulas, and Ahmet Hascalik. 2008. "Use of the grey relational analysis to determine optimum laser cutting parameters with multi-performance characteristics." *Optics & Laser Technology* 40 (7): 987-994. doi:https://doi.org/10.1016/j.optlastec.2008.01.004.

Chakraborty , Sukanta , Amit Shaw, and Biswanath Banerjee. 2015. "An axisymmetric model for Taylor impact test and estimation of metal plasticity." *Proceedings of the Royal Society A.* https://doi.org/10.1098/rspa.2014.0556.

Chen, G, C Ren, L Lu, Z Ke, X Qin, and X Ge. 2018. "Determination of ductile damage behaviors of high strain rate compression deformation for Ti-6Al-4V alloy using experimental-numerical combined approach." *Engineering Fracture Mechanics* 200: 499-520. doi:https://doi.org/10.1016/j.engfracmech.2018.08.020.

Chen, G, J Li, Y He, and C Ren. 2014. "A new approach to the determination of plastic flow stress and failure initiation strain for aluminum alloys cutting process." *Computational Materials Science* 568-578. doi:https://doi.org/10.1016/j.commatsci.2014.08.029.

Chen, G, Z Ke, C Ren, and J Li. 2016. "Constitutive modeling for Ti-6Al-4V alloy machining based on the SHPB tests and simulation." *Chinese Journal of Mechanical Engineering* 29: 962–970. doi:https://doi.org/10.3901/CJME.2016.0406.046.

Chen, Guang, Chengzu Ren, Lianpeng Lu, Zhihong Ke, Xuda Qin, and Xiang Ge. 2018. "Determination of ductile damage behaviors of high strain rate compression deformation for Ti-6Al-4V alloy using experimental numerical combined approach." *Engineering Fracture Mechanics* 200: 499-520. doi:https://doi.org/10.1016/j.engfracmech.2018.08.020.

Chen, Guang, Chengzu Ren, Wei Yu, Xiaoyong Yang, and Lifeng Zhang. 2012. "Application of genetic algorithms for optimizing the Johnson–Cook constitutive model parameters when simulating the titanium alloy Ti-6Al-4V machining process." *Proceedings of the Institution of Mechanical Engineers, Part-B: Journal of Engineering Manufacture* 226 (8): 1-11.

Chen, Ling, Jan- Eric Stahl, Wu Zhao, and Jinming Zhou. 2018. "Assessment on abrasiveness of high chromium cast iron material on the wear performance of PCBN cutting tools in dry machining." *Journal of Materials Processing Technology* (Elsevier) 255: 110-120. https://doi.org/10.1016/j.jmatprotec.2017.11.054.

Chen, Y, and N Wang. 2019. "Cuckoo search algorithm with explosion operator for modeling proton exchange membrane fuel cells." *International Journal of Hydrogen Energy* 44 (5): 3075-3087. doi:https://doi.org/10.1016/j.ijhydene.2018.11.140.

Chen, Z, R Lin Peng, J Zhou, R M'Saoubi, D Gustafsson, and J Moverare . 2019. "Effect of machining parameters on cutting force and surface integrity when high-speed turning AD 730™ with PCBN tools." *The International Journal of Advanced Manufacturing Technology* 100: 2601–2615. doi:https://doi.org/10.1007/s00170-018-2792-1.

Cheng, Z, J Wang, M Zhang, H Song, T Chang, Y Bi, and K Sun. 2019. "Improvement and Application of AdaptiveHybrid Cuckoo Search Algorithm." *IEEE Access* 7: 145489 - 145515. doi: 10.1109/ACCESS.2019.2944981.

Ciro, G.C, F Dugardin, F Yalaoui, and R Kelly. 2016. "A NSGA-II and NSGA-III comparison for solving an open shop scheduling problem with resource constraints." *8th IFAC Conference on Manufacturing Modelling, Management and Control MIM 2016.* Troyes, France: IFAC-PapersOnLine. 1272-1277. doi:https://doi.org/10.1016/j.ifacol.2016.07.690.

Coates, R.S., and K.T. Ramesh. 1991. "The rate-dependent deformation of a tungsten heavy alloy." *Materials Science and Engineering: A* 145 (2): 159-166. doi:https://doi.org/10.1016/0921-5093(91)90245-I.

Coelho, Reginaldo T., Eu-Gene Ng, and M.A. Elbestawi. 2007. "Tool wear when turning hardened AISI 4340 with coated PCBN tools using finishing cutting conditions." *International Journal of Machine Tools and Manufacture* 47 (2): 263-272. doi:https://doi.org/10.1016/j.ijmachtools.2006.03.020.

Cotterell, M., E. Ares, J. Yanes, F. Lopez, P. Hernandez, and G. Peláez. 2013. "Temperature and strain measurement during chip formation in orthogonal cutting conditions applied to Ti-6Al-4V." *Procedia Engineering* 63: 922-930. doi:https://doi.org/10.1016/j.proeng.2013.08.216.

Crowe, C.R, D.F Hasson, and J.A Joyce. 1980. "Effect of microstructure on mechanical properties of a depleted uranium-2wt.%molybdenum alloy." *Journal of the Less Common Metals* 72 (2): 219-224. doi:https://doi.org/10.1016/0022-5088(80)90140-X.

Dali, M.N.A.M., J.A. Ghani, and C.H. CheHaron. 2017. "Comparison between Dynamic and Non-Dynamic Cutting Tool Option in FEM Simulation for Producing Dimple Structure." *16th CIRP Conference on Modelling of Machining Operations.* Burgundy, France: Procedia CIRP. 613-616. doi:https://doi.org/10.1016/j.procir.2017.03.335.

Dargusch, Matthew S, Shoujin Sun, Ji Won Kim, Tong Li, and Patrick Trimby. 2018. "Effect of tool wear evolution on chip formation during dry machining of Ti-6Al-4V alloy." *International Journal of Machine Tools and Manufacture* (Elsesvier) 126: 13-17. https://doi.org/10.1016/j.ijmachtools.2017.12.003.

Das , Jiten, Appa G Rao , S.K. Pabi, , M. Sankaranarayana, and T.K. Nandy. 2014. "Thermo-mechanical processing,microstructure and tensile properties of a tungsten heavy alloy." *Materials Science & Engineering A* 613: 48-59. doi:doi.org/10.1016/j.msea.2014.06.072.

Das, Jiten, A. Chakraborty, T.P. Bagchi, and Bijoy Sarma. 2008. "Improvement of machinability of tungsten by copper infiltration technique." *International Journal of Refractory Metals and Hard Materials* 26 (6): 530-539. doi:https://doi.org/10.1016/j.ijrmhm.2007.12.005.

Das, Jiten, G. Appa Rao, and S.K. Pabi. 2010. "Microstructure and mechanical properties of tungsten heavy alloys." *Materials Science and Engineering: A* 527 (29-30): 7841-7847. doi:https://doi.org/10.1016/j.msea.2010.08.071.

Das, Jiten, G. Appa Rao, S.K. Pabi, M. Sankaranarayana, and Bijoy Sarma. 2011. "Deformation behaviour of a newer tungsten heavy alloy." *Materials Science and Engineering A* 528 (19-20): 6235-6247. doi:https://doi.org/10.1016/j.msea.2011.04.067.

Das, Jiten, R Sarkar, G. Appa Rao, M. Sankaranarayana, T.K. Nandy, and S.K. Pabi. 2012. "Flow behaviour of a heat treated tungsten heavy alloy." *Materials Science and Engineering A* 553: 119-127. doi:https://doi.org/10.1016/j.msea.2012.05.101.

Das, M.K, K Kumar, T.K Barman, and P Sahoo. 2014. "Application of Artificial Bee Colony Algorithm for Optimization of MRR and Surface Roughness in EDM of EN31 Tool Steel." *3rd International Conference on Materials Processing and Characterisation.* Hyderabad, India: Procedia Materials Science. 741-751. doi:https://doi.org/10.1016/j.mspro.2014.07.090.

Deb, K. , A. Pratap , S. Agarwal , and T. Meyarivan. 2002. "A fast and elitist multiobjective genetic algorithm: NSGA-II." *IEEE Transactions on Evolutionary Computation* 6 (2): 182-197. doi:10.1109/4235.996017.

Devotta, A, T Beno, R Siriki, R Lof, and M Eynian. 2017. "Finite Element Modeling and Validation of Chip Segmentation in Machining of AISI 1045 Steel." *16th CIRP Conference on Modelling of Machining Operations.* Burgundy, France: Procedia CIRP. 499-504. doi:https://doi.org/10.1016/j.procir.2017.03.259.

Diaz-Alvarez, J., J.L. Cantero, H. Miguelez, and X. Soldani. 2014. "Numerical analysis of thermomechanical phenomena influencing tool wear in finishing turning of Inconel 718." *International Journal of Mechanical Sciences* 82: 161-169. doi:https://doi.org/10.1016/j.ijmecsci.2014.03.010.

Diaz-Alvarez, Jose, Alberto Tapetado, Carmen Vazquez, and Henar Miguelez. 2017. "Temperature Measurement and Numerical Prediction in Machining Inconel 718." *sensors* 17 (7): 1531. doi:https://doi.org/10.3390/s17071531.

Dikshit, S.N. 1998. "Ballistic Behaviour of Thick Steel Armour Plate under Oblique Impact: Experimental Investigation." *Defence Science Journal* 48 (3): 271-276. doi:https://doi.org/10.14429/dsj.48.3947 .

Ding, J, Q Wang, Q Zhang, Q Ye, and Y Ma. 2019. "A Hybrid Particle Swarm Optimization-Cuckoo Search Algorithm and Its Engineering Applications." *Mathematical Problems in Engineering* 2019: 1-12. doi:https://doi.org/10.1155/2019/5213759.

Filho, J. M. Crichigno. 2017. "Applying extended Oxley's machining theory and particle swarm optimization to model machining forces." *The International Journal of Advanced Manufacturing Technology* (Springer) 89 (1-4): 1127–1136.

Filho, Sergio Luiz Moni Ribeiro, Robson Bruno Dutra Pereira, Carlos Henrique Lauro, and Lincoln Cardoso Brandao. 2019. "Investigation and modelling of the cutting forces in turning process of the Ti-6Al-4V and Ti-6Al-7Nb titanium alloys."

The International Journal of Advanced Manufacturing Technology 101: pages2191–2203. doi:https://doi.org/10.1007/s00170-018-3110-7.

Frueh, Patrick, Andreas Heine, Karl Ernst Weber, and Matthias Wickert. 2016. "Effective depth-of-penetration range due to hardness variation for different lots of nominally identical target material." *Defence Technology* 12 (2): 171-176. https://doi.org/10.1016/j.dt.2015.10.002.

Gaitonde, V.N., S.R. Karnik, M. Faustino, and J. Paulo Davim. 2010. "Machinability analysis in turning tungsten–copper composite for application in EDM electrodes." *International Journal of Refractory Metals and Hard Materials* 28 (2): 221-227. doi:https://doi.org/10.1016/j.ijrmhm.2009.10.002.

Ghetiya, N D , K M Patel, and A J Kavar. 2016. "Multi-objective Optimization of FSW Process Parameters of Aluminium Alloy Using Taguchi-Based Grey Relational Analysis." *Transactions of the Indian Institute of Metals* (Springer Link) 69 (4): 917–923. doi:DOI 10.1007/s12666-015-0581-1.

Gmili, N.EI, M Mjahed, A.EI Kari, and H. Ayad. 2019. "Particle Swarm Optimization and Cuckoo Search-Based Approaches for Quadrotor Control and Trajectory Tracking." *Applied Sciences* 9 (8): 1719. doi:https://doi.org/10.3390/app9081719.

Gong, Xing, Jinglian Fan, and Fei Ding. 2015. "Tensile mechanical properties and fracture behavior of tungsten heavy alloys at 25–1100 °C." *Materials Science and Engineering: A* 646: 315-321. doi:https://doi.org/10.1016/j.msea.2015.08.079.

Goyal, Ajay , Suresh Dhiman, Shailendra Kumar, and Rajesh Sharma. 2014. "A Study of Experimental Temperature Measuring Techniques used in Metal Cutting." *Jordan Journal of Mechanical and Industrial Engineering* 8 (2): 82 - 93.

Goyal, Ajay, Suresh Dhiman, Shailendra Kumar, and Rajesh Sharma. 2014. "A Study of Experimental Temperature Measuring Techniques used in Metal Cutting." *Jordan Journal of Mechanical and Industrial Engineering* 8 (2): 82-93. http://jjmie.hu.edu.jo/vol%208-2/JJMIE-131-13-01.pdf.

Gupta, Amit Kumar, Hansoge Nitin Krishnamurthy, Yashjeet Singh, and Kaushik Manga Prasad. 2013. "Development of constitutive models for dynamic strain aging regime in Austenitic stainless steel 304." *Materials and design* 45: 616-627.

Hascalık, Ahmet, and Ulas Caydas. 2007. "Optimization of turning parameters for surface roughness and tool life based on the Taguchi method." *The International Journal of Advanced Manufacturing Technology* 38: 896–903. doi:https://doi.org/10.1007/s00170-007-1147-0.

Heigel, J.C, E. Whitenton, B. Lane, M.A. Donmez, and V. Madhavan. 2017. "Infrared measurement of the temperature at the tool–chip interfacewhile machining Ti–6Al–4V." *Journal of Materials Processing Technology* 243: 123-130. doi:https://doi.org/10.1016/j.jmatprotec.2016.11.026.

Hibbitt,, and Karlsson & Sorensen. 2007. *ABAQUS Analysis User's manual, Version 6.7–4.* http://130.149.89.49:2080/v6.7/books/usb/default.htm.

Hoier, Philipp, Amir Malakizadi, Sven Friebe, Uta Klement, and Peter Krajnik. 2019. "Microstructural variations in 316L austenitic stainless steel and their influence on tool wear in machining." *Wear* 428-429: 315-327. https://doi.org/10.1016/j.wear.2019.02.024.

Hong, S.H, H.J Ryu, and W.H Baek. 2002. "Matrix pools in a partially mechanically alloyed tungsten heavy alloy for localized shear deformation." *Materials Science and Engineering: A* 333 (1-2): 187-192. doi:https://doi.org/10.1016/S0921-5093(01)01839-1.

Hossain, M.S.J, and T.W Liao. 2017. "Cutting Parameter Optimization for End Milling OpeRation Using Advanced Metaheuristic Algorithms." *International Journal of Advanced Robotics and Automation* 2 (2): 1-12. doi:10.15226/2473-3032/2/2/00125.

Iqbal, S. A, P. T Mativenga, and M. A Sheikh. 2009. "A comparative study of the tool–chip contact length in turning of two engineering alloys for a wide range of cutting speeds." *The International Journal of Advanced Manufacturing Technology* (Springer) 42:30. https://doi.org/10.1007/s00170-008-1582-6.

Islam, S H, Q U Xuanhur, S J Askan, M Tufail, and HE Xinbo. 2007. "Effect of microstructural parameters on the properties of W-Ni-Fe alloys." *Rare Metals* 26 (3): 200. doi:DOI: 10.1016/S1001-0521(07)60201-0.

Jahan, Muhammad Pervej, Jianfeng Ma, Craig Hanson, and Greg K Arbuckle. 2019. "Tool wear and resulting surface finish during micro slot milling of polycarbonates using uncoated and coated carbide tools." *Proceedings of the Institution of Mechanical Engineers, Part B: Journal of Engineering Manufacture* (SAGE Publications) accepted: 1-14. doi:10.1177/0954405419862479.

Jaspers, S.P.F.C, and J.H Dautzenberg. 2002. "Material behaviour in conditions similar to metal cutting: flow stress in the primary shear zone." *Journal of Materials Processing Technology* 122 (2-3): 322-330. doi:https://doi.org/10.1016/S0924-0136(01)01228-6.

Jiang, Langlang, and Dazhong Wang. 2019. "Finite-element-analysis of the effect of different wiper tool edge geometries during the hard turning of AISI 4340 steel." *Simulation Modelling Practice and Theory* 94: 250-263. doi:https://doi.org/10.1016/j.simpat.2019.03.006.

Jinxu, Liu, Li Shukui, Fan Ailing, and Sun Hongchan. 2008. "Effect of fibrous orientation on dynamic mechanical properties and susceptibility to adiabatic shear band of tungsten heavy alloy fabricated through hot-hydrostatic extrusion." *Materials Science and Engineering: A* 487 (1-2): 235-242. doi:https://doi.org/10.1016/j.msea.2007.10.012.

Johnson , G.R., and W.H. Cook. 1983. "A constitutive model and data for materials subjected to large strains, high strain rates, and high temperatures." *International Ballistics committee*. The Hague, Netherlands: Proceedings of the Seventh International Symposium on Ballistics. 541-547.

Johnson, G.R, and W.H Cook. 1985. "Fracture characteristics of three metals subjected to various strains, strain rates, temperatures and pressures." *Engineering Fracture Mechanics* 21 (1): 31-48. doi:https://doi.org/10.1016/0013-7944(85)90052-9.

Jomaa, W, O Mechri, J Levesque, V Songmene, P Bocher, and A Gakwaya. 2017. "Finite element simulation and analysis of serrated chip formation during high–speed machining of AA7075–T651 alloy." *Journal of Manufacturing Processes* 26: 446-458. doi:https://doi.org/10.1016/j.jmapro.2017.02.015.

Kagnaya, T, T Boher, L Lambert, M Lazard, and T Cutard. 2014. "Microstructural analysis of wear micromechanisms of WC–6Co cutting tools during high speed dry machining." *International Journal of Refractory Metals and Hard Materials* (Elsevier) 42: 151-162. https://doi.org/10.1016/j.ijrmhm.2013.08.017.

Karaboga, D., and B. Basturk. 2008. "On the performance of artificial bee colony (ABC) algorithm." *Applied Soft Computing* 8 (1): 687-697. doi:https://doi.org/10.1016/j.asoc.2007.05.007.

Kaveh, A., and N. Farhoudi. 2013. "A new optimization method: Dolphin echolocation." *Advances in Engineering Software* 59: 53-70. doi:https://doi.org/10.1016/j.advengsoft.2013.03.004.

Kenji, Higuchi, and Takai Hideo. 1961. "Stress-Strain Diagram, Young's Modulus and Poisson's Ratio of Textile Fibers." *Journal of the Textile Machinery Society of Japan* (J-Stage) 7 (1): 4-12. doi:https://doi.org/10.4188/jte1955.7.4.

Kennedy, J, and R Eberhart . 1995. "Particle swarm optimization." *Proceedings of ICNN'95 - International Conference on Neural Networks*. IEEE Xplore. 1942-1948. doi: 10.1109/ICNN.1995.488968.

Khan, A.S, and H Liu. 2012. "Strain rate and temperature dependent fracture criteria for isotropic and anisotropic metals." *International Journal of Plasticity* 37: 1-15. doi:https://doi.org/10.1016/j.ijplas.2012.01.012.

Khare, Sanchit Kumar, Sanjay Agarwal, and Shivam Srivastava. 2018. "Analysis of Surface Roughness during Turning Operation by Taguchi Method." *International Conference on Composite Materials: Manufacturing, Experimental Techniques, Modeling and Simulation.* Jalandhar-Delhi: Materialstoday: PROCEEDINGS. 28089-28097. doi:https://doi.org/10.1016/j.matpr.2018.10.050.

Kiran, U. Ravi, Jalaj Kumar, Vikas Kumar, M. Sankaranarayana, G.V.S. Nageswara Rao, and T.K. Nandy. 2016. "Effect of cyclic heat treatment and swaging on

mechanical properties of the tungsten heavy alloys." *Materials Science and Engineering: A* 656 (22): 256-265. doi:https://doi.org/10.1016/j.msea.2016.01.024.

Kuczmaszewski, Jozef, and Ireneusz Zagorski. 2013. "Methodological Problems of Temperature Measurement in The Cutting Area During Milling Magnesium Alloys." *Management and Production Engineering Review* 4 (3): 26–33. doi:10.2478/mper-2013-0025.

Kuram, Emel. 2016. "The effect of monolayer TiCN-, AlTiN-, TiAlN-and two layers TiCN + TiN- and AlTiN + TiN-coated cutting tools on tool wear, cutting force, surface roughness and chip morphology during high-speed milling of Ti6Al4V titanium alloy." *Proceedings of the Institution of Mechanical Engineers, Part B: Journal of Engineering Manufacture* (Sage journals) 232 (7): 1273-1286 . doi:https://doi.org/10.1177/0954405416666905.

Kus, Abdil, Yahya Isik, M. Cemal Cakir, Salih Coşkun, and Kadir Ozdemir. 2015. "Thermocouple and Infrared Sensor-Based Measurement of Temperature Distribution in Metal Cutting." *sensors* 15: 1274-1291. doi:https://doi.org/10.3390/s150101274.

Lalwani, D.I., N.K. Mehta, and P.K. Jain. 2009. "Extension of Oxley's predictive machining theory for Johnson and Cook flow stress model." *Journal of Materials Processing Technology* (Elsevier) 209 (12-13): 5305-5312. doi:doi.org/10.1016/j.jmatprotec.2009.03.020.

Lauro, C.H, L.C Brandao, and S.L.M.R Filho. 2013. "Monitoring the temperature of the milling process using infrared camera." *Scientific Research and Essays* 8 (23): 1112-1120. doi:10.5897/SRE12.579 .

Lee, W, G Xiea, and C Lin. 1998. "The strain rate and temperature dependence of the dynamic impact response of tungsten composite." *Materials Science and Engineering: A* 257 (2): 256-267. doi:https://doi.org/10.1016/S0921-5093(98)00852-1.

Li, X, K Hu, S Qu, L Li, and C Yang. 2014. "93W–5.6Ni–1.4Fe heavy alloys with enhanced performance prepared by cyclic spark plasma sintering." *Materials Science and Engineering: A* 599: 233-241. doi:https://doi.org/10.1016/j.msea.2014.01.089.

Li, Yingguang, Changqing Liu, Jiaqi Hua, James Gao, and Paul Maropoulos. 2019. "A novel method for accurately monitoring and predicting tool wear under varying cutting conditions based on meta-learning." *CIRP Annals* 68 (1): 487-490. doi:https://doi.org/10.1016/j.cirp.2019.03.010.

Liang , G. X, and E. D Wang. 1996. "Influence of hot extrusion on microstructure and mechanical properties of tungsten based heavy alloy." *Materials Science and Technology* (Taylor & Francis) 12 (12): 1032-1034. doi:https://doi.org/10.1080/02670836.1996.11665718.

Lim, S.C, Y.B Liu, S.H Lee, and K.H.W Seah. 1993. "Mapping the wear of some cutting-tool materials." *Wear* (Elsevier) 162-164 (Part B): 971-974. doi:https://doi.org/10.1016/0043-1648(93)90105-U.

Liu, C, Y He, Y Wang, Y Li, S Wang, L Wang, and Y Wang. 2020. "Effects of process parameters on cutting temperature in dry machining of ball screw." *ISA Transactions* 101: 493-502. doi:https://doi.org/10.1016/j.isatra.2020.01.031.

Liu, K., and X.P. Li. 2001. "Ductile cutting of tungsten carbide." *Journal of Materials Processing Technology* 113 (1-3): 348-354. doi:https://doi.org/10.1016/S0924-0136(01)00582-9.

Lorenzo, P, M Miralda, S Iyengar, S Melin, and Etam Noah. 2013. "Fatigue properties and characterization of tungsten heavy alloys IT180 & D176." *International Journal of Refractory Metals and Hard Materials* 41: 250-258. https://doi.org/10.1016/j.ijrmhm.2013.04.010.

Luo, X, K Cheng, R Holt, and X Liu. 2005. "Modeling flank wear of carbide tool insert in metal cutting." *Wear* (Elsevier) 259 (7-12): 1235-1240. https://doi.org/10.1016/j.wear.2005.02.044.

Mabrouki, T, C Courbon, Y Zhang, J Rech, D Nelias, MD Asad, H Hamdi, S Belhadi, and F Salvatore. 2016. "Some insights on the modelling of chip formation and its morphology during metal cutting operations." *Computational simulation of manufacturing processes* 344 (4-5): 335-354. doi:https://doi.org/10.1016/j.crme.2016.02.003.

Mabrouki, Tarek, François Girardin, Muhammad Asad, and Jean-François Rigal. 2008. "Numerical and experimental study of dry cutting for an aeronautic aluminium alloy (A2024-T351)." *International Journal of Machine Tools and Manufacture* 48 (11): 1187-1197. doi:https://doi.org/10.1016/j.ijmachtools.2008.03.013.

Magness Jr., L.S. 1994. "High strain rate deformation behaviors of kinetic energy penetrator materials during ballistic impact." *Mechanics of Materials* 17 (2-3): 147-154. doi:https://doi.org/10.1016/0167-6636(94)90055-8.

Majzoobi, G.H., and F. R Dehgolan. 2011. "Determination of the constants of damage models." *11th International Conference on the Mechanical Behavior of Materials.* Como, Italy: Procedia Engineering. 764-773. doi:https://doi.org/10.1016/j.proeng.2011.04.127.

Martin Bäker, Aviral Shrot. 2013. "Inverse parameter identification with finite element simulations using knowledge-based descriptors." *Computational Materials Science* 69: 128–136.

Masoudi, S, M.A Gholami, J.M Iariche, and A Vafadar. 2017. "Infrared temperature measurement and increasing infrared measurement accuracy in the context of machining process." *Advances in Production Engineering & Management* 12 (4): 353–362. doi:https://doi.org/10.14743/apem2017.4.263.

Mathias, Agmell, Ahadi Aylin, and Stahl Jan-Eric. 2014. "Identification of plasticity constants from orthogonal cutting and inverse analysis." *Mechanics of Materials* (Lund University Publications) 77: 43-51. doi:10.1016/j.mechmat.2014.07.005.

Mativenga, P T, and K K B Hon. 2005. "Wear and cutting forces in high-speed machining of H13 using physical vapour deposition coated carbide tools." *Proceedings of the Institution of Mechanical Engineers, Part B: Journal of Engineering Manufacture* (Sage journals) 219 (2): 191-199. doi:https://doi.org/10.1243/95440505X8127.

Matsumura, T, T Shirakashi, and E Usui. 2008. "Identification of Wear Characteristics in Tool Wear Model of Cutting Process." *International Journal of Material Forming* (Springer) 1: 555-558. https://link.springer.com/article/10.1007/s12289-008-0297-4.

Michalski, D, K Strąk, and M Piasecka. 2017. "Comparison of two surface temperature measurement using thermocouples and infrared camera." *The European Physical Journal Conferences* 143: 02075. doi:10.1051/epjconf/201714302075 .

1997. *Modern metal cutting : a practical handbook.* Sandviken, Sweden : Sandvik Coromant.

Murugesan, M, and D.W Jung. 2019. "Johnson Cook Material and Failure Model Parameters Estimation of AISI-1045 Medium Carbon Steel for Metal Forming Applications." *materials* 12 (4): 609. doi:https://doi.org/10.3390/ma12040609.

Najar, Kaleem Ahmad, and Mohammad Mursaleen Butt. 2018. "Development of a dual-layered diamond-coated WC–Co cutting tool for enhancing tool life in the dry machining of mild-steel alloy." *Proceedings of the Institution of Mechanical Engineers, Part B: Journal of Engineering Manufacture* (SAGE Publications) 233 (5): 1515-1528. doi:10.1177/0954405418780179.

Nandam, Srinivasa Rao, U. Ravikiran, and A. Anand Rao. 2014. "Machining of Tungsten Heavy Alloy under Cryogenic Environment." *3rd International Conference on Materials Processing and Characterisation.* Hyderabad: Procedia Materials Science. 296-303. doi:https://doi.org/10.1016/j.mspro.2014.07.037.

Nguyen, T.H, and Q.C Hsu. 2017. "Study on Cutting Forces and Material Removal Rate in Hard Milling of SKD 61 Alloy Steel." *Journal of the Chinese Society of Mechanical Engineers, Transactions of the Chinese Institute of Engineers - Series C* 38 (1): 41-51.

Niaki, Farbod Akhavan , Durul Ulutan, and Laine Mears. 2015. "In-ProcessTool Flank WearEstimation in Machining Gamma-Prime Strengthened Alloys Using Kalman Filter." *Procedia Manufacturing.* 696-707. doi:doi: 10.1016/j.promfg.2015.09.018 .

Ning, Jinqiang, and Steven Y. Liang. 2019. "Inverse identification of Johnson-Cook material constants based on modified chip formation model and iterative gradient

search using temperature and force measurements." *The International Journal of Advanced Manufacturing Technology* 102 (9-12): 2865-2876.

Ning, Jinqiang, and Steven Y. Liang. 2019. "Inverse identification of Johnson-Cook material constants based on modified chip formation model and iterative gradient search using temperature and force measurements." *The International Journal of Advanced Manufacturing Technology* 102: 2865-2876. doi:https://doi.org/10.1007/s00170-019-03286-0.

Ning, Jinqiang, and Steven Y. Liang. 2018. "Model-driven determination of Johnson-Cook material constants using temperature and force measurements." *The International Journal of Advanced Manufacturing Technology* 97: 1053-1060. doi:https://doi.org/10.1007/s00170-018-2022-x.

Oxley, P. L. B. 1963. "Rate of Strain Effect in Metal Cutting." *Journal of Manufacturing Science and Engineering* (ASME) 85 (4): 335-337. doi:https://doi.org/10.1115/1.3669884.

Ozel, T., I. Llanos, J. Soriano, and P.J. Arrazola. 2011. "3D Finite Element modedlling of Chip formation Process for Machining INCONEL 718: Comparison of FE Software Predictions." *Machining Science and Technology* 15 (1): 21-46. doi:https://doi.org/10.1080/10910344.2011.557950.

Ozel, Tugrul, and Yigit Karpat. 2007. "Identification of Constitutive Material Model Parameters for High-Strain Rate Metal Cutting Conditions Using Evolutionary Computational Algorithms." *Materials and Manufacturing Processes* 22 (5): 659-667. doi:https://doi.org/10.1080/10426910701323631.

Palanisamy, N.K, E.R Lorphevre, F Ducobu, and P.J Arrazola. 2020. "Influence of the Choice of the Parameters on Constitutive Models and their Effects on the Results of Ti6Al4V Orthogonal Cutting Simulation." *23rd International Conference on Material Forming.* Cottbus, Germany: Procedia Manufacturing. 458-465. doi:https://doi.org/10.1016/j.promfg.2020.04.335.

Pandey, A, A Goyal, and R Meghvanshi. 2017. "Experimental Investigation and Optimization of Machining Parameters of Aerospace Material Using Taguchi's DOE Approach." *International Conference on Advancements in Aeromechanical Materials for Manufacturing.* Hyderabad, India: Materialstoday: Proceedings. 7246-7251. doi:https://doi.org/10.1016/j.matpr.2017.07.053.

Parida, Asit Kumar, and Kalipada Maity. 2018. "Comparison the machinability of Inconel 718, Inconel 625 and Monel 400 in hot turning operation." *Engineering Science and Technology, an International Journal* 21 (3): 364-370. doi:https://doi.org/10.1016/j.jestch.2018.03.018.

Pawade, R. S., and Suhas S. Joshi. 2011. "Mechanism of Chip Formation on High-speed Turning of INCONEL 718." *Machining Science and Technology* 15 (1): 132-152. doi:https://doi.org/10.1080/10910344.2011.557974.

Pawade, Raju shrihari, and Auhas S. Joshi. 2011. "Multi-objective optimization of surface roughness and cutting forces in high-speed turning of Inconel 718 using Taguchi grey relational analysis (TGRA)." *The international Journal of Advanced Manufacturing Technology* 56: 47-62. doi:https://doi.org/10.1007/s00170-011-3183-z.

Piispanen, Vaino. 1948. "Theory of Formation of Metal Chips." *Journal of Applied Physics* 19 (10): 876. https://doi.org/10.1063/1.1697893.

Prabhu, G., R. Arockia Kumar, and T.K Nandy. 2018. "Effect of Yttrium Oxide Dispersion on the Microstructure and Properties of Tungsten Heavy Alloys." *Defence Science Journal* 68 (4): 406-411. doi: https://doi.org/10.14429/dsj.68.12255 .

Prakash, K.S, P.M. Gopal, and S. Karthik. 2020. "Multi-objective optimization using Taguchi based grey relational analysis in turning of Rock dust reinforced Aluminum MMC." *Measurement* 157: 107664. doi:https://doi.org/10.1016/j.measurement.2020.107664.

Prakash, K.Soorya , P.M Gopal, and S Karthik. 2020. "Multi-objective optimization using Taguchi based grey relational analysis in turning of Rock dust reinforced Aluminum MMC." *Measurement* 157. doi:https://doi.org/10.1016/j.measurement.2020.107664.

Pramanik, A. 2013. "Problems and solutions in machining of titanium alloys." *The International Journal of Advanced Manufacturing Technology* 70: 919–928. doi:https://doi.org/10.1007/s00170-013-5326-x.

Pramanik, Alokesh, and Guy Littlefair. 2015. "Machining of Titanium Alloy (Ti-6Al-4V)—Theory to Application." *Machining Science and Technology* 19 (1): 1-49. doi:https://doi.org/10.1080/10910344.2014.991031.

Priyadarshini, A, S.K Pal, and A.K Samantaray. 2012. "Finite Element Modeling of Chip Formation in Orthogonal Machining." In *Statistical and Computational Techniques in Manufacturing*, by J.P Davim, 101-144. Springer, Berlin, Heidelberg. doi:https://doi.org/10.1007/978-3-642-25859-6_3.

Qiang, Z, X Miao, M Wu, and R Sawhney. 2018. "Optimization of abrasive waterjet machining using multi-objective cuckoo search algorithm." *The International Journal of Advanced Manufacturing Technology* 99: 1257–1266. doi:https://doi.org/10.1007/s00170-018-2549-x.

R.Yildiz, Ali. 2013. "Optimization of cutting parameters in multi-pass turning using artificial bee colony-based approach." *Information Sciences* (Elsevier) 220: 399-407. https://doi.org/10.1016/j.ins.2012.07.012.

Rabin, B. H, and R. M German. 1988. "Microstructure effects on tensile properties of tungsten-Nickel-Iron composites." *Metallurgical Transactions A* 19 (6): 1523-1532. doi:https://doi.org/10.1007/BF02674026.

Rajendra, B., and D. Deepak. 2016. "Optimization of Process Parameters for Increasing Material Removal Rate for Turning Al6061 Using S/N Ratio." *International Conference on Emerging Trends in Engineering, Science and Technology.* Trissur, india: Procedia Technology. 399-405. doi:https://doi.org/10.1016/j.protcy.2016.05.055.

Rakesh, Merugu, and Saurav Datta. 2019. "Effects of Cutting Speed on Chip Characteristics and Tool Wear Mechanisms During Dry Machining of Inconel 718 Using Uncoated WC Tool." *Arabian Journal for Science and Engineering* 44: 7423–7440. doi:https://doi.org/10.1007/s13369-019-03785-y.

Rani, K.N.A, M.F AbdulMalek, and S Neoh. 2012. "Nature-inspired Cuckoo Search Algorithm for Side Lobe Suppression in a Symmetric Linear Antenna Array." *Radio Engineering* 21 (3): 868-874.

Rao, C. J, D.N Rao, and P Srihari. 2013. "Influence of cutting parameters on cutting force and surface finish in turning operation." *International Conference on Design and Manufacturing.* Chennai, India: Procedia Engineering. 1405-1415. doi:https://doi.org/10.1016/j.proeng.2013.09.222.

Rao, V.Durga Prasad, Sk.R.S. Mahaboob Ali, Sk.M.Z.M. Saqheed Ali, and V.Navya Geethika. 2018. "Multi-objective optimization of cutting parameters in CNC turning of stainless steel 304 with TiAlN nano coated tool." *Materialstoday Proceedings* 5 (12, Part 1): 25789-25797. doi:https://doi.org/10.1016/j.matpr.2018.06.571.

Ravi, S, and P Gurusamy. 2020. "Experimental investigation of cryogenic cooling on cutting force, surface roughness and tool wear in end milling of hardened AISI D3 steel using uncoated tool." *Materials today: Proceedings* In press, corrected proof. doi:https://doi.org/10.1016/j.matpr.2020.04.741.

Raykar, S.J., D.M. D'Addona, and A.M. Mane. 2015. "Multi-objective Optimization of High Speed Turning of Al 7075 Using Grey Relational Analysis." *9th CIRP Conference on Intelligent Computation in Manufacturing Engineering.* Elsevier. 293-298. doi:https://doi.org/10.1016/j.procir.2015.06.052.

Raykar, S.J., D.M. D'Addona, and A.M. Mane. 2015. "Multi-objective optimization of high speed turning of Al 7075 using grey relational analysis." *9th CIRP Conference on Intelligent Computation in Manufacturing Engineering.* Capri, Italy: Procedia CIRP. 293 – 298. doi:https://doi.org/10.1016/j.procir.2015.06.052.

Rodriguez, J.M., P. Jonsen, and A. Svoboda. 2017. "Simulation of metal cutting using the particle finite-element method and a physically based plasticity model." *Computional Particle Mechanics* 4: 35-51. doi:https://doi.org/10.1007/s40571-016-0120-9.

Rohr, I., H. Nahme, K. Thoma, and C.E. Anderson. 2008. "Material characterisation and constitutive modelling of a tungsten-sintered alloy for a wide range of strain rates." *International Journal of Impact Engineering* 35 (8): 811-819. doi:https://doi.org/10.1016/j.ijimpeng.2007.12.006.

Sagar, Chithajalu Kiran, Amrita Priyadarshini, and Amit Kumar Gupta. 2020. "Optimization of Machining Parameters During Turning of Tungsten Heavy Alloys Using Taguchi Analysis." *ASME International Mechanical Engineering Congress and Exposition.* ASME. V001T03A017; 10 pages. doi:https://doi.org/10.1115/IMECE2019-10958.

Sagar, Chithajalu Kiran, Tarun Kumar, Amrita Priyadarshini, and Amit Kumar Gupta. 2019. "Prediction and optimization of machining forces using oxley's predictive theory and RSM approach during machining of WHAs." *Defence Technology* (In press, corrected proof). https://doi.org/10.1016/j.dt.2019.07.004.

Saini, S, I.S Ahuja, and V.S Sharma. 2012. "Influence of cutting parameters on tool wear and surface roughness in hard turning of AISI H11 tool steel using ceramic tools." *International Journal of Precision Engineering and Manufacturing* 13: 1295–1302. doi:https://doi.org/10.1007/s12541-012-0172-6.

Saleem, Waqas, Muhammad Zain-ul-abdein, Hassan Ijaz, Abdullah Salmeen Bin Mahfouz, Anas Ahmed, Muhammad Asad, and Tarek Mabrouki. 2017. "Computational Analysis and Artificial Neural Network Optimization of Dry Turning Parameters—AA2024-T351." *Applied Sciences* 7. doi:doi:10.3390/app7060642.

Salimiasl, Aydin. 2017. "Modeling of the Tool Flank Wear in Turning Process." *International Journal of Manufacturing Systems* 7 (1): 1-9. doi:10.3923/ijmsaj.2017.1.9.

Sassi, I., and F. Ghmari. 2009. "The emissivity of conductor Gaussian random rough surfaces: the surface impedance boundary condition method." *Physics Procedia* 2 (3): 773-779. doi:https://doi.org/10.1016/j.phpro.2009.11.024.

Seker, Ulvi, Abdullah Kurt, and İbrahim Ciftci. 2004. "The effect of feed rate on the cutting forces when machining with linear motion." *Journal of Materials Processing Technology* 146 (3): 403-407. doi:https://doi.org/10.1016/j.jmatprotec.2003.12.001.

Senthilkumar, N. , T. Tamizharasan, and V. Anandakrishnan. 2014. "An Hybrid Taguchi-Grey Relational Technique and Cuckoo Search Algorithm for Multi-Criteria Optimization in Hard Turning of AISI D3 Steel." *Journal of Advanced Engineering Research* 1 (1): 16-31. https://dl.jaeronline.com/papers/vol01issue012014/03_JAER_V1N1.pdf.

Senthilnathan, N., A.R Annamalai, and G. Venkatachalam. 2018. "Microstructure and mechanical properties of spark plasma sintered tungsten heavy alloys." *Materials Science and Engineering: A* 710: 66-73. doi:https://doi.org/10.1016/j.msea.2017.10.080.

Serra, R., H. Chibane, and A. Duchosal. 2018. "Multi-objective optimization of cutting parameters for turning AISI 52100 hardened steel." *The International Journal of Advanced Manufacturing Technology* 99: 2025-2034. doi:https://doi.org/10.1007/s00170-018-2373-3.

Shihab, S.K, Z.A Khan, and A.N Siddiquee. 2013. "Effect of Cutting Parameters on Cutting Forces and MRR During Turning Hard Alloy Steel With and Without Coolant." *International Journal of Engineering and Advanced Technology* 3 (1): 14-30. https://www.semanticscholar.org/paper/Effect-of-Cutting-Parameters-on-Cutting-Forces-and-Shihab-Khan/0c80dc8e9e5f9ff749962e254e143335342d7140.

Silva, Marcio Bacci da, and James Wallbank. 1999. "Cutting temperature: prediction and measurement methods—a review." *Journal of Materials Processing Technology* 88 (1-3): 195-202. doi:https://doi.org/10.1016/S0924-0136(98)00395-1.

Singh, Devendra, Vimanyu Chadha, and Ranganath M Singari. 2016. "Effect of Nose Radius on Surface Roughness during CNC Turning using Response Surface Methodology." *International Journal of Recent advances in Mechanical Engineering* 5 (2). doi:10.14810/ijmech.2016.5203.

Sredanovic , B, D Cica , S Tesic, and D Kramar. 2019. "Optimization of Cutting Parameters for Minimizing Specific Cutting Energy and Maximizing Productivity in Turning of AISI 1045 Steel." *International Scientific Journal "Machnes, Technologies, Materials"* 13 (11): 491-494. doi:https://stumejournals.com/journals/mtm/2019/11/491.

Stephenson, D. A. 1991. "Assessment of Steady-State Metal Cutting Temperature Models Based on Simultaneous Infrared and Thermocouple Data." *Journal of Manufacturing Science and Engineering* 113 (2): 121-128. doi:https://doi.org/10.1115/1.2899668.

Stephenson, David A, and John S Agapiou. 2016. *Metal Cutting Theory and Practice*. 3. Taylor and Francis.

Sutter, G, and N Ranc. 2007. "Temperature fields in a chip during high-speed orthogonal cutting—An experimental investigation." *International Journal of Machine Tools and Manufacture* 47 (10): 1507-1517. doi:https://doi.org/10.1016/j.ijmachtools.2006.11.012.

Tang, Linhu, Yongji sun, Baodong Li, Jiancheng shen, and Guoliang Meng. 2019. "Wear performance and mechanisms of PCBN tool in dry hard turning of AISI D2 hardened steel." *Tribology International* (Elsevier) 132: 228-236. https://doi.org/10.1016/j.triboint.2018.12.026.

Thakur, A, V Sharma, S.S Bhadauria, and A Gupta. 2020. "Effect of Cutting Parameters on MRR and Surface Roughness in Turning of AISI 1018 and AISI P20 Using Taguchi Method." In *Optimization Methods in Engineering.*, by M Tyagi, A Sachdeva and V Sharma, 185-196. Optimization Methods in Engineering. Lecture Notes on Multidisciplinary Industrial Engineering. doi:https://doi.org/10.1007/978-981-15-4550-4_11.

Thakur, Ankit, Varun Sharma, Shailendra Singh Bhadauria, and Ajay Gupta. 2020. "Effect of Cutting Parameters on MRR and Surface Roughness in Turning of AISI 1018 and AISI P20 Using Taguchi Method." In *Optimization Methods in*

Engineering. Lecture Notes on Multidisciplinary Industrial Engineering., by M Tyagi, A Sachdeva and V Sharma, 185-196. Springer, Singapore. doi:https://doi.org/10.1007/978-981-15-4550-4_11.

Thakur, D. G., B. Ramamoorthy, and L. Vijayaraghavan. 2009. "Machinability investigation of Inconel 718 in high-speed turning." *The International Journal of Advanced Manufacturing Technology* 421 (45). doi:https://doi.org/10.1007/s00170-009-1987-x.

Thirugnanasambandam, K, S Prakash, V Subramanian, S Pothula, and V Thirumal. 2019. "Reinforced cuckoo search algorithm-based multimodal optimization." *Applied Intelligence* 49: 2059–2083. doi:https://doi.org/10.1007/s10489-018-1355-3.

Trimble, D., A. Agarwal, D. McDonnell, S. Barron, E. Ahearne, and G.E. O'Donnell. 2020. "Finite element simulation of orthogonal machining of biomedical grade Co–Cr–Mo alloy." *CIRP Journal of Manufacturing Science and Technology* 28: 8-14. doi:https://doi.org/10.1016/j.cirpj.2020.01.008.

Twari, A, A Mandal, and K Kumar. 2015. "Multi-objective Optimization of Electro-chemical Machining by Non-dominated Sorting Genetic Algorithm." *4th International Conference on Materials Processing and Characterzation.* Hyderabad, India: Materials Today: Proceedings. 2569-2575. doi:https://doi.org/10.1016/j.matpr.2015.07.208.

Usui, E, T Shirakashi, and T Kitagawa. 1984. "Analytical prediction of cutting tool wear." *Wear* (Elsevier) 100 (1-3): 129-151. https://doi.org/10.1016/0043-1648(84)90010-3.

Venkatesan, N.S. 1985. "Recent Developments in Anti-Tank Ammunition." *Defence Science Journal* 35 (2): 225-230. doi:https://doi.org/10.14429/dsj.35.6015 .

Venugopal, K.A, S. Paul, and A.B Chattopadhyay. 2007. "Growth of tool wear in turning of Ti-6Al-4V alloy under cryogenic cooling." *Wear* 262 (9-10): 1071-1078. https://doi.org/10.1016/j.wear.2006.11.010.

Woodward, R.L., N.J. Baldwin, I. Burch, and B.J. Baxter. 1985. "Effect of strain rate on the flow stress of three liquid phase sintered tungsten alloys." *Metallurgical Transactions A* (Springer) 16 (11): 2031–2037.

Wu, Xian, Liang Li, Ning He, Guolong Zhao, Feng Jiang, and Jianyun Shen. 2018. "Study on the tool wear and its effect of PCD tool in micro milling of tungsten carbide." *International Journal of Refractory Metals and Hard Materials* (Elsevier) 77: 61-67. https://doi.org/10.1016/j.ijrmhm.2018.07.010.

Wyen, C.-F., and K. Wegener. 2010. "Influence of cutting edge radius on cutting forces in machining titanium." *CIRP Annals - Manufacturing Technology* 59 (1): 93-96. doi:https://doi.org/10.1016/j.cirp.2010.03.056.

Xiaoqing, Zhou, Li Shukui, Liu Jinxu, Wang Yingchun, and Wang Xing. 2010. "Self-sharpening behavior during ballistic impact of the tungsten heavy alloy rod

penetrators processed by hot-hydrostatic extrusion and hot torsion." *Materials Science and Engineering: A* 527 (18-19): 4881-4886. doi:https://doi.org/10.1016/j.msea.2010.04.050.

Xie, Zhi, Daochun Xu, Ziyi Cui, and Miaoxuan Li. 2019. "Evaluation of a cutting simulation using a cupronickel B10 constitutive model considering the deformation temperature." *Journal of Mechanical Science and Technology* 1349-1356. doi:https://doi.org/10.1007/s12206-019-0235-z.

Yang, Xin She. 2014. *Nature-Inspired Optimization Algorithms*. 1st. Elsevier. Accessed February 2017. https://www.elsevier.com/books/nature-inspired-optimization-algorithms/yang/978-0-12-416743-8.

Yang, B, J Miao, Z.C Fan, J Long, and X.H Liu. 2018. "Modified cuckoo search algorithm for the optimal placement of actuators problem." *Applied Soft Computing* 67: 48-60. doi:https://doi.org/10.1016/j.asoc.2018.03.004.

Yang, S. H., and U. Natarajan. 2010. "Multi-objective optimization of cutting parameters in turning process using differential evolution and non-dominated sorting genetic algorithm-II approaches." *The International Journal of Advanced Manufacturing Technology* 49: 773–784. doi:https://doi.org/10.1007/s00170-009-2404-1.

Yang, X.S, and S Deb. 2013. "Multiobjective cuckoo search for design optimization." *Computers & Operations Research* 40 (6): 1616-1624. doi:https://doi.org/10.1016/j.cor.2011.09.026.

Yang, Xin-She, and Suash Deb. 2013. "Multiobjective cuckoo search for design optimization." *Computers & Operations Research* 40 (6): 1616-1624. doi:https://doi.org/10.1016/j.cor.2011.09.026.

Yen, Yung- Chang, Jorg Sohner, Blaine Lilly, and Taylan Altan. 2004. "Estimation of tool wear in orthogonal cutting using the finite element analysis." *Journal of Materials Processing Technology* (Elsevier) 16 (1): 82-91. https://doi.org/10.1016/S0924-0136(03)00847-1.

Yildiz, A.R. 2013. "Optimization of cutting parameters in multi-pass turning using artificial bee colony-based approach." *Information Sciences* (Elsevier) 220: 399-407. https://doi.org/10.1016/j.ins.2012.07.012.

Young, Hong Tsu. 1996. "Cutting temperature responses to flank wear." *Wear* (Elsevier) 201 (1-2): 117-120. https://doi.org/10.1016/S0043-1648(96)07227-4.

Zabel, A, T Rödder, and M Tiffe. 2017. "Material Testing and Chip Formation Simulation for Different Heat Treated Workpieces of 51CrV4 Steel." *Procedia CIRP* 58: 181-186. doi:https://doi.org/10.1016/j.procir.2017.03.218.

Zabel, A., T. Rodder, and M. Tiffe. 2017. "Material Testing and Chip Formation Simulation for Different Heat Treated Workpieces of 51CrV4 Steel." *Procedia CIRP* 58: 181-186. doi:https://doi.org/10.1016/j.procir.2017.03.218.

Zang, Jian, Jun Zhao, Anhai Li, and Jiming Pang. 2018. "Serrated chip formation mechanism analysis for machining of titanium alloy Ti-6Al-4V based on thermal property." *The International Journal of Advanced Manufacturing Technology* 98: 119–127. doi:https://doi.org/10.1007/s00170-017-0451-6.

Zanger, F, and V Schulze. 2013. "Investigations on Mechanisms of Tool Wear in Machining of Ti-6Al-4V Using FEM Simulation." *Procedia CIRP* (Elsevier) 8: 158-163. https://doi.org/10.1016/j.procir.2013.06.082.

Zhang, H, J Zhao, F Wang, J Zhao, and A Li. 2014. "Cutting forces and tool failure in high-speed milling of titanium alloy TC21 with coated carbide tools." *Proceedings of the Institution of Mechanical Engineers, Part-B: Journal of Engineering Manufacture* 229 (1): 20-27. doi:https://doi.org/10.1177/0954405414526578.

Zhang, Z, S Ding, and W Jia. 2019. "A hybrid optimization algorithm based on cuckoo search and differential evolution for solving constrained engineering problems." *Engineering Applications of Artificial Intelligence* 85: 254-268. doi:https://doi.org/10.1016/j.engappai.2019.06.017.

Zhao, H, G.C Barber, and Q Zou. 2002. "A study of flank wear in orthogonal cutting with internal cooling." *Wear* (Elsevier) 253 (9-10): 957-962. https://doi.org/10.1016/S0043-1648(02)00248-X.

Zheng, G, R Xu, X Cheng, G Zhao, L Li, and J Zhao. 2018. "Effect of cutting parameters on wear behavior of coated tool and surface roughness in high-speed turning of 300M." *Measurement* 125: 99-108. doi:https://doi.org/10.1016/j.measurement.2018.04.078.

Zheng, Hongyu, and Kui Liu. 2014. *Machinability of Engineering Materials.* London: In: Nee A. (eds) Handbook of Manufacturing Engineering and Technology.Springer. doi:https://doi.org/10.1007/978-1-4471-4976-7_2-1.

Zhou, Jinhua, Junxue Ren, Yazhou Feng, Weijun Tian, and Kaining Shi. 2017. "A modified parallel-sided shear zone model for determining material constitutive law." *The International Journal of Advanced Manufacturing Technology* 91 (1-4): 589-603.

Zimmerman , C, SP Boppana, and K Katbi . 1989. *Machinability test methods In: Metals Handbook.* 9. Vol. 16. ASM international.

APPENDIX

Extended Oxley's machining theory

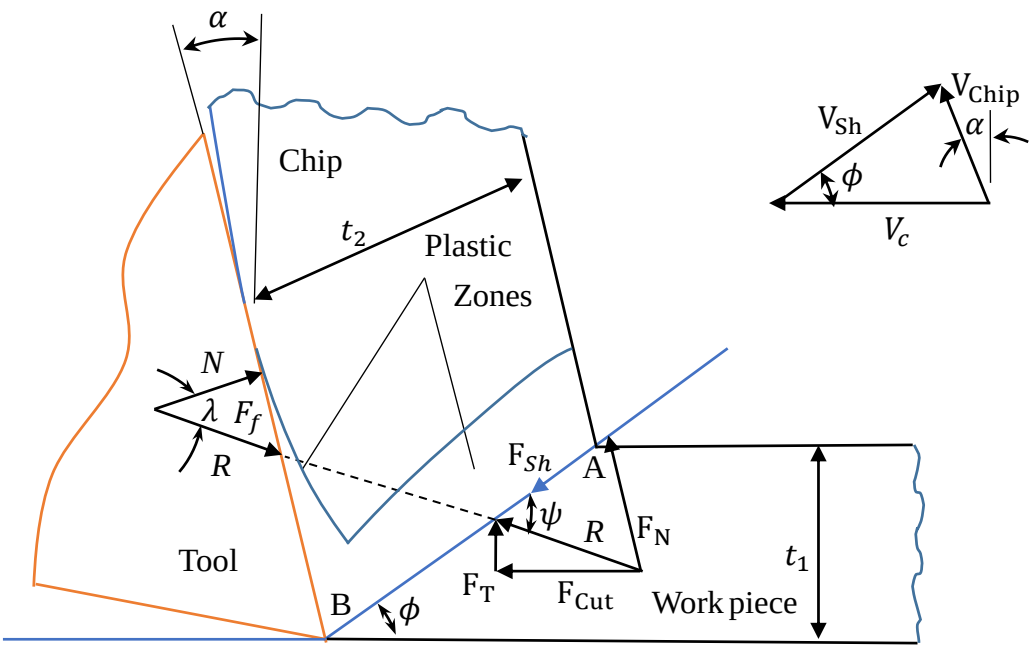

Figure A.1 Parallel sided shear zone model

The equivalent strain hardening exponent n_{eq} was calculated using following equation

$$n_{eq} = \frac{nB\varepsilon_{AB}^{n}}{A + B\varepsilon_{AB}^{n}} \tag{A.1}$$

where, ε_{AB} equivalent strain along shear plane and l the length of shear plane AB is obtained from t_1 the undeformed chip thickness and ϕ shear angle

$$l = \frac{t_1}{sin(\phi)} \tag{A.2}$$

Shear velocity v_{sh} is calculated by considering v_c cutting velocity, α rake angle and shear angle in following form:

$$V_{Sh} = \frac{V_c\, cos(\alpha)}{cos(\phi - \alpha)} \tag{A.3}$$

The ε_{AB} equivalent strain and $\dot{\varepsilon}_{AB}$ strain-rate at AB are determined considering the Von-Mises criterion:

$$\varepsilon_{AB} = \frac{\eta_{AB}}{\sqrt{3}} = \frac{1}{2\sqrt{3}} \times \frac{cos(\alpha)}{sin(\phi)\, cos(\phi - \alpha)} \tag{A.4}$$

$$\dot{\varepsilon}_{AB} = \frac{\dot{\eta}_{AB}}{\sqrt{3}} = \frac{1}{\sqrt{3}} \times \frac{C_0 V_{sh}}{l} \tag{A.5}$$

The T_{AB} average temperature along shear plane AB is given by:

$$T_{AB} = T_w + \varsigma \frac{(1-\xi) F_{Sh} V_{Sh}}{m_{chip} C_P} \tag{A.6}$$

where, T_w work piece initial temperature, ς sensible heat along shear plane, ξ coefficient of heat partition, F_{sh} shear force at shear plane, m_{chip} chip mas per unit time, c_p specific heat of workpiece. For the present analysis, ς was assumed to be 0.9. Following equations were used for further analysis:

if $0.04 \leq M_T \tan\phi \leq 10$

$$\xi = 0.5 - 0.35\, log_{10}(M_T \tan\phi) \tag{A.7}$$

if $M_T \tan\phi \geq 10$

$$\xi = 0.3 - 0.15\, log_{10}(M_T \tan\phi) \tag{A.8}$$

$$M_T = \frac{\rho C_P V_c t_1}{k_w} \tag{A.9}$$

where, M_T non-dimensional thermal number, ρ density of workpiece, k_w thermal conductivity of workpiece.

Using Equation (A.5) m_{chip} has been calculated

$$m_{chip} = \rho V_c T d \tag{A.10}$$

The average flow stress in the primary shear zone q_{AB} is calculated using the JC Material Model:

$$q_{AB} = \frac{\sigma_{AB}}{\sqrt{3}} = (A + B\varepsilon_{AB}^n)\left(1 + C\, ln\left(\frac{\dot{\varepsilon}_{AB}}{\dot{\varepsilon}_0}\right)\right)\left(1 - \left(\frac{T_{AB} - T_w}{T_m - T_w}\right)^m\right) \tag{A.11}$$

The shear force F_{Sh} along the shear plane, AB can be calculated from q_{AB}, d depth of cut:

$$F_{Sh} = q_{AB} l d \tag{A.12}$$

The angle ψ between shear plane AB and the resultant force R is given by

$$\psi = tan^{-1}(1 + 2\left(\frac{\pi}{4} - \phi\right) - C_0 n_{eq}) \tag{A.13}$$

where, C_0 ratio of shear plane length by thickness of primary shear zone.

Using the value of ψ, the average friction angle at the tool-chip interface λ can be determined:

$$\lambda = \psi - \phi + \alpha \tag{A.14}$$

R Resultant cutting force, F_f Friction force and F_N Normal force at the tool-chip interface, F_c cutting force and F_t thrust force are given by:

$$R = \frac{F_{Sh}}{cos\,\psi} \tag{A.15}$$

$$F_f = R\,sin\,\lambda \tag{A.16}$$

$$N = R\,cos\,\lambda \tag{A.17}$$

$$F_C = R\,cos(\lambda - \alpha) \tag{A.18}$$

$$F_t = R\,sin(\lambda - \alpha) \tag{A.19}$$

t_2 cut chip thickness can be calculated from f feed rate, α rake angle and ϕ shear angle using the equation:

$$t_2 = \frac{t_1\,cos(\phi - \alpha)}{sin(\phi)} \tag{A.20}$$

Similarly, velocity of chip V_{Chip} is given as:

$$V_{Chip} = \frac{V_c\,sin(\phi)}{cos(\phi - \alpha)} \tag{A.21}$$

The tool-chip interface length L_{int} and shear stress at the tool-chip interface τ_{int} can be evaluated by:

$$L_{int} = \frac{t_1\,sin(\psi)}{cos\,\lambda\,sin(\psi)}\left(1 + \frac{C_0 n_{eq}}{3\left(1 + 2\left(\frac{\pi}{4} - \phi\right) - C_0 n_{eq}\right)}\right) \tag{A.22}$$

$$\tau_{int} = \frac{F_f}{L_{int} d} \tag{A.23}$$

The maximum shear strain at the tool-chip interface ε_{int} is given by:

$$\varepsilon_{int} = \frac{\eta_{int}}{\sqrt{3}} = \frac{1}{\sqrt{3}} * (2\eta_{AB} + 0.5\eta_M) \tag{A.24}$$

Where, η_{AB} is shear strain across shear plane, total maximum shear strain across chip-tool interface $\eta_M = \frac{L_{int}}{\zeta t_2}$ and ζ is the ratio of plastic zone tool-chip interface thickness to chip thickness

The equivalent strain-rate at the tool-chip interface $\dot{\varepsilon}_{int}$is given by:

$$\dot{\varepsilon}_{int} = \frac{\dot{\eta}_{int}}{\sqrt{3}} = \frac{1}{\sqrt{3}} * \frac{V_{Chip}}{\zeta t_2} \tag{A.25}$$

It is derived based on the assumption that the plastic zone formed at the tool-chip interface is a rectangular zone of thickness ζt_2.

The average temperature at the tool-chip interface T_{int} is given by:

$$T_{int} = T_w + \frac{(1-\xi)F_{Sh}V_{Sh}}{m_{chip}C_P} + \Psi \Delta T_M \tag{A.26}$$

The value of maximum temperature increase in chip ΔT_M and average temperature increase in chip ΔT_C is as follows:

$$log_{10}\left(\frac{\Delta T_M}{\Delta T_C}\right) = 0.06 - 0.195(\zeta)\sqrt{\frac{M_T t_2}{t_1}} + 0.5 log_{10}\left(\frac{M_T t_2}{L_{int}}\right) \tag{A.27}$$

$$\Delta T_C = \frac{F_f V_{Chip}}{m_{chip}C_P} \tag{A.28}$$

Once T_{int} is calculated, q_{chip} can be determined as:

$$q_{chip} = \frac{1}{\sqrt{3}}(A + B\varepsilon_{int}^n)\left(1 + C\ ln\left(\frac{\dot{\varepsilon}_{int}}{\dot{\varepsilon}_0}\right)\right)\left(1 - \left(\frac{T_{int} - T_w}{T_m - T_w}\right)^m\right) \tag{A.29}$$

$$\sigma'_N = q_{AB}\left(1 + \frac{\pi}{2} - 2\alpha - 2C_0 n_{eq}\right) \tag{A.30}$$

$$\sigma_N = \frac{N}{L_{int}w} \tag{A.31}$$

Table A 1 Full factorial data set for optimization

SN	V	f	α	G	Fc	T	VB
1	30	0.05	2	90	47.22	83	285.77
2	50	0.05	2	90	45.44	116	336.86
3	70	0.05	2	90	43.41	119	371.33
4	30	0.1	2	90	62.25	142	316.83
5	50	0.1	2	90	52.36	157	355.41
6	70	0.1	2	90	36.28	165	352.22
7	30	0.15	2	90	87.35	153	355.28
8	50	0.15	2	90	66.39	161	384.86
9	70	0.15	2	90	52.83	168	399.34
10	30	0.05	-5	90	28.96	98	196.04
11	50	0.05	-5	90	30.8	105	237.57
12	70	0.05	-5	90	40.61	165	294.51
13	30	0.1	-5	90	32.3	137	204.61
14	50	0.1	-5	90	45.43	152	272.48
15	70	0.1	-5	90	47.76	170	310.76
16	30	0.15	-5	90	43.89	147	226.91
17	50	0.15	-5	90	64.59	167	306.95
18	70	0.15	-5	90	68.88	203	352.23
19	30	0.05	-8	90	45.09	91	217.78
20	50	0.05	-8	90	31.84	134	243.31
21	70	0.05	-8	90	28.56	156	268.01
22	30	0.1	-8	90	80.12	117	250.24
23	50	0.1	-8	90	77.59	140	295.69
24	70	0.1	-8	90	51.11	164	301.05
25	30	0.15	-8	90	80.31	131	251.09
26	50	0.15	-8	90	74.41	159	293.59
27	70	0.15	-8	90	51.67	166	301.82
28	30	0.05	2	95	27.89	78	239.49
29	50	0.05	2	95	29.52	113	291.55
30	70	0.05	2	95	47.76	114	383
31	30	0.1	2	95	52.56	106	297.45
32	50	0.1	2	95	47	164	343.19
33	70	0.1	2	95	46	148	380.31
34	30	0.15	2	95	56.36	131	305.89
35	50	0.15	2	95	64.77	153	381.25
36	70	0.15	2	95	66.61	124	428.38
37	30	0.05	-5	95	38.41	94	215.19
38	50	0.05	-5	95	41.39	125	263.18
39	70	0.05	-5	95	45.44	138	304.41
40	30	0.1	-5	95	42.28	158	224.57

41	50	0.1	-5	95	47.73	167	277.65
42	70	0.1	-5	95	49	162	313.11
43	30	0.15	-5	95	45.01	136	228.38
44	50	0.15	-5	95	54	138	289.24
45	70	0.15	-5	95	73.14	168	357.99
46	30	0.05	-8	95	50.07	90	222.71
47	50	0.05	-8	95	41.4	168	257.54
48	70	0.05	-8	95	29	197	270.2
49	30	0.1	-8	95	35.73	117	208.89
50	50	0.1	-8	95	79.36	134	297.03
51	70	0.1	-8	95	82.74	168	337.81
52	30	0.15	-8	95	63.61	149	237.99
53	50	0.15	-8	95	64.69	153	283.51
54	70	0.15	-8	95	70.05	160	323.67
55	30	0.05	2	97	38.38	111	268.28
56	50	0.05	2	97	49.2	121	346.27
57	70	0.05	2	97	51.96	132	395.23
58	30	0.1	2	97	59.22	132	311.08
59	50	0.1	2	97	52	169	355.19
60	70	0.1	2	97	47	173	384.34
61	30	0.15	2	97	65.22	206	324.09
62	50	0.15	2	97	66.42	198	386.4
63	70	0.15	2	97	33.65	243	344.87
64	30	0.05	-5	97	49.89	120	236.01
65	50	0.05	-5	97	28.3	136	232.37
66	70	0.05	-5	97	37.17	230	287.11
67	30	0.1	-5	97	51.58	177	240.58
68	50	0.1	-5	97	40.9	198	264.59
69	70	0.1	-5	97	52	217	321.03
70	30	0.15	-5	97	54.04	212	245.06
71	50	0.15	-5	97	61.25	150	300.81
72	70	0.15	-5	97	89.56	281	384.51
73	30	0.05	-8	97	50	99	223.1
74	50	0.05	-8	97	55.02	111	270.91
75	70	0.05	-8	97	57.12	138	307.38
76	30	0.1	-8	97	57.97	130	232.08
77	50	0.1	-8	97	78.04	155	296.92
78	70	0.1	-8	97	81.61	165	336.48
79	30	0.15	-8	97	84.9	138	255.01
80	50	0.15	-8	97	66.41	161	285.67
81	70	0.15	-8	97	106.04	165	360.19

Non-dominating sorting genetic algorithm:

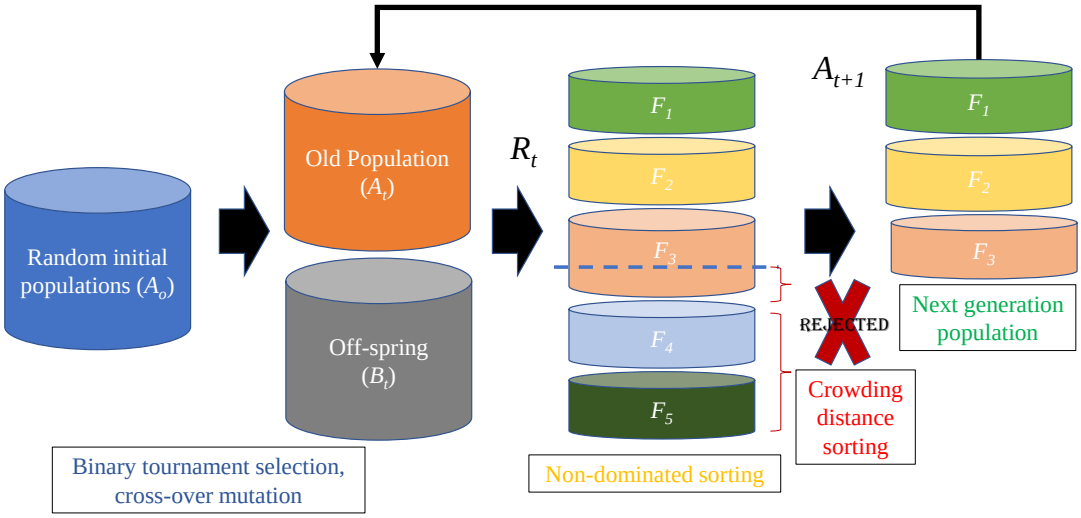

Figure A.2 Flow chart for NSGA II

The steps are detailed as follows:

Step 1: Initially, a random parent population A_0 is created. Then the population size is sorted by the non-domination process. The solution containing the population is assigned a fitness equal to its non-domination level. Thus, fitness is assumed as a minimization function. In the first iteration, the binary tournament selection, recombination, and mutation operators are used to create an offspring population B_o of size N_p.

Step 2: Then, the procedure changes after the first generation. The total of t = 400 generations was assigned. Firstly, a combined population $R_t = A_t \cup B_t$ is formed. The population R_t is sorted according to non-domination, A_t is old population, B_t is off spring population and its size is taken as $2N$. Since R_t includes the present and older population, elitism is ensured.

Step 3: Further, the best non-dominated solution set for the combined population is considered as R_t. If the size of F_1 is smaller than N_p, then all members of the set F_1 are selected for the new population A_{t+1}. The other remaining set of the A_{t+1} population is chosen from the subsequent non-dominated fronts in the order of their ranking, as shown in Figure A.2 Thus, solutions from the set F_2, F_3 ...F_i is chosen until maximum possible sets could be accommodated.

Step 4: Further to choose N_p population members accurately and to fill all population slots, the best population size from F_1 to F_i are selected, using a crowding distance

operator γ_n to sort the solutions according to their rank and crowding distance in descending order. The new population A_{t+1} of size N_p is used for selection, crossover, and mutation to create a new population B_{t+1} of size N_p. It is noted that first-generation binary tournament is used to find F_1 solution and a crowding distance operator γ_n is used to find other solution sets in further generations. The operator γ_n requires rank and crowding distance of each population to evaluate the quantities to form population $A_{t+1.}$

Step 5: According to non-domination, sorting an entire population of 2 N_p need not be sorted as the sorting procedure has found enough number of fronts to have N members in A_{t+1}. Thus, the diversity among the non-dominated solutions is introduced by using crowding distance comparison operators. The crowding distances are calculated in objective function space and the solution with a lower rank is preferred. If there is a clash between the solutions that belong to the same front, then the solution that is located in a lesser crowded region is selected as the best solution.

Step 6: Further, the procedure from step 2 to step 5 will continue till there is no further improvement in the solution for a successive number of generations, and the algorithm terminations this acts as stopping criteria for NSGA-II.

LIST OF PUBLICATIONS

Journals Papers

1. Chithajalu Kiran Sagar, Tarun Kumar, Amrita Priyadrashini and Amit Kumar Gupta "Prediction and Optimization of Machining Forces using Oxley's Predictive Theory and RSM Approach during machining of WHAs," Defence Technology Journal (KeAi),15(6), 2019, 923-935, https://doi.org/10.1016/j.dt.2019.07.004. (IF: 1.261, Indexing: SCI-E)
2. Chithajalu Kiran Sagar, Amrita Priyadrashini, Amit Kumar Gupta and Devanshi Mathur, "Experimental investigation of tool wear characteristics and analytical prediction of tool life using a modified tool wear rate model while machining 90 WHA," Part B: Journal of Engineering Manufacture (Sage), 235(1-2), 2020, 242-254, https://doi.org/10.1177/0954405420933113. (IF: 1.982, Indexing: SCI)
3. Chithajalu Kiran Sagar, Amrita Priyadrashini, Amit Kumar Gupta, Tarun Kumar and Shreya Sexana, "An alternate approach to SHPB tests to compute Johnson-Cook material model constants for 97 WHA at high strain rates and elevated temperatures using machining tests", Journal of Manufacturing Science and Engineering (ASME), 143(2):021004,2020, https://doi.org/10.1115/1.4047738. (IF: 2.875, Indexing: SCI-E)
4. Chithajalu Kiran Sagar, Amrita Priyadrashini and Amit Kumar Gupta, "Effect of tungsten content on the machinability of Tungsten Heavy alloys," Defence Science Journal (DRDO), 71(2), 2021, 162-170, https://doi.org/10.14429/dsj.71.15857. (IF: 0.73, Indexing: SCI-E)
5. Chithajalu Kiran Sagar, Amrita Priyadrashini, Amit Kumar Gupta, Manmohan Das and Abhideep Tripathy, "Formulation of Novel FE based Hybrid algorithms for Multi objective Optimization of Process Parameters while Machining Tungsten Heavy Alloys", Sadhana, paper communicated.

Book Chapter

1. Chithajalu Kiran Sagar, Amrita Priyadrashini and Amit Kumar Gupta, "Effect of Johnson Cook Material Model Constants on Predicted Chip Morphology and Forces in FE Simulations of Machining Operation for 93% WHA Alloy," Shunmugam M., Kanthababu M. (eds) Advances in Simulation, Product Design

and Development. Lecture Notes on Multidisciplinary Industrial Engineering. Springer, Singapore. https://doi.org/10.1007/978-981-32-9487-5_18. (Indexing: SCOPUS)

Conference Proceedings

1. Chithajalu Kiran Sagar, Amrita Priyadrashini and Abhiram Chilukuri, "Determination of high strain rate Material model constants for 93% WHA and optimization using Genetic Algorithm," ICMPC_2018, Materials Today: Proceedings 5, 2018, 18911-18919. https://doi.org/10.1016/j.matpr.2018.06.240 (Indexing: SCOPUS)
2. Chithajalu Kiran Sagar, Amrita Priyadrashini, Amit Kumar Gupta and S. K. Shukla, "Determination of Johnson Cook Material Model Constants and Their Influence on Machining Simulations of Tungsten Heavy Alloy," ASME, ASME International Mechanical Engineering Congress and Exposition, Vol. 1: Advances in Aerospace Technology, Pittsburgh, PA, USA, 2019. https://doi.org/10.1115/IMECE2018-88270 (Indexing: SCOPUS)
3. Chithajalu Kiran Sagar, Amrita Priyadrashini, Amit Kumar Gupta, "Optimization of Machining Parameters during Turning of Tungsten Heavy Alloys using Taguchi Analysis," ASME, ASME International Mechanical Engineering Congress and Exposition, Vol. 1: Advances in Aerospace Technology, Salt Lake city, Utah, USA, 2020. https://doi.org/10.1115/IMECE2019-10958 (Indexing: SCOPUS)

BIOGRAPHY

Biography of the Candidate

Chithajalu Kiran Sagar (author), graduated in Mechanical Engineering (B.E) from Nitte Meenakshi Institute of Technology, Bengaluru, India in the year 2010. Thereafter, he completed his master degree (M.Tech) in 2012 with specialization in Tool Engineering, from R V College of Engineering, Bengaluru, India. On completion of his post-graduation, he preferred to build his career in teaching and worked as Assistant professor in Dayananda Sagar Academy of Technology and Management, Bengaluru, India for a period of three years. Thereafter to enhance his knowledge and to build research oriented career he joined the Doctoral research program in the Department of Mechanical Engineering, Birla Institute of Technology and Science, Pilani, Hyderabad campus in 2015. He is a member of The American Society of Mechanical Engineers (ASME). He has 11 publications in various journals and conferences of international repute.

Biography of the Supervisor

Dr. Amrita Priyadarshini received her Doctoral degree from the Department of Mechanical Engineering, Indian Institute of Technology Kharagpur in the year 2012. Her research interest lies in the area of machinability studies, material characterization, surface coatings, finite element analysis and optimization of machining and other manufacturing processes. Currently, she is working as Assistant Professor in the Department of Mechanical Engineering, Birla Institute of Technology and Science, Pilani, Hyderabad campus and has a post PhD teaching experience of 7 years. So far, she has 20 publications in various journals and conferences of international repute. She has one ongoing sponsored research project, as Principal Investigator, funded by ARMREB-DRDO and is supervising two more PhD students, one in the area of machining while other in the area of mechanical alloying and surface coatings.

Biography of the Co-supervisor

Dr. Amit Kumar Gupta is working as a Professor in the Department of Mechanical Engineering, Birla Institute of Technology and Science (BITS), Pilani, Hyderabad

Campus. He obtained his Doctoral degree from Nanyang Technological University (NTU), Singapore and Bachelor's degree from Indian Institute of Technology (IIT), Delhi in Mechanical engineering. For his PhD, he has received the prestigious Singapore Millennium Foundation award and for the excellence in teaching and research at BITS, he has been awarded the Prof. S. Venkateswaran Faculty Excellence Award, 2013. His research interest lies in the area of sheet metal forming, tensile testing and constitutive modeling, production scheduling, manufacturing simulation and modeling, predictive modeling and optimization of manufacturing processes. He has successfully completed funded projects from BRNS, DST, UGC, DRDO, etc. and authored more than 150 publications in journals and conferences of international repute.